Virtual forming of metallic sheet materials : influence of complex strain paths on service life prediction

Diane Hérault

To cite this version:

Diane Hérault. Virtual forming of metallic sheet materials : influence of complex strain paths on service life prediction. Materials. Université de Bretagne Sud, 2021. English. NNT : 2021LORIS800 . tel-03770186

HAL Id: tel-03770186
https://theses.hal.science/tel-03770186
Submitted on 6 Sep 2022

THÈSE DE DOCTORAT DE

L'UNIVERSITÉ DE BRETAGNE SUD

ÉCOLE DOCTORALE N° 602
Sciences pour l'Ingénieur
Spécialité : *Mécanique des Solides, des Matériaux,*
des Structures et des Surfaces

Par
Diane HERAULT

Du formage virtuel à la tenue en service de pièces métalliques : influence des trajets complexes de déformation

Virtual forming of metallic sheet materials : influence of complex strain paths on service life prediction

Thèse présentée et soutenue à distance, le 30 juin 2021
Unité de recherche : Institut de Recherche Dupuy de Lôme (IRDL), UMR CNRS 6027
Thèse N° : 600

Rapporteurs avant soutenance :

Laurent TABOUROT	Professeur des universités, Université Savoie Mont Blanc
Luc PENAZZI	Maître de conférence, HDR, IMT Mines Albi-Carmaux

Composition du Jury :

Président :	Carl LABERGERE	Professeur des universités, Université de Technologie de Troyes
Examinateurs :	Elisabeth MASSONI	Directrice de recherche, Mines Paris Tech
	Cédric DOUDARD	Professeur des universités, ENSTA Bretagne
	Mustapha ZIANE	Ingénieur de recherche, ESI Group
	Laurent TABOUROT	Professeur des universités, Université Savoie Mont Blanc
	Luc PENAZZI	Maître de conférence, HDR, IMT Mines Albi-Carmaux
Dir. de thèse :	Sandrine THUILLIER	Professeur des universités, Université Bretagne Sud
Co-dir. de thèse :	Pierre-Yves MANACH	Professeur des universités, Université Bretagne Sud

À la mémoire de mon père...

REMERCIEMENTS

Les travaux de recherche présentés dans ce manuscrit, ont été réalisés au cours d'une thèse CIFRE en collaboration entre l'Institut de Recherche Dupuy de Lôme (IRDL) et l'entreprise ESI Group. Je tiens tout d'abord à remercier mes directeurs de thèse, Sandrine Thuillier et Pierre-Yves Manach, pour m'avoir soutenue et guidée pendant ces trois années. Du côté d'ESI, je remercie Anne Chambard pour son encadrement et sa réactivité, ainsi que Mustapha Ziane pour son implication dans le projet et pour le temps précieux qu'il m'a accordé. Je remercie également tous les partenaires du projet, Hongjin Choi, Myoung-Gyu Lee, Pei Shan Wang, Houssem Badreddine, Khémais Saanouni et Carl Labergère pour nos échanges pendant ces trois années de collaboration.

Je remercie sincèrement tous les membres du jury et particulièrement, Laurent Tabourot, Luc Penazzi et Elisabeth Massoni, pour l'intérêt porté à mes travaux.

Je tiens aussi à exprimer ma reconnaissance envers Cédric Doudard et Bruno Levieil pour leur accueil à l'ENSTA Bretagne et pour leur aide particulièrement bénéfique aux travaux de ma thèse. Je remercie également Arcelor Mittal et particulièrement Bastien Weber pour l'intérêt porté à mes travaux et le soutien matériel.

Mes remerciements vont aussi à Frédéric Barlat pour m'avoir accueilli dans son laboratoire en Corée du Sud et pour m'avoir appris beaucoup. Je remercie également tous les étudiants avec qui j'ai travaillé sur place pour leur accueil chaleureux.

Je remercie aussi particulièrement Anthony Jegat pour son implication tout au long de ma thèse me permettant ainsi d'obtenir de nombreux résultats expérimentaux. Je souhaite également remercier Yann Guevel et Hervé Bellegou pour leurs disponibilités à la moindre question. Je ne manquerai pas de remercier aussi tous mes collègues de bureau, et plus particulièrement Cynthia Tayeh, pour tous les bons moments passés ensemble.

Enfin, un grand merci à ma famille, mes amis pour m'avoir toujours encouragée et à Maxime pour son soutien jour après jour.

TABLE OF CONTENTS

LIST OF FIGURES

LIST OF TABLES

INTRODUCTION

Virtual prototyping and integrated design

Virtual manufacturing is a priority for automotive constructors that need to balance between costs, quality and performance of the products in order to fulfill the safety, comfort and environmental requirements. The weight reduction of the vehicle, already essential in order to reduce greenhouse gas emissions and fuel consumption, is now mandatory with the large scale development of hybrid and electric vehicles to increase their range. The efforts are concentrated on the car body structures including chassis and suspensions that represent approximately 60% of the weight, excluding the powertain according to a study performed for a Toyota Venza [1], cf. Figure 1(a).

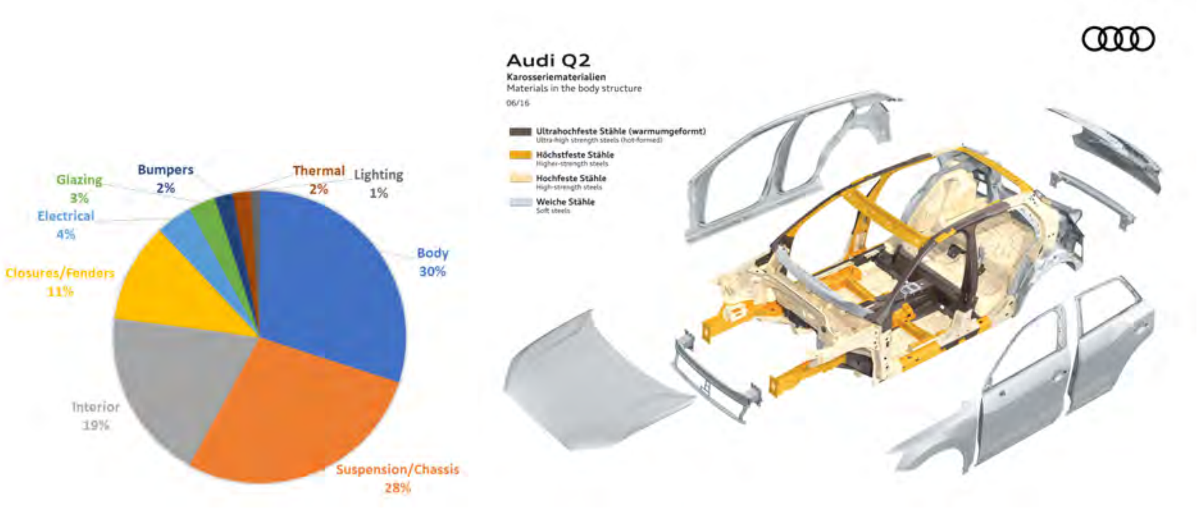

(a) Example of weight ratios for a Toyota Venza (2010)

(b) Example of car body materials for an Audi Q2 (2016)

Figure 1 – Examples of weight ratios and car body materials for two different automotive models [1], [2]

To achieve a weight reduction, the use of lightweight materials such as aluminium and composites has largely increased but they do not fulfill safety requirements for some body components and thus steels are still preferred, considering also that steels are easier to recycle. An example of the materials used for the car body components of an Audi Q2 from 2016 [2] in Figure 1(b) shows that steelis still predominant. A reduction of steel sheet thickness is sought in order to reduce weight and high strength steels such as dual phase (DP) steels, twinning-induced plasticity (TWIP) steels and transformation-induced plasticity (TRIP) steels, have been developed in order to increase the strength-to-weight ratio of the steels [3]. The use of lightweight components added a new level of complexity during the mechanical design phase with the choice of the most suited material, the optimization of the geometries and thicknesses and the joining of different materials.

The goal of virtual prototyping is to propose an evolution from single-point numerical simulation dedicated to each design phases towards end-to-end simulations with an improved design chain. The aim is to reach an integrated design that takes into account the manufacturing effects during all the design phases, from the feasibility study of the product to its resistance to crash or fatigue. For car body components, the main manufacturing process is sheet metal forming considered in this study. Different studies have already made progress towards integrated design with the aim of coupling the virtual forming with the in-service life prediction [4]–[8]. The integrated design approach is illustrated in that case in Figure 2 and shows that in order to optimize the geometry and material choice a simulation loop may be put in place in order to use the residual stresses obtained from the virtual forming process as an input in the simulation of the service load. The simulation loop is then performed until the predicted service life fulfill the requirements to validate the material and geometry choices.

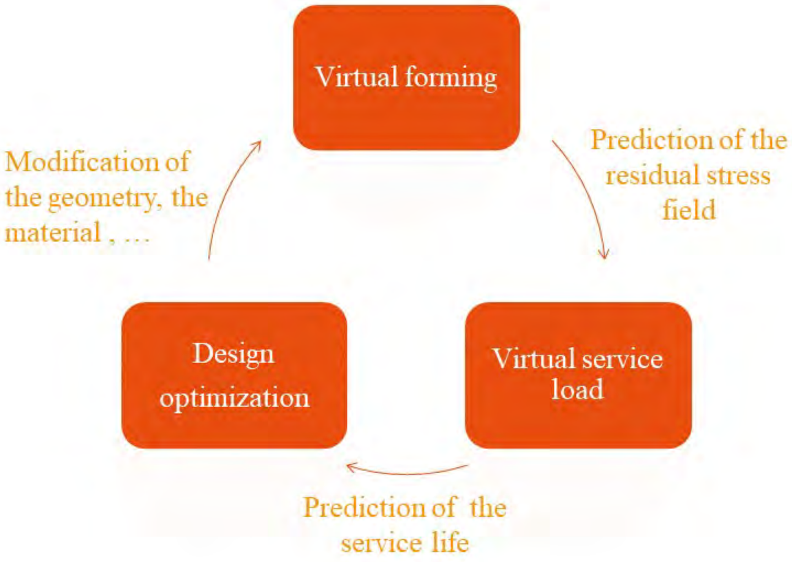

Figure 2 – Illustration of the integrated design approach in the case of a coupling of forming and fatigue

This study is performed as part of a CIFRE collaboration with ESI Group, which is a leader in virtual prototyping and develop a zero-prototype strategy to achieve a design with virtual tests that can replace the physical prototyping. Reaching the goal of zero prototype is complex but solutions are developed to obtain a first physical prototype that is directly good. The effects of the manufacturing process need to be anticipated during the product engineering phase in order to detect potential problems. This virtual approach, compared to the typical industrial workflow in Figure 3, has the advantage of reducing the cost and time dedicated to the development of a product.

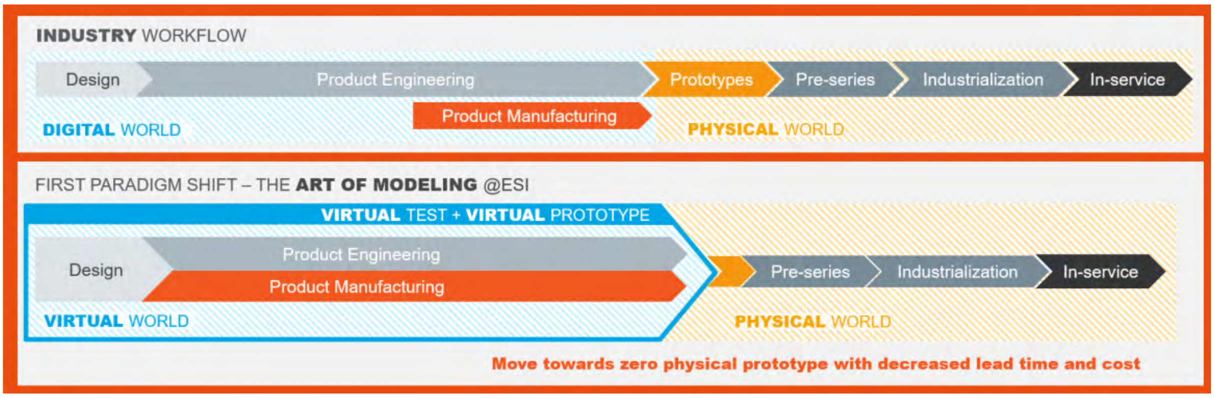

Figure 3 – Illustration of the zero-prototype strategy of ESI Group

Industrial project

ESI Group has initiated a collaborative project with the aim to achieve an integrated design of sheet metal components in collaboration with three academic partners, the University of Technology in Troyes (UTT), the Seoul National University (SNU) and the University of South Britanny (UBS). The aim of this project is to develop virtual forming models including the ductile damage occurrence during sheet metal forming but also a low cycle fatigue damage model in order to predict the fatigue life of the mechanical components obtained by sheet metal forming. Two advanced models dedicated to sheet metal forming are considered as a starting point because the influence of large plastic strains and complex strain paths, characteristic of sheet metal forming, are already included in their formulation. A thermodynamically-consistent approach with the Anisotropic Fully Coupled (AFC) model developed in UTT [9] is compared to a different approach aiming to reproduce the microstructural behavior at a macroscopic scale with the Homegenous Anisotropic Hardening (HAH) model developed by F. Barlat [10], [11] and implemented in finite element codes by M.G. Lee, supervisor of the project in SNU.

The overall aim of the project is to compare the influence of these two modeling approaches on the residual stress prediction and thus on the service life prediction. At the beginning of the project, the ductile damage occurring during sheet metal forming was already developed in the AFC model but not the consideration of low cycle fatigue damage whereas damage was not introduced in HAH model. The implementation of each model in ESI Group finite element code, PAM-STAMP, is performed by PhD students of UTT and SNU for AFC and HAH models respectively. The UBS contribution in this study is positioned at the interface between numerical and experimental work with the aim of calibrating and validating the implementations of the models. Due to the degree of progress in the development of the models, a collaborative strategy was put in place. The calibration and numerical validation of the AFC model is performed in UTT whereas the calibration and numerical validation of the HAH model is performed in UBS without damage and in SNU for the addition of damage. The same experimental database composed of characterization, forming and fatigue tests performed in IRDL, is used for the different calibrations.

The aim of this PhD study is therefore to investigate both numerically and experimentally the influence of complex strain paths occurring during the forming process on the subsequent service life of demonstrators that are representative of the behavior of automotive structural parts. However, due to different time schedules and progress of the PhD students, the virtual forming models with the addition of ductile damage was not available to develop the forming and fatigue demonstrators. Thus, the ductile damage occurrence during sheet metal forming is not considered in this study in order to focus on the fatigue behavior of formed parts. The forming model considered is the HAH model and an uncoupled fatigue criterion is considered as a first approach for service life prediction. A dual phase steel of grade DP600, provided by ArcelorMittal, is selected for the study as a reference of high strength steels used to manufacture car body components. The study is presented in five chapters, starting from the characterization of the DP600 behavior regarding forming and fatigue, following with the sheet metal forming of a demonstrator and ending by a prediction of the demonstrator service life.

Overview of the manuscript

In the first chapter, the mechanical behavior of a dual phase steel DP600 is studied regarding linear, non-linear and cyclic strain paths. A bibliographic review is firstly presented about the two main behaviors of interest for this study, the strain path changes and the low cycle fatigue behavior of metallic materials. Microstructural observations and characterization tests are then performed for the DP600 material and different strain paths. Uniaxial tensile test, simple shear test and bulge test are considered for linear strain paths whereas sequential tests composed of shear and tension are considered for non-linear ones. The cyclic behavior studied in the low cycle fatigue range is characterized by alternated tension-compression test performed with a strain control.

In the second chapter, the different characterization tests are used to calibrate the material constitutive law dedicated to the forming simulation and the fatigue criterion. For the forming process, the equations of the constitutive law composed of an isotropic hardening law, an anisotropic yield criterion Yld2000-2d and a distortional hardening law, the enhanced HAH model are presented with the respective calibration procedure. The identified parameters are presented with a comparison of predicted and experimental stress-strain curves for the different characterization tests. For the fatigue criterion, after a review of different criteria, the calibration procedure and parameter identification of the modified Morrow criterion are presented.

In the third chapter, forming processes sensitive to strain path changes are presented including the deep-drawing in one and two stages of cylindrical cups. The experimental procedure of both processes is detailed with the specific methods used to measure the strain and residual stress fields of the different cups. The results composed of punch force-displacement curves and local evolutions along both rolling and transverse direction of the major and minor strains and the residual stresses are analyzed.

In the fourth chapter, the virtual forming of both processes is firstly simulated in Abaqus finite element code with comparison of a standard material taking into account pure isotropic hardening and the HAH model. The force-displacement curves are used to calibrate the simulations and the local evolutions of both strains and residual stresses are compared with the model predictions for both processes. The occurrence of complex strain paths is specifically considered and their influence on model predictions are analyzed. Finally, the implementation of e-HAH model in the industrial finite element code developed by ESI Group, PAM-STAMP, is validated and the results of forming simulations are compared to the experiments and the Abaqus predictions.

In the last chapter, the fatigue behavior of formed parts is presented with the selection of a fatigue loading for the cylindrical cups. Even if fatigue tests on cylindrical cups has not succeeded in the time allowed for this study, the numerical approach is presented with the adaptation of uniaxial criterion to multiaxial loads and the procedure for the finite element simulation of the fatigue loading. Finally, the predicted service life obtained for both processes with the standard and HAH models are compared and analyzed with regard to complex strain paths occuring during the forming process.

Conclusions and perspectives are then presented.

CHAPTER 1

MECHANICAL BEHAVIOR OF A DP600 DUAL PHASE STEEL

Dual phase steels are largely used for the manufacturing of automotive parts. High strength and formability are sougth-after properties for deep-drawing of sheet metals and the dual phase microstructure of these materials provides such properties [12]. These steels have also a high hardening rate and a yield strength higher than mild steel one, also largely used in sheet metal forming. A good energy absorption and fatigue strength result from these behaviors and make dual phase steels suitable to form structural and safety parts such as B-pillar reinforcement and bumper represented in Figure 1.1.

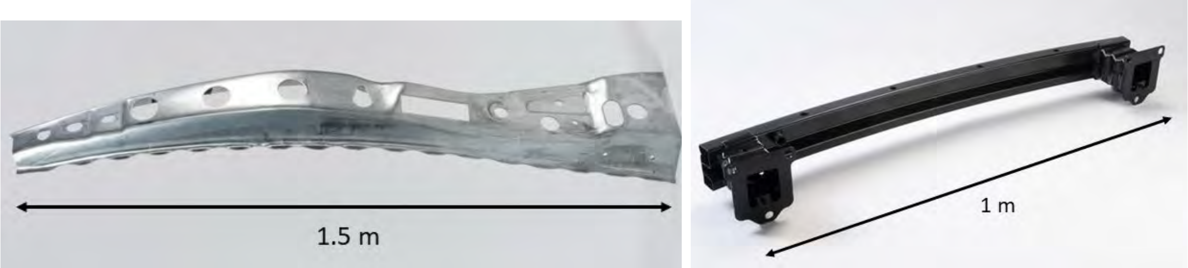

(a) B-pillar reinforcement

(b) Bumper

Figure 1.1 – Example of automotive parts formed from dual phase steel sheet material [12]

Considering these properties, a DP600 dual phase steel of thickness 1.2 mm is selected for this study where both forming and fatigue design of deep-drawn parts are investigated. The aim is to describe accurately the material behavior during forming with an advanced constitutive model in order to predict numerically a material state after forming and then to determine the fatigue properties of the formed part. The material behavior during sheet metal forming processes is influenced by complex strain paths which are of particular interest in this study. Characterization tests reproducing linear and non-linear strain paths are used to evaluate the material behavior with regards to forming whereas cyclic tests are performed to characterize the behavior in fatigue.

In this chapter, a general presentation of the behavior of sheet metals during complex strain paths and cyclic ones for the fatigue aspect is firstly performed. Then, the material microstructure is analyzed to evaluate the proportions of the two phases. Finally, the mechanical behavior of the material is presented for different linear, non-linear and cyclic strain paths.

1.1 Mechanical behavior of metallic sheet materials

1.1.1 Strain path change

To characterize the mechanical behavior of the dual phase steel considered in this study, two particular aspects of sheet metal forming process need to be studied, large strains and complex strain paths. Indeed, sheet metal forming processes such as deep-drawing exhibit strain path changes that can be represented on the graph of the major strain as a function of the minor strain, defined in the sheet plane. One example is shown in Figure 1.2 for a deep-drawn P-channel [13], which is a variation of the U-channel more classically used, with a curved side and a straight one. The evolution of the major and minor strains is represented for different locations of the part during the forming process and represents a strain path. Depending on the locations, linear strain path corresponding to change of strain levels with the same ratio between minor and major strains, or non-linear strain paths, characterized by a change of the minor-major strain ratio, are observed. This variation from the U-rail is carried out in order to observe a wider range of strain path changes that can be smooth or abrupt depending on the considered location of the P-rail.

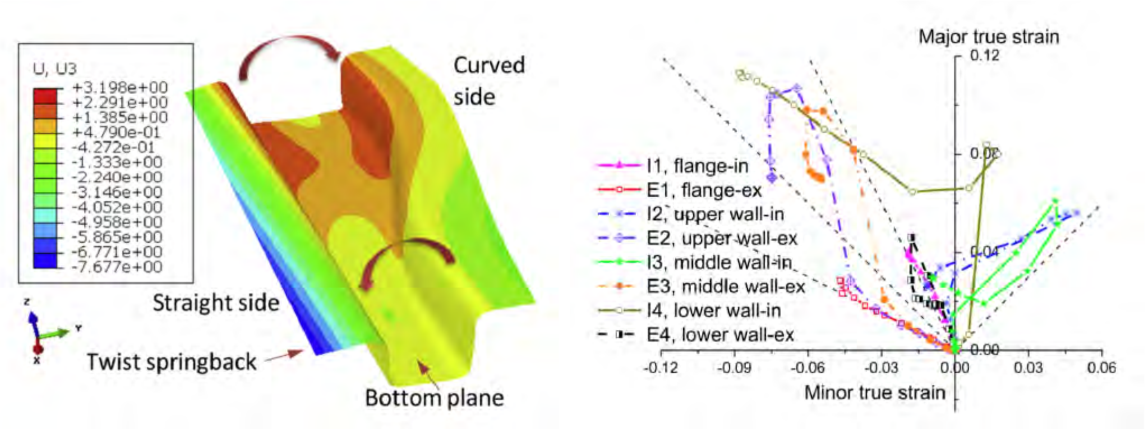

(a) P-rail geometry

(b) Strain paths of different points of the rail represented on the graph of the major-minor true strain

Figure 1.2 – Illustration of the strain path change occurrence during forming processes with the example of a deep-drawn P-channel [13]

Strain path change indicators

Different macroscopic indicators are proposed in the literature to quantify the magnitude of the strain path change, based either on strain or stress tensors. The oldest one is the Schmitt indicator [14] defined as

$$\theta = \frac{\dot{\boldsymbol{\varepsilon}}_1^p : \dot{\boldsymbol{\varepsilon}}_2^p}{\|\dot{\boldsymbol{\varepsilon}}_1^p\| : \|\dot{\boldsymbol{\varepsilon}}_2^p\|} \tag{1.1}$$

with $\dot{\boldsymbol{\varepsilon}}_1^p$ and $\dot{\boldsymbol{\varepsilon}}_2^p$ corresponding respectively to the plastic strain rate tensor of the first strain path and the one after the strain path change. Three main categories of strain path changes are distinguished, monotonic or quasi-monotonic, reverse and orthogonal strain path changes which correspond respectively to the value 1, -1 and 0 of the Schmitt indicator. It is possible to reproduce each case with dedicated tests. A monotonic strain path change is equivalent to the absence of strain path change, the plastic strain rate tensors $\dot{\boldsymbol{\varepsilon}}_1^p$ and $\dot{\boldsymbol{\varepsilon}}_2^p$ being proportional, the Schmitt indicator value is one. This value is obtained for example during a uniaxial tensile test but also during a loading-unloading-loading tensile test if the two loadings are performed along the same direction and in that case, the strain path change is quasi-monotonic. Then, reverse strain path changes are characterized for example by tension-compression test or forward-reverse shear test. In both cases, the plastic strain rate tensors $\dot{\boldsymbol{\varepsilon}}_1^p$ and $\dot{\boldsymbol{\varepsilon}}_2^p$ are identical but have opposite directions, the Schmitt indicator is thus equal to -1. Finally, orthogonal strain path change is obtained for example with a uniaxial tensile test followed by a simple shear test. For this sequence, the Schmitt indicator can be rewritten as

$$\theta = -\frac{\operatorname{sign}(\dot{\gamma}^p)(2r+1)}{\sqrt{1+r+r^2}} \sin(2\alpha) \tag{1.2}$$

with $\dot{\gamma}^p$ the shear strain rate during the second test, r the Lankford coefficient and α the angle between the first and the second loading directions [15]. If the two tests are performed along the same direction, the angle α is equal to 0 and so is the Schmitt indicator.

This indicator is effective when the change of strain path is abrupt because it considers two sequential strain increments. For example, it works very well when the second strain path is applied on a sample cut out of the first sample submitted to the pre-strain. However, when the change of strain path is more continuous and occurs rather smoothly over several strain increments, large variations of the Schmitt factor values can be recorded. A stabilizing procedure is proposed via the definition of a tensorial internal variable $\boldsymbol{G}$, that takes into account the strain path history [16]. The strain path change indicator ξ and the evolution law of $\boldsymbol{G}$ are described by

$$\xi = \frac{\boldsymbol{G} : \dot{\boldsymbol{\varepsilon}}^p}{\|\boldsymbol{G}\|\|\dot{\boldsymbol{\varepsilon}}^p\|} \text{ with } \dot{\boldsymbol{G}} = \dot{\boldsymbol{\varepsilon}}^p - c\|\dot{\boldsymbol{\varepsilon}}^p\|G \tag{1.3}$$

where the parameter c quantifies the weight of the strain path history and controls the rate at which ξ returns to a monotonic state. The use of ξ reduces oscillations of the indicator value that could be misinterpreted as strain path changes and can deal with multiple strain path changes [17], [18].

Conversely to the strain-based indicators, a stress-based formulation is used in the Homogenoeous Anisotropic Hardening (HAH) model

$$\cos\chi = H\ \hat{\boldsymbol{h}} : \hat{\boldsymbol{s}} \tag{1.4}$$

where H is a parameter equal to $\frac{8}{3}$ to simplify the constitutive equations and the normalized stress deviator $\hat{\mathbf{s}}$ is compared to the normalized microstructure deviator $\hat{\mathbf{h}}$ representing the stress history [10]. For these two indicators considering strain or stress history, the three particular cases of monotonic, reverse and orthogonal loading are equally described by the respective values 1, -1 and 0.

Strain path changes significantly influence the material behavior with particularities for reverse and orthogonal categories defined by the strain path change indicators. The macroscopic behavior of the metallic materials is presented thereafter for these two categories.

Reverse and orthogonal strain paths

The behavior of steel sheets regarding reverse and orthogonal strain path changes has been largely studied with the development of the indicators and characterization tests adapted for each category. Firstly, for reverse strain path changes, the sheets exhibit a decrease of the flow stress after a strain path reversal associated to the Bauschinger effect. Depending on the materials, a transient behavior is then observed or not. In the case of dual phase steels, it is present with a rounded yield point followed by a work-hardening stagnation for large pre-strains and then a resumption of the work-hardening with permanent softening. These behaviors are illustrated in Figure 1.3 with curves of the absolute shear stress as function of the accumulated shear strain for three forward-reverse shear tests performed on a dual phase steel DP600 of thickness 0.7 mm [19]. Reverse strain path changes are characterized at large strains by forward-reverse shear tests [15], [19], [20] but it is also possible to perform tension-compression tests, though at lower strains, due to the buckling risk in compression. The same behavior is observed in tension-compression for dual phase steels except for the work-hardening stagnation which is only present at large strains [21], [22].

Some studies have investigated the microstructural behavior of the material during the different strain path change tests and shown a link between the dislocation structures and the macroscopic mechanical behavior [19], [23]. During monotonic loading, dislocations arranged themselves with polarized boundaries in the loading direction called dislocation walls. When a

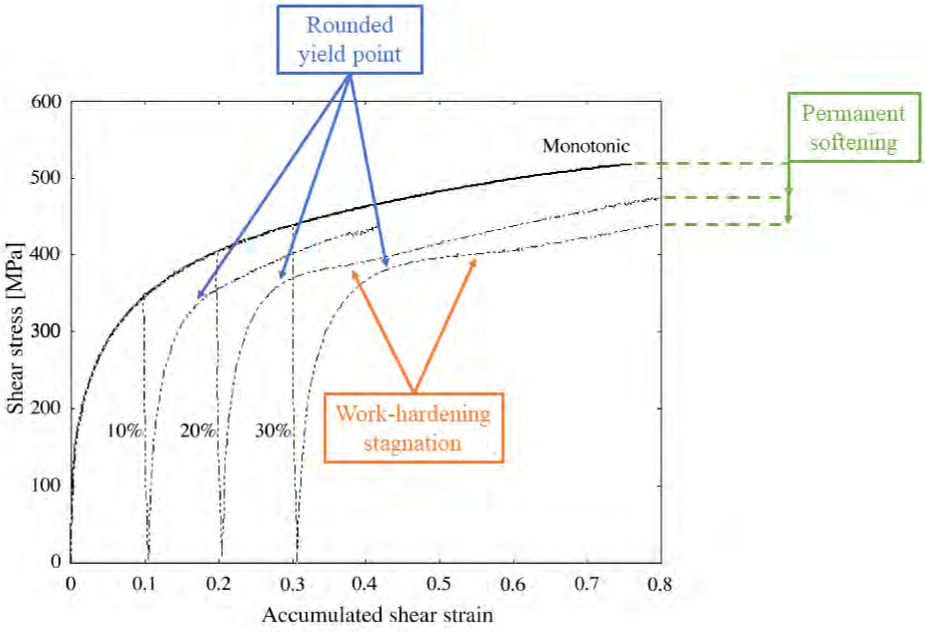

Figure 1.3 – Absolute shear stress as function of the accumulated shear strain for three forward-reverse shear tests (forward shear strain of 10 %, 20 % and 30 %) performed on a dual phase steel DP600 of thickness 0.7 mm [19]

reverse loading occurs, slip systems are activated in the opposite direction, which creates first a deletion of the predeformed dislocation walls corresponding to the work-hardening stagnation and then the resumption is caused by the creation of new walls.

For orthogonal strain path changes, sequential tests are performed with a first test consisting of a pre-strain in tension on a large sample and after unloading, shear specimens are cut from the first sample to perform the second test. The material behavior during the shear test after a pre-strain in tension is compared to a simple shear test by converting the pre-strain in tension into shear strain using usually the von Mises yield criterion. Two different features are observed depending on the materials, i.e. a cross-hardening corresponding to an overshoot of the flow stress after a strain path change is usually observed for mild steels contrary to dual phase steels which present a cross-contraction composed of a transient behavior followed by a hardening resumption to the monotonic level [15], [19], [24]. Both behaviors are illustrated in Figure 1.4 with the stress-strain curves of shear tests carried out along TD after pre-strains in tension along RD on a dual phase steel DP600 and a mild steel DC06 [23].

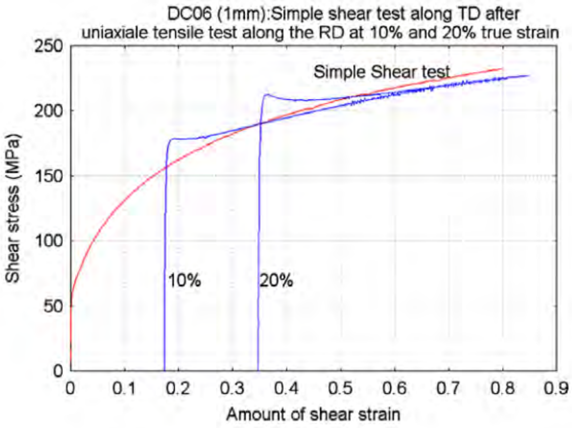

(a) DC06 - Cross-hardening

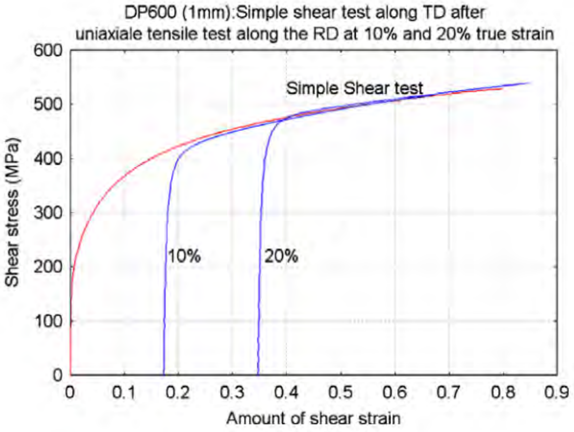

(b) DP600 - Cross-contraction

Figure 1.4 – Stress-strain curves for shear tests carried out along TD after pre-strains in tension along RD on a DP600 dual phase steel and a DC06 mild steel are represented in blue and compared with the monotonic shear stress-strain curves in red [23].

These specific behaviors are also linked to the dislocation structures, the stress overshoot is associated to latent hardening, i.e., activation of new slip systems whereas in the case of dual phase steel, it seems that a progressive deletion and creation of new dislocations walls occurs with no pronounced impact on the macroscopic behavior [19], [23]. In the same way, due to the microstructure evolution, a cyclic repetition of non-linear strain path changes, usually reverse ones, applied on materials until fatigue damage, causes specific behaviors that are detailed in the following section.

1.1.2 Fatigue behavior

The characterization of the fatigue behavior corresponds to the study of the material endurance under cyclic loadings until the initiation of a crack. Two main scenarios of fatigue are distinguished as a function of the number of cycles until failure ranging between the ultimate tensile stress in the case of a monotonic failure and the fatigue limit which corresponds to an infinite service life. The high cycle fatigue is characterized by a loading applied in the endurance range of the material, i.e. for a loading usually under the yield stress, corresponding to lifespan above 10^6 cycles approximately whereas for the low cycle fatigue situated under this lifespan value, the yield stress is exceeded locally during loading [25]. The number of cycles until failure depends on the stress amplitude of the cyclic loading. To characterize the fatigue behavior of a material, cyclic tests are performed for different stress or strain amplitudes in order to obtain the Wöhler curve, also called S-N curve, represented in Figure 1.5.

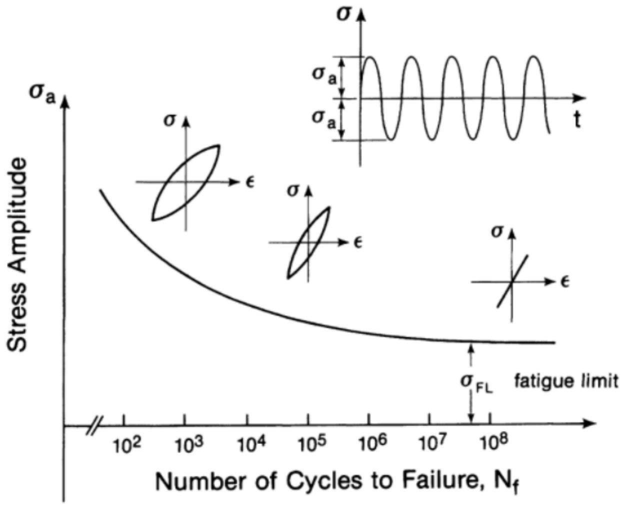

Figure 1.5 – Wöhler curve corresponding to the stress amplitude represented as a function of the number of cycle until failure [26]

The hysteresis loops also represented in Figure 1.5, illustrate the influence of the energy dissipated by mechanical hysteresis. Indeed, it is equal to the area of the hysteresis cycle and is linked to the fatigue damage [27]. In fact, the more the cycle is open, the more fatigue failure will occur for a low number of cycles. The two main categories of fatigue can be distinguished by the cycle opening which is large in low cycle fatigue because there is a cyclic plasticity and closed cycle in high cycle fatigue because the cycle are performed in the elastic range of the material. To be able to carry out the characterization tests and then the fatigue tests on deep-drawn parts over short enough times not exceeding one day, only the low cycle fatigue behavior of the considered material is studied thereafter.

Low cycle fatigue behavior of metallic materials

To characterize the fatigue behavior of a material, cyclic tension-compression tests are usually performed with strain control for low cycle fatigue whereas a load control is used in high cycle fatigue. With strain control, the E-N curve is considered instead of the S-N curve and corresponds to the total strain amplitude as a function of the number of cycles until failure instead of the stress amplitude. In that context, the parameters of the cyclic tension-compression test are [27]:

- the shape of the monitored signal, i.e. triangular or sinusoidal waveform, represented in Figure 1.6 as examples.
- the total strain amplitude $\Delta\varepsilon = \varepsilon_{max} - \varepsilon_{min}$
- the frequency $f = \dfrac{1}{T} = \dfrac{\dot{\varepsilon}}{2\Delta\varepsilon}$ with T the period of one cycle and $\dot{\varepsilon}$ the strain rate
- the strain ratio $R_\varepsilon = \dfrac{\varepsilon_{min}}{\varepsilon_{max}}$

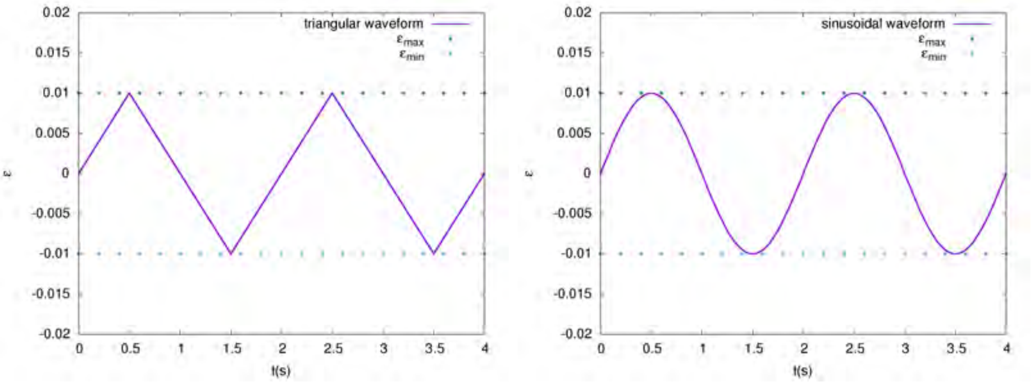

(a) Triangular cycles (b) Sinusoidal cycles

Figure 1.6 – Examples of monitoring signals for tension-compression tests

During the strain controlled tests, a transitional phase is first observed where the maximum and minimum stresses of the cycle evolve rapidly. Then, a stabilized behavior appears until the crack initiation which leads to an abrupt decrease and increase of the maximum and minimum stress of the cycle respectively. During the transitional phase, different behaviors may be observed that are represented in Figure 1.7. For alternated tests corresponding to a strain ratio equal to -1, a cyclic hardening or a cyclic softening, corresponding to a increase or a decrease of the maximum stresses of the cycle is observed due to the interactions or the rearrangement of the dislocations. When the strain ratio is not equal to -1, a partial or total relaxation of the mean stress may occur. Moreover, in certain cases, particularly for high mean stress and high stress amplitude, a cyclic creep, also called ratcheting, is observed corresponding to an accumulation of plastic strain at each cycle leading to a positive mean strain.

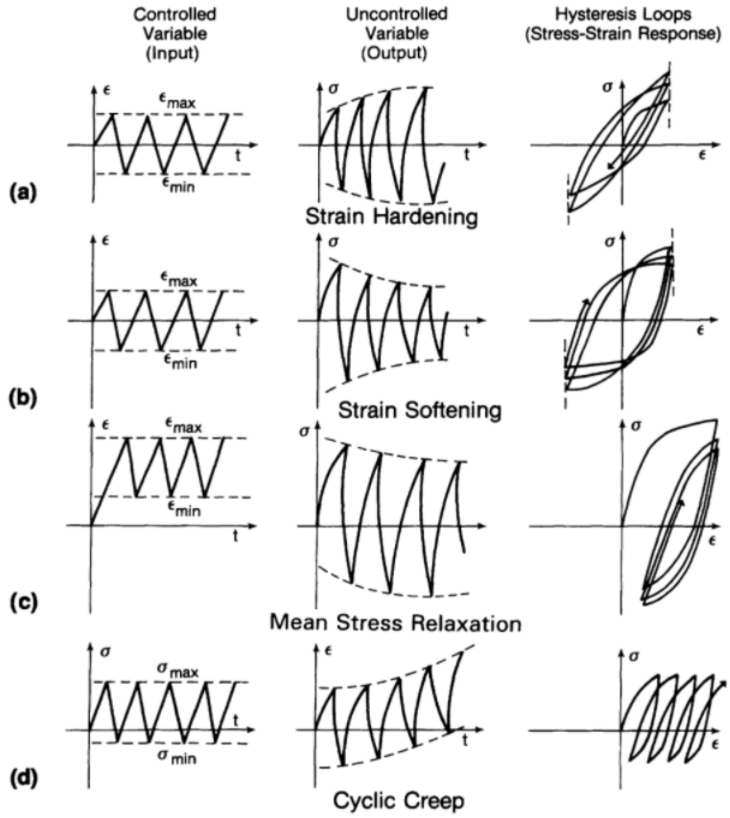

Figure 1.7 – Different material responses in function of the applied cyclic loading [26]

For dual phase steels, a cyclic softening is observed for strain controlled alternated tests performed with different strain amplitudes between 1.2% and 0.2% [28]–[31]. For the highest strain amplitudes above 0.5% a cyclic hardening is observed for the very first cycles, less than 10, and then a cyclic softening occurs as for lower strain amplitudes [30], [31]. Most of the studies on low cycle fatigue of dual phase steel considers material with large thickness between 2 mm and 4 mm in order to avoid buckling problems [29]–[31]. However, considering the material thickness equal to 1.2 mm in this study, it is necessary to take precautions against buckling.

Adaptation of the fatigue tests for sheet materials

Indeed, the performance of alternated tests on thin sheet specimens causes difficulties because different buckling modes can occur. To avoid this issue, it is possible to perform tests with a positive strain ratio but the relaxation of the mean stress in certain case may also lead to buckling. Three main buckling modes, represented in Figure 1.8 [32], has been identified in the literature [32] each corresponding to a parameter of the specimen geometry, t for the thickness, W for the width and L for the space between the jaws and the anti-buckling device. The t-buckling can be avoided by the use of an anti-buckling system and the other parameters can be optimized via the calculation of the maximal admissible stress or strain with the standard beam buckling equations [32], [33]. Without going into details, the aim is to minimize the ratio of the gauge length of the specimen to the thickness [34]. However, it is necessary to keep a gauge area large enough to ensure the uniformity of the stress and strain fields. A dogbone geometry has been proposed in the literature to respect these two conditions as well as possible [35].

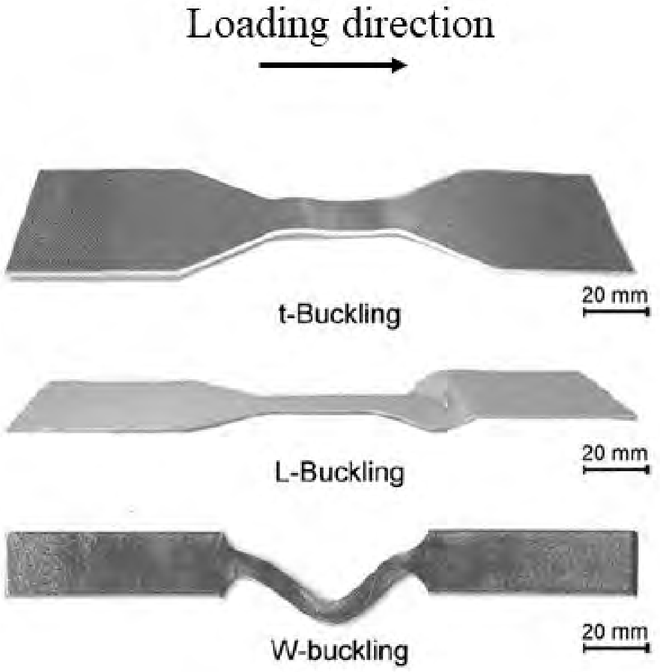

Figure 1.8 – Illustration of the different buckling modes during tension-compression test on sheet specimens [32]

Even if the specimen geometry is optimized, the use of anti-buckling devices is rather recommended. An example of a commonly used system is shown in Figure 1.9 where two plates are positioned on both sides of the specimen. The plates are screwed with each other to apply a lateral pressure on the specimen and Teflon sheets are placed between the plates and the specimen to minimize friction. However, the use of an anti-buckling device requires to modify the strain control and measurement methods because the specimen surface is no more accessible. Different solutions have been proposed in the literature which can be classified in two categories depending on the measurement system. Indeed, it can be either with contact (extensometer or gauges) [32], [34], [36], [37] or without contact (digital image correlation or laser extensometer) [33], [35], [38]–[40]. An example with contact is presented in Figure 1.9, where the extensometer is set up on the specimen edge. In that case, the edge has to be previously polished in order to reduce the microdefects that can introduce a dispersion of the number of cycle until rupture. Finally, it has to be noticed that as an alternative, the pack method [41] which consists to glue some specimens together can also be used additionally for very thin materials [34], [37] or instead the anti-buckling device [29].

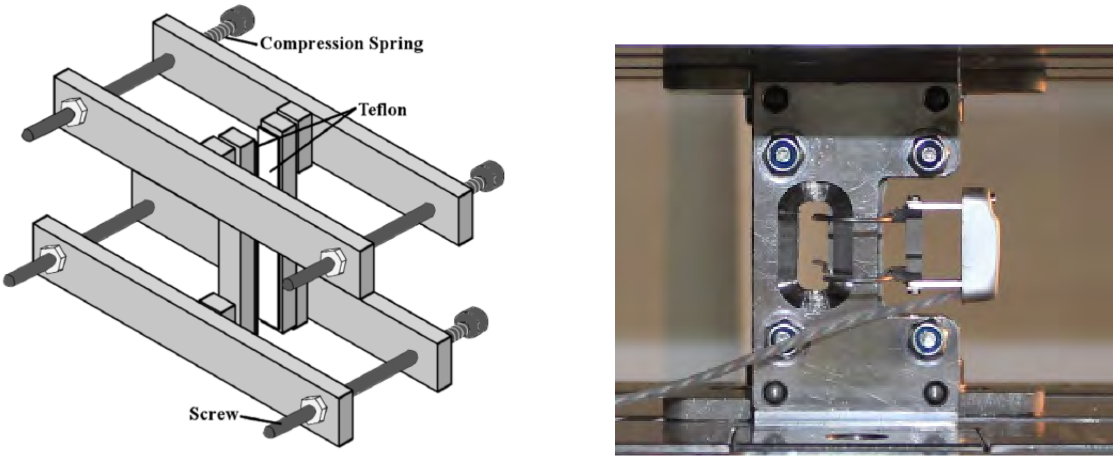

Figure 1.9 – Examples of anti-buckling device [34], [36]

In this study, an anti-buckling device is used and an extensometer positioned on the specimen edge is used to control and measure the strain during the test similarly to the example from the literature. The procedure is presented in details thereafter with all the material characterization tests but first an analysis of the material microstructure is performed.

1.2 Material microstructure

The material DP600 is provided by ArcelorMittal, with a chemical composition of 0.15% C, 0.8% Si, 2.5% Mn (in weight %). Typical microstructure of dual phase steels is made of a dispersed hard phase within a ductile ferritic matrix, which depends on the processing route [42], [43]. In the literature, the volume fraction of martensite is located between 10% and 40% depending on the steel grades and on the heat treatments applied [44]–[48] with values around 20% for DP600 steels [47], [48]. Microstructural observations of the material have been performed with a scanning electron microscope (SEM). The samples are electro-polished and then etched two times with a nital 2% solution. The observation is carried out under different cutting planes, RD-TD (Rolling Direction-Transverse Direction), RD-ND (Rolling Direction-Normal Direction) and TD-ND (Transverse Direction-Normal Direction). The images obtained for the different planes in Figure 1.10 show a typical microstructure of dual phase material with a dark ferritic main phase and a lighter martensitic secondary phase [46].

A numerical post-processing of the images has been performed to estimate the volume fractions of each phase. Indeed, an adjustment of the grey levels is carried out to obtain a segmentation of the picture, represented for each observation planes in Figure 1.10. The percentage of each phase is calculated by counting the black and white pixels. The segmentation performed for 12 different images gives a volume fraction of martensite equal to $14\% \pm 4\%$ in agreement with the values observed in the literature but moderately lower than the ones observed for DP600.

1.3 Mechanical characterization of the DP600

Different characterization tests have been performed on the DP600 steel in order to reproduce a wide range of strain paths. Firstly, monotonic and sequential experiments composed of unixial tension tests, simple shear tests, bulge tests, forward-reverse shear tests and tension-shear tests have been performed at IRDL with MAT&SIM[1] for the specimen preparations, the conduct of the tests and an assistance for the post-processing. Additional in-plane biaxial tensile tests have been performed by S.Y. Lee in the Graduate Institute of Ferrous Technology (GIFT) in South Korea to characterize the material behavior for different linear strain paths. Finally, cyclic tension-compression tests, to characterize the low cycle fatigue behavior of the material, have been performed at ENSTA Bretagne (IRDL) with the help of ArcelorMittal for the specimen preparations and the anti-buckling device and of C. Doudard and B. Levieil for the conduct of the tests. All the tests are carried out in quasi-static conditions, i.e. with a strain rate about $10^{-3}\,\mathrm{s}^{-1}$, and at least 2 times to check the repeatability of the results.

1.3.1 Linear strain paths

Uniaxial tensile tests are performed every 15° in the range [0°,90°] for an angle α between the tensile load direction and the rolling direction to determine the initial anisotropy of the material. The tensile load is applied along the Y axis according to Figure 1.11, and the X axis corresponds to the transverse direction of the sample in the sheet plane of normal Z. The logarithmic strain components ε_{YY} and ε_{XX} are calculated by Digital Image Correlation (DIC) as average values over the blue area on the surface of the specimen, of approximate dimensions $10\,\mathrm{mm} \times 30\,\mathrm{mm}$ and where the strain field represented with the major strain in Figure 1.12(a) is homogeneous. The Cauchy stress σ_{YY} is calculated from the force F recorded by the load cell and the specimen section S,

$$\sigma_{YY} = \frac{F}{S} \text{ with } S = S_0 \exp(-\varepsilon_{YY}) \tag{1.5}$$

where S_0 is the initial section of the specimen.

---

[1] MAT&SIM, https://www.matandsim.fr/

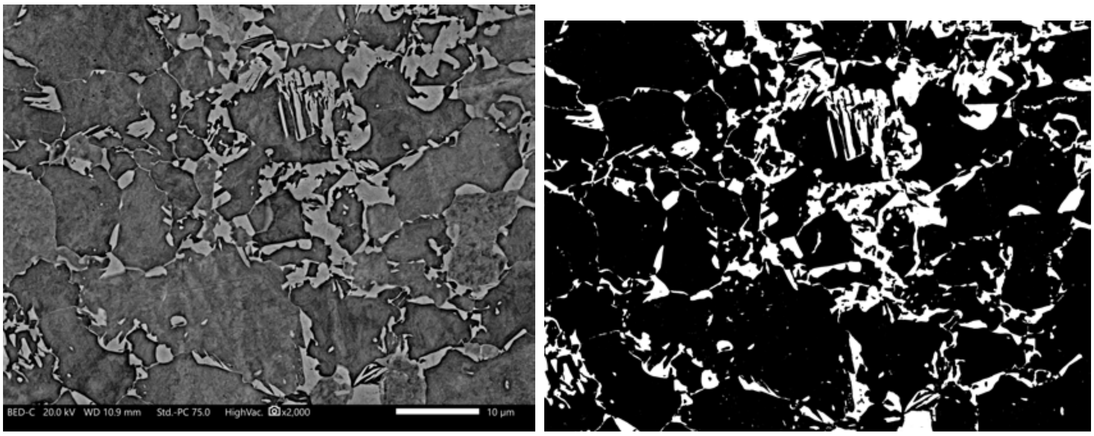

(a) RD-TD (b) 18% martensite

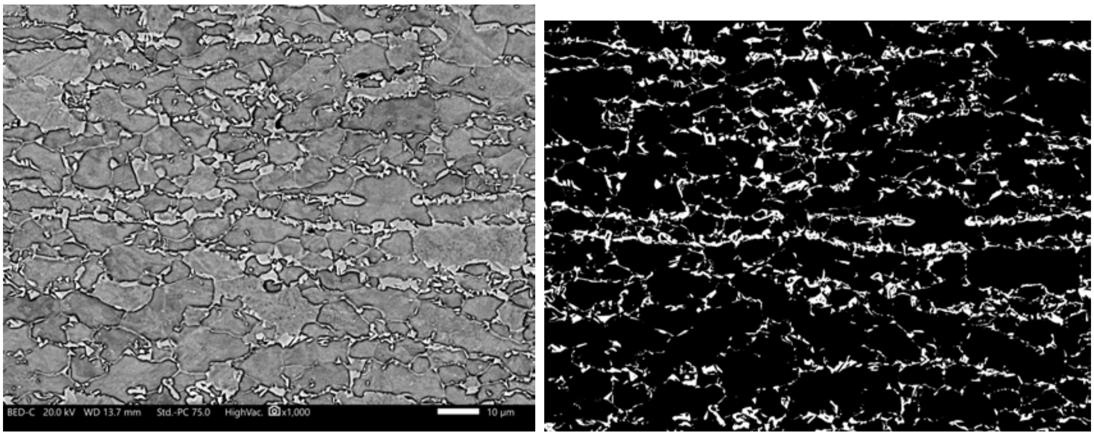

(c) RD-ND (d) 12% martensite

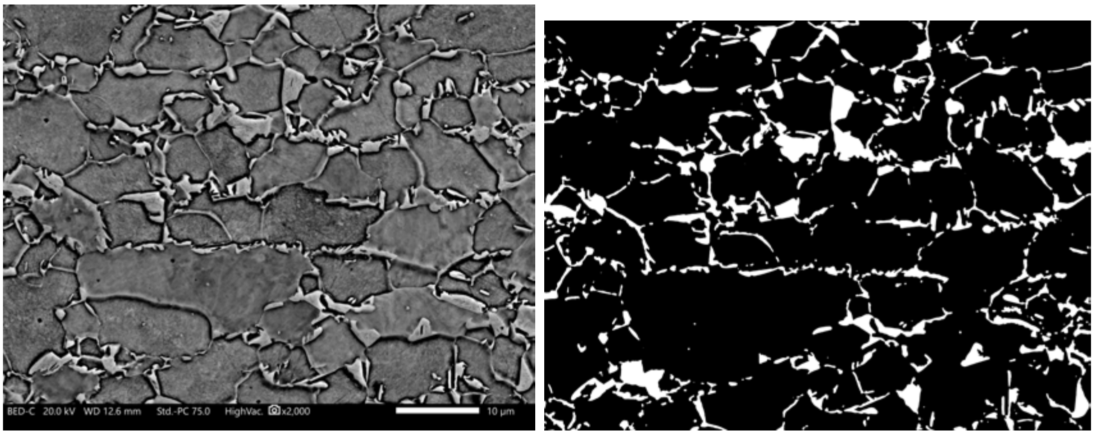

(e) TD-ND (f) 14% martensite

Figure 1.10 – SEM and segmented images of the material microstructure for the different observation planes, (a) and (b) : RD-TD, (c) and (d) : RD-ND, (e) and (f) : TD-ND

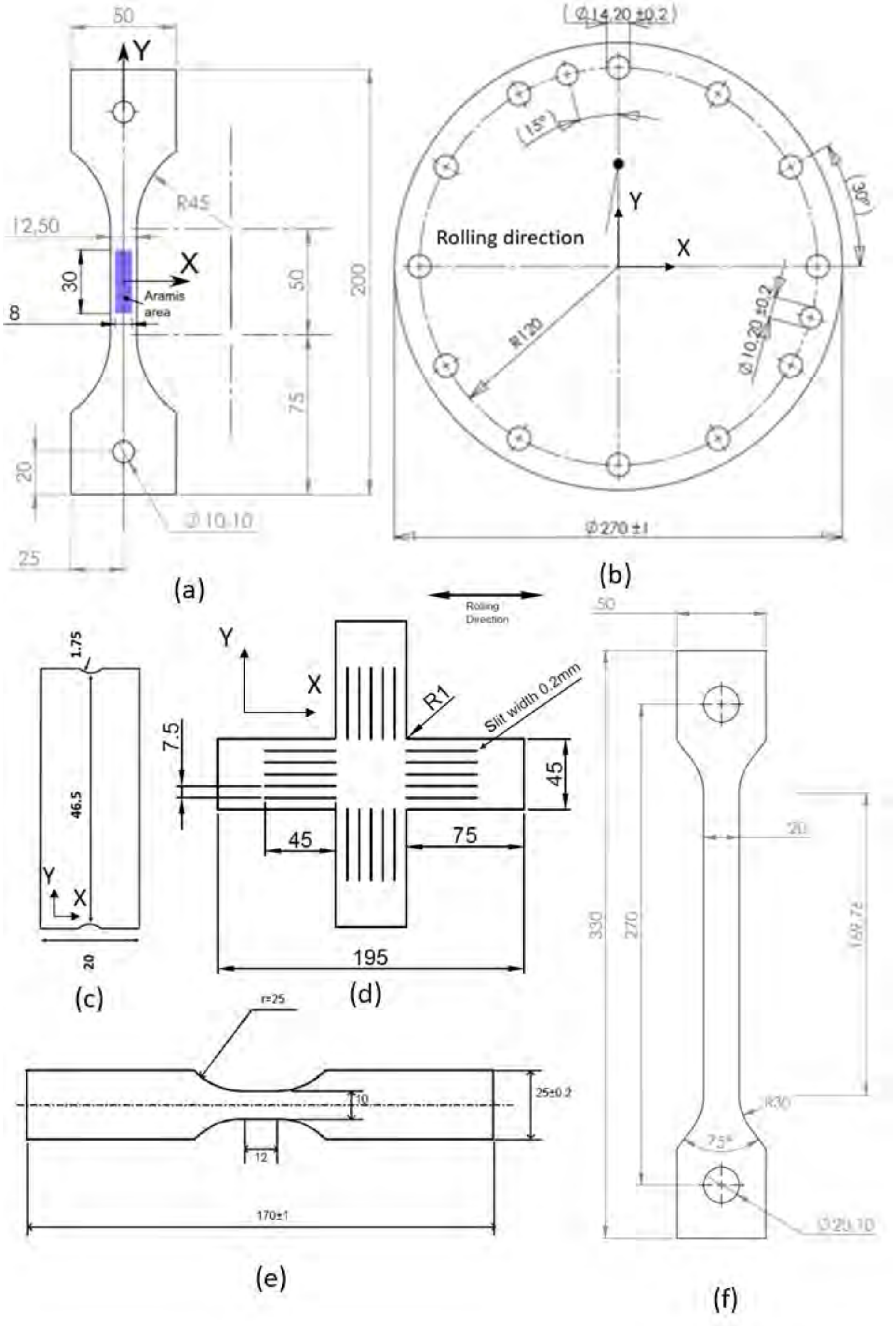

Figure 1.11 – Specimen geometries of the tests with dimensions in mm, (a) Uniaxial tension, (b) Hydraulic bulge, (c) Simple shear, (d) Biaxial tension, (e) Tension-compression, (f) Pre-strain in tension

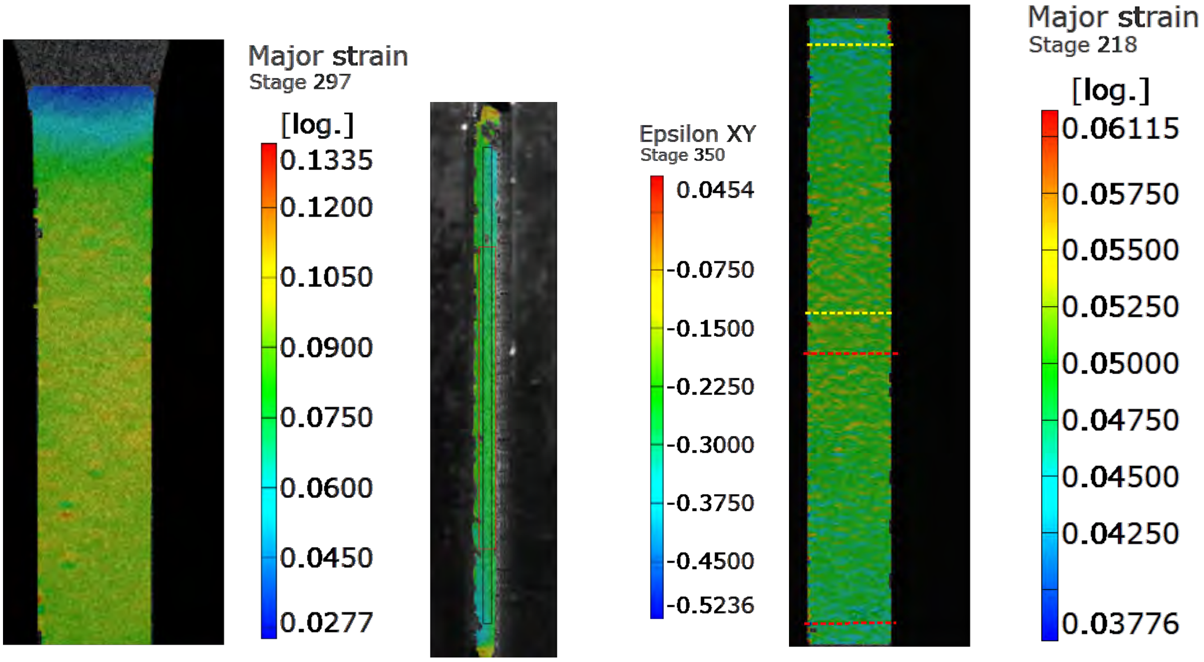

(a) Uniaxial tension (width=12.5 mm) (b) Simple shear (width=4 mm) (c) Pre-strain in tension (width=20 mm)

Figure 1.12 – Strain field recorded by DIC for the different tests (logarithmic major strain field for the uniaxial tensile test (a) and the tension test performed to obtained a pre-strain (c), and the logarithmic strain component ε_{XY} for the simple shear test (b))

There is an excellent repeatability of the tests for all of the orientations, presented in Appendix A, except for 60° for which two stress levels are observed depending on the tests. Thus, one of the lowest stress-strain curves is selected as a representative one because it is more consistent with the stress and strain evolutions between the different orientations. One stress-strain curve is selected as a representative one for each orientation and the comparison of all the representative curves is presented in Figure 1.13. Few differences between the orientations are observed on stress levels except for the test along the diagonal direction 45° which is slightly higher.

The Young modulus values calculated from DIC measures are very scattered and some are exaggeratedly high, thus additional loading-unloading tensile tests are performed with an extensometer to determine it precisely. Four loading-unloading are performed in the elastic range to obtain a stabilized value of the Young modulus. An average value equal to 199 GPa is finally obtained with a variation of ±6 GPa.

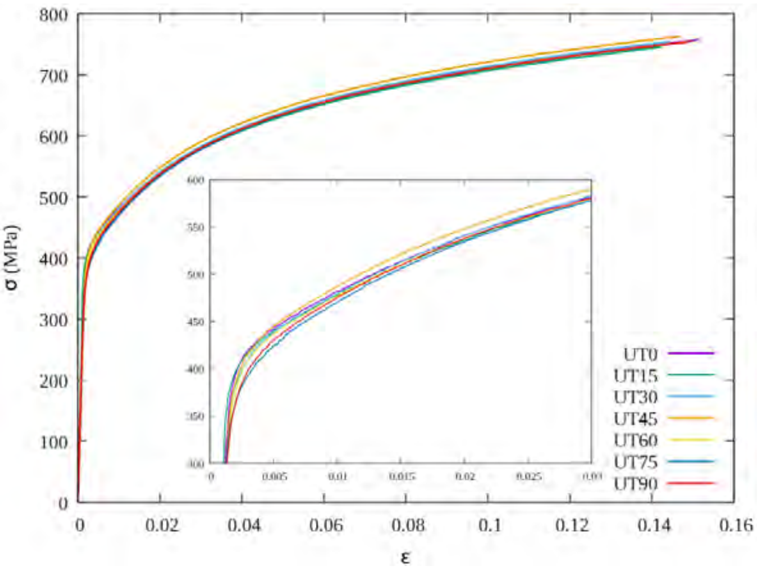

Figure 1.13 – Overlay of the representative stress-strain curves for each orientation of the uniaxial tensile (UT) tests

Stress ratios $s_\alpha = \dfrac{\sigma_\alpha}{\sigma_0}$ are also calculated for a value of plastic work $W = \boldsymbol{\sigma} : \boldsymbol{\varepsilon_p} = 60$ MPa corresponding to the stabilization of the stress ratio values, $\boldsymbol{\sigma}$ and $\boldsymbol{\varepsilon_p}$ are respectively the Cauchy stress and the plastic strain tensors. In addition, the plastic anisotropy coefficients $r_\alpha = \dfrac{d\varepsilon^p_{XX}}{d\varepsilon^p_{ZZ}}$ are also calculated with $\varepsilon^p_{XX} = \varepsilon_{XX} + \nu\dfrac{\sigma}{E}$ and $\varepsilon^p_{ZZ} = -(\varepsilon^p_{YY} + \varepsilon^p_{XX})$ (the Poisson's coefficient ν is taken equal to 0.3). The values obtained for the representative tests are presented in Table 1.1. The isotropy of the stress is again observed with all the stress ratios really close to one, since only the test along the diagonal direction (DD) present a slightly higher stress level. More anisotropy is noticed in strain with a variation of r_α between values equal to 0.88 and 1.16 obtained along the rolling and transverse directions (RD and TD) respectively. A non-linear evolution of the plastic anisotropy coefficients is observed between RD and DD and between DD and TD. However, it is difficult to compare with the literature because only the three values corresponding to RD, DD and TD are measured in most cases and scattered values are obtained. The values obtained in this study are in agreement with the ranges observed in the literature which are $(0.835 - 1.01)$, $(0.76 - 0.96)$ and $(0.869 - 1.13)$ respectively for RD, DD and TD except for r_{90} which is a little higher than the maximal value of the range [49]–[54].

Table 1.1 – Stress ratios s_α and plastic anisotropy coefficients r_α of the representative uniaxial tensile tests

α (°)	0	15	30	45	60	75	90
s_α	1.0000	0.9945	1.0030	1.0120	0.9990	0.9998	0.9994
r_α	0.8803	0.9477	0.9172	0.9505	0.9360	1.1160	1.1680

In addition to the tensile tests, bulge tests are performed with circular specimens of diameter 270 mm [55], cf. Figure 1.11, to evaluate the material behavior at large strain closer to the strain levels obtained in forming. The logarithmic strain components ε_{XX} and ε_{YY} are extracted from two perpendicular sections. The stress is calculated from the pressure P, the curvature at the pole ρ_{out} and the initial thickness t_0 and the two strain components:

$$\sigma_b = \frac{P\rho_{out}}{2t_0 \exp(-\varepsilon_{XX} - \varepsilon_{YY})} \tag{1.6}$$

The bulge stress of the representative test, selected for the largest strain value achieved, cf. Appendix A, is plotted as a function of the equivalent plastic strain in Figure 1.14 and is in agreement with the uniaxial tensile test along RD.

Simple shear tests are also carried out along RD with a rectangular geometry presented in Figure 1.11 of gauge width 4 mm and length 46.5 mm in the center. Though a significant strain localization is present at the ends close to the grips, the strain field represented in Figure 1.12(b) remains rather homogeneous in the center. Thus, the logarithmic strain component ε_{XY} is calculated as an average value over an area in the center of the specimen represented in red in Figure 1.12(b). Then the shear strain is calculated as $\gamma = 2\varepsilon_{XY}$ and the shear stress τ is obtained by dividing the recorded force by the initial section $S_0 = l_0 \times w_0$ with l_0 the average length of the specimen between 47 mm and 47.5 mm depending on the specimens and w_0 the width between the grips equal to 4 mm. One simple shear test is selected from all the tests, cf. Appendix A, as a representative one and the equivalent von Mises stress is calculated from the shear stress in order to compare this test with the other monotonic tests in Figure 1.14. The curve of the equivalent simple shear test is similar to those of the bulge test and the uniaxial tensile test but is slightly higher.

Finally, in order to characterize for additional strain paths, in-plane biaxial tensile tests are performed with cruciform specimen [56] presented in Figure 1.11. The loads on each arm of the specimen, F_X and F_Y, respectively in the rolling and the transverse directions, are controlled to apply specific load ratios between the two directions. In this study, tests are performed with two load ratios, $F_X = \frac{1}{2}F_Y$ and $F_X = 2F_Y$. The strains are measured with gauges positioned at each base of the arms. Logarithmic strains and Cauchy stress components are then calculated [57]. The Cauchy stress components σ_{XX} and σ_{YY} are presented for all tests in Appendix A, as a function of the equivalent plastic strain calculated by neglecting the contribution of the lower component. For one test of each load ratio, the equivalent von Mises stress as function of the equivalent plastic strain is compared with other monotonic curves in Figure 1.14. The stress-strain curves of both load ratios are superimposed with the curves of the other tests and closer to the simple shear tests and the uniaxial tensile test than the tension test.

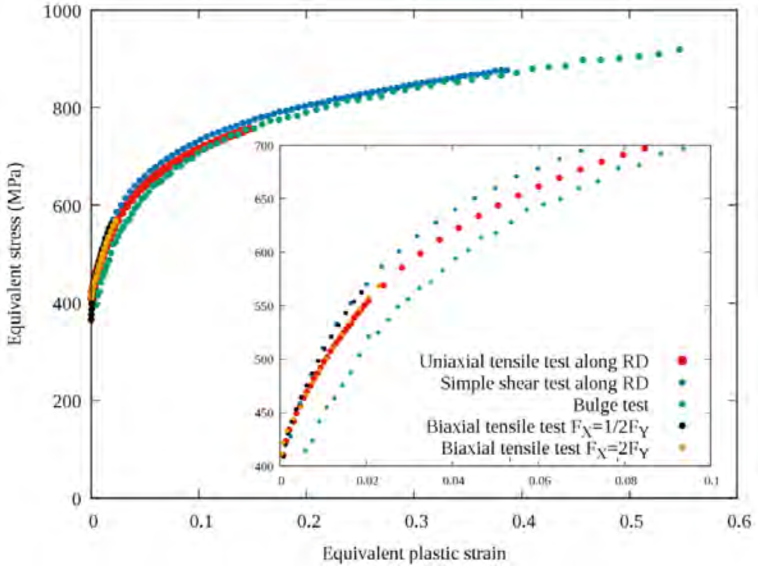

Figure 1.14 – Cauchy stress versus equivalent plastic strain for the different monotonic tests

Overall, a consistency of the experimental database is observed whereas a wide range of linear strain paths is considered. The database is then completed with sequential tests in order to characterize the material behavior under non-linear strain paths.

1.3.2 Non-linear strain paths

Firstly, reverse strain path changes are considered with forward-reverse simple shear tests, performed with the same geometry as the monotonic tests. Three different values of forward strain are considered, $\gamma = 0.09, 0.2, 0.4$ (approximate values). Between all the shear stress-strain curves, cf. Appendix A, the three tests in better agreement with the representative simple shear tests are selected and their shear stress-strain curve are presented in Figure 1.15. A rounded yield point is observed after the inversion as expected and a work-hardening stagnation appears progressively with the increase of the forward shear strain value.

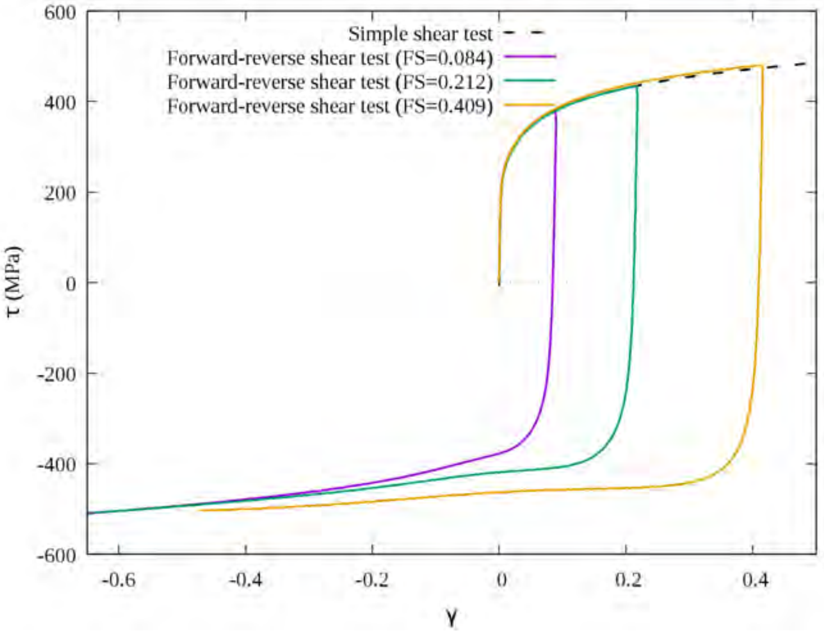

Figure 1.15 – Shear stress-strain curves of the forward-reverse shear tests (FS=Forward shear strain value)

Then, sequential tests composed of a pre-strain in uniaxial tension followed by a simple shear tests are performed to characterize the material behavior under orthogonal strain path changes. In a first step, uniaxial tensile tests are carried out in the rolling direction with a larger and longer geometry than for monotonic tests, cf. Figure 1.11. Two shear specimens are cut out for each tensile specimen, with a metal circular saw, to perform the subsequent tests also in the rolling direction. Two different values of tensile pre-strain are considered, $\varepsilon = 0.049$ and $\varepsilon = 0.093$. These values are calculated at the end of the pre-strain, i.e. after unloading, and correspond to average strains over the shear specimen area represented between the dotted lines in Figure 1.12(c). To compare the simple shear tests after pre-strain with the monotonic test, the tensile pre-strain values are converted into shear strain using the von Mises yield cirterion. Between all the shear stress-strain curves, cf. Appendix A, one of each pre-strain value in tension is represented in Figure 1.16 and compared with the shear stress-strain curve of the monotonic simple shear test. A transient behavior is observed, with a stress upon reloading slightly lower than the monotonic one, for both pre-strains. Then, the stress level resumes the one for the monotonic test.

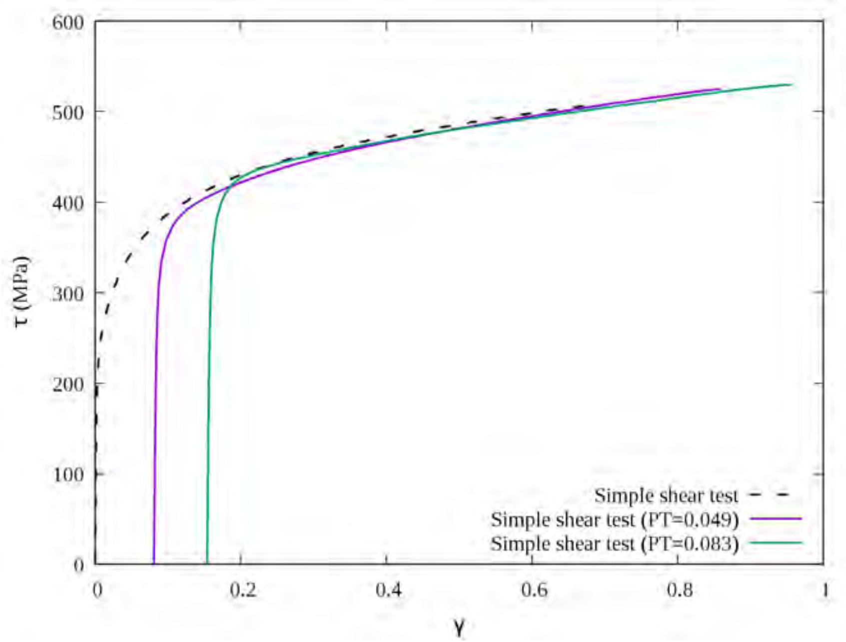

Figure 1.16 – Shear stress-strain curves of the simple shear tests performed after pre-strains in tension that are converted into shear strain with the von Mises criterion (PT=Tensile pre-strain value)

The material behavior under both reverse and orthogonal strain path changes is in good agreement with the literature observations presented at the beginning of this chapter. Another case of reverse strain path changes is considered in order to complete this study with cyclic repetitions to characterize the material behavior in fatigue.

1.3.3 Cyclic strain paths

The cyclic tension-compression tests carried out to characterize the low cycle fatigue behavior of the DP600 steel sheets are strain controlled with a sinusoidal waveform and a strain ratio R_ε equal to -1. The specimen geometry dedicated for the low cycle fatigue tests is coming from the German VDEh [58], cf. Figure 1.11. The specimens have been machined at high-speed with two finishing passes by ArcelorMittal. The specimen edges are polished with sandpaper before the test in order to suppress a possible residual roughness and thus to limit crack initiation from the lateral surfaces. First, some tests are performed in the transverse direction to ensure the feasibility of the tests because this direction is less subject to buckling than the rolling direction due to dislocation arrangement created by the rolling process. Then, the tests are performed twice per strain levels in the rolling direction to ensure the repeatability of the results. The tests are carried out with an Instron fatigue machine at ENSTA Bretagne (cf. Figure 1.17(a)). An anti-buckling device, shown in Figure 1.17(b), is necessary to perform cyclic tension-compression tests on a sheet of thickness 1.2 mm and thus the extensometer is set on the lateral sides of the specimen.

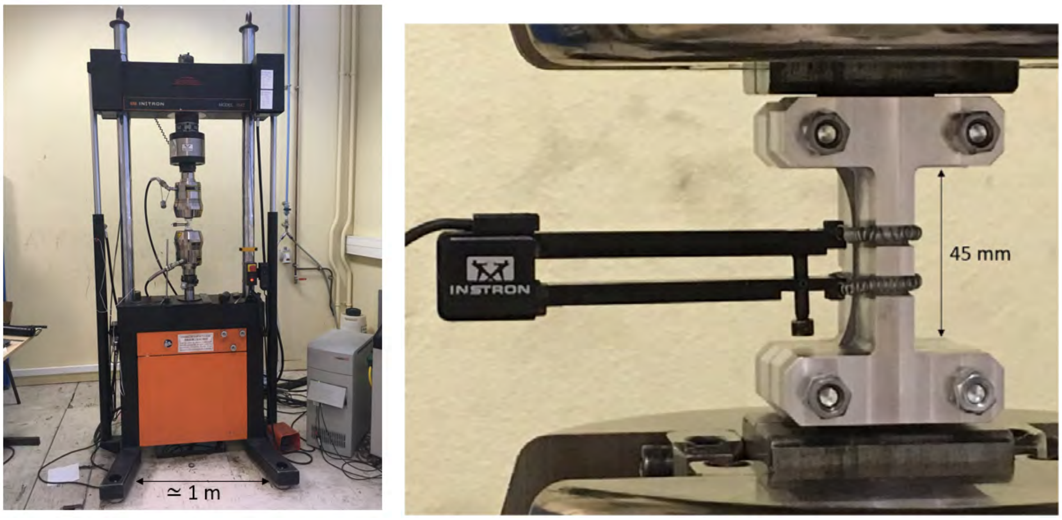

(a) Fatigue test machine

(b) Specimen in the grips with the anti-buckling device on the specimen surface and the extesometer positionned on the side

Figure 1.17 – Experimental device for low cycle fatigue test on thin sheets

The tests are performed for different values of the total strain amplitude between 0.18% and 0.6% in order to obtain different points of the E-N curve. The frequency f is adapted for each strain amplitude to maintain a constant value of the strain rate $\dot{\varepsilon}$, approximately equal to $5 \times 10^{-3}\,\mathrm{s}^{-1}$. Moreover, the tests are performed until crack initiation which is identified on the evolution of the maximum engineering stress for each cycle, cf. Figure 1.18. The test is stopped when the force and thus the stress is 25% lower than the value of the reference cycle (here equal to cycle number 250) but the crack initiation occurs when the slope of the curve begins to change and the corresponding number of cycles defines the lifetime. However, during most of the tests, the force is increasing at the end of the test because the crack initiates outside of the measurement area of the extensometer, according to Figure 1.19. Because of the surface decrease outside of the extensometer, a higher value of force is necessary to apply the imposed strain level in the measurement area that is not cracked. Thus, the stress is increasing but the crack initiation is always visible via the slope change. Furthermore, the crack is located in the gauge area of the sample, i.e. with constant section. Thus, no additional treatment is needed in the post-processing for these tests.

An end criterion is defined for each test on the maximum engineering stress to define the number of cycles until failure following the recommendation of the ISO12106 standard [59].

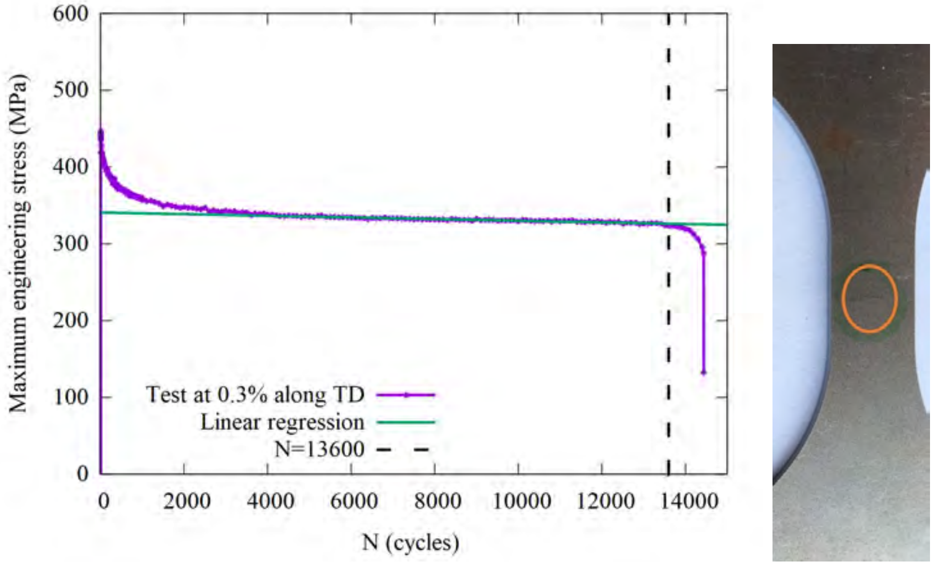

(a) Evolution of maximum engineering stress as a function of the number of cycles N (N_f is represented by the dashed line and N_{tot} is the last point)

(b) Specimen

Figure 1.18 – Example of a crack initiation in the center of the specimen (0.3% along TD)

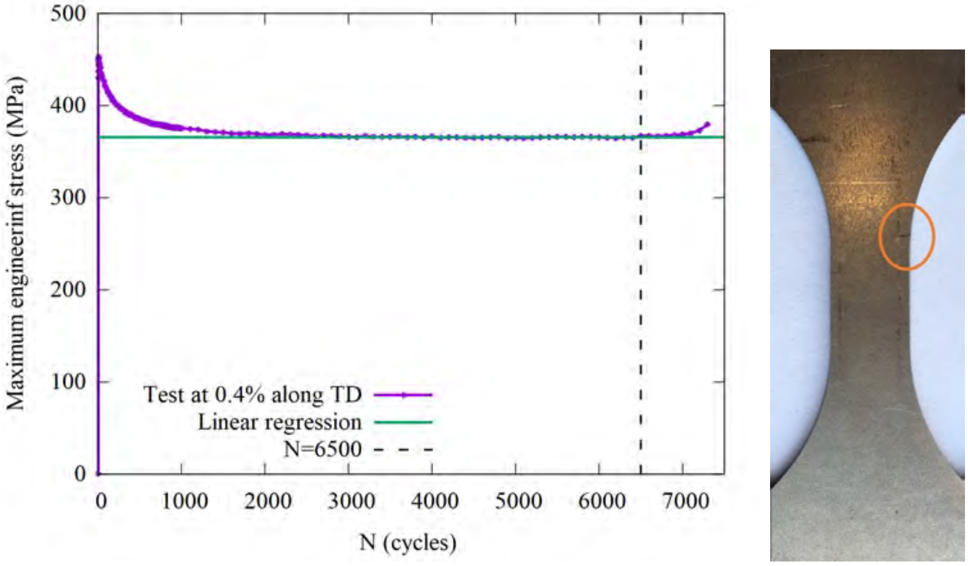

(a) Evolution of maximum engineering stress as a function of the number of cycles N (N_f is represented by the dashed line and N_{tot} is the last point)

(b) Specimen

Figure 1.19 – Example of a crack initiation outside the extensometer (0.4% along TD)

Only the methodology and orders of magnitude are given by the standards, thus the following procedure has been defined specifically for this study with N_f corresponding rather to a number of cycles until crack initiation than until failure. To detect the change of slope of the maximum engineering stress, a linear function is fitted between $\frac{N_{tot}}{2}$ and $N_{tot} - \frac{N_{tot}}{50}$ when the stress is decreasing and between $\dfrac{N_{tot}}{2}$ and $N_{tot} - \dfrac{N_{tot}}{5}$ when the stress is increasing, with N_{tot} the total number of cycles. The number of cycles until crack initiation N_f is chosen as the first cycle where the gap between the maximum engineering stress and the fitted function become larger than a limit value varying between 1.0 MPa and 5.0 MPa in function of the noise.

However, the fatigue criterion is usually represented using the number of reversals $2N_f$. Thus, the numbers of reversals until crack initiation is presented for all the tests in Table 1.2. The different experimental points are compared in Figure 1.20 with E-N curves from the literature also obtained for DP600 [28], [29], without anti-buckling device for the thickest one [29]. The numbers of reversals until crack initiation are quite dispersed for the same value of strain amplitude but it is acceptable for fatigue tests. The results are closer to the curve of the thickest example whereas the thickness is lower but the usually rather scattered results in fatigue are also influenced by the definition of N_f which is not specified for theses examples. Overall, a good agreement with the E-N curves from the literature is observed.

Table 1.2 – Number of reversals until crack initiation $2N_f$ of the different tests presented as function of the strain amplitude $\frac{\Delta\varepsilon}{2}$

$\frac{\Delta\varepsilon}{2}$ (%)	$2N_f$		
	1 (RD)	2 (RD)	1 (TD)
0.6	5000	6400	3000
0.53	-	-	4800
0.5	9200	6000	-
0.4	14600	13000	13000
0.3	25200	35200	27200
0.25	42000	66400	-
0.22	61000	118000	-
0.2	-	-	96400
0.19	78600	150000	-
0.18	148000	-	-

Observations of the fracture facies are realized for specimens of the first tests along the transverse direction with visible cracks circled in Figure 1.21 corresponding to strain levels of 0.6%, 0.53%, 0.4% and 0.3% from the left to the right.

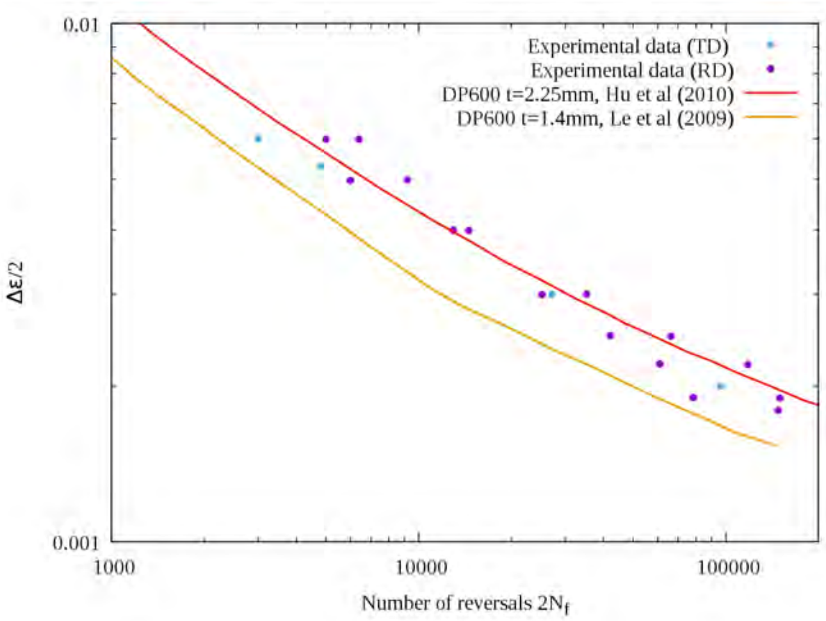

Figure 1.20 – Comparison of the number of reversals until crack initiation with E-N curves from the literature also obtained for DP600 [28], [29]

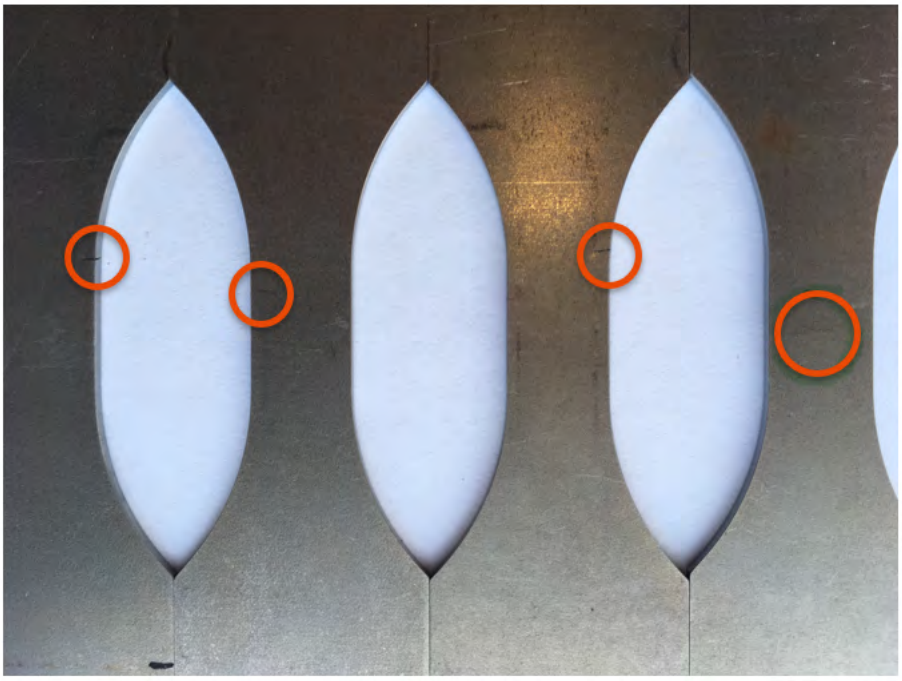

Figure 1.21 – Crack locations on the specimens of the first tests performed along the transverse direction

Thereafter, the observations, under the cutting plane RD-ND, are shown only for the strain levels of 0.3% and 0.6% because the fracture surface are quite similar for the three specimens with a crack in the specimen thickness. Between these three samples, the highest strain level is chosen to show its influence. The fracture surfaces are compared at three scales. First, an overview is presented in Figure 1.22 and then two magnifications are shown in Figures 1.23 and 1.24, respectively at the scales 10 and 1 µm.

On the overview, for the initiation on the surface (0.3%), the fracture surface has an elliptical shape whereas for the initiation on the lateral side (0.6%), the fracture boundaries are more angular and no particular shape is visible for the three specimens. The magnifications at the scale 10 µm shows the presence of a multitude of microcracks distributed on the surface and their number increases with the strain level. At the scale 1 µm, fatigue striations, corresponding to the formation of persistent slip bands which are at the origin of the microcracks, are visible in some areas and their spacing increases with the strain level. The observations of fatigue striations in both cases confirms that specimen with a crack initiation on the edge can also be taken into account.

The evolution of the ten first true stress-strain cycles are represented for two tests with different strain levels in Figure 1.25. Considering only the first cycle, an even more rounded yield point than for the forward-reverse shear test is observed and no work-hardening stagnation considering the very low strain level. For the cyclic evolution, a softening is observed in each case as shown by the decrease of the maximum stress in function of the cycle number in Figures 1.18 and 1.19. For the highest levels the first cycle is lower than the others because of the strain control parameters of the machine. Indeed, to avoid a strain overshoot during the first cycles, the parameters are chosen to achieve the imposed strain without exceeding it, even if it takes several cycles.

To identify the fatigue criterion parameters, it is necessary to consider stabilized strain amplitudes. The stabilized cycle is chosen at half of the N_f cycles until crack initiation. The stabilized cycles of each strain level performed along the rolling and the transverse direction are compared in Figure 1.26. A progressive opening of the cycle with the increase of the applied strain amplitude is observed as expected and similar results are obtained forboth directions. Moreover, a good repeatability of the stabilized cycle is observed for every strain level, cf. Appendix A.

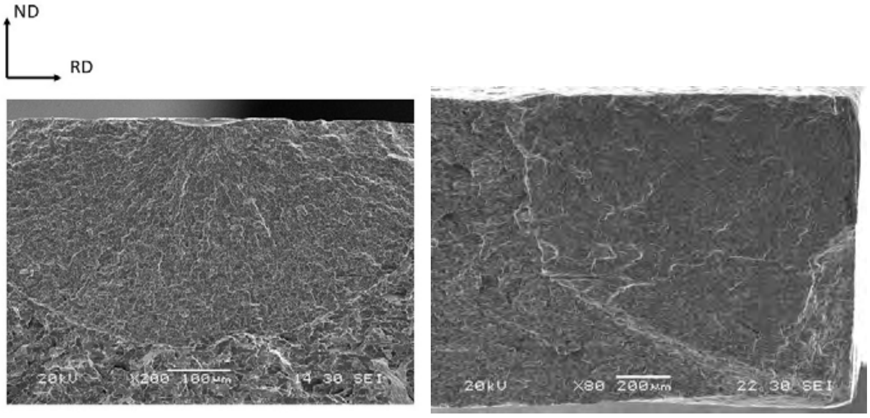

(a) Strain level : 0.3% (b) Strain level : 0.6%

Figure 1.22 – Overview of the fracture surfaces

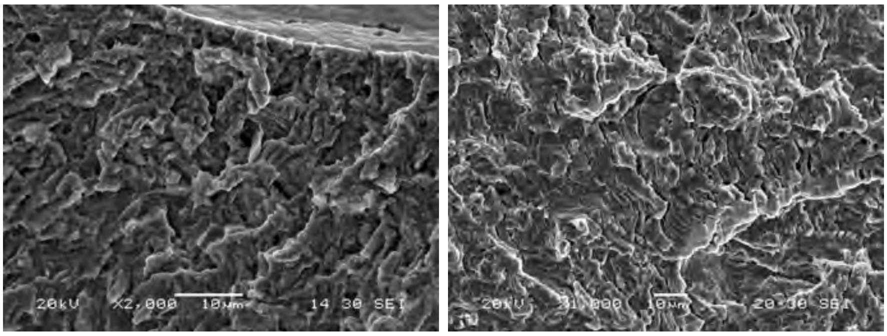

(a) Strain level : 0.3% (b) Strain level : 0.6%

Figure 1.23 – Fracture surfaces at the scale 10 µm

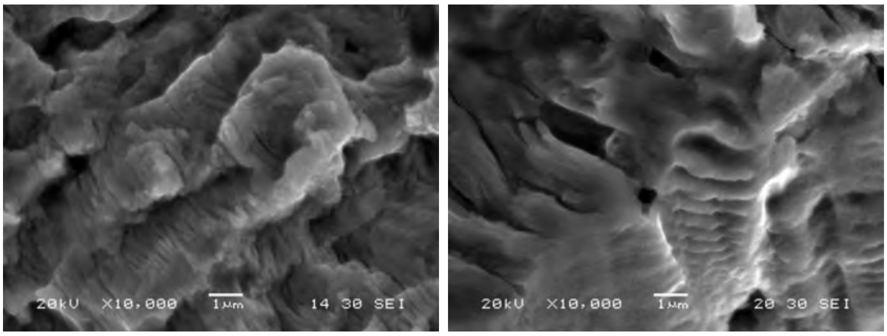

(a) Strain level : 0.3% (b) Strain level : 0.6%

Figure 1.24 – Fracture surfaces at the scale 1 µm

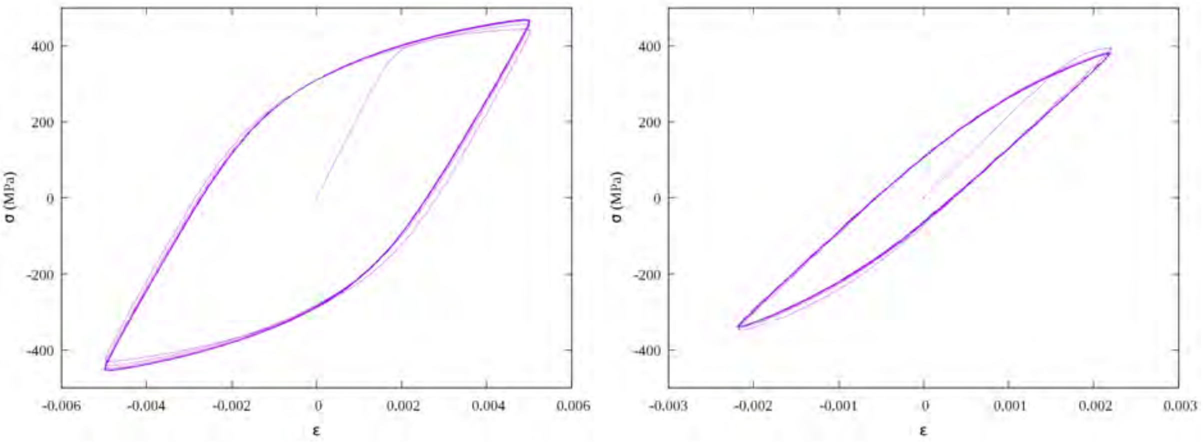

(a) 0.5 %

(b) 0.25%

Figure 1.25 – Evolution of the ten first cycles of Cauchy stress in function of the logarithmic strain for two tests with different strain levels performed along RD

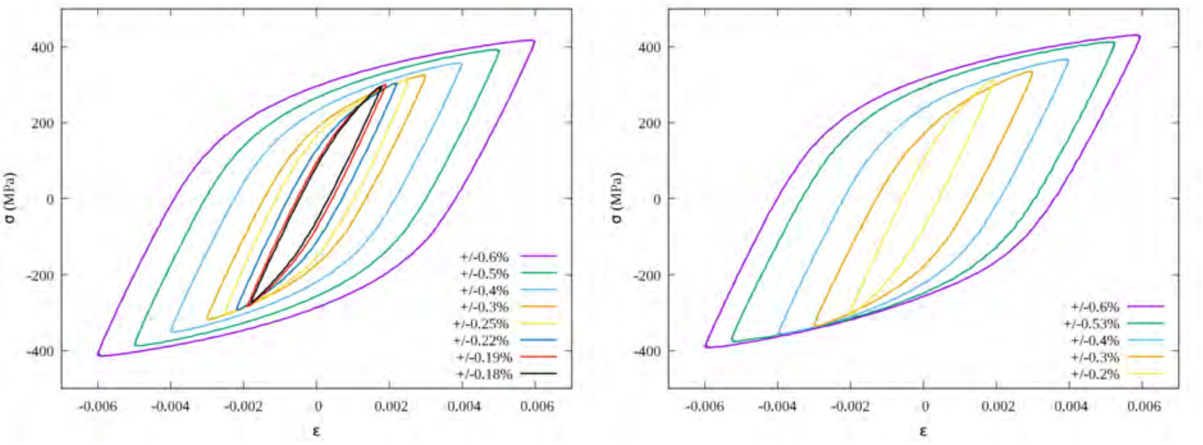

(a) RD

(b) TD

Figure 1.26 – Superposition of the stabilized cycles at $\frac{N_f}{2}$ for tests of each strain amplitude $\frac{\Delta\varepsilon}{2}$, performed along both RD and TD

1.4 Conclusion

The mechanical behavior of a dual phase steel DP600 is investigated in this chapter regarding linear, non-linear and cyclic strain paths. Firstly, observations of the microstructure show a ferritic main phase and a martensitic secondary phase with a volume fraction of 14%. Then, a wide range of linear strain paths is presented with uniaxial tensile tests, bulge tests, simple shear tests and biaxial tensile tests. The hardening behavior is consistent for all the tests and is close to an isotropic behavior. Reverse strain paths are also considered with forward-reverse shear tests. The material exhibits the Bauschinger effect with a rounded yield point and a work-hardening stagnation which appears progressively for the forward-reverse shear tests with the highest forward strains. Moreover, sequential tests composed of pre-strains in tension followed by simple shear tests are carried out to characterize the orthogonal strain path change behavior of the material which is composed of a transient behavior followed by a resumption of the monotonic level. Finally, cyclic tension-compression tests are performed to characterize the fatigue behavior of the material. The material presents a cyclic softening followed by a stabilized behavior until the fatigue failure. The numbers of cycles until crack initiation are somewhat scattered but they are in agreement with the literature and the stabilized cycles are very repeatable. All of these characterization tests are performed in order to model the material behavior with an hardening constitutive law and a fatigue criterion that are presented and calibrated in the following chapter.

Chapter 2

MODELING OF THE MECHANICAL BEHAVIOR: HARDENING AND FATIGUE

The characterization tests performed on the DP600 dual phase steel are used to identify a constitutive model adapted to forming simulations and a fatigue criterion to predict lifespans of formed part. The forming model chosen for this study is the enhanced Homogeneous Anisotropic Hardening (e-HAH) model that takes into account the influence on the material behavior of the two main categories of strain path changes, reverse and orthogonal. The enhancements of virtual forming simulations with the consideration of strain path change effects are beneficial for the design of the forming process but can also improve complementary aspects of the design such as the service life prediction of the part. To model the material fatigue behavior, a criterion decoupled of the hardening model is considered in order to quite easily predict the fatigue life of deep-drawn parts. The modified Morrow criterion is used because it can take into account the influence of the residual stresses from forming. The aim of this study is to use in a complementary way an advanced constitutive model for forming simulations and a criterion for fatigue analysis in order to evaluate the effects of strain path changes on the service life of formed parts.

In this chapter, the different ways to model the strain path change behaviors are first presented and the e-HAH model is presented in details. Then, different low cycle fatigue criteria are introduced and one is selected for this study. Finally, the calibration of both hardening model and fatigue criterion is performed for the DP600. Results presented for the calibration of e-HAH model are mainly coming from a paper already published [60].

2.1 Hardening and fatigue models

2.1.1 Modeling the strain path change behaviors

Advanced constitutive models have been developed to represent the specific material behaviors under complex loading paths that occur during deep drawing processes. Firstly, reverse strain path change models have been largely proposed. The simplest and most used one is mixed hardening of Chaboche type [61] composed of an isotropic and one or several kinematic contributions, which respectively expands and translates the yield surface, which corresponds to the limit between the elastic and plastic domains of the material represented in the three-dimensional principal stress space. However, some limitations of Chaboche type models have been highlighted, as they cannot represent some transient behaviors and in addition, the translation of the yield surface is not enough to model specific features coming from orthogonal strain path changes.

Physically-based models have been developed to take into account the macroscopic behavior induced by the microstructural modifications via a strain path change indicator. Firstly, Teodosiu and Hu [62] proposed to modify the kinematic hardening formulation of Chaboche type using the Schmitt indicator to represent the material behavior during both reverse and orthogonal strain paths. Several studies compared the Teodosiu and Hu model to Chaboche type ones [23], [63]–[65] and conclude that a better description of the transient behavior for reverse loading allows to obtain more accurate springback predictions and the consideration of all strain path changes improves the results for two stage deep-drawing processes, where orthogonal loading is present. In the past decade, other models have been developed based on the kinematic approach [17], [66] or on a distortion of the yield surface [10], [67], [68] or on a combination of the two approaches [69]. The HAH model, which belongs to the distortional category, can represent strain path changes with a reduced number of parameters. The original version [10] takes into account only reverse strain path changes but is then enhanced (e-HAH) to model the two main features observed during orthogonal loading for sheet metals, i.e. latent hardening [70] and cross-loading contraction [11].

The e-HAH model is considered in this study to investigate the new perspective of distortional hardening in the modeling of strain path change effects. Without considering anisotropy, only three different tests are necessary to identify the material parameters, a monotonic test for isotropic hardening, and two sequential tests for reverse and orthogonal strain path changes. Tension-compression tests or forward-reverse shear tests can be used for the identification of the reverse parameters but forward-reverse simple shear tests [10], [20], [71]–[73] can characterize the behavior at large strain contrary to tension-compression tests [71], [73]–[76]. Indeed, it is necessary to use an anti-buckling device to perform compression tests with sheet metals and it is not possible to obtain the same level of strain than with shear tests (cf. section 1.3.3). The values of pre-strains are often different, usually pre-strain values in tension are between 1 and 10 % [71], [74]–[76] whereas the von Mises equivalent values of the pre-strain in shear can reach 5 to 25 % [10], [20], [71], [72]. One recent study about the identification of HAH parameters for a DP780 [73] has considered both kind of tests with equivalent values of pre-strain and shown that the identifications performed from either test are able to describe correctly both tests considering that the material behavior is for the two tests when the pre-strains are the same. Moreover, since the enhancement of HAH model, two-step tension tests have been increasingly used because it is possible to cover a rather large range of strain path change magnitude with different orientations

[11], [13], [70], [77]–[79]. After a tensile test along the rolling direction (RD), a quasi-orthogonal strain path change ($\cos\chi = 0.25$) is obtained for the following tensile test carried out along the diagonal direction (DD) and a quasi-reverse strain path change ($\cos\chi = -0.5$) is obtained for the second tensile test performed along the transverse direction. However, orthogonal strain path changes ($\cos\chi = 0.0$) are rarely considered, it would be necessary to perform a second tension with an angle of 54.7° from the rolling direction or instead a sequential test composed of a pre-strain in tension followed by a simple shear test can be used, though it is not widely used for identification purpose [67], [80]. The different sequential tests previously mentioned that can be used for the calibration of e-HAH model and the associated values of $\cos\chi$ are summarized in Table 2.1 and the model is then presented in details.

Table 2.1 – Synthesis of the sequential tests that can be used for the calibration of e-HAH model and the associated values of $\cos\chi$

Strain path changes	Test 1	Test 2	$\cos\chi$
Reverse	Forward shear (RD)	Reverse shear (RD)	-1
	Tension (RD)	Compression (RD)	-1
		Tension (DD)	-0.5
Orthogonal	Tension (RD)	Tension (54.7° from RD)	0
		Shear (RD)	0
		Tension (TD)	0.25

2.1.2 Enhanced Homogeneous Anisotropic Hardening (e-HAH) model

The e-HAH model considered in this study is coupled to an isotropic hardening law and an anisotropic yield criterion.

Yield criteria

A slight anisotropy regarding hardening is observed for the DP600 whereas it is more pronounced regarding strain ratios. Thus, the Yld2000-2d anisotropic yield criterion proposed in [81], is compared in this study with von Mises isotropic criterion. Within the framework of sheet metal forming, the plane stress assumption is usually used whereas it is not the case in fatigue. However, 3D e-HAH model is not available in finite element codes at our disposal and thus the plane stress assumption is used in this study. In that case, von Mises yield function reduces to

$$\bar{\sigma} = \sqrt{\sigma_1^2 - \sigma_1\sigma_2 + \sigma_2^2} \tag{2.1}$$

with $\bar{\sigma}$ the equivalent stress and $\sigma_i (i = 1, 2)$ the principal stresses.

Yld2000-2d yield criterion is an extension of an isotropic criterion performed with two linear transformations of the Cauchy stress tensor $\boldsymbol{\sigma}$, by means of tensors $\mathbf{X}' = \mathbf{L}'.\boldsymbol{\sigma}$ and $\mathbf{X}'' = \mathbf{L}''.\boldsymbol{\sigma}$. Each linear transformation is carried out via the respective tensor $\mathbf{L}'$ or $\mathbf{L}''$, the components of which in the anisotropy frame $\left(\vec{1}, \vec{2}\right)$ are expressed as

$$\begin{bmatrix} L'_{11} \\ L'_{12} \\ L'_{21} \\ L'_{22} \\ L'_{66} \end{bmatrix} = \frac{1}{3} \begin{bmatrix} 2 & 0 & 0 \\ -1 & 0 & 0 \\ 0 & -1 & 0 \\ 0 & 2 & 0 \\ 0 & 0 & 3 \end{bmatrix} \begin{bmatrix} \alpha_1 \\ \alpha_2 \\ \alpha_7 \end{bmatrix} \tag{2.2}$$

$$\begin{bmatrix} L''_{11} \\ L''_{12} \\ L''_{21} \\ L''_{22} \\ L''_{66} \end{bmatrix} = \frac{1}{9} \begin{bmatrix} -2 & 2 & 8 & -2 & 0 \\ 1 & -4 & -4 & 4 & 0 \\ 4 & -4 & -4 & 4 & 0 \\ -2 & 8 & 2 & -2 & 0 \\ 0 & 0 & 0 & 0 & 9 \end{bmatrix} \begin{bmatrix} \alpha_3 \\ \alpha_4 \\ \alpha_5 \\ \alpha_6 \\ \alpha_8 \end{bmatrix} \tag{2.3}$$

with eight parameters $\alpha_i (i = 1..8)$. The yield condition is defined as

$$\phi = |X'_1 - X'_2|^a + |2X''_2 + X''_1|^a + |2X''_1 + X''_2|^a = 2\bar{\sigma}^a \tag{2.4}$$

where $X'_i, X''_i (i = 1, 2)$ are the principal values of the tensors $\mathbf{X}'$ and $\mathbf{X}''$ and the exponent a is a parameter. For body centered cubic (bcc) materials, a value of 6 is suggested for the exponent a [81]. The criterion reduces to von Mises when the exponent a is equal to 2 and all the parameters α are equal to 1.

e-HAH model

The Homogeneous Anisotropic Hardening (HAH) model is a distortional hardening law proposed originally to model reverse strain path change effects on the material behavior [10]. Then, recent enhancements (e-HAH) extended the model to cross-loading effects [11], [70]. Though the model is macroscopic, it aims at simulating the microstructural behavior of the material via the microstructure deviator $\boldsymbol{h}$. Strain path changes are detected with the indicator $\cos\chi$, presented in Eq. 1.4, involving the normalized microstructure deviator $\hat{\mathbf{h}}$, defined as

$$\hat{h}_{ij} = \frac{h_{ij}}{\sqrt{H h_{kl} h_{kl}}} \tag{2.5}$$

using Einstein summation convention and the normalized stress deviator, $\hat{\mathbf{s}}$ defined such that

$\hat{\mathbf{s}} : \hat{\mathbf{s}} = \dfrac{1}{H}$ with H a scalar equal to $\dfrac{8}{3}$ to simplify the model equations. The microstructure deviator which represents a collective behavior of the dislocations is first aligned with the stress deviator $\mathbf{s}$, leading to $\cos\chi = 1$ and when a strain path change occurs, it rotates to regain this alignment, with the evolution law given by

$$d\hat{\mathbf{h}} = k sign(\cos\chi)\left[\left|\frac{\cos\chi}{H}\right|^{\frac{1}{z}} + g_R\right]\left(\hat{\mathbf{s}} - \cos\chi\hat{\mathbf{h}}\right) d\bar{\varepsilon}_p \tag{2.6}$$

where $\bar{\varepsilon}_p$ is the equivalent plastic strain defined according to plastic work conservation, z and k are two parameters and g_R is a state variable defined with the evolution law

$$\frac{dg_R}{d\bar{\varepsilon}_p} = k_R\left[k'_R\left(1 - \cos^2\chi\right) - g_R\right] \tag{2.7}$$

with k_R and k'_R two material parameters.

The comparison of the microstructure and stress deviators is included in the definition of the yield function

$$\Phi(\mathbf{s}) = [\xi(\mathbf{s})^q + f_1^q|\hat{\mathbf{h}} : \mathbf{s} - |\hat{\mathbf{h}} : \mathbf{s}||^q + f_2^q|\hat{\mathbf{h}} : \mathbf{s} + |\hat{\mathbf{h}} : \mathbf{s}||^q]^{\frac{1}{q}} = \bar{\sigma} \tag{2.8}$$

The model is developped as part of associated plasticity with the yield condition $\bar{\sigma} - \sigma_y\left(\bar{\varepsilon}_p\right) = 0$ and is compatible with any isotropic hardening law $\sigma_y\left(\bar{\varepsilon}_p\right)$, and any isotropic or anisotropic yield function $\phi(\mathbf{s})$. In this study, a hybrid formulation between Swift and Voce law is used for isotropic hardening and defined as

$$\sigma_y\left(\bar{\varepsilon}_p\right) = R\left[K\left(\varepsilon_0 + \bar{\varepsilon}_p\right)^n\right] + (1 - R)\left[Q_1\left(1 - Q_2\exp\left(-Q_3\bar{\varepsilon}_p\right)\right)\right] \tag{2.9}$$

where $R, K, \varepsilon_0, n, Q_1, Q_2, Q_3$ are seven parameters.

The two functions $f_j(j = 1, 2)$, given by

$$f_j = \left[\frac{\sqrt{6H}}{4}\left(\frac{1}{g_j} - 1\right)\right]^{\frac{1}{q}} \tag{2.10}$$

distort the yield surface when a strain path change occurs, in order to model the Bauschinger effect for reverse ones in particular. They depend on the two state variables $g_j(j = 1, 2)$ corresponding respectively to the amplitude and the rate of distortion. Moreover, two state variables are added to model the permanent softening. The evolution law of these four variables, presented in Table 2.2, are dependent on the sign of $\cos\chi$ and are controlled by the parameters $k_j(j = 1..5)$.

Table 2.2 – Evolution laws of the state variables g_1 to g_4 where $\bar{\sigma}_0$ is the value of $\bar{\sigma}$ when the equivalent plastic strain $\bar{\varepsilon}_p$ is equal to zero

$\cos\chi$	> 0	< 0
$\frac{dg_1}{d\bar{\varepsilon}_p}$	$k_2\left(k_3\frac{\bar{\sigma}_0}{\bar{\sigma}} - g_1\right)$	$k_1\frac{g_4 - g_1}{g_1}$
$\frac{dg_2}{d\bar{\varepsilon}_p}$	$k_1\left(\frac{g_3 - g_2}{g_2}\right)$	$k_2\left(k_3\frac{\bar{\sigma}_0}{\bar{\sigma}} - g_2\right)$
$\frac{dg_3}{d\bar{\varepsilon}_p}$	0	$k_5(k_4 - g_3)$
$\frac{dg_4}{d\bar{\varepsilon}_p}$	$k_5(k_4 - g_4)$	0

The first term of the yield condition, Eq. 2.8, is equal to

$$\xi(\mathbf{s}) = \sqrt{\left[\phi\left(\mathbf{s_c} + \frac{\mathbf{s_o}}{g_L}\right)\right]^2 + \left[\phi\left(\frac{4(1-g_s)}{g_L}\mathbf{s_o}\right)\right]^2} \tag{2.11}$$

with ϕ the anisotropic yield function defined either by von Mises or Yld2000-2d criteria, cf. Eqs. 2.1 and 2.4, and $\mathbf{s_c}$ and $\mathbf{s_o}$ the stress deviator components, respectively coaxial and orthogonal to the microstructure deviator. The additional state variables g_L and g_S added to model the effects of orthogonal strain path changes, respectively latent hardening and cross-loading contraction, evolve according to

$$\frac{dg_L}{d\bar{\varepsilon}_p} = k_L\left[\frac{\sigma_y(\bar{\varepsilon}_p) - \sigma_0}{\sigma_y(\bar{\varepsilon}_p)}\left(\sqrt{L(1-\cos^2\chi) + \cos^2\chi} - 1\right) + 1 - g_L\right] \tag{2.12}$$

$$\frac{dg_S}{d\bar{\varepsilon}_p} = k_S[1 + (S-1)\cos^2\chi - g_S] \tag{2.13}$$

where k_L, L, k_S and S are four material parameters.

Altogether, 29 material parameters, with 7 related to isotropic hardening, 9 for the anisotropic yield criterion and 13 for the e-HAH hardening, need to be identified without counting the parameters of the fatigue criterion.

2.1.3 Low cycle fatigue criteria

Most of the low cycle fatigue criteria are based on the Manson-Coffin-Basquin (MCB). It is a uniaxial criterion which relates the number of reversals until failure $2N_f$ to the total strain amplitude $\frac{\Delta\varepsilon}{2}$, which is also equal to the sum of the plastic and elastic strain, respectively $\frac{\Delta\varepsilon^e}{2}$ and $\frac{\Delta\varepsilon^p}{2}$ [82], [83],

$$\frac{\Delta\varepsilon}{2} = \frac{\Delta\varepsilon^e}{2} + \frac{\Delta\varepsilon^p}{2} = \frac{\sigma_f^{'}}{E}(2N_f)^b + \varepsilon_f^{'}(2N_f)^c \tag{2.14}$$

with E the Young modulus identified with tensile tests and 4 parameters $\sigma_f^{'}$, $\varepsilon_f^{'}$, b and c that need to be identified with alternated cyclic tests. $\sigma_f^{'}$ and $\varepsilon_f^{'}$ are respectively the fatigue strength and ductility coefficients while b and c are respectively the fatigue strength and ductility exponents.

The MCB criterion is then modify by Morrow to take into account the mean stress $\sigma_m == (\sigma_{max} + \sigma_{min})/2$, with σ_{max} and σ_{min} respectively the maximum and the minimum stress during the cycle [84].

$$\frac{\Delta\varepsilon}{2} = \frac{\sigma_f^{'} - \sigma_m}{E}(2N_f)^b + \varepsilon_f^{'}(2N_f)^c \tag{2.15}$$

With the addition of the mean stress in the criterion, the influence of a strain ratio different of -1 or of eventual residual stresses can be modeled. However, the modification operated by Morrow has an influence on both elastic and plastic strain amplitudes that could be inaccurate when the plastic strain amplitude is high. Thus, to dissociate the influence of mean stress and the plastic strain amplitude, a modification of the Morrow criterion is proposed by Manson and Halford [85],

$$\frac{\Delta\varepsilon}{2} = \frac{\sigma_f^{'} - p\sigma_m}{E}(2N_f)^b + \varepsilon_f^{'}(\frac{\sigma_f^{'} - p\sigma_m}{\sigma_f^{'}})^{\frac{c}{b}} p'^{b-\frac{c}{b}}(2N_f)^c \tag{2.16}$$

with p and $p^{'}$ two additional parameters that need to be identified with cyclic test with a mean stress different of zero.

Instead of taking into account residual stress influence with the addition of the mean stress, it is also possible to include the pre-strain influence in the MCB criterion [86]

$$\frac{\Delta\varepsilon}{2} = \frac{\Delta\varepsilon^p}{2} + \frac{\Delta\varepsilon^e}{2} = \alpha\frac{\sigma_f^{'}}{E}(2N_f)^{b+\gamma} + \beta\varepsilon_f^{'}(2N_f)^{c+\lambda} \tag{2.17}$$

with four additional parameters α, β, λ and γ defined as

$$\alpha = c_1\varepsilon_{\text{effective}},\ \gamma = 0.01,\ \beta = \frac{\varepsilon_{\text{effective}}\varepsilon_f^{'} + c_2}{\varepsilon_f^{'}},\ \lambda = \varepsilon_2 \tag{2.18}$$

but only two constants c_1 and c_2 need to be identified with alternated cyclic tests performed on pre-strained specimen. Moreover, the parameters are dependent of the effective strain $\varepsilon_{\text{effective}}$

corresponding to the equivalent strain of von Mises criterion in the example of the literature,

$$\varepsilon_{\text{effective}} = \frac{\sqrt{2}}{3}\{(\varepsilon_1 - \varepsilon_2)^2 + (\varepsilon_2 - \varepsilon_3)^2 + (\varepsilon_3 - \varepsilon_1)^2\}^{\frac{1}{2}} \tag{2.19}$$

where the strains ε_1, ε_2 and ε_3 are corresponding respectively to the major, intermediate and minor strains. This modification of MCB criterion is proposed in a study about the influence of pre-strain on the low cycle fatigue behavior of a DP600 with two different strain path, uniaxial and plane tensile strain. The behavior of the as-received material of this study [28] has been already presented in the first chapter, cf. Figure 1.20. The fatigue life is influenced by the pre-strain in all case but in different way depending on the pre-strain path. For uniaxial pre-strain, an increase of the lifespan compared to the as-received material is observed over 10^4 reversals whereas under this value, the lifespan of pre-strain specimens is lower than the as-received ones. For plane pre-strain, an increase of the lifespan compared to the as-received material is observed for the whole range of reversals. Their modification of MCB criterion is able to reproduce the effect of pre-strain in both strain path case.

As only alternated cyclic tests are available in this study, the Morrow criterion is then used for the lifespan predictions but the mean stress is consider only if it is positive [87]

$$\frac{\Delta\varepsilon}{2} = \frac{\sigma_f^{'} - < \sigma_m >}{E}(2N_f)^b + \varepsilon_f^{'}(2N_f)^c \tag{2.20}$$

where $<.>$ denotes the Macaulay brackets. Indeed, similar lifespans are obtained experimentally for cyclic tests performed with a compressive mean stress and a zero means stress whereas the Morrow criterion predict a decrease of the lifespan [87]. The modified Morrow criterion does not introduce additional parameters compared to the MCB criterion and thus the calibration of both criteria is similar. The parameter identifications of e-HAH model and the modified Morrow criterion are then presented.

2.2 Parameter identifications for the DP600

2.2.1 e-HAH model calibration procedure

The calibration procedure is composed of three different steps in order to identify the 23 materials parameters, i.e. 7 for the isotropic hardening, 9 for the anisotropic yield criterion and only 8 for the enhanced HAH model. Indeed, three parameters of the microstructure deviator evolution, z, k_R and k_R', are fixed to recommended values to simplify the model use [11]. As dual phase steels do not exhibit latent hardening during orthogonal strain path changes, the parameters L and k_L are fixed to default values. The calibration procedure is detailed below and also illustrated by a flowchart in Figure 2.1.

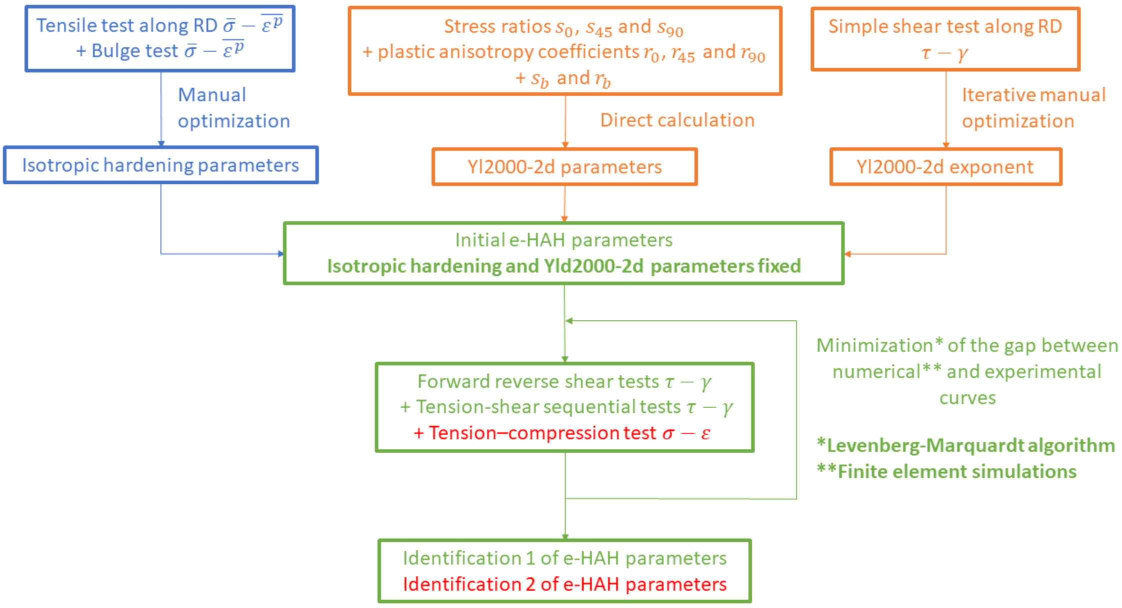

Figure 2.1 – Illustration of the calibration procedure. Isotropic hardening (in blue) and Yld2000-2d (in orange) parameters are first determined, sequentially, and then considered fixed in the iterative determination of e-HAH parameters (in green). 2 different databases are used, without (identification 1) or with tension-compression tests at very low strain (identification 2 in red).

Firstly, the isotropic hardening parameters are identified by fitting the plastic strain-stress curves from uniaxial tensile test along the rolling direction and bulge test. For the yield criterion, on one hand, the eight parameters α_i are calculated directly with a Newton-Raphson algorithm available in PAMSTAMP software developped by ESI Group, from the stress ratio s_0, s_{45}, s_{90} and s_b corresponding to the ratio of the balanced biaxial stress with the uniaxial tensile stress along RD, and from the plastic anisotropy coefficients r_0, r_{45}, r_{90} and r_b equal to the slope of the yield surface at the balanced biaxial stress state [81]. σ_b is taken equal to 1 considering the ratio of the bulge stress on the Cauchy stress from the uniaxial tensile test along the rolling direction and r_b is assumed equal to 1 because the anisotropy is rather small. On the other hand, the exponent of the yield criterion is manually adjusted with an iterative approach to fit the simple shear stress level. The exponent is usually equal to 6 for body-centered cubic (bcc) materials but it is necessary to decrease it in order to fit the simple shear tests. The exponent is progressively decreased and the eight other parameters are calculated at each iteration in order to represent the simple shear test and check the stress level.

Finally, the parameters of the e-HAH model are identified with an inverse approach, i.e. the gap between the numerical predictions obtained by finite element analysis and the experimental results is minimized similarly to previous studies [88], [89]. For that, finite element simulations are performed in Abaqus Explicit with an user subroutine provided by M.G Lee in Seoul National University [90] and with one shell element to simulate homogeneous test. Firstly, two different tests are considered for the identification, forward-reverse shear tests with two different forward strains, $\gamma = 0.084$ and 0.212, and sequential tests with two different values of pre-strain in tension, $\varepsilon = 0.049$ and 0.093, before simple shear test. Each of these tests corresponding to a category of strain path change has been performed in order to characterize a constitutive model dedicated to forming simulation, thus high values of pre-strain are considered in forward shear and in pre-tension. However, in the context of integrated design, the model is expected to be versatile and can be used for both fatigue and forming analysis. To ensure the accuracy of the model at low strains, a second identification is performed with the addition of a cyclic tension-compression test at a strain level of 0.006, originally carried out for the characterization of the fatigue behavior. The boundary conditions used to simulate simple shear and tension or compression are represented in Figure 2.2. Symmetries are applied on the edges $X = 0$ and $Y = 0$ and the displacement is applied on the top side following Y axis whereas in simple shear, all the degrees of freedom of the left and right sides are fixed except for the rotation around the normal of the shell element and the displacement is applied on the right side along Y axis.

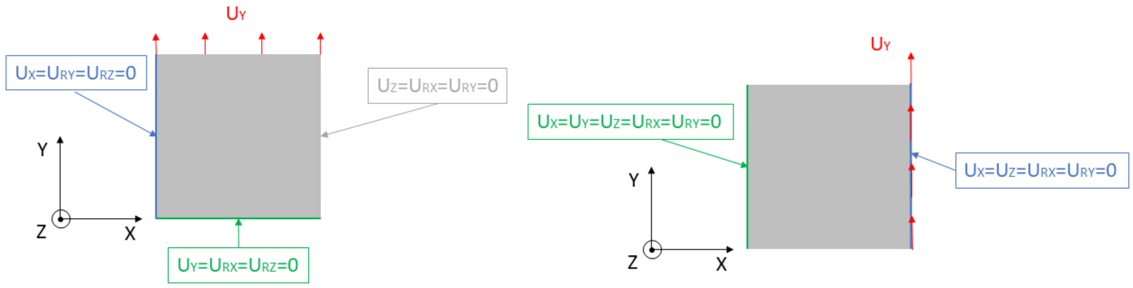

(a) Uniaxial tension

(b) Simple shear

Figure 2.2 – Boundary conditions used for uniaxial tension and simple shear simulations with one shell element (U and U_R are respectively corresponding to displacement and rotation)

For all tests, the imposed displacement U_Y is coming from the experiments and the stresses obtained with the model are optimized. The program SiDolo, using a gradient-base method, is coupled to Abaqus in order to perform the optimization with the method detailed in Figure 2.3.

The tests are simulated for a given set of parameters A and an objective function S_{obj} is calculated by SiDoLo [91] with a least square formulation expressed as

$$S_{obj} = \sum_{k=0}^{j} \frac{1}{n_p^k} \sum_{i=0}^{n_p^j} \left(Z_i^{exp}(t_i) - Z_i^{num}(t_i, A)\right)^2 \tag{2.21}$$

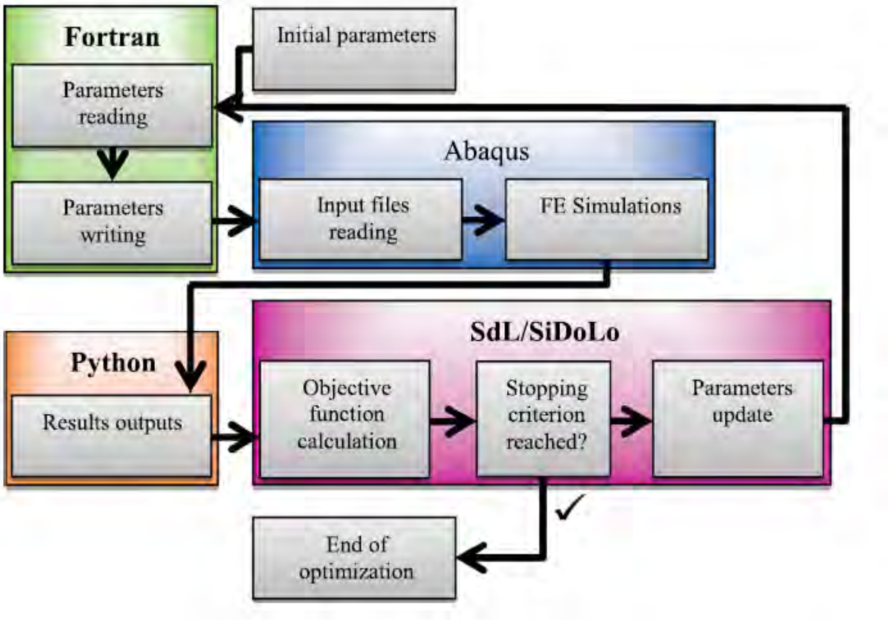

Figure 2.3 – Illustration of the optimization method coupling Abaqus and Sidolo [89]

where j is the number of tests, n_p^j the number of points for each test, Z_i^{exp} the experimental ouptut at time t_i and Z_i^{num} the numerical output calculated with the set of parameters A and interpolated at the same time. Weights must be assigned for each test with this method but the same value is used for all the tests which are thus all considered with the same importance because only stresses are optimized. The initial set of parameters A_0 is chosen from other sets of parameters identified for similar materials in the literature [10], [92] and maximal and minimal values are also given for each parameter. The set of parameters A_0, A_{min} and A_{max} are summarized in Table 2.3. The Levenberg-Marquart gradient-based algorithm [93], [94] is used to minimize the objective function and the optimization ends when the gap between the value of the objective function at the current iteration and the best value during the optimization is lower than $1e^{-20}$ or if the number of iterations is higher than 500.

Table 2.3 – Initial, minimal and maximal set of parameters of the e-HAH model ($q = 2$, $z = 5$, $k_r = 15$, $k'_r = 0.2$, $L = 1$, $k_L = 0$)

A	k	S	k_S	k_1	k_2	k_3	k_4	k_5
0	30	0.7	100	70	20	0.2	0.9	6
min	15	0.4	20	20	10	0.1	0.7	1
max	150	1.0	250	250	250	1	1	10

Eight parameters need to be identified to calibrate the e-HAH model for the dual phase steel considered in this study. The parameters dedicated to the microstructure deviator evolution are all fixed to values recommended by the literature apart from k which should be identified with the cross-loading parameters. First, it was attempted to identify all the parameters simultaneously but the parameter k always diverged to the lower bound A_{min} fixed for the inverse analysis. Thus, the parameter k is fixed to 30 because it is the generic value proposed in the original model [10] and it is used in several studies [74], [75], [95]. Then, the identification of the 7 remaining parameters is carried out, considering or not the tension-compression test.

2.2.2 Isotropic hardening parameters

The isotropic hardening parameters are identified with both tensile test along the rolling direction and bulge test by curve fitting. Indeed, the equivalent stresses $\bar{\sigma}$ as function of the equivalent plastic strains $\bar{\varepsilon}_p$ derived from these tests are really close to each other suggesting an isotropic behavior of the material, according to Figure 2.4. In order to describe accurately the whole curve up to an equivalent plastic strain of 0.6, a hybrid Swift-Voce law presented in Eq. 2.9 is chosen using 7 parameters presented in Table 2.4. Furthermore, the simple shear test along the rolling direction is also represented using the equivalent stress and strain of von Mises criterion. The simple shear curve is slightly higher than the two others but the difference between the curves is not greater than the dispersion for each type of test.

Table 2.4 – Parameters of the hybrid Swift-Voce law

Parameters	R	ε_0	K (MPa)	n	Q_1 (MPa)	Q_2	Q_3
Values	0.8	0.0032	1060.0	0.175	756.4	0.437	26.05

2.2.3 Yield criterion parameters

In order to better reproduce the stress level in simple shear, which is essential in the following calibration, and to take also into account the strain anisotropy, the yield criterion Yld2000-2d is considered. The exponent of the yield criterion a, is found equal to 3.6. The parameters identified with this value of the exponent are presented in Table 2.5. Projections of the yield surface are represented in the planes $\sigma_{11} - \sigma_{22}$ and $\sigma_{11} - \sigma_{12}$ in Figure 2.5 with the directions 1 and 2 corresponding to the rolling and the transverse direction. The shape of the yield surface in the $\sigma_{11} - \sigma_{22}$ plane is close to the von Mises one. The two biaxial tests validate such a shape even if a slight difference is visible for the point with $\sigma_{11} = 2\sigma_{22}$. To describe correctly this point of the yield surface it is necessary to use an intermediate value of the exponent a between 3.6 and 6 but with this intermediate value the shear level represented in the $\sigma_{11} - \sigma_{12}$ plane is not

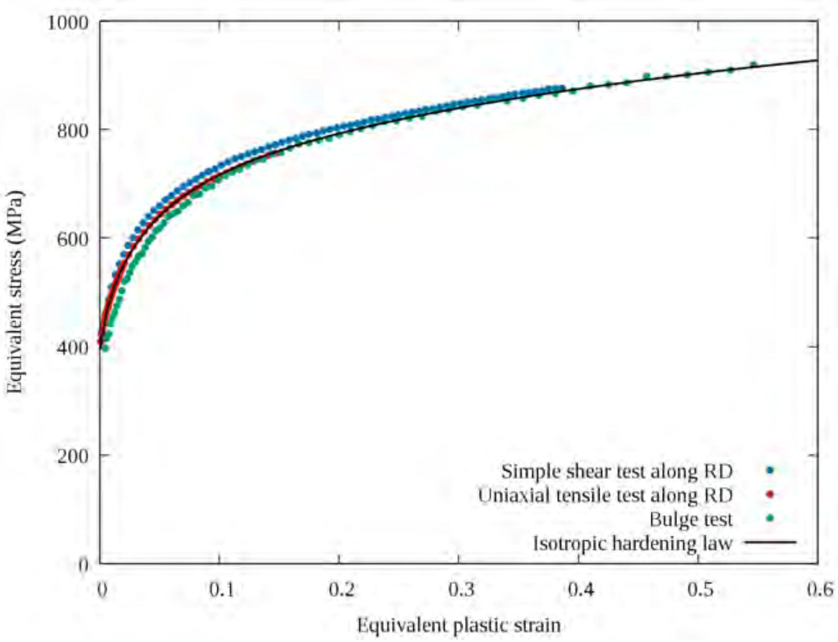

Figure 2.4 – Cauchy stress versus equivalent plastic strain for the different monotonic tests and the isotropic hardening law

correctly predicted. Considering the experimental database composed mainly of shear tests, a good description of the shear level is preferred and the value of 3.6 is selected for the exponent.

Table 2.5 – Yld2000-2d parameters

a	α_1	α_2	α_3	α_4	α_5	α_6	α_7	α_8
3.6	1.2410	0.7422	0.6935	0.9793	0.9969	1.2720	0.9878	0.9783

The use of an anisotropic criterion leads to a more suitable representation than the von Mises one for both stress and strain anisotropy. Stress anisotropy represented in the different projection planes in Figure 2.5 is also characterized by the stress ratios evolution in Figure 2.6(a) with the orientation α from the rolling direction. The calibrated Yld2000-2d criterion captures the slightly higher level of stress observed at 45° from the rolling direction. It also captures the evolution of the plastic anisotropy coefficients in Figure 2.6(b), characteristics of the strain anisotropy. The evolution does not fit exactly the values of the representative tests used as inputs in the identification because the exponent has been changed from the recommended value but the tendency is described in an acceptable way. The non-linear evolution observed between 0° and 45° and between 45° and 90° cannot be described by a plane stress formulation because it necessitates more parameters and thus these evolutions are neglected in this study.

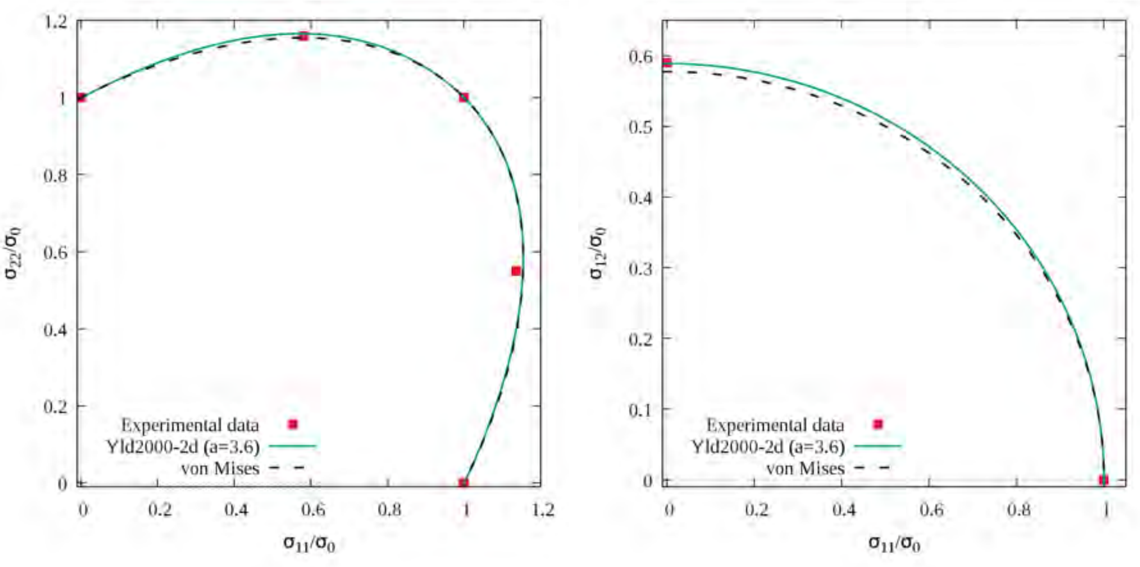

(a) $\sigma_{11} - \sigma_{22}$ (b) $\sigma_{11} - \sigma_{12}$

Figure 2.5 – Initial yield surfaces represented in different projection planes

The Yld2000-2d criterion calibrated with $a = 3.6$ predicts a consistent description of both tensile and shear tests together with the representation of the strain anisotropy. For the identification of the e-HAH parameters with a database composed mainly of shear tests, the use of Yl2000-2d with an exponent equal to 3.6 is chosen. Despite the quality of the identification of Yld2000-2d criterion, the effects of anisotropy are relatively low on this material and the use of an isotropic criterion such as the von Mises one gives a good approximation of the behavior and can be reasonably used in further applications like forming and fatigue.

2.2.4 e-HAH parameters

The identification of orthogonal strain path change parameters is presented first because only one kind of test is used for the calibration and because the two parameters S and k_S are not influenced by the addition of the tension-compression test in the database. Indeed, the experimental database considered in this study is only composed of strain path changes characterized by either $\cos\chi = 0$ or -1 and thus it is possible to completely dissociate the material behavior observed for each strain path. The parameter values of both identification are presented in Table 2.6.

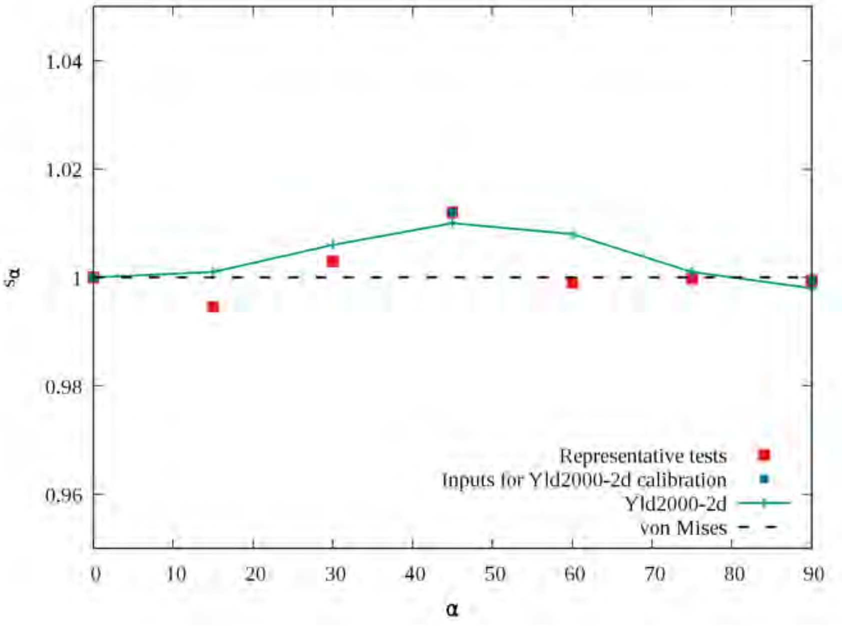

(a) s_α

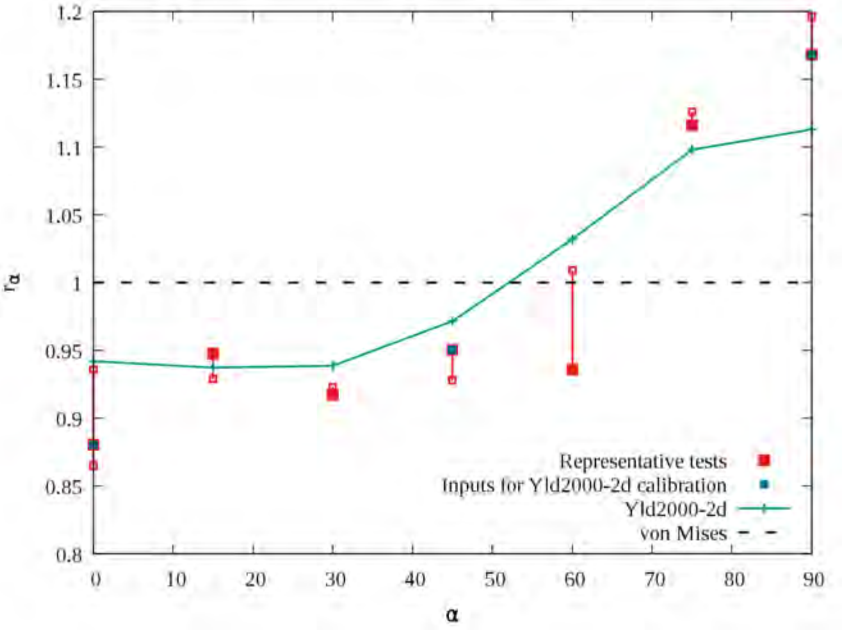

(b) r_α

Figure 2.6 – Evolution of the stress ratios s_α and the plastic anisotropy coefficients r_α as a function of the orientation α.

Table 2.6 – Identifications (Id) 1 and 2 of the e-HAH parameters for this study ($q = 2$, $z = 5$, $k_r = 15$, $k'_r = 0.2$, $L = 1$, $k_L = 0$) compared with the e-HAH model calibrations already presented in the literature for dual phase steels (d=database : S=forward-reverse shear, 2T=two-step tension, TC=tension-compression)

Id	k	S	k_S	k_1	k_2	k_3	k_4	k_5	d
1	30/130	0.773	135	132	45.3	0.1	0.858	7.15	S
2				232	250	0.1	0.835	6.72	S+TC
DP600									
[10]	30	/	/	70	20	0.1	0.9	6	S
[20]	30	/	/	80	8	0.1	0.9	6	S
[96]	30	/	/	35	20	0.	0.95	4	S
[96]	30	/	/	70	20	0.1	0.9	6	S
[92]	43.8	0.825	148	200.7	16.1	0.31	0.85	3	2T
DP780									
[75]	30	/	/	100	90	0.6	0.9	30	TC
[11]	120	0.8	75	150	78.5	0.25	1.0	0.0	2T
[72]	45	/	/	50	26.2	0.3	0.9	6.5	S
[92]	45	0.7	110	90	26.2	0.3	0.8	5	2T
[76]	195.3	/	/	135.5	197.2	0.431	0.834	16.1	TC
[79]	140	0.46	8	130	20	0.47	0.94	8	2T
DP980									
[95]	30	/	/	180	120	0.43	0.7	10	TC

Pre-strains in tension followed by simple shear tests are considered with two values of pre-strain but the behavior during pre-tension is only simulated and not included in the optimization because it is similar to the monotonic tension. The optimization is thus performed only on the subsequent shear tests. The shear stress-strain curves obtained after both pre-strains in tension are represented with dotted lines in Figure 2.7(a) in comparison with the monotonic shear test and the predicted behaviors which are the same for both identification. For both pre-strains, the transient behavior and the resumption of the hardening rate until the monotonic one are described by the model. However, a decrease of the flow stress is observed between the transient hardening and the resumption of the hardening behavior.

This decrease of the flow stress is controlled by the parameters k and k_S. The parameter k was fixed due to the divergence issue encountered in optimization and previously mentioned. A value of 30 is chosen because it is often used in the literature, cf. Table2.6. However, the synthesis of the parameters already identified for similar materials presented in Table 2.6 shows that this value is only used with the original version of the model that does not take into account cross-loading contraction and k is higher than 30 with the enhanced HAH model [72], [76], [92]. Thus, modifications of this parameter are tried to improve the description of the

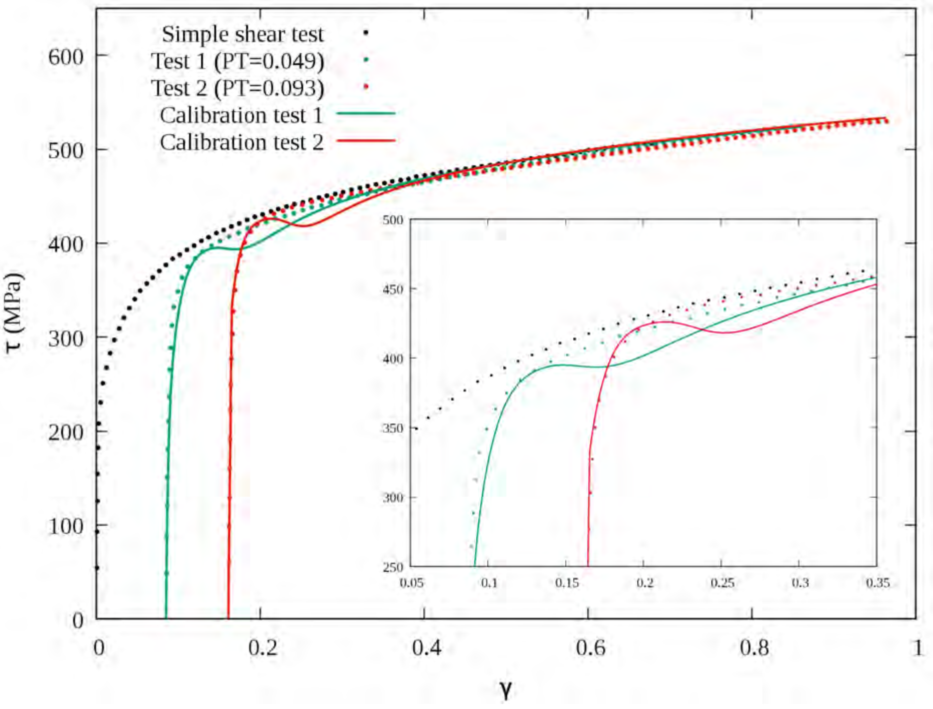

(a) $k = 30$

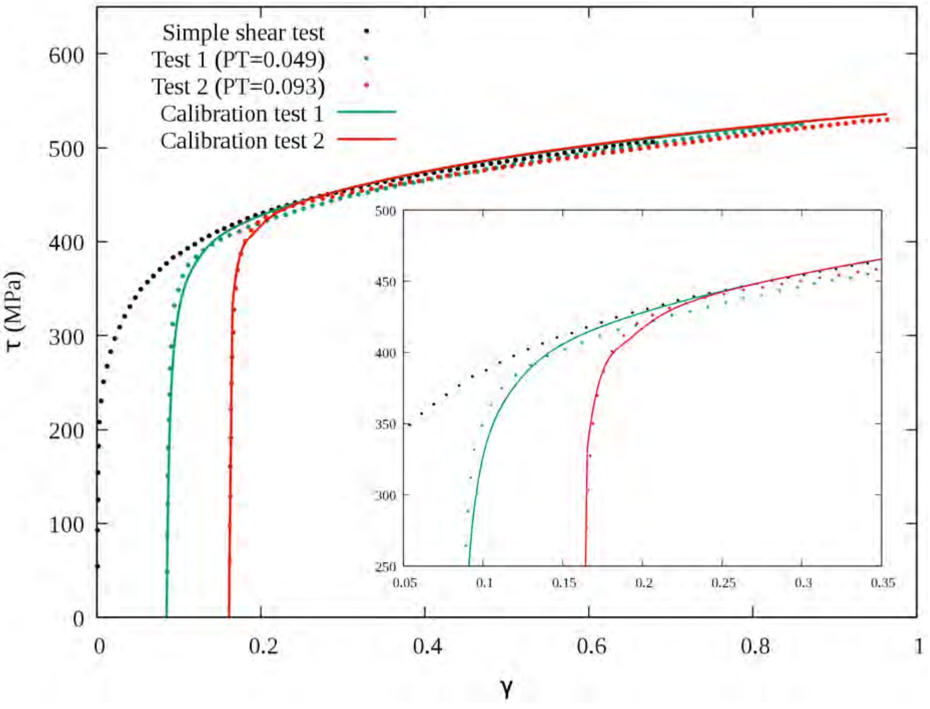

(b) $k = 130$

Figure 2.7 – Comparison of the predicted and experimental stress-strain curve of the simple shear tests after pre-tensions (PT= Tensile pre-strain value).

material behavior and the value of 130 appears to suppress the decrease effect observed on the flow stress. The comparison of the experimental and predicted stress-strain curves obtained for both tests with k equal 130 are presented in Figure 2.7(b). The decrease of the flow stress is not present anymore but for the highest forward strain, a non-continuous increase of the stress is observed which suggests that the decrease of the flow stress could still exist for higher forward strains.

The evolutions of the yield surface with plastic strain for both values of the parameter k are also presented in Figure 2.8. They are represented with the same plastic strain step and thus the increase of the value of k increases the evolution rate of the yield surface but the shape of the surface is not modified. Indeed, the evolution of the strain path change indicator $\cos\chi$ and the internal variable g_S that controls cross-loading in function of the equivalent plastic strain represented in Figure 2.9 for the first sequential tests are very different in function of the value of the parameter k. At the beginning of the orthogonal strain path, the indicator is equal to zero and it returns progressively to one with a speed controlled by k. With k equal to 130, the strain path change is shorter, thus the influence of the variable g_S is reduced and it prevents the flow stress from decreasing.

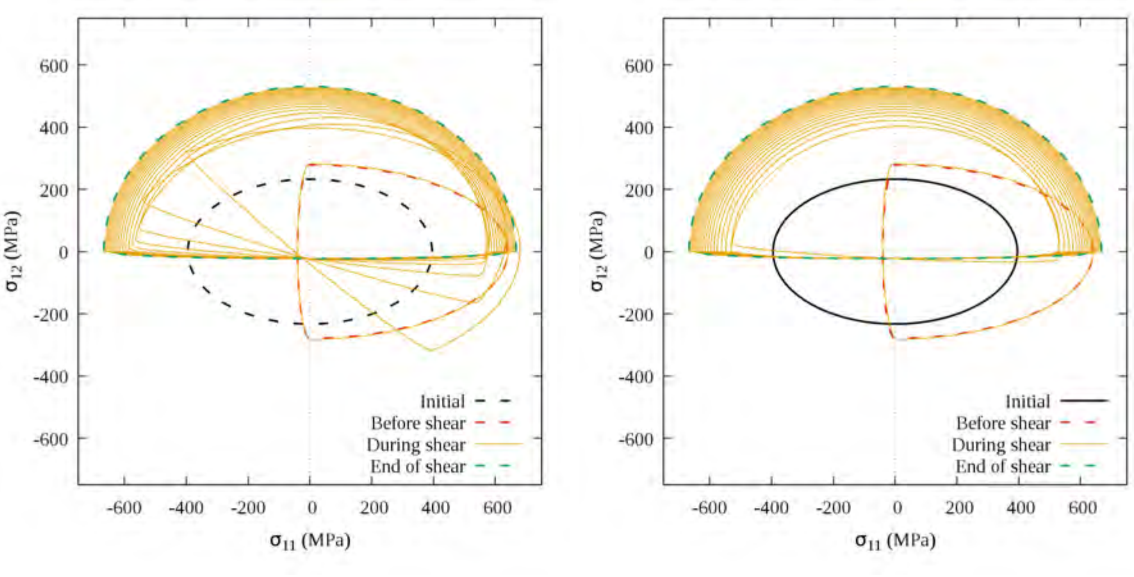

(a) $k = 30$ (b) $k = 130$

Figure 2.8 – Evolutions of the yield surface during a pre-tension (PT=0.049) followed by a simple shear test for the two k values and the first set of parameters

The increase of the value of the parameter k improves the description of the material behavior while the value is reduced when the parameter is included in the optimization loop. This

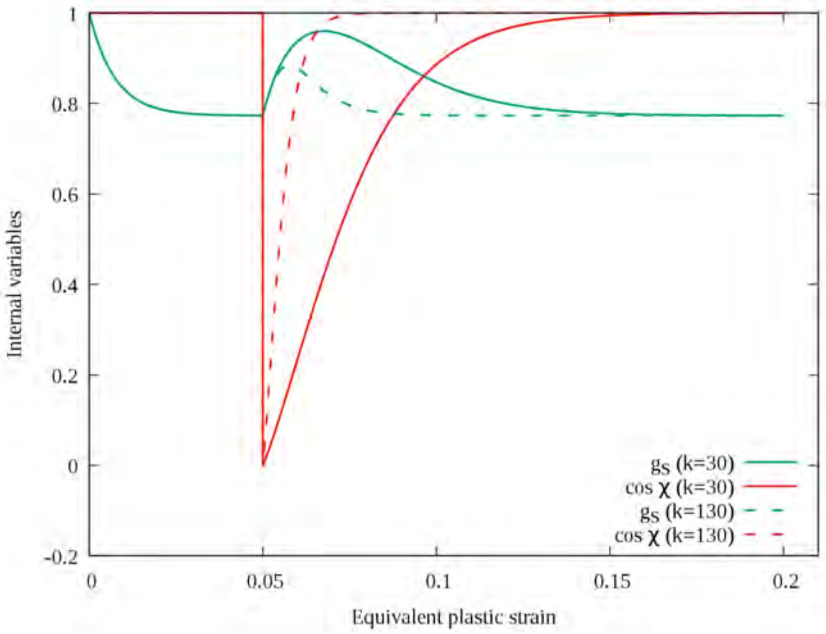

Figure 2.9 – Comparison of the evolutions of the strain path change indicator $\cos\chi$ and the internal variable that controls cross-loading g_S as a function of the equivalent plastic strain during the first sequential test simulation with k equal to 30 or 130

inconsistency creates difficulties to calibrate the model and the use of a fixed value of k finally gives a good description of the material behavior during cross-loading. However, the modification of the parameter k after the identification of the other parameter is only possible if dissociate orthogonal and reverse strain path changes are considered in the database because in that case there is no influence on the reverse behavior.

Forward-reverse shear tests with two forward shear strains values of $\gamma = 0.084$ and 0.212 are used for the calibration. A tension-compression test is also considered with a strain level of 0.006, considerably lower than the shear tests. The shear stress-strain curves are represented in Figure 2.10 with absolute stress and cumulative strain to compare the reversal behavior with the predictions obtained with the parameters of the identifications 1 and 2, respectively without and with the tension-compression in the database. The stress-strain curve of the tension-compression test is also compared with both prediction in Figure 2.11.

For both identification, the Bauschinger effect observed in forward-reverse shear is well described but the curve shape after reversal is different from the experimental one because the work-hardening stagnation is not captured by the model. The second identification leads to parameters k_1 to k_5 significantly different in particular k_1 and k_2, cf. Table 2.6, but their influence is not really visible on the predictions of forward-reverse shear tests. The predictions obtained with both set of parameters are really close to each other with only differences dur-

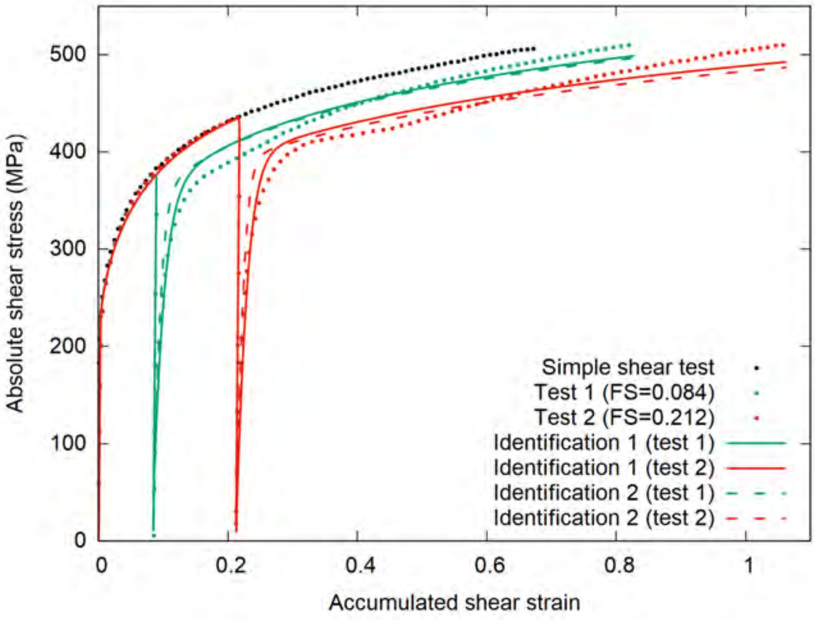

Figure 2.10 – Comparison of the absolute shear stress as a function of the cumulative strain for the forward-reverse shear tests and predictions (FS=Forward shear)

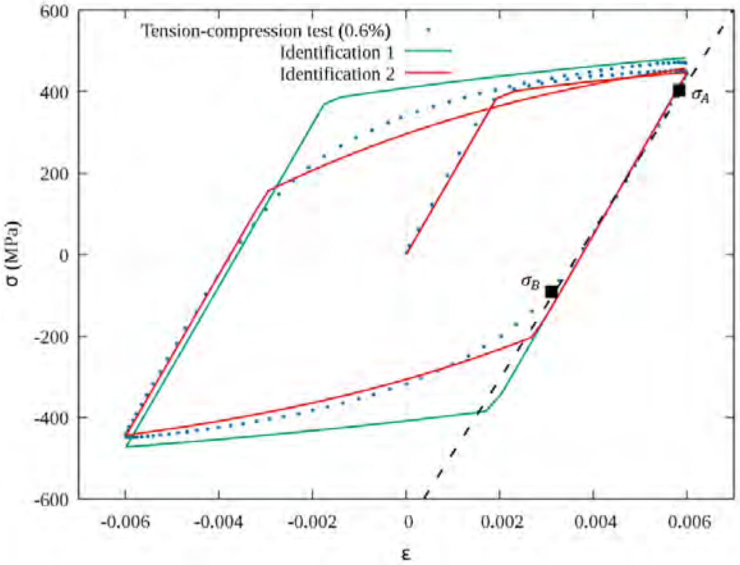

Figure 2.11 – Comparison of the Cauchy stress as a function of the logarithmic strain for the cyclic tension-compression tests and predictions (The dashed line is a linear approximation of the unloading curve, σ_A defines the stress before reversal whereas σ_B is the yield stress after reversal)

ing the transient hardening whereas a large difference is visible between the two predictions for the tension-compression test. The yield stress after reversal is overestimated with the parameters from the first identification. The addition of the test in the identification database gives an acceptable value of the yield stress with the second set of parameters. An influence of the database used for the identification on the reverse parameter values is also observed in the literature, cf. Table 2.6. Indeed, higher values of the parameters k_1 and k_2 are obtained when tension-compression tests are used for the identification or two-step uniaxial tension because the forward strains are lower than those considered during forward-reverse shear tests. The evolution of the internal variables g_1 and g_2, controlled by k_1 and k_2 and represented in Figure 2.12 for the first forward-reverse shear test and the tension-compression test, shows an exponential decrease of g_1 during the first path and g_2 during the second one.

In the case of the forward-reverse shear test, the evolutions are really different depending on the identification but the values of g_1 before the strain path change are close to each other. Indeed, the saturated value of g_1 which is controlled by k_3, is the same for both identification and is almost reached at the end of the first strain path. Thus, a similar stress-strain behavior is observed with both set of parameters during the strain path change in shear whereas the evolution of the internal variables shows really different values before each strain path change in tension-compression. The strain range is lower and thus the variables do not reach their stabilized values before the following strain path change. The influence of the set of parameters is also visible on the yield surface evolution in Figure 2.13. Both identifications lead to different yield surfaces at the end of the test. An extra strain path change, e.g. in plane strain tension, would be necessary to differentiate the 2 sets of parameters. It should be highlighted that other authors [56], [79] have already made such a comparison but it is out of the scope of this study.

The consistency of the experimental database is analyzed with the predictions obtained for both set of parameters. In order to compare the two identifications for the whole database, the evolution of the internal variable g_1 that controls the value of the yield stress after the first reverse strain path change is considered. This variable decreases during the forward loading and in the case of tension-compression, at the end of the forward loading, g_1 is equal to the ratio of the following yield stress in compression over the stress in tension before reversal [10]. It is possible to calculate the same value experimentally for all tests with different forward strains. Indeed, the yield stress after reversal, represented by σ_B in Figure 2.11, is determined on the stress-strain curve. To define this value, a linear approximation of the unloading curve is performed and represented with the black dashed lines. Then, the gap between that line and the stress-strain curve is calculated and a threshold value is taken to define the yield stress. Specifically, σ_B is fixed to the stress value when the gap between the stress and the linear approximation is greater than 10 MPa in tension and 6 MPa in shear. The stress before reversal, represented with σ_A in Figure 2.11 is calculated with the same method. Thus, it does not correspond exactly to the

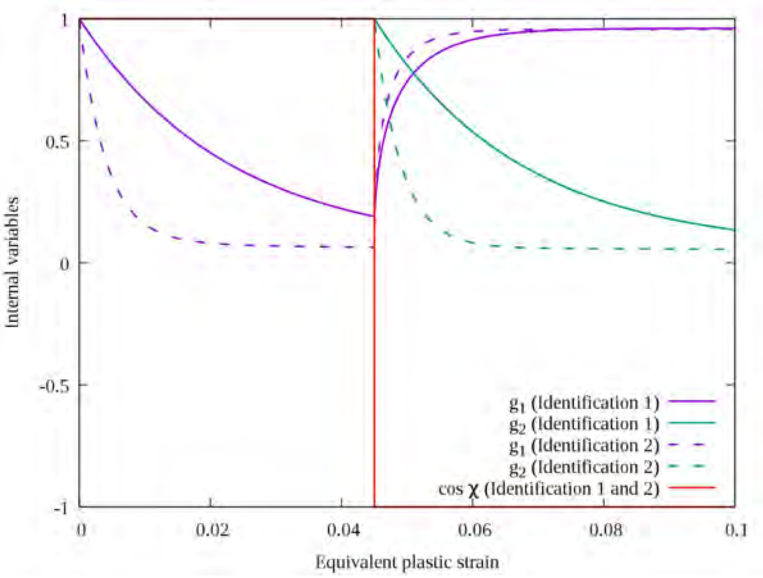

(a) Forward-reverse shear test (FS=0.049)

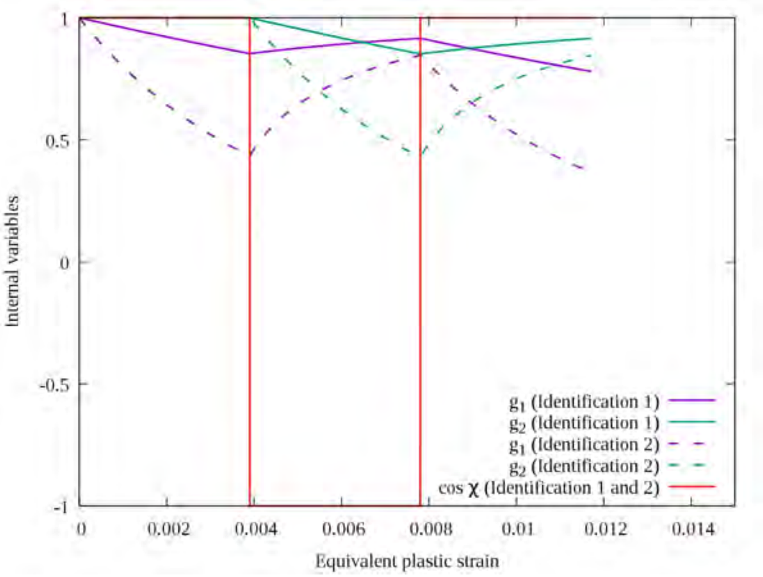

(b) Tension-compression test

Figure 2.12 – Comparison of the evolution of the internal variables g_1 and g_2 and the strain path change indicator $\cos\chi$ as a function of the equivalent plastic strain for both identification

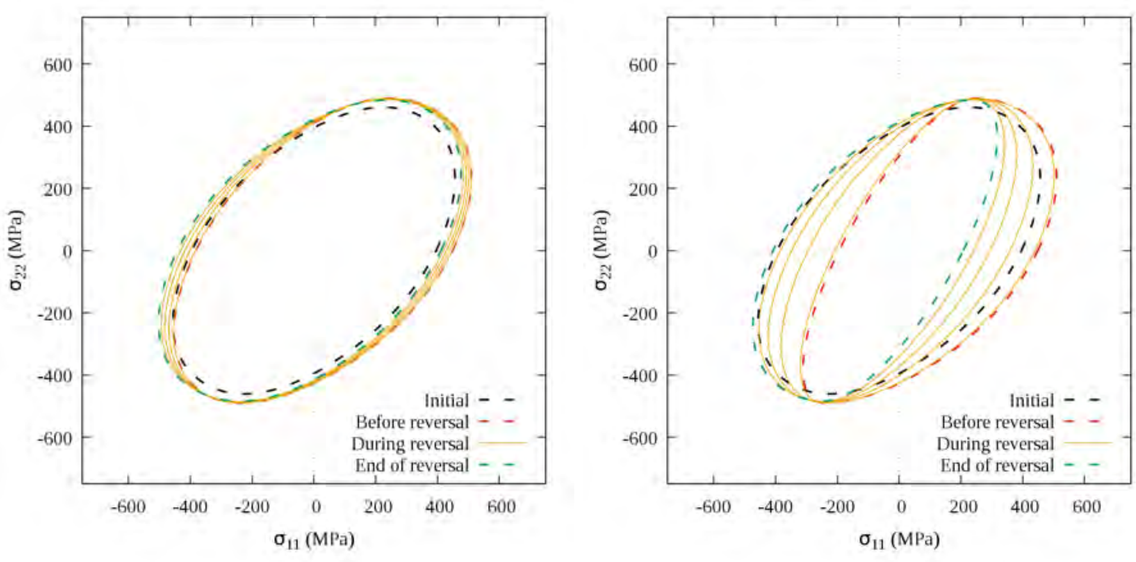

(a) Identification 1

(b) Identification 2

Figure 2.13 – Evolutions of the yield surface during the tension-compression test with the different sets of parameters

stress at the end of the first strain path because velocity effects create a rounded point at the beginning of the reversal [97]. The experimental evolution of the ratio -σ_B/σ_A is calculated for all the tests available in the database, i.e. cyclic tension-compression tests performed at different strain levels (0.18,0.19,0.22,0.25,0.3,0.4,0.5 and 0.6 %) for fatigue characterization and forward-reverse simple shear tests performed with three values of pre-shear (0.084, 0.212 and 0.452). The comparison of the ratios obtained experimentally with the evolution of g_1 predicted by both set of parameters is represented in function of the equivalent plastic strain in Figure 2.14.

An exponential decrease is observed experimentally until a saturated value which is already achieved with the shear tests whereas a steep evolution is observed in the strain range of tension-compression tests. A consistent evolution of this ratio is observed for both forward-reverse shear tests and tension-compression tests. The saturated value of g_1 is well predicted with both set of parameters whereas the evolution at low strain controlled by the parameter k_2 is only described correctly with the second set of parameters. Indeed, the first identification with only shear tests does not contain enough information to represent the material behavior under reverse strain path changes in a very low strain range. To obtain a better description of the behavior at this level it is thus necessary to consider the strong evolution of g_1 under 2% of equivalent plastic strain. In addition, to model the cyclic behavior at low strains, the low cycle fatigue criterion need to be calibrated.

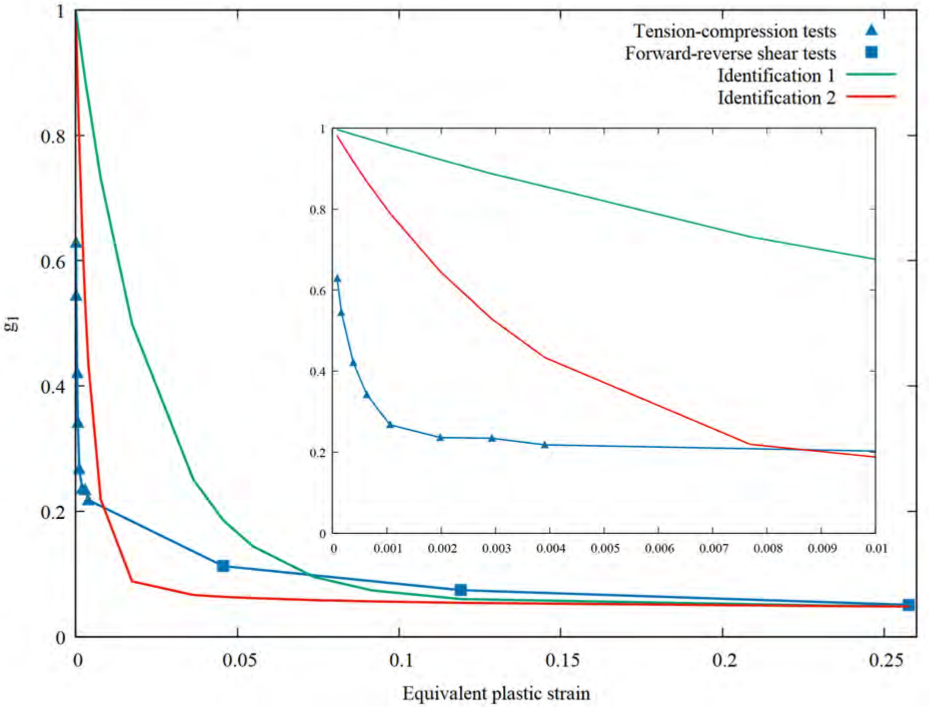

Figure 2.14 – Comparison of the ratio -σ_B/σ_A calculated for tension-compression tests and forward-reverse shear tests with the two predicted evolutions of g_1 as a function of the equivalent plastic strain

2.2.5 Fatigue criterion calibration

For a calibration with alternated cyclic tests, which is the case here considering the tension-compression tests presented previously, the mean stress is equal to 0 and thus the modified Morrow criterion is equivalent to the MCB criterion. Thus, the calibration of the modified Morrow criterion is the same as the MCB criterion because it contains no additional parameters. The plastic and elastic strain amplitudes are calculated for the stabilized cycle, cf. Figure 2.15, chosen as half of N_f. Then, the parameters $\sigma_f^{'}$ and b, respectively $\varepsilon_f^{'}$ and c, are calculated by linear regression of the logarithm of the elastic strain, respectively the plastic strain, as a function of the logarithm of the number of reversals until failure. The linear regressions and the curve of the MCB criterion are represented in Figure 2.16 and the identified parameters are summarized in Table 2.7. The MCB criterion represented in purple is in good agreement with the numbers of cycles until crack initiation obtained for the different tests performed with strain amplitudes between 0.6 % and 0.18 %.

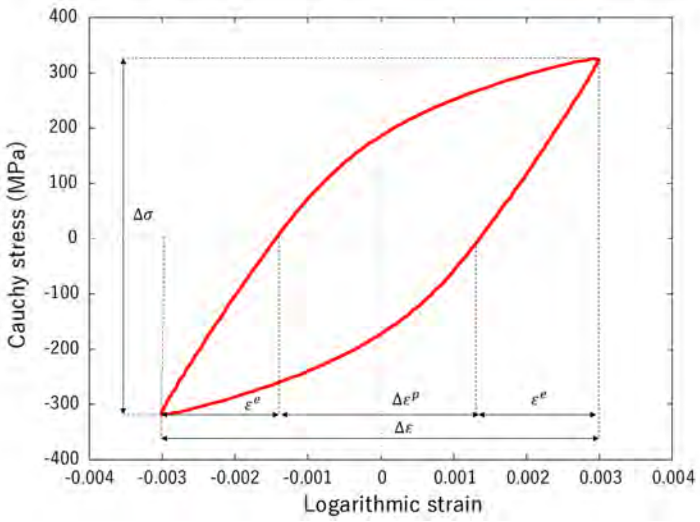

Figure 2.15 – Definition of the stress and strain amplitudes on a stabilized cycle

Table 2.7 – Parameters of the MCB and Morrow criteria

Parameters	σ'_f (MPa)	b	ε'_f	c
Values	1313.5	-0.135	1.211	-0.662

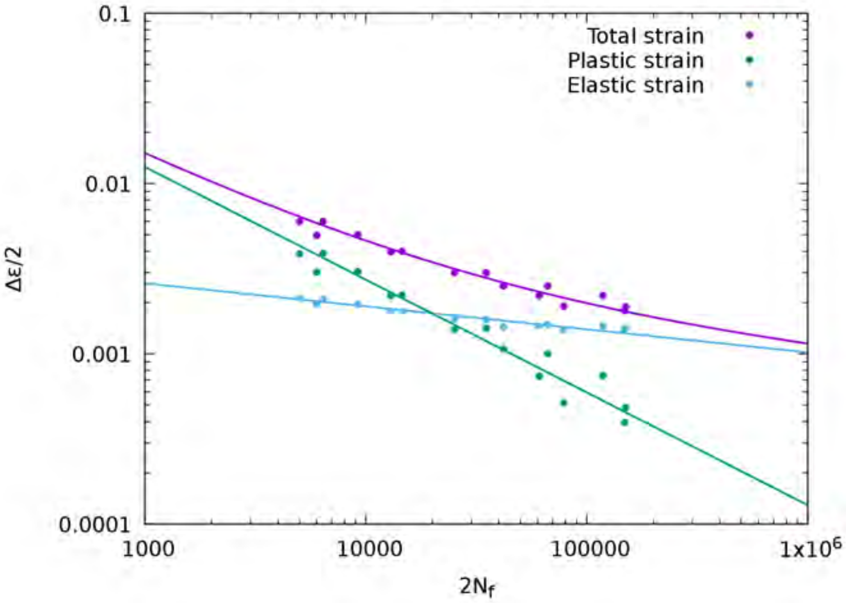

Figure 2.16 – Elastic, plastic and total strain amplitudes in function of the number of reversals

The criterion can then predict the lifespan N_f of the material for different fatigue loadings but it is necessary to simulate at least one cycle with the hardening model to calculate the strain amplitude and the mean stress. The ten first cycles of the tension-compression with a strain amplitude of 0.6% are simulated with both set of parameters of e-HAH model and compared with the experimental curve in Figure 2.17. For both identifications, a cyclic hardening is observed during the 10 first cycles. The hardening decreases with the number of cycles and tends towards a stabilized value. For identification2 including the first cycle of this test in the calibration database, the stabilized value is reached faster than for the identification 1 and the amount of cyclic hardening is lower. However, a cyclic softening is observed experimentally contrary to the model predictions. Thus, the simulation of only one cycle of the fatigue loading is preferred with this hardening model, in order not to introduce additional errors in the fatigue simulation.

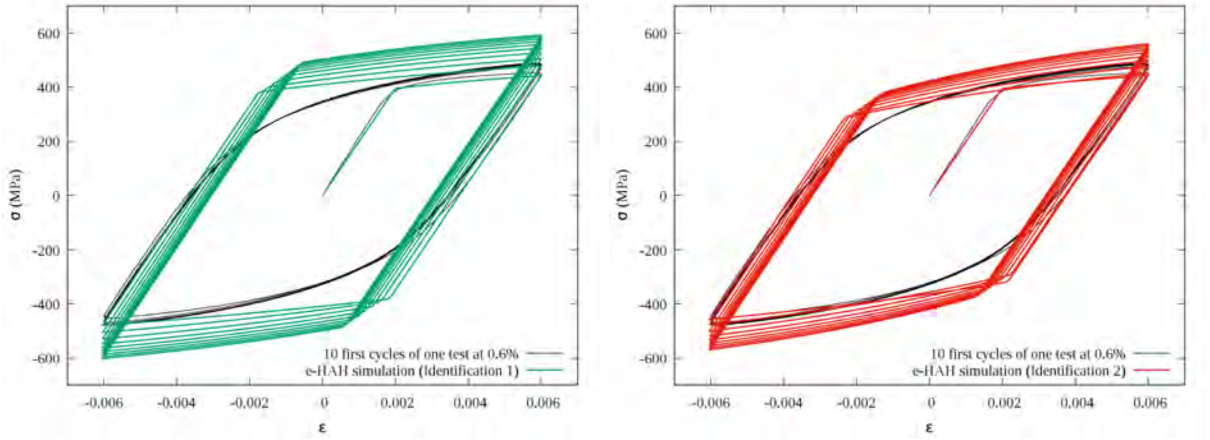

(a) Identification 1

(b) Identification 2

Figure 2.17 – Simulation of the ten first cycles of a tension-compression test at 0.6% for both set of e-HAH parameters

2.3 Conclusion

In conclusion, the e-HAH model is considered in this study to represent the strain path change behavior of the material and the modified Morrow criterion is used to predict its lifespan. The distortional hardening is coupled with an isotropic hardening and the Yld2000-2d criterion to describe the initial anisotropy of the material which is adapted to model the almost isotropic behavior in stress with a more anisotropic behavior in strain. To model exactly the shear stress level, the criterion exponent is decreased from 6 recommended for bcc materials to 3.6. A consistent description of all the monotonic tests of the database is obtained with this modification of the exponent value. Then, the e-HAH model associated to the Yld2000-2d criterion gives an accurate prediction of the material behavior under the different strain path changes and a consistency between the different strain levels.

However, difficulties are encountered to model certain particular behaviors observed for the DP600 steel. For sequential tests composed of pre-tension followed by simple shear considered for orthogonal strain path changes, the cross-loading transient behavior is not described correctly because an hardening stagnation is present on the model predictions for most of the values tried for the parameter k which is manually fixed due to a divergence issue in optimization. Improvements of the model to suppress the hardening stagnation have been proposed recently [98], [99] and could be used in the future. In the case of reverse strain path changes, a smooth evolution of the yield stress after inversion is obtained as a function of the plastic strain level for both forward-reverse shear tests and tension-compression tests which reflects a consistency of the material behavior. But for reverse strain path changes in shear, the model does not predict the work-hardening stagnation observed after reversal at large strains. Finally, two calibrations of the model with and without the tension-compression tests are compared and it can be concluded that to describe accurately the material behavior for the whole range of strains considered in different applications such as forming and fatigue, it is necessary to identify the reverse parameters of the model with different forward strain levels.

In a second time, different uniaxial low cycle fatigue criteria are presented to model this aspect of the material behavior decoupled from the strain path change behavior. The modified Morrow criterion is selected for this study because it takes into account the residual stress influence via the addition of mean stress in the MCB criterion with no additional parameters. The calibration performed with the stabilized results of the cyclic tension-compression tests along the rolling direction is a good average of the numbers of cycles until crack initiation obtained for different strain levels. It could be noted that the hardening model does not take into account of the cyclic softening recorded during fatigue test, leading to an overestimation of the stabilized stress level.

Afterwards, the models calibrated in this chapter will be used for the simulations of the forming of cylindrical cups and the predictions of their lifespan for a specific loading. Two forming processes are considered with different amounts of strain path changes in order to investigate their influence on the fatigue behavior of the cups.

Chapter 3

DEEP DRAWING OF CYLINDRICAL CUPS

The forming process considered in this study is the deep drawing which consists in forming a solid part from a sheet metal under the movement of a punch through a die. Deep drawing is largely used to form industrial parts, in the automotive field for example, and different benchmarks have been proposed in the literature to study this kind of process at a laboratory scale. The two main aspects largely studied are the formability of the sheet and the springback after forming, which often cause problems at the industrial level. Most of the demonstrators studied in the literature are coming from the Numisheet conference benchmarks such as the U-channel [75], [100] and the S-channel [101], [102] for springback study and the square cup [102], the cylindrical cup [103] and the cross-shaped cup [104] rather dedicated to formability study. In order to reproduce strain path changes that occur during the forming processes of automotive structural parts, some of these benchmarks are used and some modifications of these geometries are also proposed. The most widespread one is the U-channel test represented in Figure 3.1(a), often used for springback prediction, as it involves reverse strain path changes [63], [69], [75], [105]. However, orthogonal strain path changes do not occur with this process. Thus, variations with S shape [69], [101] shown in Figure 3.1(b) or P and C shapes [13], cf. Figure 1.2, have been proposed to obtain both reverse and orthogonal strain path changes. The cross die test, represented in Figure 3.1(c), exhibits also orthogonal strain path changes [16], [17] but with the limitation of only one strain path change at each material point. Multi-stage processes such as direct or reverse redrawing of cylindrical cups involve multiple strain path changes with both reverse and orthogonal ones [65]. An example of the reverse redrawing process in Figure 3.1(d), proposed as a Benchmark at Numisheet'99, has highlighted particularly the occurrence of orthogonal strain path changes in the second step.

The deep drawing in one and two stages of cylindrical cups is considered in this study. The first process in one stage is considered as the tools are available in the laboratory for the BUP200 machine. The process in two stages is specifically designed for this study, using as a starting point the process of reverse redrawing presented in Figure 3.1(d) and reducing the dimensions to obtain a similar cup to the one obtained with the one-stage process. The aim is to compare two cups with similar geometries but with different strain path histories. Preliminary finite element analysis showed that direct or reverse redrawing exhibit similar strain path changes, thus the direct redrawing is chosen because it is easier to set up experimentally on the BUP200 machine.

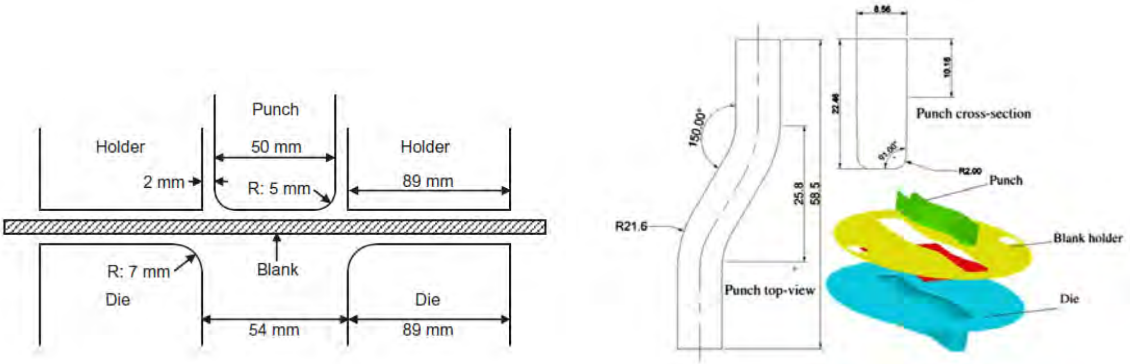

(a) U-channel [75] (b) S-channel [101]

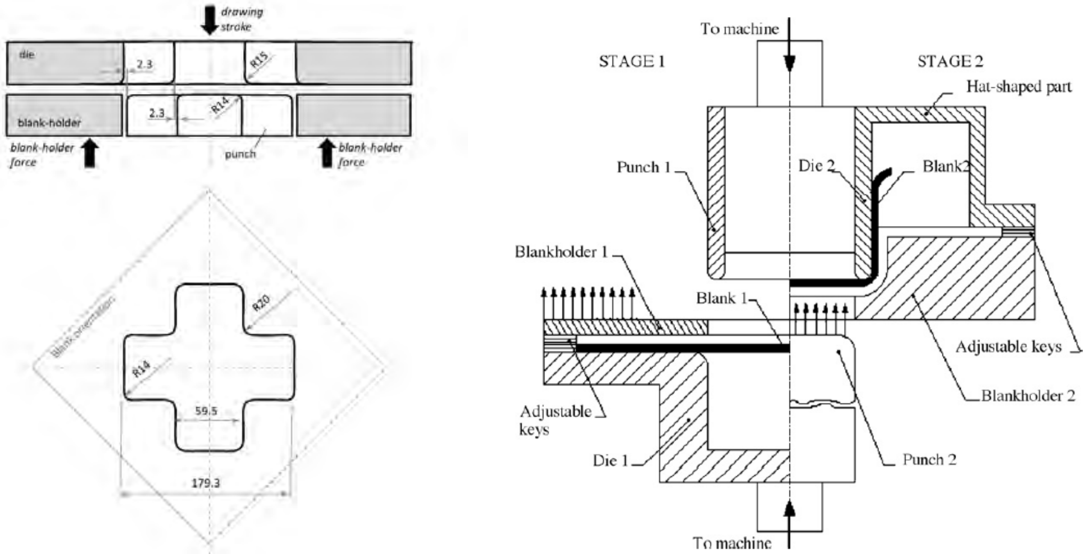

(c) Cross [17] (d) Reverse cup [65]

Figure 3.1 – Examples of deep-drawing demonstrators which exhibits strain path changes

The drawings of the tools designed to perform the direct redrawing are given in Appendix B. Moreover, to ensure the feasibility of this test, finite element simulations of the process have been performed with PAM-STAMP code. Forming limit diagrams, which define the maximum allowable strain levels in function of the different strain modes represented on a graph of major strain versus minor strain, are used to validate the design (cf. Appendix B).

In this chapter, the experimental procedure associated to the two processes is firstly presented with the different measurement methods. Indeed, strain and residual stress measurements are performed for both processes to get additional results on top of automatically recorded efforts and displacements of the tools, in order to validate the finite element analysis and to investigate the strain path change influence. The results of both processes are finally analyzed and compared.

3.1 Experimental procedure

3.1.1 Deep drawing setups

Firstly, for the process in one stage, a cup of diameter 33 mm is obtained from a blank of diameter 60 mm whereas in two stages, a blank of diameter 80 mm is used to draw firstly a cup of diameter 48 mm and then a smaller one of diameter 36 mm. The two punches move in the same direction, thus it is called redrawing process thereafter. The cups obtained in one stage are called cups 1 (C1) and for the process in two stages, they are called redrawing cups 1 and 2 (RC1 and RC2). The dimensions of the forming tools of C1 and each of the redrawing cups are presented in Figure 3.2 with mention of the drawing ratios corresponding to the ratio of the blank diameter on the punch diameter. The limiting drawing ratio (LDR), which is the maximum allowable value of the drawing ratio, is an indicator of the material formability. Regardless of the material, the ratio cannot exceed 2.72 [106] and for deep drawing of steel sheets, the literature suggests that the limiting drawing ratio is between 1.66 and 1.81 for the first stage and between 1.25 and 1.33 for the second stage [107]. For high strength steels like dual phase ones, these values may vary because the limiting drawing ratio is influenced by different parameters including the material properties with in particular the anisotropy [106], [108] but also process parameters like the friction and the tool geometries especially the die radius [109], [110]. For DP600, a drawing ratio of 1.82, corresponding to the drawing ratio of C1 process, is allowable but it was tried to use the same punch with an initial blank of diameter 70 mm corresponding to a drawing ratio of 2.12 and this led to a rupture of the blank. The limiting drawing ratio of DP600 seems to be around 2 for the first stage but in the case of RC1, a drawing ratio value in the low range has been chosen for safety whereas it is in the upper range for RC2 in order to obtain a cup with a diameter close to the one of C1. Moreover, for C1 and RC1, a force is applied by the blank-holder to hold the blank during the punch displacement. For the second stage of the redrawing process, a constant gap between the blank-holder and the die is used. Circular spacers are positioned on the blank holder to control the gap value. The spacer thickness corresponds exactly to the gap value between the die and the blank-holder at the cup level.

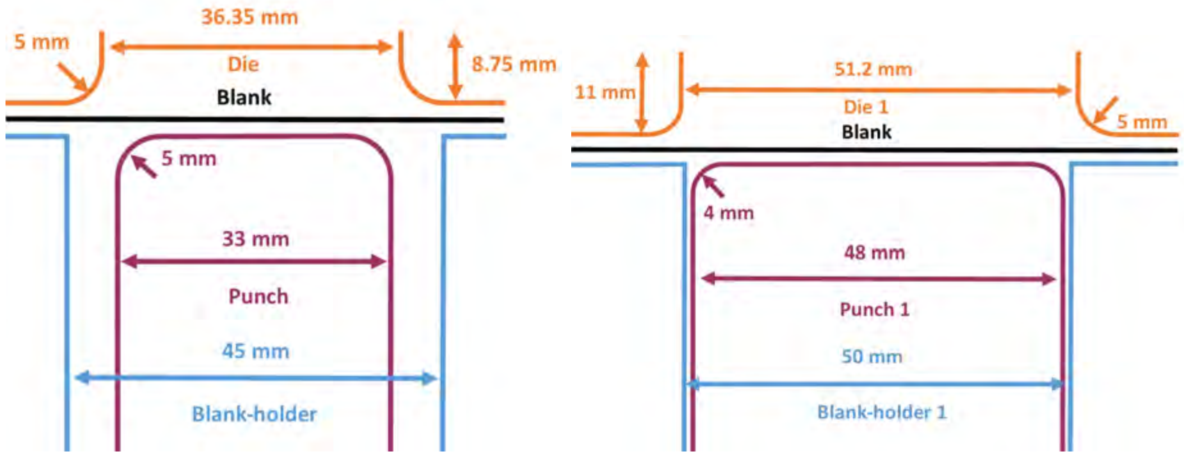

(a) C1 (DR=1.82, $\phi_{blank} = 60\,\text{mm}$, Gap=1.675 mm) (b) RC1 (DR=1.66, $\phi_{blank} = 80\,\text{mm}$, Gap=1.6 mm)

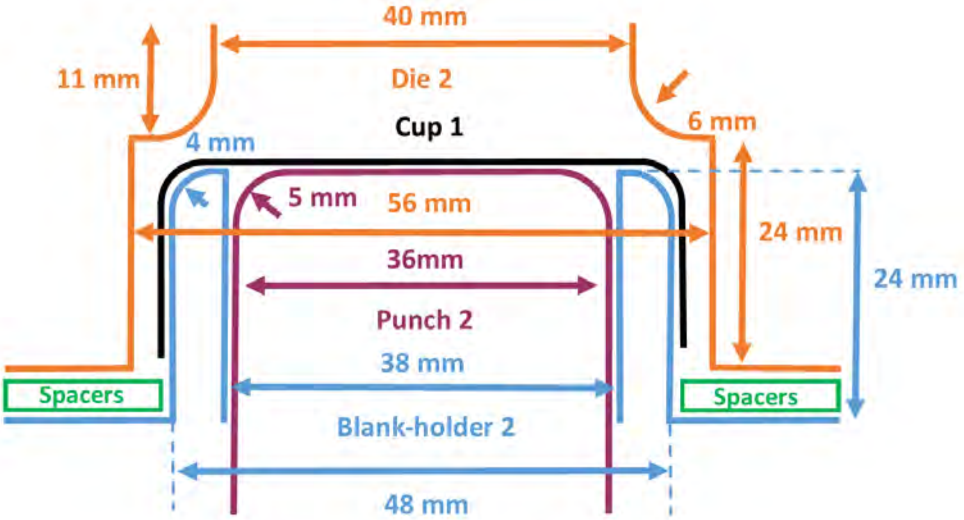

(c) RC2 (DR=1.33, Gap=2 mm)

Figure 3.2 – Tools dimensions for the two processes, in mm (DR=Drawing Ratio, ϕ_{blank}= initial blank diameter, Gap= half the difference between the die and the punch diameter)

One-stage process

Different values of the blank-holder force, from 80 kN down to 4 kN and respectively equivalent to clamping pressures applied to the blank from 64.7 MPa down to 3.2 MPa, are used to find out the optimal value that prevents the wrinkle formation, without leading to the stretching of the blank. A squeezing of the outer part of the cup edge, creating burrs, is observed in particular for high values of the blank-holder force according to Figure 3.3. This effect is observed also for other materials during the deep drawing of cups on the BUP200 machine [111]. Indeed, due to the absence of a blank-holder stopper, the blank-holder force is applied during the whole test even when it is no longer in contact. Thus, just before the interruption of contact with the blank, the flange is pinched between the die and the blank-holder. The squeezing of the cup is visible on the punch force-displacement curves represented in 3.4(a) with a plateau at the maximum force level which appears for a blank-holder force above 20 kN and increases together with the blank-holder force. After the plateau, an abrupt decrease of the punch force corresponds to the contact interruption between the blank and the blank-holder. It is possible to attenuate the squeezing of the cup by decreasing the blank-holder force to a value less or equal to 10 kN and a smoother evolution of the punch force-displacement curve is obtained until a displacement equal to 17 mm. Indeed, an abnormal displacement evolution is observed at this point on the punch force-displacement curves for blank-holder forces equal to 10 kN and 4 kN. Due to the squeezing of the blank, a sticking point is encountered by the punch which stops or steps back to continue the deep-drawing of the cup. In spite of this issue, a blank-holder of 4 kN is used for the following tests because this value gives the smoothest cup edge.

(a) 80 kN (b) 40 kN (c) 20 kN (d) 10 kN (e) 4 kN

Figure 3.3 – Evolution of the squeezed edge with the blank-holder force (burrs are surrounded in red)

Moreover, the tests are usually performed with a punch speed of 1 mm/s to be the closest to a quasi-static condition because the characterization tests are performed in such conditions. To solve the issue presented above, the punch speed is increased. Different values within the available range of the machine between 1 mm/s and 10 mm/s are used. The punch force-displacement curves in Figure 3.4(b), are smoother when the punch velocity is higher. The value of 6 mm/s seems to be a good compromise because there is no effect of the strain rate contrary to 10 mm/s and the curve is fairly smooth. Three punch speeds are investigated then for the strain field measurements of the C1 cups. The value of 1 mm/s is considered in order to have a measurement in condition close to the quasi-static one, the value of 6 mm/s because it is enough to suppress the sticking point and 10 mm/s because the increase of speed better preserves the speckle pattern during the process and thus gives a larger strain measurement.

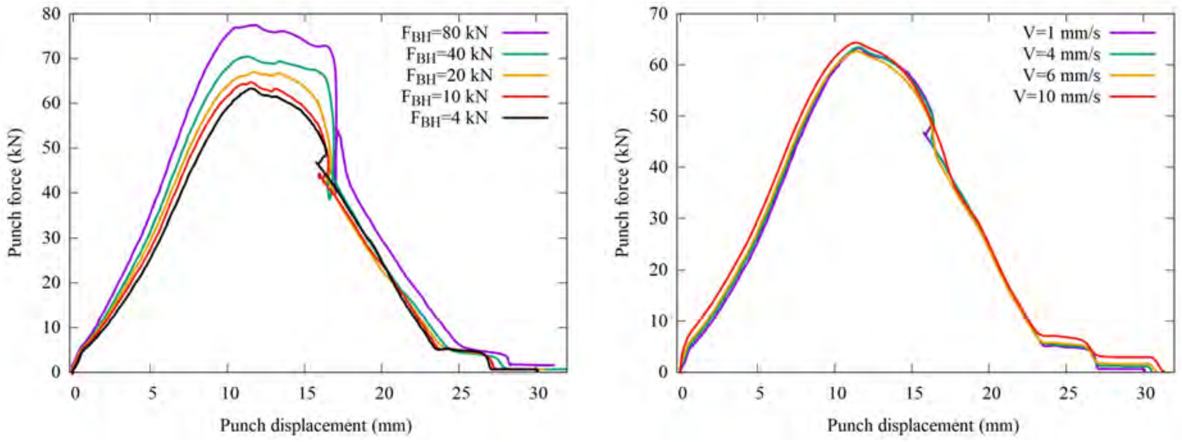

(a) V=1 mm/s (b) F_{BH}=4 kN

Figure 3.4 – Influence of the blank-holder force F_{BH} and the punch velocity V on the punch force-displacement curves

Redrawing process

In the same way, the first stage of the redrawing process is first performed with different blank-holder forces, to find out the optimal one. As no stretching nor wrinkles are observed for this process, the value of 5 kN, corresponding to a clamping pressure applied to the blank of 1.6 MPa, is chosen for the subsequent tests because the force displacement curve is smoother for this value, cf. Figure 3.5(a). Furthermore, it is not necessary to increase the punch speed during the redrawing test because there is no sticking point observed on the punch force-displacement curve of the first stage. During the second stage, there is no holding force but the spacer thickness can be adjusted. Two spacer values are tried, 1.7 mm and 2.4 mm, and one test is also performed without spacers to check whether a rupture of the blank occurs. Unfortunately, the cup wall is laminated but there is no rupture. A slight influence of the spacer value is visible on the force-displacement curve except for the test without spacers for which the curve shape is different. Finally, the largest spacer value of 2.4 mm is used for all the tests.

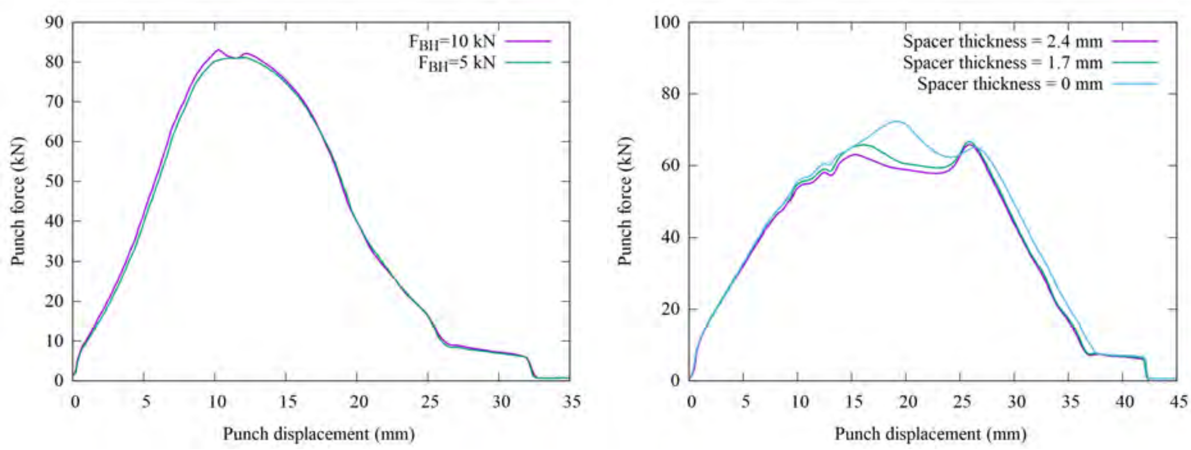

(a) RC1 (b) RC2

Figure 3.5 – Punch force-displacement curves of the different stages of the redrawing process

3.1.2 Measurement methods

Different measurements are performed during or after the test in order to check the numerical predictions. First, the major and minor strains are measured by Digital Image Correlation (DIC), and then the residual stresses are measured by X-Ray Diffraction (XRD). In each case, the results are presented along the profiles in function of the coordinate along $\vec{Y}$ axis, normal to the cup floor according to Figure 3.6. Different methods of measurement are used but the definition of this axis is consistent with an origin fixed on the outer surface of the cup floor, where the blank is not deformed. Three other parts of the cup can be distinguished, the radius which has the same shape than the punch, the wall which is the straight vertical part and the flange corresponding to the end of the wall which is slightly curved.

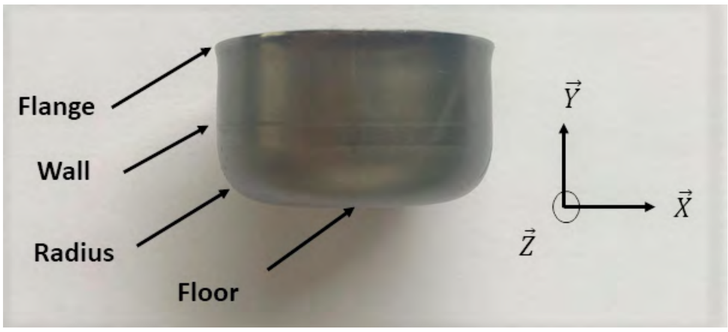

Figure 3.6 – Definition of the cup coordinate system used for the measurements

Strain field measurement

Because of the tools, it is not possible to continuously record the images with the DIC measurement system during the tests. Thus, the strains are calculated using only two images, one before and one after the test. The blank is initially placed on marks to be able to set the cup in the same position after deep-drawing. The measurement system is shown in Figure 3.7 with the two cameras for DIC, the cup and two spotlights. The parameters of the DIC measurements are summarized in Table 3.1.2.

Figure 3.7 – Strain measurement system

In order to measure the strain field, a speckle pattern is painted on one of the blank face with white and black paints. First, its application on the outer surface of C1 cup is tried and a polyethylene film is placed between the die and the blank to reduce the friction [88], [111]. However, the film is broken next to the cup radius and thus the speckle pattern is not visible anymore for the cup wall, cf. Figure 3.8(a). Then, the speckle pattern is applied on the inner surface of the cup, in contact with the punch where the friction is lower. Some tests with a plastic film were performed but the same problems as on the outer faces occurs. Finally, tests are performed without any film and it is possible to measure the strain over a large part of the cup except near the flange, cf. Figure 3.8(b). To obtain intermediate measurements of the strain field, some tests are stopped at a value of 10 mm for the punch displacement. Inner and outer speckle pattern are also tried for this case but with the outer speckle pattern, the painting is too damaged in the radius to be able to measure the strain field, cf. Figure 3.8(c). Thus, the speckle pattern is also applied on the inner surface for the intermediate test according to Figure 3.8(d).

Table 3.1 – DIC hardware and analysis parameters [112]

Camera	DALSA FALCON 4M60
Image resolution	2352 x 1728 pixels^2
Lens	Schneider Kreuznach 50 mm macro
Aperture	f/16
Field-of-view	90 mm (C1) or 85 mm (RC1 and RC2)
Image scale	25 pixels/mm
Stereo angle	20.5 degrees (RC1 and RC2)
Stand-off distance	345 mm (RC1 and RC2)
Image acquisition rate	1 Hz
Patterning technique	Base coat of white spray paint with black ink speckles
Pattern feature size (approximate)	10 pixels / 0.4 mm
DIC Software	Aramis 4M GOM v6.3
Image filtering	Gaussian filter with 3x3 pixel kernel
Subset size	20 pixels / 0.8 mm
Step size	10 pixels / 0.4 mm
Subset shape function	Affine
Matching criterion	Zero-normalized sum of square differences (ZNSSD)
Interpolant	Linear strain
Virtual strain gauge size (approximate)	1000 pixels / 40 mm
Strain formulation	Logarithm

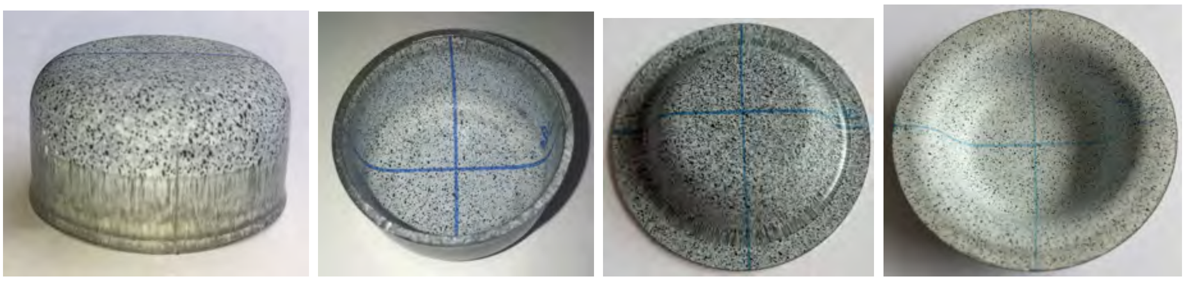
(a) Outer surface + full test (b) Inner surface + full test (c) Outer surface + intermediate test (d) Inner surface + intermediate test

Figure 3.8 – Examples of speckle patterns after deep drawing on the inner and outer surfaces of the C1 cups (the lines corresponds to the rolling and transverse direction)

The same protocol is used for the strain measurement of the redrawing cups. In addition of the measurement at the end of each stage of the redrawing process, intermediate measurements are performed for three different values of the punch displacement, i.e. 5, 15 and 25 mm, cf. Figure 3.9. For both processes, the strain field measurement is performed by quarter or a little more of the full geometry in order to measure completely the strain field of each cup. Finally, a summary of the different tests performed is presented in Tab. 3.1.2 with the respective cup heights.

Figure 3.9 – Different steps of measurement for the redrawing process (from left to right: end of the stage 1, stage 2 with a punch stroke of respectively 5, 15 and 25 mm, end of the stage 2)

Table 3.2 – Synthesis of the different tests

Test	Punch stroke	Punch speed (mm/s)	Number of test				Height (mm)
			DIC	Thickness	XRD	Total	
C1	Full	1	1	0	1	2	20.2 ± 0.1
		6	3	1	1	4	20.2 ± 0.4
		10	2	1	1	3	20.3 ± 0.3
	10 mm	1	1	0	0	1	11 ± 0.2
		6	2	0	0	2	11.6 ± 0.3
		10	2	0	0	2	12 ± 0.3
RC1	Full stage 1	1	3	2	3	5	22.1 ± 0.3
RC2	Stage 2, 5 mm	1	1	0	0	1	25.6 ± 0.4
	Stage 2, 15 mm		3	0	0	3	29 ± 0.3
	Stage 2, 25 mm		3	0	0	3	30.2 ± 0.5
	Full stage 2		4	2	3	6	33.9 ± 0.7

Residual stresses

Residual stresses are the self-equilibrated internal stresses obtained in the cup after the forming process resulting from the different strain modes and levels [113]. X-ray diffraction (XRD) is one of the non-destructive methods used to measure the magnitude of the residual stresses at certain locations of the specimens. It is based on the spacing variation of the inter-atomic lattice created by the stress field. The distance between atomic planes d^{hkl} is linked to the incident angle θ and the wavelength λ by the Bragg law, $2d^{hkl}\sin\theta = n\lambda$, illustrated in Figure 3.10. The wavelength value is fixed and depends on the chemical composition of the X-ray source, a chrome tube is used in this study to measure residual stresses in the ferritic phase of the material. The variation of the angle between the incident and the diffracted beams $\Delta(2\theta)$ is measured with the comparison of the diffraction peaks. The variation of distance $(d^{hkl} - d_0^{hkl})$, linked to the elastic strain $\varepsilon = (d^{hkl} - d_0^{hkl})/d_0^{hkl}$, is then deduced. The stresses are finally calculated with Hooke's law.

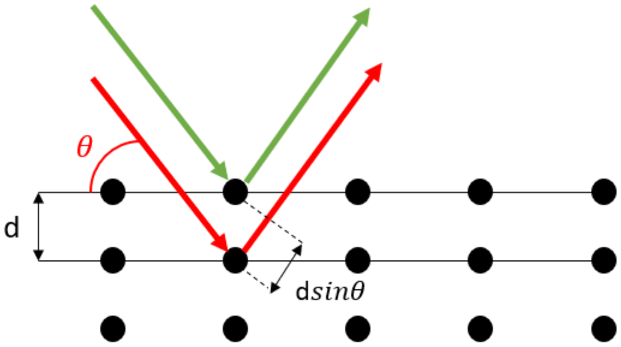

Figure 3.10 – Illustration of the Bragg law with two incident X-rays, $d = d^{hkl}$ for a given plane family (hkl)

The incident beam is emitted by the X-ray source in direction of the specimen which returns diffracted beams that are received by one or two detectors. The reference position of the different elements is represented in Figure 3.11(a) where the specimen coordinate system $(\vec{S}_1, \vec{S}_2, \vec{S}_3)$ and the goniometric coordinate system $(\vec{G}_1, \vec{G}_2, \vec{G}_3)$ are superimposed. Three angles (ω,φ,χ) are represented and correspond to the different rotations that are possible to define an acquisition mode. The modified χ mode with two detectors used for the measurements, performed at ENSTA Bretagne (IRDL) with a Stresstech G2R machine, is represented in Figure 3.11(b). This acquisition mode corresponds to an angle ω fixed at $\pi/2$ and a variation of the two other angles χ and φ to investigate different measurement directions.

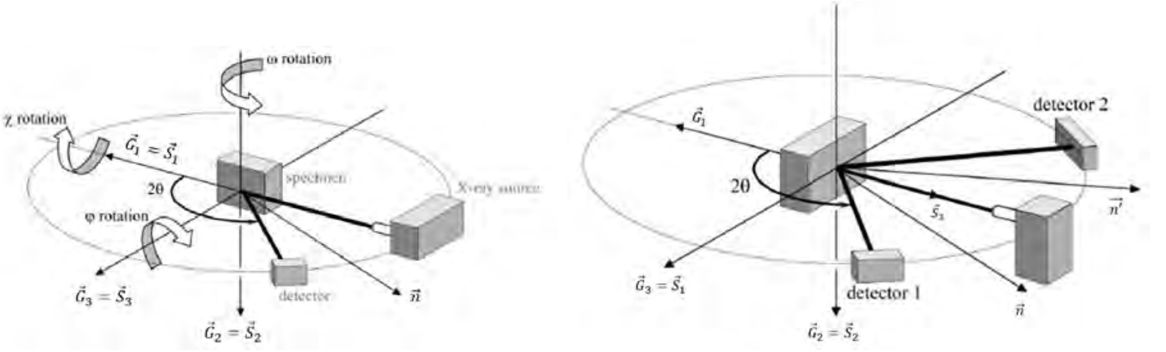

(a) Reference position

(b) Modified χ mode ($\omega = \pi/2$)

Figure 3.11 – Representation of the reference position and the modified χ mode of acquisition for XRD measurement with two detectors [114]

The measurement direction, also called scaterring vector, is represented by a unit vector $\vec{n}$ which is the bisector of the incident and diffracted beam. The coordinates of this vector in the specimen coordinate system are expressed as :

$$\vec{n} = \begin{bmatrix} \cos\Phi \sin\Psi \\ \sin\Phi \sin\Psi \\ \cos\Psi \end{bmatrix}_{(\vec{S}_1,\vec{S}_2,\vec{S}_3)} \tag{3.1}$$

where the two angles Φ and Ψ are defined in Figure 3.12(a). The rotation η around the vector $\vec{n}$ controls the penetration depth. In this study, the penetration depth is constant and is around a few micrometers. In the case of cylindrical cups, measures are performed along a line of the wall aligned with the rolling or transverse direction. The specimen axes $\vec{S}_1$ and $\vec{S}_2$ are also represented on a cup in Fig 3.12(b) with the axis $\vec{S}_3$ normal to the cup wall. An X-ray source with a collimator of diameter 1 mm is used and thus measurements are performed at points spaced by 1 mm apart from each other.

Only particular cases of Φ equal to 0° or 90°, equivalent to measurements performed along the axis $\vec{S}_1$ or $\vec{S}_2$, are investigated in this study. In these conditions, the elastic strain in the measurement direction is calculated by projection of the strain tensor and given by:

$$\varepsilon_\Psi(\Phi = 0°) = (\varepsilon_{11} - \varepsilon_{33}) \sin^2\Psi + \varepsilon_{13} \sin 2\Psi + \varepsilon_{33} \tag{3.2}$$

$$\varepsilon_\Psi(\Phi = 90°) = (\varepsilon_{22} - \varepsilon_{33}) \sin^2\Psi + \varepsilon_{23} \sin 2\Psi + \varepsilon_{33} \tag{3.3}$$

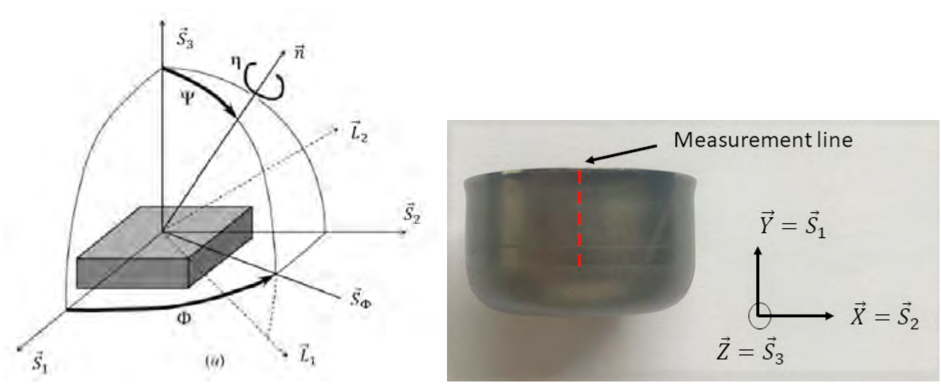

(a) General definition of the specimen axes and angles (b) Definition of the specimen axes on a cup

Figure 3.12 – Definition of the specimen axes and angles in a general way [114] and for a cup

Then, the elastic strain components are expressed in function of the stress components using Hooke's law and considering the free edge condition equivalent to a stress component $\sigma_{33} = 0$. The elastic strain for both values of Φ is given by

$$\varepsilon_\Psi(\Phi = 0°) = \frac{1}{2}S_2^{hkl}\sigma_{11}\sin^2\Psi + \frac{1}{2}S_2^{hkl}\sigma_{13}\sin 2\Psi + S_1^{hkl}(\sigma_{11} + \sigma_{22}) \tag{3.4}$$

$$\varepsilon_\Psi(\Phi = 90°) = \frac{1}{2}S_2^{hkl}\sigma_{22}\sin^2\Psi + \frac{1}{2}S_2^{hkl}\sigma_{23}\sin 2\Psi + S_1^{hkl}(\sigma_{11} + \sigma_{22}) \tag{3.5}$$

where S_1^{hkl} and S_2^{hkl} are two diffraction elastic constants, different from the constants of the Hooke's law because they depend on the atomic plane $\{hkl\}$. They need to be calibrated with XRD measurement during a tensile test where the stress can be also evaluated directly from the force. In the modified χ acquisition mode with two detectors, it is assumed that $\Psi = \chi$ with minor errors on the $\sin^2\Psi$ slope due to the use of two detectors [114].

It is thus possible to express the angle between the incident and diffracted beams $\Delta(2\theta)$ as a function of $\sin^2\Psi$. In the case of Φ equal to zero, the relation is given by

$$\Delta(2\theta)(\Phi = 0°) = -2\tan\theta_0(\frac{1}{2}S_2^{hkl}\sigma_{11}\sin^2\Psi + \frac{1}{2}S_2^{hkl}\sigma_{13}\sin 2\Psi + S_1^{hkl}(\sigma_{11} + \sigma_{22})) \tag{3.6}$$

with θ_0, the angle corresponding to the initial distance between atomic planes d_0^{hkl}. This equation can be represented as an elliptic function of $\sin^2\Psi$, cf. Figure 3.13, where σ_{11} corresponds to the major axis and σ_{13} to the minor axis. When Φ is equal to 90°, the major and minor axis corresponds respectively to σ_{22} and σ_{23}. In order to obtain a good description of the ellipse and then to deduce the stresses, the angle $\Delta(2\theta)$ is measured for different values of Ψ, seven in this

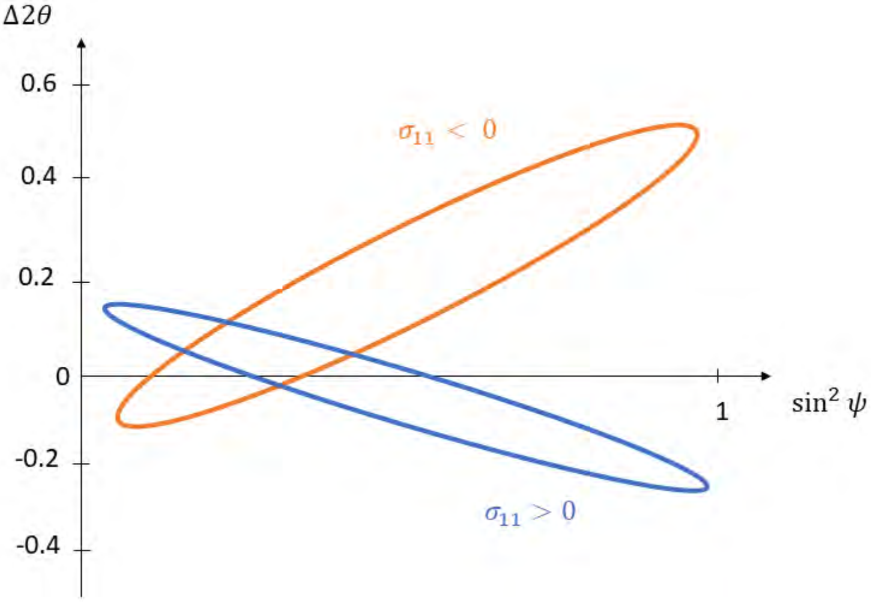

Figure 3.13 – Representation of the ellipse of $\Delta(2\theta)$ in function of $\sin^2\Psi$

study.

The studied material (a DP600 steel) is composed of two phases, the ferritic one is predominant, considering the percentage of martensite between 10 and 18 %, cf. Figure 1.10, and thus the stress components are not measured in the secondary phase. Moreover, since calibration of the diffraction elastic constants could not take place before the measurements, conventional values for ferritic steels were used ($S_1^{hkl} = 1.35 \times 10^{-6}\,\mathrm{MPa}^{-1}$ and $\frac{1}{2}S_2^{hkl} = 6.15 \times 10^{-6}\,\mathrm{MPa}^{-1}$). The calibration was performed after the measurements, and a correction is applied on the stress components. In practice, during the uniaxial tensile test used for calibration, the stress component calculated from the force applied on the specimen is compared with the stress component measured by XRD. It is measured by XRD on the specimen surface, beforehand electropolished to eliminate the possible residual stresses due to the rolling of the sheet and the cutting of the specimens. The applied stress component and the one measured by XRD are compared for different values in the elastic range of the material, i.e. for stresses below 350 MPa. The applied stress component is represented in function of the measured stress component in Figure 3.14, as well as the associated linear regression. The slope of the linear regression represents the coefficient to apply on the measured stress component to calibrate all the previous measurements. A multiplication factor egal to 1.07 is thus applied to all the measurements performed on the cups.

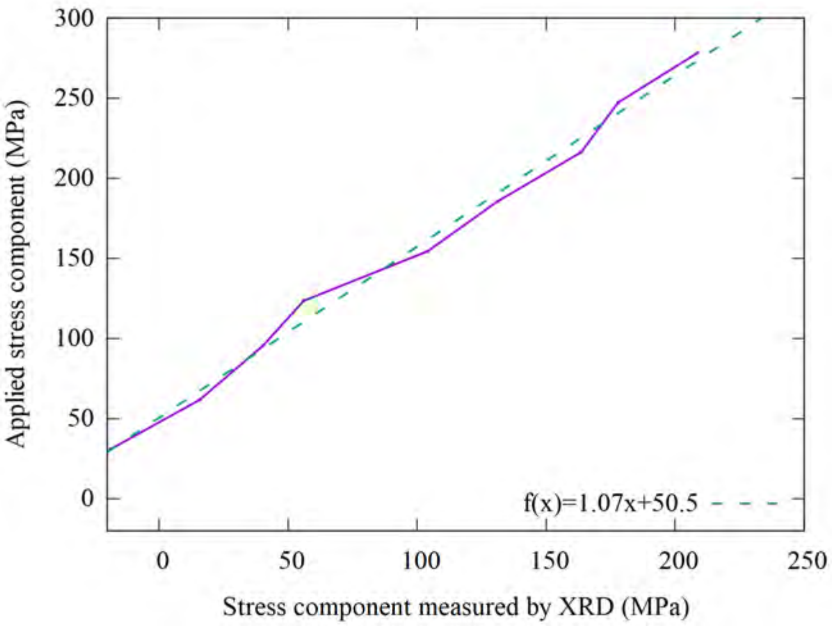

Figure 3.14 – Comparison of the applied and measured stress of the tensile test used for the calibration of XRD measurement

3.2 Results

3.2.1 Punch force-displacement curves

The punch force-displacement curve represents the overall material behavior during the process. A correction, detailed in Appendix C, is applied on the experimental curves presented thereafter. Firstly, the punch force-displacement curves of the full C1 tests are presented for a punch speed equal to 6 mm/s in Figure 3.15(a). A good repeatability of the curves is observed with only few differences on the maximum force between 60 kN and 65 kN for a punch displacement of 12 mm and on the plateau at the end of the tests from 23 mm to 27 mm of punch displacement. These differences came from the friction variation which depends on the quantity of grease on the tools but also on the painting used in the case of tests performed with DIC measurements. Considering the small difference between tests with and without painting, the effect of the painting on the friction coefficient is neglected. Moreover, the comparison of the curves with the three different speeds presented in Figure 3.15(b) shows the progressive attenuation of the sticking point mentioned previously and visible at a punch displacement of 16 mm approximately.

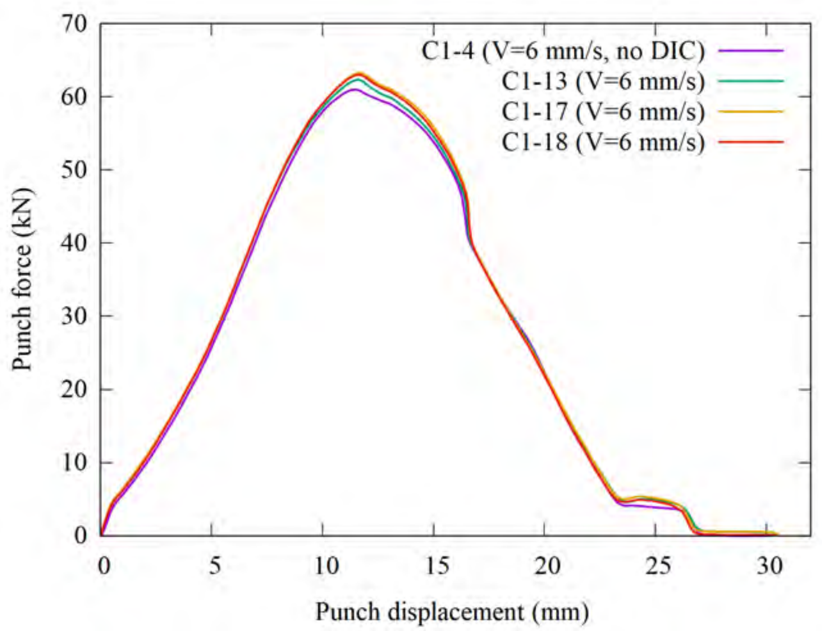

(a) Full tests - V=6 mm/s

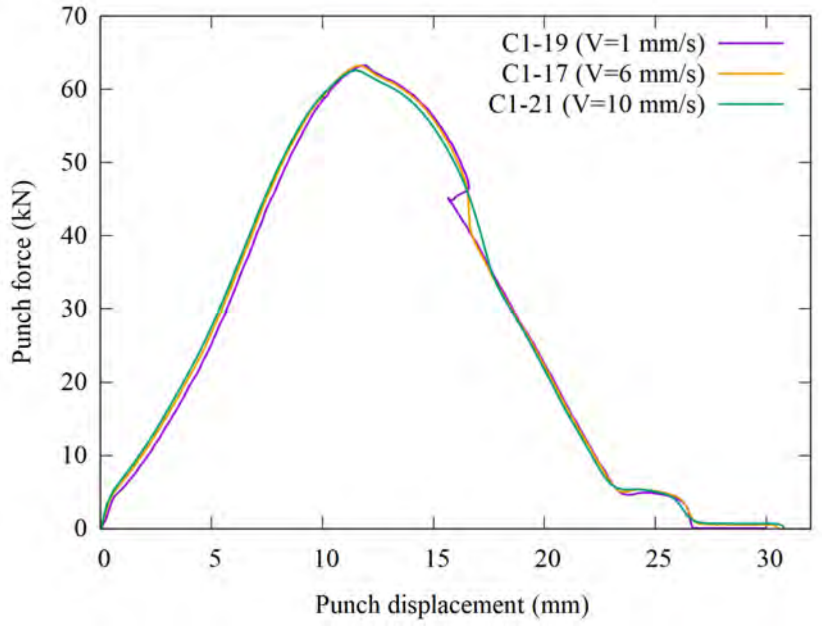

(b) Full tests with different V values

Figure 3.15 – Punch force-displacement curves of the full C1 tests (V is the punch speed)

Then, the punch force-displacement curves of the intermediate tests are also presented in Figure 3.16(a) for a punch speed equal to 6 mm/s and in Figure 3.16(b) for comparison of the three different punch speeds. The tests should stop at a punch displacement value of 10 mm but this value is not exactly reached or slightly exceeded with the respective punch speeds of 1 mm/s and 10 mm/s. A good repeatability of the curves is observed for each speed but a slight difference is visible between the velocities on the force levels.

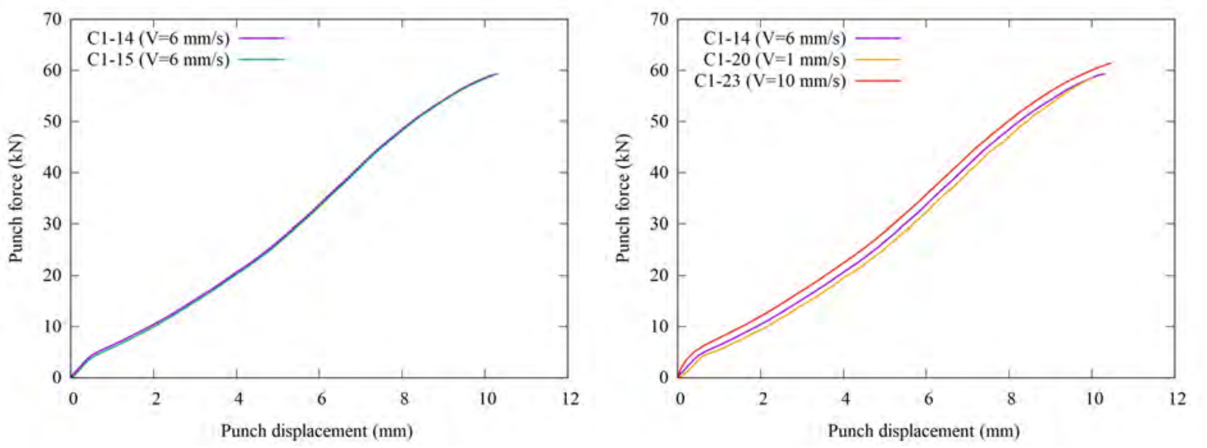

(a) Intermediate tests - V=6 mm/s

(b) Intermediate tests with different V values

Figure 3.16 – Punch force-displacement curves of the intermedite C1 tests (V is the punch speed)

For the redrawing process, the punch force-displacement curves of the full RC1 tests are shown in Figure 3.17. A good repeatability is observed with few differences at the same positions as for the C1 test, i.e. at the maximum force here equal to 80 kN and only at the beginning of the plateau for a displacement value of 26 mm. For the test without DIC measurement, a difference with the other tests is also visible at a punch displacement value of 19 mm which corresponds to the contact rupture with the blank-holder which must be influenced by the presence of painting on the blank.

Then, the punch force-displacement curves of one of each RC2 tests performed, i.e. full tests and tests stopped at different punch displacement values (5, 15 and 25 mm approximately), are compared in Figure 3.18 and are consistent. The repeatability of the RC2 full tests is shown in Figure 4.18, the beginning of the curves is similar for the four tests but some differences appear at a punch displacement value of 10 mm just before the first force peak. A decrease of the force is observed from a punch displacement value of 15 mm corresponding to the loss of contact with the blank-holder, the force decreases until 25 mm where a second force peak starts created by the folding of the cup edges (cf. Figure 3.9). The maximum punch force value of the second stage is reached for this second peak and is equal to approximately 65 kN. A lower

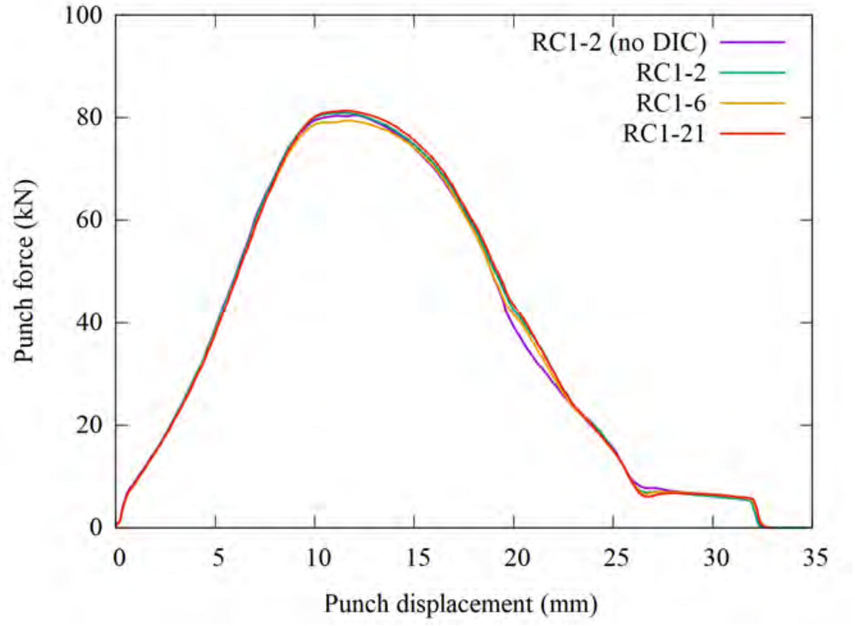

Figure 3.17 – Punch force-displacement curves of the full RC1 tests

maximum punch force is observed for the second stage than in the first stage in accordance with the results obtained for the reverse deep-drawing process of NUMISHEET'99 benchmark [65], [115]–[117]. But for the reverse process, a constant increase, more or less abrupt, of the punch force is observed until a peak and then a decrease [116], [117] and in some case, a first peak is observed due to the pinching of the blank between the die and the blank-holder [65]. In the direct redrawing case of this study, a first peak is observed even if the blank is not stuck between the die and the blank-holder and thus the contact with the blank-holder during the second stage has an impact more important here than in the case of the reverse process. Finally, the repeatability of the intermediate tests are presented in Figure 3.19(b) only for the punch displacement values of 15 and 25 mm because only one test is performed with a punch value of 5 mm. Same observations as for the full tests are visible, similar curves until 10 mm of punch displacement and then a slight difference appears between the curves.

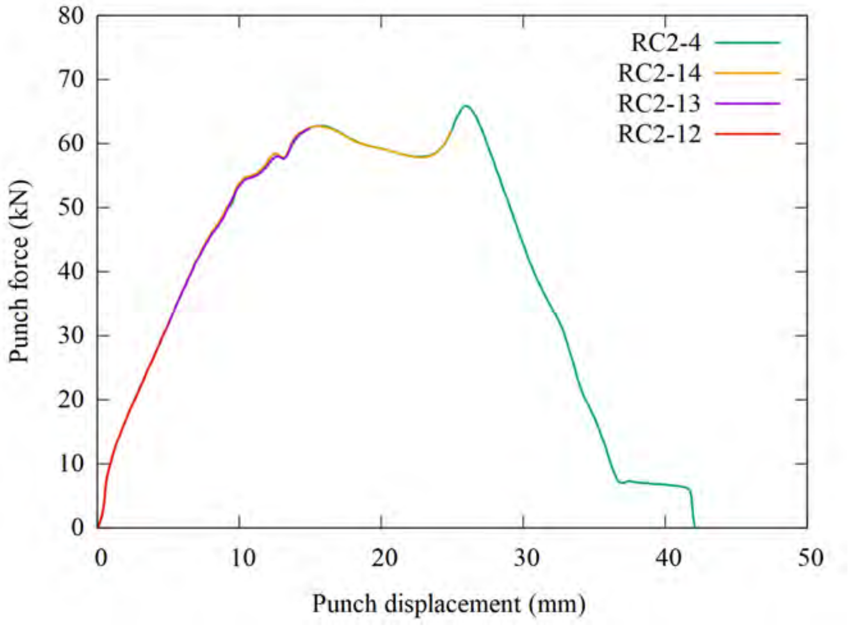

Figure 3.18 – Punch force-displacement curves of one RC2 full test and one test of each punch displacement (5, 15 and 25 mm approximately)

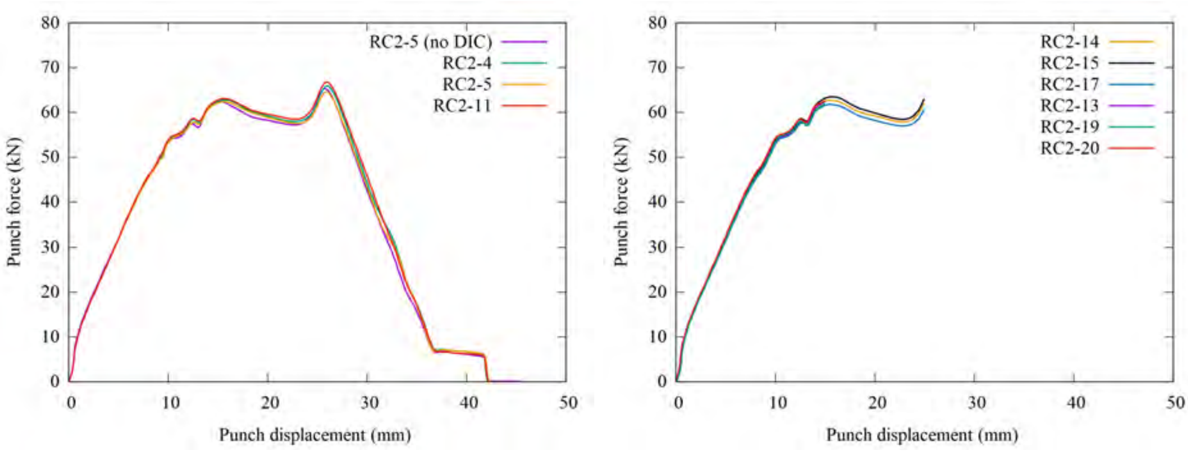

(a) RC2 full tests

(b) RC2 tests with punch displacement values of 15 and 25 mm

Figure 3.19 – Punch force-displacement curves of RC2 tests

3.2.2 Major and minor strain fields

Firstly, the global evolution of the minor and major strains is represented for both processes. It is necessary to specify that major and minor strains measured in this study are strains in the sheet plane and thus it is possible to observe negative values for both major and minor strains. For the C1 test in Figure 3.20, the major strain is positive and evolves between zero at the cup floor and 0.3 in the radius for the intermediate tests and 0.45 in the cup flange for the full test whereas the minor strain is negative between zero at the cup floor and -0.2 in the radius for the intermediate tests and -0.64 in the cup flange for the full test. The quality of the measurement is degraded on the cup flange because the painting is damaged by the process. The same observation is visible on the strain field of the redrawing cups in Figure 3.21 particularly at the end of the second stage. At the end of the first stage, a major strain of 0.3 and a minor strain of -0.5 are obtained on the cup flange similarly to the C1 cup. Then, a progressive increase of the major strain and decrease of the minor strain are visible until 0.57 and -0.81 respectively for the major and minor strain on the cup flange at the end of the second stage.

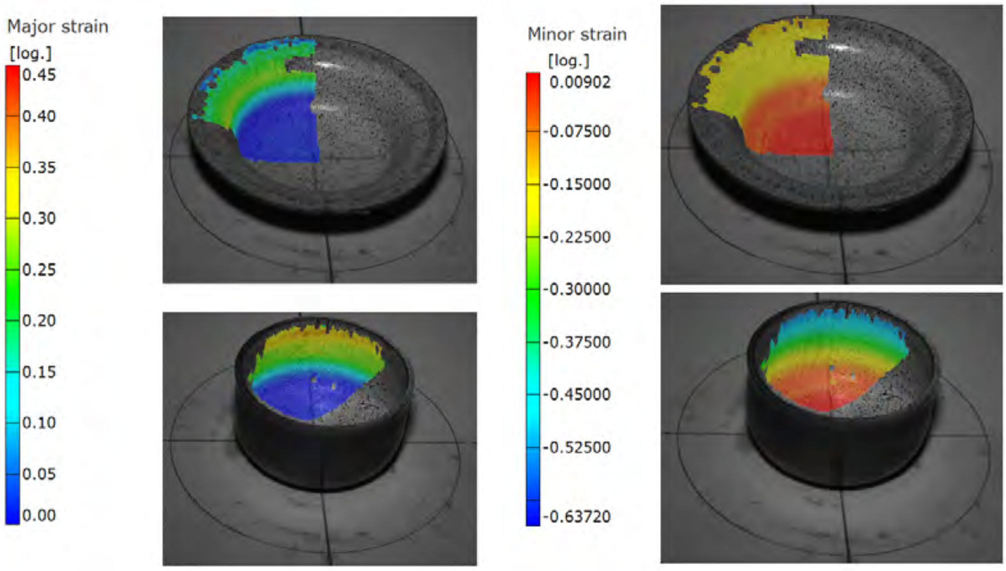

(a) Major strain (b) Minor strain

Figure 3.20 – Major and minor strain fields during the one-stage process (Intermediate test is at the top side and the full test at the bottom)

Major and minor strains evolutions are also output along sections parallel to the rolling and transverse direction. Thus, two measures in each direction are available for each cup but only the best quality measurement is represented. The major and minor strains of the C1 test are

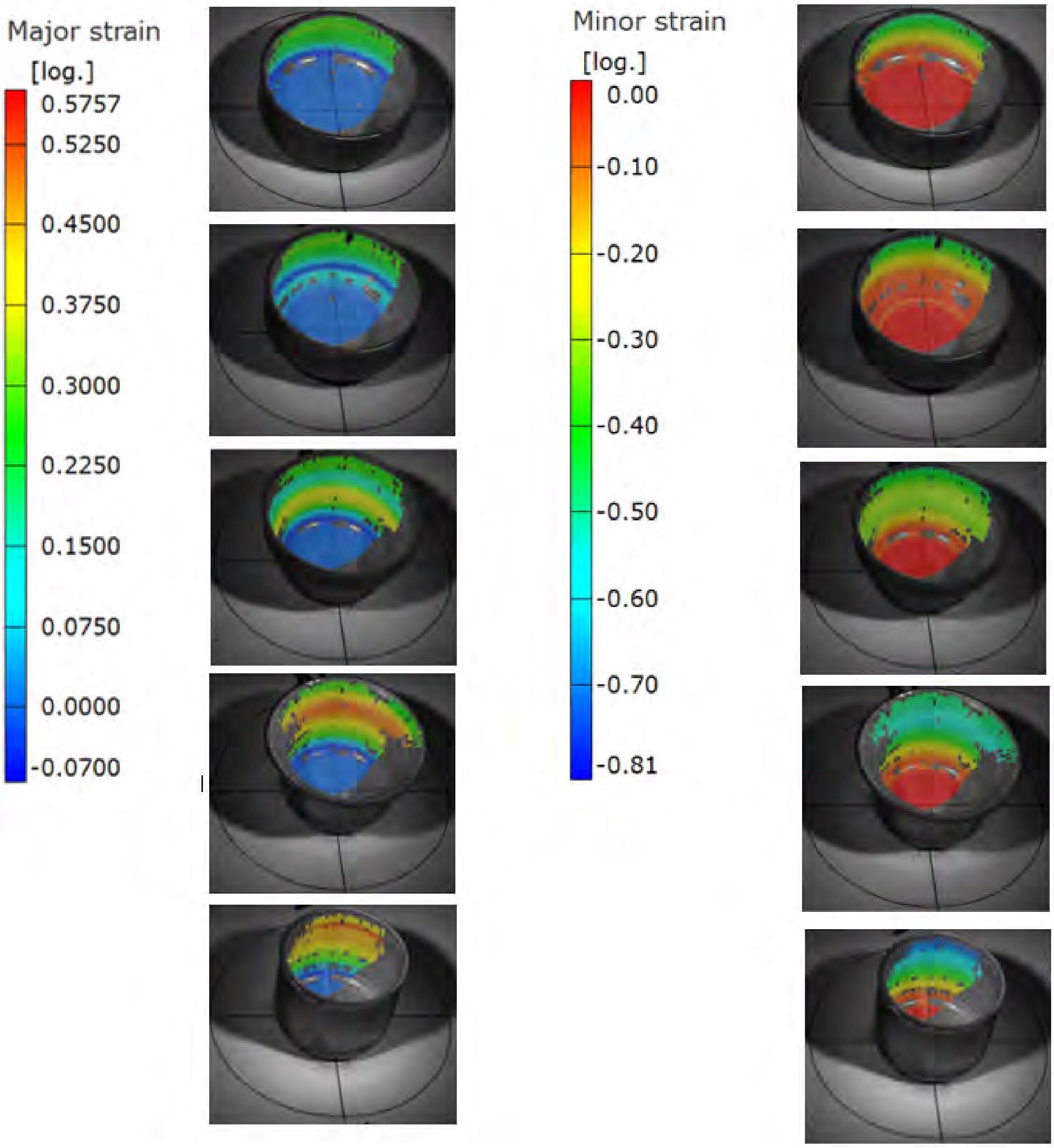

(a) Major strain

(b) Minor strain

Figure 3.21 – Evolution of major and minor strain field during the redrawing process (from top to bottom: end of the stage 1, stage 2 with a punch stroke of respectively 5, 15 and 25 mm, end of the stage 2)

represented for the tests performed with a punch speed equal to 6 mm/s in Figures 3.22 and 3.23, for the intermediate and full tests respectively. Only the strains along the rolling direction are presented for the intermediate tests considering that the results along both directions are really similar for the full tests, as shown in Figure 3.23.

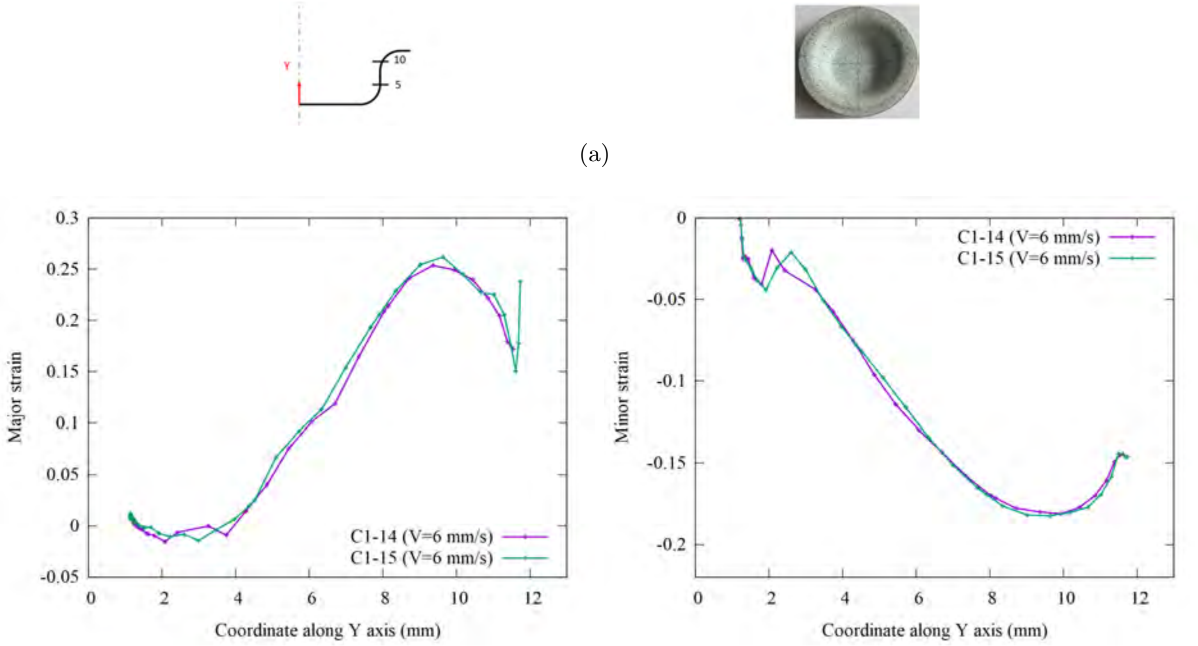

(a)

(b) Major strain (RD)

(c) Minor strain (RD)

Figure 3.22 – Comparison of the strain evolution along the rolling direction for intermediate C1 tests with a punch speed V=6 mm/s

A good repeatability is observed for the measurement performed with the same punch speed but differences appear when the punch speed is modified. Indeed, for the intermediate state, the final punch displacement values are not exactly the same for the different punch speeds, leading to an increase of the strains with the speed value according to Figure 3.24. For the full tests also represented in Figure 3.24, the curves are close to each other despite the different punch speeds used, but the strain profiles are shorter at low speeds because the degradation of the measurement quality on the cup flange is increased and thus the measurement are not possible until the top of the cups.

For the redrawing test, the major and minor strain represented in Figure 3.25 corresponds only to the cup obtained at the end of the first stage and not used for the second stage. Only the strain profiles along the rolling direction are presented because similar results are obtained along the transverse direction. Morver, the results are really close to those obtained for the C1 test, the maximum and the minimum of respectively the major and minor strain are just slightly

(a)

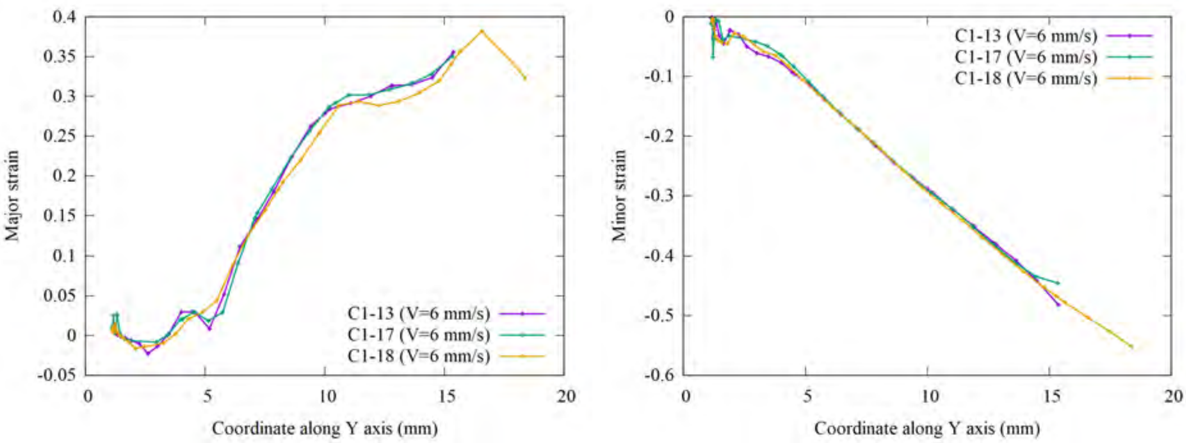

(b) Major strain (RD) (c) Minor strain (RD)

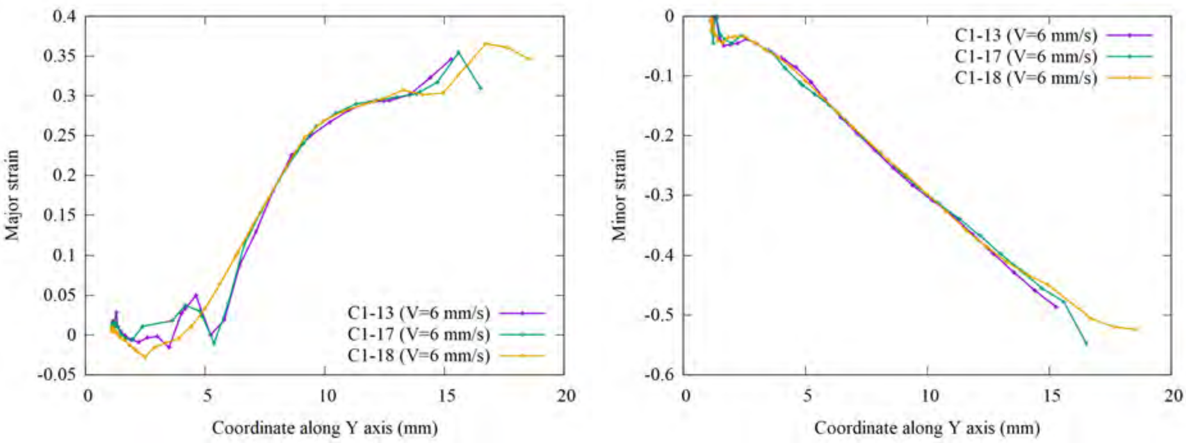

(d) Major strain (TD) (e) Minor strain (TD)

Figure 3.23 – Comparison of the strain evolution along the rolling or the transverse direction for full C1 tests with a punch speed V=6 mm/s

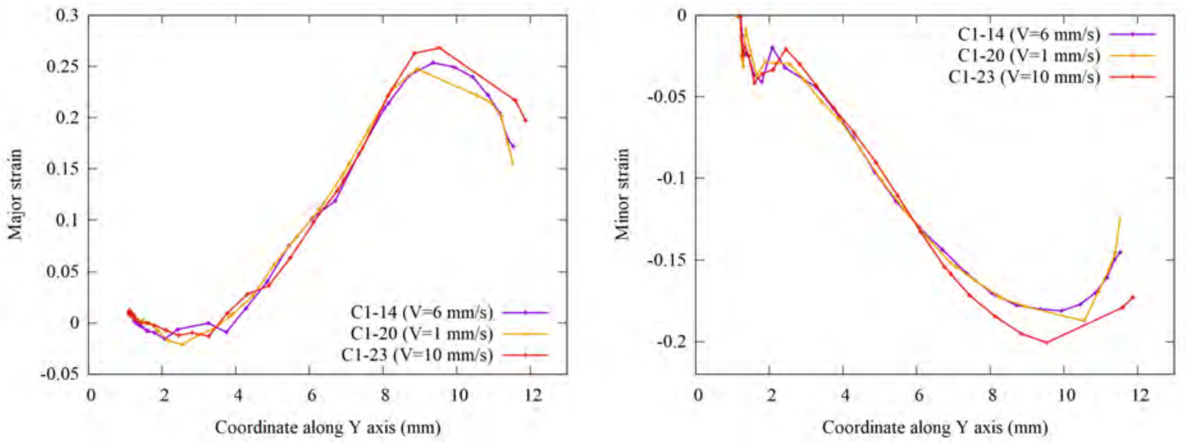

(a) Intermediate tests - Major strain (RD)

(b) Intermediate tests - Minor strain (RD)

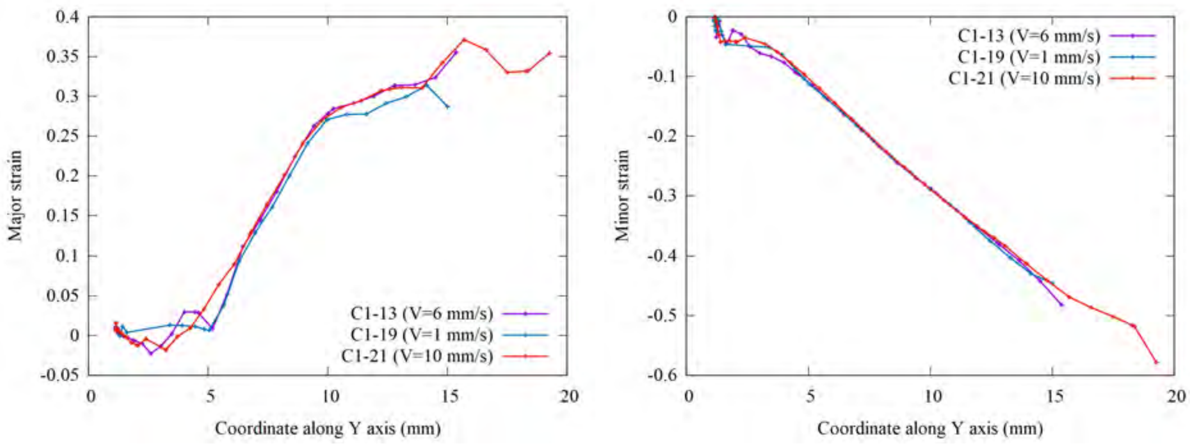

(c) Full tests - Major strain (RD)

(d) Full tests - Minor strain (RD)

Figure 3.24 – Comparison of the strain evolution along the rolling for intermediate and full C1 tests with different punch speeds V

lower.

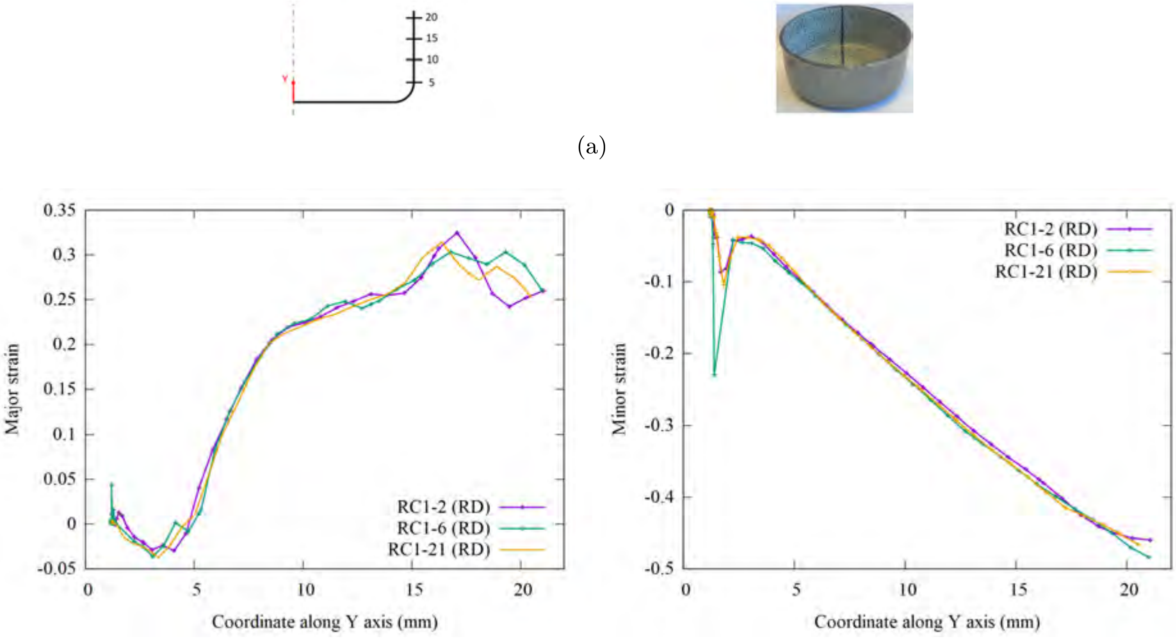

(a)

(b) Major strain (RD)

(c) Minor strain (RD)

Figure 3.25 – Comparison of the strain evolution along the rolling direction for RC1 tests

Then, the strains obtained for the tests with a punch displacement values of 15 mm and 25 mm during the second stage are represented in Figure 3.26. Only the strains along the rolling direction are presented for these two cases considering that the results along both directions are really similar for the full tests, as shown in Figure 3.27. The stop of the drawing at a value of 15 mm or 25 mm is visible on the strain profiles. In case the punch stops at 15 mm, the major strain increases until 0.38 approximately for a coordinate along the vertical axis of 15 mm and then decrease to recover the strain level of the first stage. In the same way, the minor strain decreases until -0.32 approximately for a coordinate along the vertical axis of 15 mm and then increases to recover the strain evolution of the first stage. While when the punch stops at 25 mm, the major strain increases until 0.5 for a coordinate along the vertical axis of 23 mm and then decrease in the cup flange and the minor strain decreases until -0.55 for the same coordinate and then increases in the cup flange.

Finally, the major and minor strain profiles obtained at the end of second stage in Figure 3.27, present smooth evolutions until 0.5 and -0.85 respectively for the major and minor strains. A good repeatability is observed for all the measurements performed during the second stage notably due to the selection of tests with the best quality during the first stage.

(a)

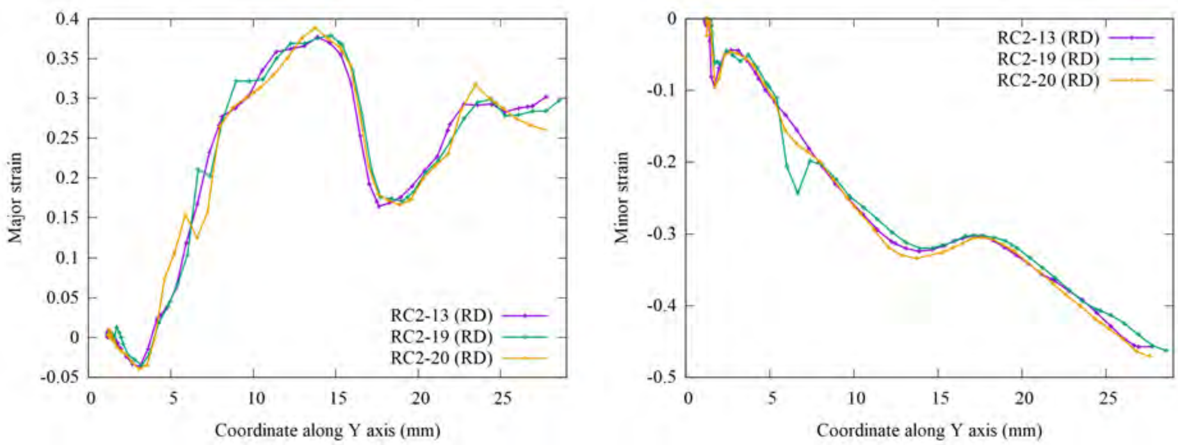

(b) D=15 mm - Major strain (RD)

(c) D=15 mm - Minor strain (RD)

(d)

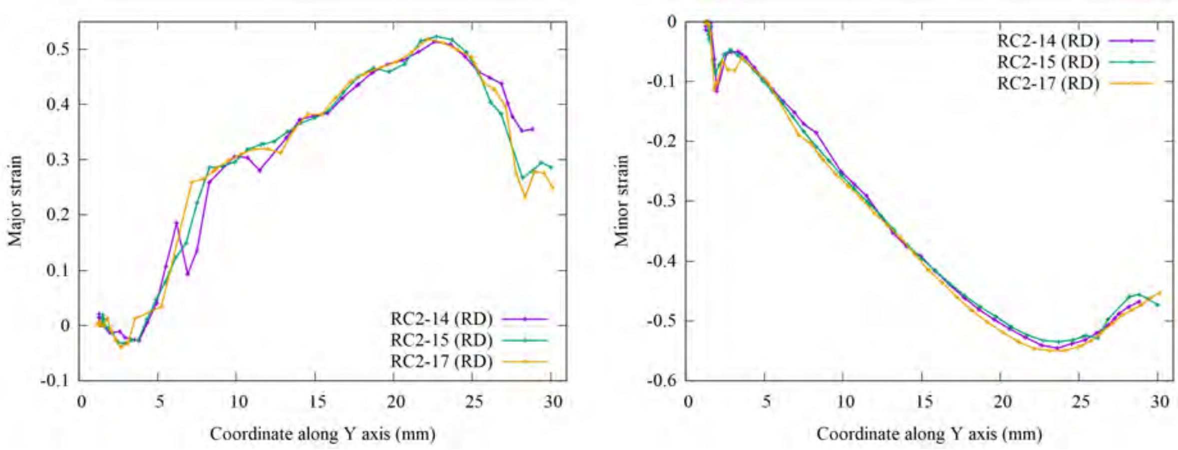

(e) D=25 mm - Major strain (RD)

(f) D=25 mm - Minor strain (RD)

Figure 3.26 – Comparison of the strain evolution along the rolling direction for RC2 tests with punch displacements (D) of 15 mm and 25 mm

(a)

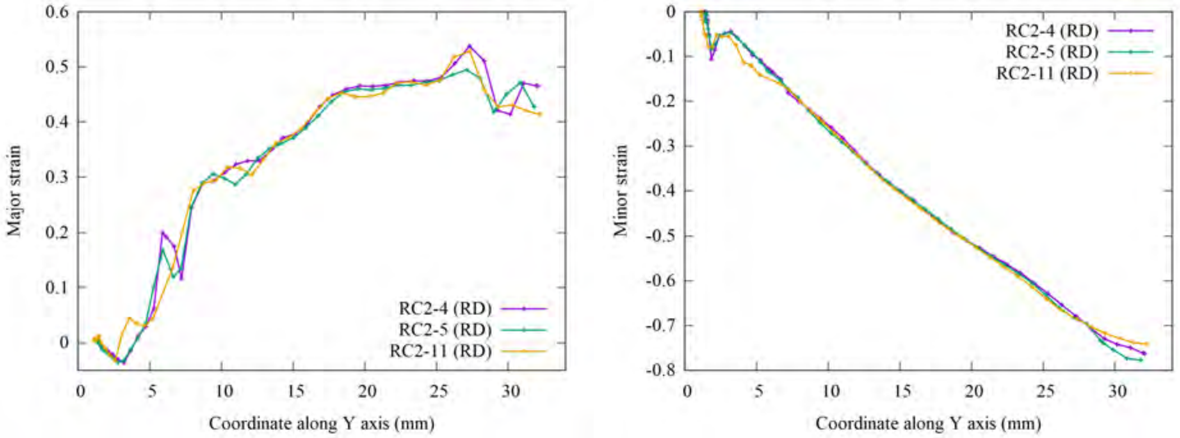

(b) Major strain (RD)

(c) Minor strain (RD)

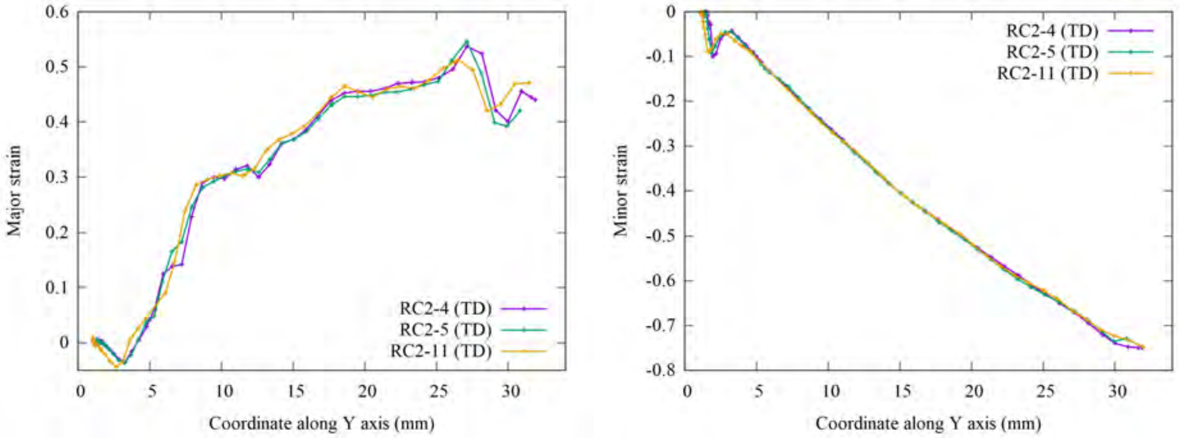

(d) Major strain (TD)

(e) Minor strain (TD)

Figure 3.27 – Comparison of the strain evolution along the rolling or the transverse direction for full RC2 tests

The major strain is also represented as a function of the minor strain for both process in Figure 3.28. One of the major strain and one of the minor strain profiles , previously presented, are selected and combined in order to present all the points of the profile on the graph of major-minor strains for each step of the different processes. For the C1 test, the major-minor strain profile is represented at the intermediate punch displacement and the end of test and for the redrawing test, at the end of each stage and at the three intermediate punch displacements. First, for the C1 cups represented in Figure 3.28(a), the strains of the intermediate test in green color are in compression for the bottom part of the cup and the highest points of the wall are located between shear and uniaxial tension whereas for the full test in red, the points of the cup wall moved between uniaxial compression and shear. Then, for the redrawing cups represented in Figure 3.28(b), the strain distribution at the end of the first stage in orange color is similar to the one of C1. At the beginning of the second stage, some points next to the radius of the cup changes from a state of compression to a state of uniaxial tension. Progressively with the punch displacement, the points of the cup wall situated between uniaxial compression and shear at the end of the first stage approaches or exceeds the line of shear. Finally, at the end of the second stage, all the points of the cup wall are situated around the shear strain state line except for the extremity which is closer to uniaxial compression strain state like at the end of the first stage. At the end of each process, C1, RC1 and RC2, for the points of the top cup wall located between the shear and uniaxial compression lines, the absolute minor strain being larger to the major strain in this part of the graph creates a thickening of the blank as expected from the literature [118].

3.2.3 Residual stresses

The stress components are represented with error bars corresponding to the error committed during the calculation of the ellipse with the 7 measurement points and as a function of the coordinate along Y-axis in Figure 3.29 for C1 and RC1 cups and in Figure 3.29 for RC2 cups. For C1 cups, σ_{11} increases until nearly 500 MPa for a coordinate of 7 mm, then it decreases progressively and reaches negative values for a coordinate of 15 mm and finally it increases to zero at the top of the cup. σ_{22} starts also by increasing until a value close to 400 MPa for a coordinate of 10 mm then decreases until 100 MPa for a coordinate of 10 mm and finally increases again to reach nearly 400 MPa at the top of the cup. A similar evolution is obtained at the end of RC1 tests, with a higher maximum of 600 MPa and a lower minimum of -400 MPa for σ_{11} whereas the stress values are similar for σ_{22}.

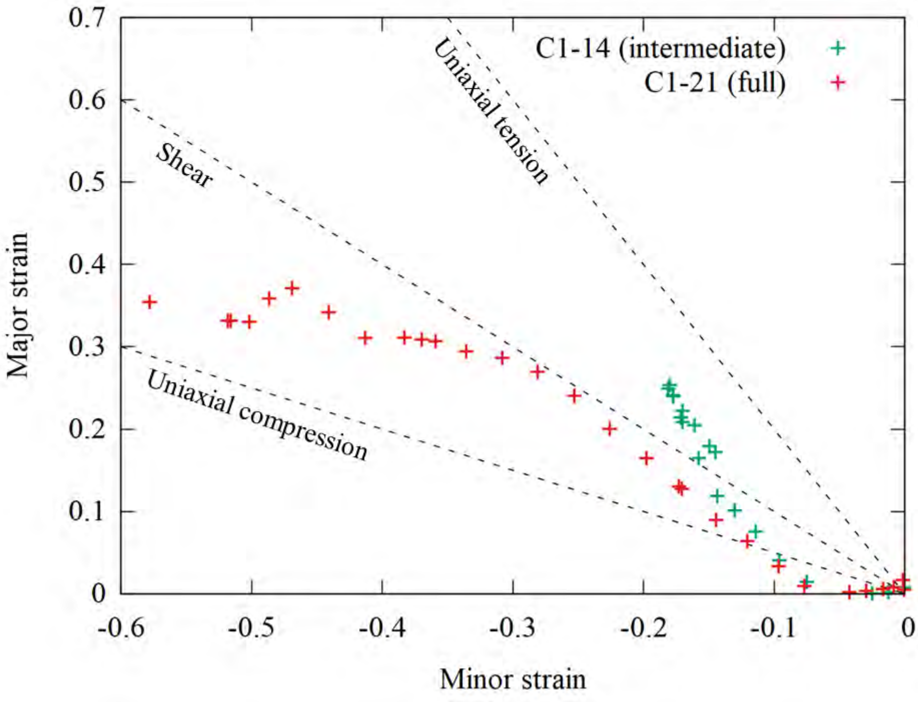

(a) One-stage process

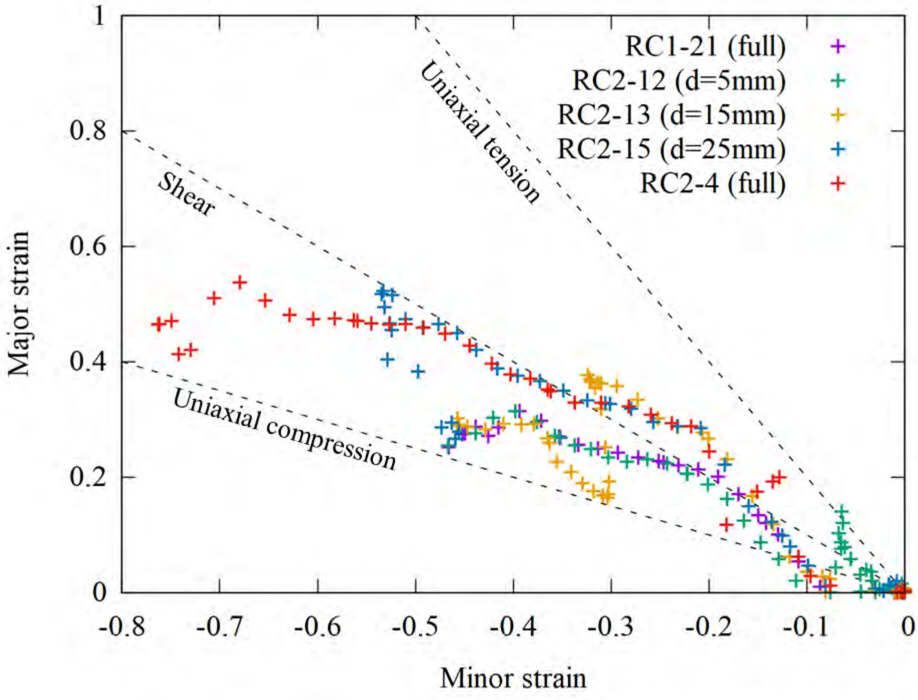

(b) Redrawing process

Figure 3.28 – Representation of the major strain in function of the minor strain for the different processes (d is corresponding to the punch displacement for RC2)

(a)

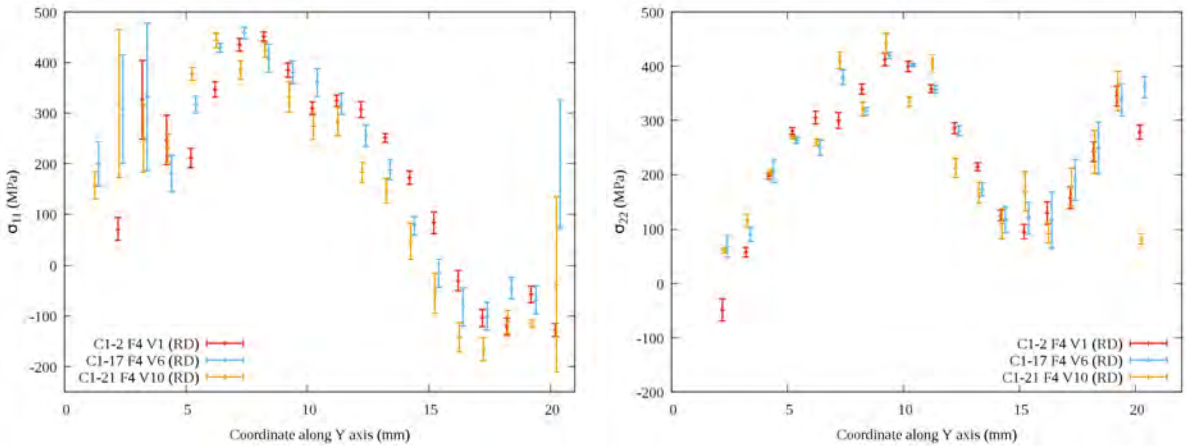

(b) C1 - σ_{11} (c) C1 - σ_{22}

(d)

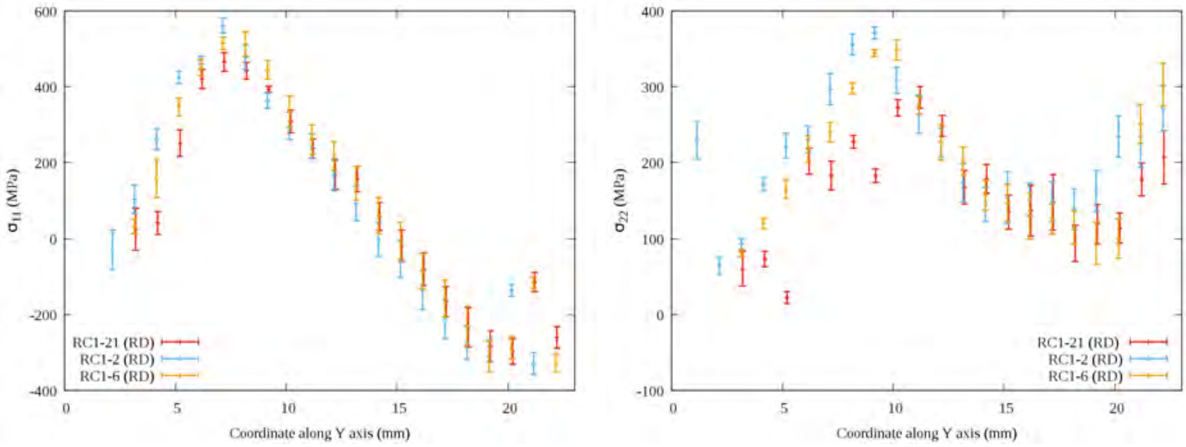

(e) RC1 - σ_{11} (f) RC1 - σ_{22}

Figure 3.29 – Evolution of the measured stress components as a function of the coordinate along Y axis for C1 and RC1 cups

Finally, the evolution of both stress components is different for the RC2 tests. For σ_{11}, the first peak at a coordinate of 7 mm is the same as for the RC1 test but then the stress component decreases only down to zero for a coordinate of 15 mm. Another peak with a stress value of 300 MPa is observed for a coordinate of 25 mm followed by a final decrease until −200 MPa at the top of the cup. In a similar way, the evolution of σ_{22} is the same as the RC1 test until a coordinate of 20 mm and then a decrease to zero is observed until a coordinate of 28 mm where the stress component increases again to reach a value of 300 MPa at the top of the cup.

(a)

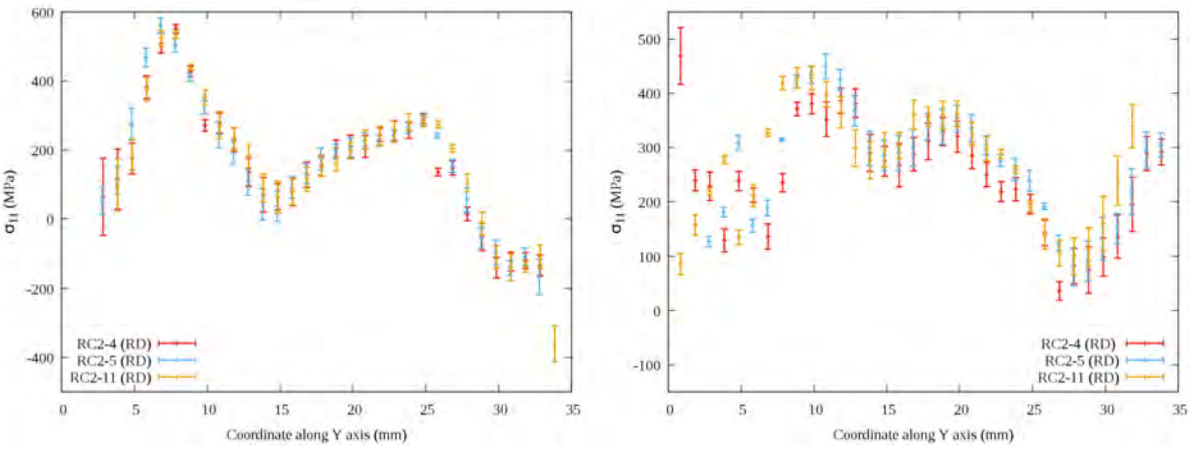

(b) σ_{11} (c) σ_{22}

Figure 3.30 – Evolution of the measured stress components as a function of the coordinate along Y axis for RC2 cups

For both processes, the stress components are measured on three different cups along the rolling direction in order to check the repeatability of the results. The repeatability of the stress levels is correct, though the estimation of the coordinate along Y-axis is calibrated manually at the beginning of the measurement. Indeed, the collimator is just placed at the top edge of the cup but a variation of approximately its diameter (1 mm) is possible. This error on the coordinates creates a slight dispersion of the results. The anisotropy is also investigated for the final cups of each process, the stresses are also measured along the transverse direction and the comparison is represented in Figure 3.31.. Anisotropy is not observed for the residual stresses of the cups 1 whereas more difference is noticed between the transverse and rolling direction for the redrawing cups. However, the difference is observed close to the radius of the cup where the error committed during the ellipse calculation is higher than in the wall.

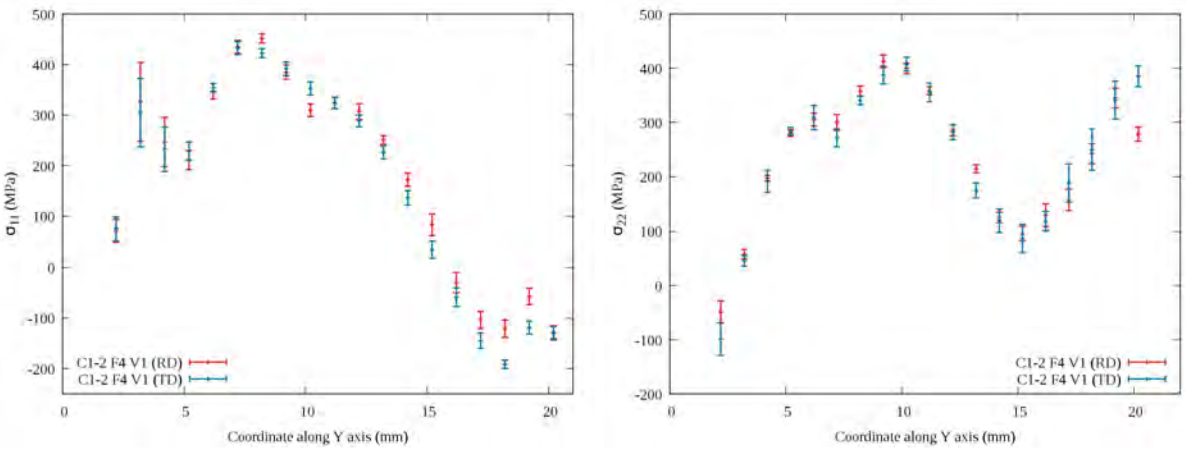

(a) C1 - σ_{11} (b) C1 - σ_{22}

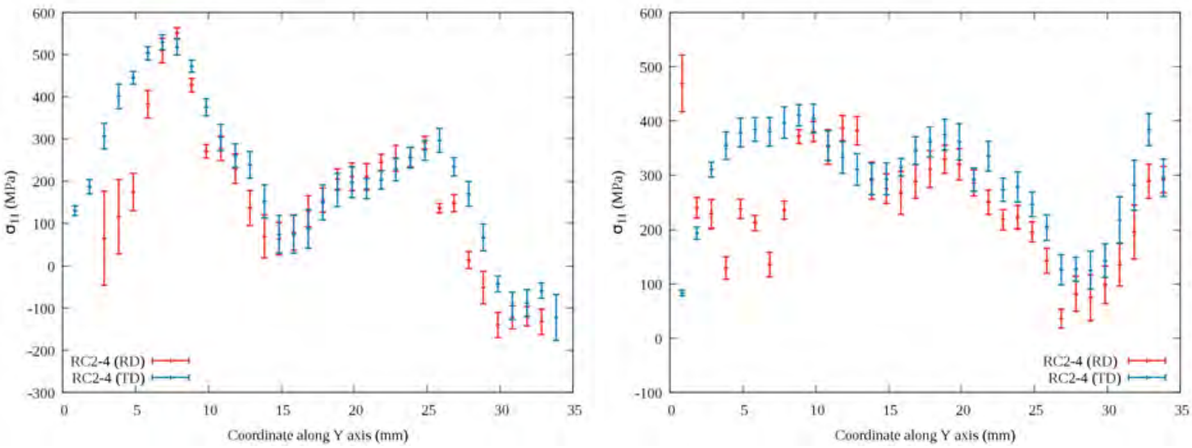

(c) RC2 - σ_{11} (d) RC2 - σ_{22}

Figure 3.31 – Comparison of the measured stress components along the rolling and the transverse directions as a function of the coordinate along Y axis for C1 and RC2 cups

3.3 Conclusion

The deep-drawing processes in one or two stages of cylindrical cups are presented in this chapter. First, the experimental procedure is detailed with the methodologies used for the strain measurement by DIC and the residual stress measurement by XRD. Then, the punch-force displacement curves are considered as a representation of the overall structural behavior. Strain and stress measurements are also used to obtain local indications of the material behavior. For all of these results, a good repeatability is obtained and a weak anisotropy is observed. Both processes exhibit large strains but the strain level is almost doubled by the addition of a deep-drawing stage in the redrawing process. The residual stresses values are not increased by a second deep-drawing stage, smaller variations of the values of both σ_{11} and σ_{22} are observed in the cup wall for RC2 in comparison with C1 and RC1. Nevertheless, the second stage of deep-drawing significantly changes the distribution of the residual stresses in particular for σ_{11}. The aim is then to model both processes by finite element analysis with the e-HAH model in order to evaluate the strain path changes occurring during both processes and their influence on the quantities presented in this chapter.

CHAPTER 4

VIRTUAL FORMING OF CYLINDRICAL CUPS

Numerical simulation is nowadays largely used to design forming processes because the cost and time dedicated to the development are considerably reduced in comparison with iterative experimental methods. The accuracy of the predictions obtained with finite element analysis depends on different numerical parameters including the element formulation and size, the methods used to model contact and friction and the constitutive law used to model the material behavior. In this chapter, the influence of the material model is investigated for the two deep drawing processes presented in Chapter 3. The predictions obtained with 3 different models are compared in order to investigate the effects of strain path changes : an isotropic hardening law and the original and enhanced versions of HAH model (o-HAH and e-HAH). The isotropic hardening is an hybrid combination of Swift and Voce (HSV) equations, presented in Eq. 2.9, and used with the parameters of Table 2.4. The identification 2 of e-HAH parameters, c.f. Table 2.6, is used, while the original version of the model is obtained by setting the parameters S and k_S to the respective default values 1 and 0. In all cases, the hardening model is associated to the von Mises criterion according to the isotropic behavior in stress of the material. Moreover, the punch force-displacement curves of each process are used to calibrate the simulations via the friction coefficients. The influence of strain path changes is investigated in particular for the evolution of strains and residual stresses along the rolling direction. The occurrence of strain path changes is highlighted by the strain path change indicator $\cos \chi$ of HAH model. The different kinds of strain path changes are distinguished by the values of the indicator, with three particular ones, 1 for the absence of strain path changes and -1 and 0 for reverse and orthogonal strain path changes respectively. The aim of this study is thus to evaluate the occurence and the influence of each category of strain path changes during the deep-drawing processes by comparing the three models, the basic one not taking into account strain path changes, o-HAH model considering only the influence of the reverse strain path changes, and e-HAH model considering also the influence of orthogonal ones.

In this chapter, deep-drawing cases already simulated with strain path change models are firstly presented. Then, the numerical procedure used to perform finite element analysis with

Abaqus is detailed and the results obtained for both processes and the different models are analyzed. The punch forces-displacement curves are presented and illustrated with isovalues of the equivalent plastic strain. Then, the major and minor strains and the residual stresses are compared with the measurements and are analyzed by means of the strain path indicator $\cos\chi$ evolution. Finally, the finite element analysis is also performed with the industrial code PAM-STAMP developed by ESI Group for the redrawing process to validate the implementation of e-HAH model in this code by comparison with the experimental results and the finite element analysis performed with Abaqus.

4.1 Strain path change influence in virtual forming

Firstly, the different deep-drawing simulations already performed in the literature with o-HAH or e-HAH model are presented. Considering o-HAH model, springback predictions has been largely studied mainly via two benchmarks, the 2D draw bending test (Numisheet'93) [20], [71] and the U-draw bending test (Numisheet 2011) [75], [95], cf. Figure 3.1(a). The springback predictions of o-HAH model are compared with isotropic hardening (IH) and kinematic hardening (KH) in theses studies for different DP, TRIP or TWIP steels. The comparison of the springback predictions is presented in Figure 4.1 for a DP590 and a TRIP590 (o-HAH parameters identified for this DP590 are available in Table 2.6). A small influence of the material model is observed around the angles corresponding respectively to the die and punch radius whereas the sidewall curl is significantly influenced by the model. For DP590 case, both KH and o-HAH are in good agreement with the experiments contrary to isotropic hardening due to the modeling of reverse strain path change features. Small differences are obtained between KH and o-HAH in this case but for TRIP590 a difference is observed between the two models due to an abrupt transient hardening behavior exhibited after reversal during forward-reverse shear tests, well reproduced by o-HAH model but not by kinematic hardening.

Overall, theses studies have shown the ability to predict springback of o-HAH model for different kind of steels [20], [71], [75], [95]. More complex cases have also been investigated with o-HAH model as the double stage U-draw bending test [71] and the curve-flanging test [72]. For the double stage case, o-HAH predicts correctly springback for both stages contrary to the isotropic hardening, exhibiting an increased error due to the addition of the second stage. For the curve flanging test, a more complex geometry is considered with a curved version of the U-channel. In that case, o-HAH model is coupled with a modeling of the elastic modulus degradation and gives also good springback predictions. Overall, theses studies have shown the ability to predict springback, hence the influence of reverse strain path changes, of o-HAH model for different kind of steels [20], [71], [72], [75], [95].

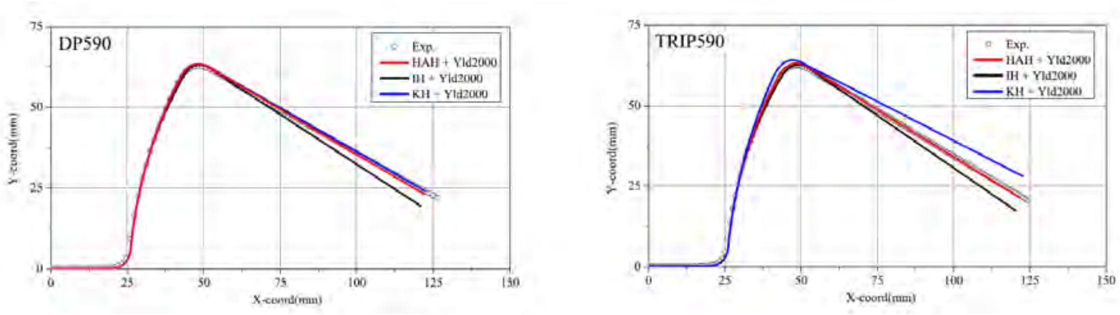

(a) DP590

(b) TRIP590

Figure 4.1 – Comparison of the springback predictions of the 2D draw bending test obtained with HAH model and isotropic and kinematic hardening (IH and KH) for a DP590 and a TRIP590 [20]

There have been fewer applications of e-HAH model to forming and springback simulations, the main study available with this version of the model is considering P and C channel forming processes of a DP500 [13], with the example of P-channel presented in Figure 1.2. Twist springback occurs with theses geometries and appears to be significantly influenced by the loading history, evaluated with the indicator of e-HAH model, $\cos\chi$. The twist springback predictions obtained with three models, isotropic hardening (IH), mixed hardening (IHKH) and e-HAH model is compared and the better results are obtained with e-HAH model. These geometries exhibit non-linear strain path changes including quasi-orthogonal ones and thus a different stress distribution, linked to the amplitude of twist springback, is obtained with e-HAH model. Recent complementary studies have investigated the effect of a tensile pre-strain before the P-channel forming process, again for DP500 [119], [120]. When the pre-strain axis is aligned with the guide axis of the P-channel, cross-loading occurs and leads to the more severe case of twist springback. e-HAH model gives predictions in agreement with the experiments in that case but they are even better when the degradation of the elastic modulus is also taken into account. The study of twist springback shows that e-HAH model is suitable to simulate forming processes involving a wide range of non-linear strain path changes.

Few other applications of e-HAH model are available in the literature and particularly none about the deep drawing of cylindrical cups in one or two stages but a study of the reverse redrawing process from Numisheet'99 benchmark has compared another strain path change model developed by Teodosiu and Hu [62], already mentioned in section 2.1.1., with isotropic and mixed hardenings for a mild steel [65]. Evolutions of the Schmitt indicator θ have shown the occurrence of quasi-orthogonal strain path changes during both stages but more pronounced in the second stage. Teodosiu and Hu model captures the transient behaviors due to strain path changes and thus leads to a decrease of the punch force-displacement curves of the second stage which is thus in better agreement with the experiments than the curves predicted by IH or IHKH. A more recent study about the same process has also highlighted the importance of the formulation of the contact model used between the blank and the forming tools [117]. Indeed, the use of a smooth description of the tools surface [117] appears to improve the results compared to the discretized approach used in the previous study [65]. Nevertheless, the occurrence of strain path changes during the deep-drawing in two stages of cylindrical cups appears to influence the material behavior and is analyzed for the redrawing case in this study by means of finite element analysis with e-HAH model.

4.2 Numerical procedure with Abaqus

Finite element analysis of the deep-drawing processes are firstly performed with Abaqus Explicit. It it possible to simulate the process with the standard version of Abaqus for the isotropic hardening law whereas a user subroutine VUMAT [90], provided by M.G. Lee in Seoul National University, is used for HAH model. With both models, the simulations are performed with double precision.

4.2.1 Suitable model for subsequent fatigue analysis

In order to be able to apply the fatigue loading on the cup after forming, cf. section 5.2, only one symmetry can be considered and thus half of the cup is simulated. The coordinate system of the finite element analysis is defined as X and Z axis corresponding initially to the rolling and the transverse direction of the blank and the Y axis is the deep-drawing direction, normal to the blank surface. The tools are modeled as analytical rigid parts, surface to surface contacts are defined between the blank and all the tools with the Coulomb law to model friction. The friction coefficient values are adjusted with the punch force-displacement curves depending on the process. The degrees of freedom of the tools are all fixed except for the displacement of the punches in the drawing direction and for the displacement of C1 and RC1 blank-holders also in the drawing direction in order to apply the forces on the blank. In the case of C1 and RC1, a first step for clamping is simulated and then the forming of the cups is divided in 2 steps, with and without contact between the blank and the blank-holder. For RC2 simulation, it is not necessary to separate the forming step since the blank-holder is fixed but a step is set before forming to initiate contact between the tools and the cup obtained from RC1 simulation. The values of punch displacement are equal to 30 mm, 32.5 mm and 42.1 mm for R1, RC1 and RC2 respectively and the values applied in the different steps are detailed in Table 4.2.1. The blank-holder forces of 4 kN and 5 kN are respectively used for C1 and RC1 simulations according to the experimental values.

The blank is meshed with reduced integration shell elements S4R and 9 section points through

Table 4.1 – Punch displacement values applied in the different steps of the simulations, F_{BH} stands for the blank-holder force

Steps	Clamping	Forming with F_{BH}		Forming without F_{BH}		Contact initiations	Forming
Process	C1 and RC1	C1	RC1	C1	RC1	RC2	
Values (mm)	0	16	17	14	15.5	0.1	42

thickness. Three partitions of the blank geometry are used for the mesh, represented for both processes in Figure 4.2. One element per degree is set on the circular part and a line of element of size 1 mm at the blank end. In the middle, the mesh size is homogeneous and equal to 0.4 mm. The partition in the center of radius 10 mm has a mesh size of 0.4 mm on the extremities and converges to a mesh size of 1 mm in the center.

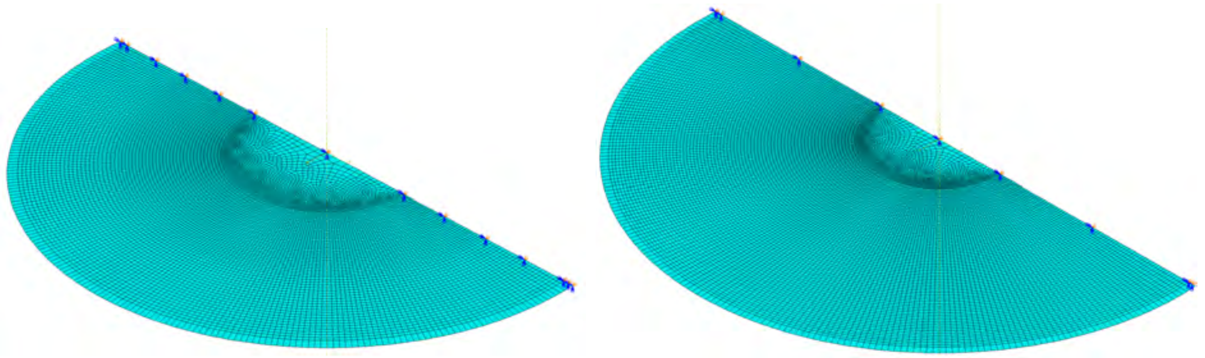
(a) One-stage process (ϕ_{blank}=60 mm)

(b) Redrawing process (ϕ_{blank}=80 mm)

Figure 4.2 – Representation of the blank mesh used for the two deep-drawing simulations

The influence of different mesh sizes has been investigated for the one-stage process and the simulation with the isotropic hardening law. The punch force-displacement curves obtained with the four different mesh sizes, i.e. 0.8, 0.6, 0.4 and 0.2 mm, are compared in Figure 4.3(a). With the mesh size of 0.8 mm, the maximum force level is slightly lower than for the other mesh sizes. But for lower mesh sizes, numerical noise appears at the end of the curve and it is reduced by decreasing the mesh size. The mesh size of 0.2 mm gives the smoothest curve but the computation time is high in that case, thus the mesh sizes of 0.6 mm and 0.4 mm are a good compromise between the result accuracy and the computation time. These two mesh sizes are tried for the redrawing process and especially the second stage which is more subject to numerical noise. The punch-force displacement curves for the two mesh sizes during the second stage are represented in Figure 4.3(b). Numerical noise is observed with the mesh size of 0.6 mm whereas it is significantly reduced with 0.4 mm. Finally, the mesh size of 0.4 mm is chosen for both processes.

4.2.2 Reduced model and modifications of the second stage for the redrawing process

The simulation of the half cup with the subroutine VUMAT is time consuming, especially in the redrawing case. To obtain faster results for the redrawing simulation, a model with only 5° of the cup is also considered since the anisotropy of the material is neglected. The computing station is a Linux PC with 24 cores, Intel(R) Xeon(R) Gold 6128 CPU 340 GHz, and 64GB RAM. The CPU time obtained without parallelization are summarized in Table 4.2.2. For e-HAH mode, the reduction of the element number reduces the CPU time from 10 days down to 14 hours. Three partitions of the blank geometry are used for the mesh and represented in Figure 4.4. In the same way as for the half cup, a line of elements of size 1 mm is set at the circular end of the blank. A middle zone is composed of elements of size 0.4 mm and there is a partition of radius 10 mm with an increase of the element size from 0.4 mm to 1 mm in the center. A symmetry in the global coordinate system is defined on one side which is along the X-axis similarly to the one applied in the half cup simulation. Another symmetry is applied on the other side and is defined in a local coordinate system for the model to be equivalent to the whole cup.

Table 4.2 – Comparison of the CPU time to run the redrawing simulation for half or 5° of the cup

Material model	HSV		e-HAH	
Cup model	Half	5°	Half	5°
CPU Time (h)	24	1,5	240	14

To check the equivalence between the half cup and the reduced simulations, the punch force-displacement curves are compared for each of the redrawing stages in Figure 4.5. The comparison is made in the cases of the isotropic hardening law. Firstly, for RC1, the punch force-displacement curves are similar in both cases. Likewise, the curves of the half cup simulation and the reduced one are consistent for RC2 though more differences than for RC1 are observed. However, the difference of the number of output time instants between the simulations, which are twice as many in the reduced case, could explain it. Thus, the results presented in the following section are those obtained with the reduced model of the redrawing process.

Moreover, during the redrawing experiments, springback of the cup occurs at the end of both stages. However, it is preferred to switch from explicit (E) to implicit (I) framework for the springback simulation due to inherent numerical instabilities. The change of framework

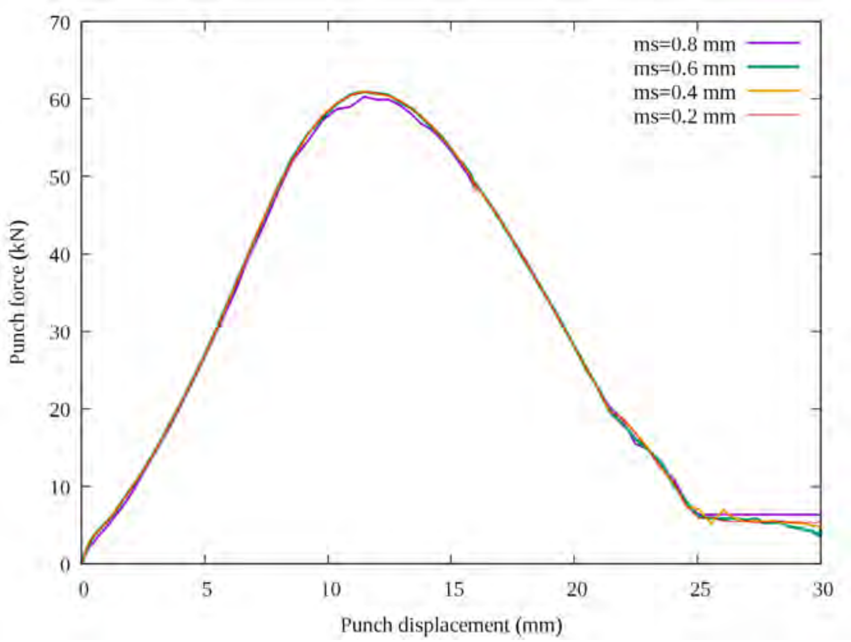

(a) C1

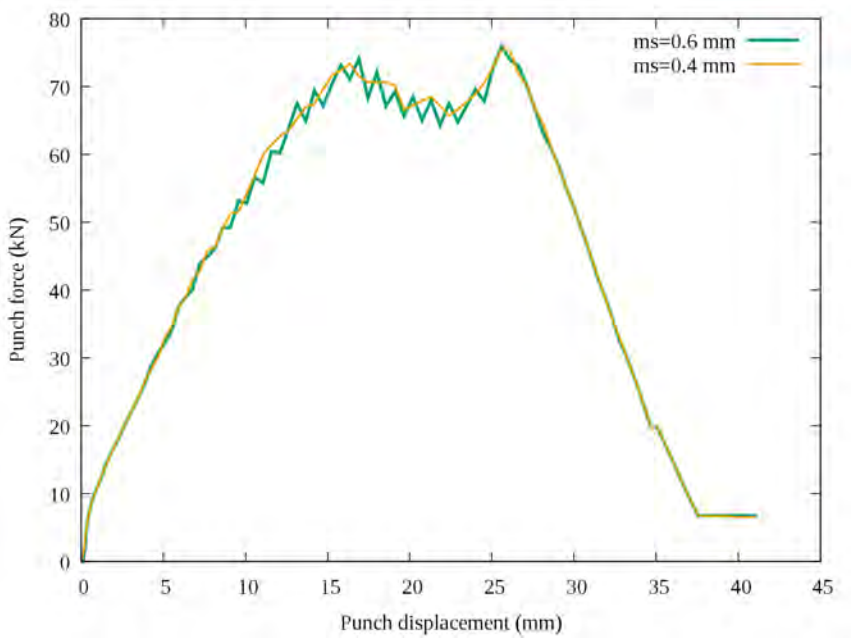

(b) RC2

Figure 4.3 – Comparison of the numerical punch force-displacement curves of C1 and RC2 for different mesh sizes (ms)

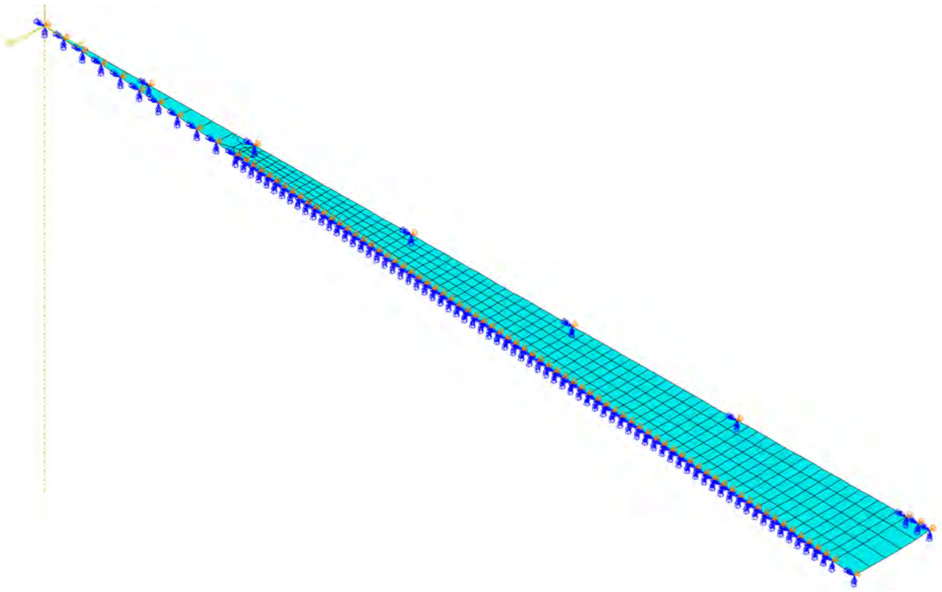

Figure 4.4 – Representation of the blank mesh used for the reduced model of the redrawing

(E/I) is difficult to manage in particular with a user subroutine. Considering the low amount of springback observed experimentally, the simulation of the springback between the two stages of forming is neglected. Considering the final springback, a first model based on the exact geometry of the tools from the experiments is developed, which leads to a springback of the cup when the contact with the die of the first stage is removed. The standard version of Abaqus Explicit is able to deal with this induced springback but, with the subroutine VUMAT, an error occurred as soon as the contact with the die of the first stage is removed. So, modifications of the geometries of the tools are performed to avoid the error obtained with e-HAH model but with the aim to stay as close as possible to the standard simulation. The dies of the two stages are connected to form only one tool and thus avoid the loss of contact. The internal diameter of the first die is kept equal to 51.2 mm and the diameter is progressively increased along the connection between the two dies until 52 mm. Furthermore, a high contact pressure is applied on the blank by the blank-holder of the second stage because the internal cup diameter is smaller without springback at the end of the first stage. So, the external diameter of the blank-holder of the second stage, which is exactly equal to the punch diameter of the first stage, is in that case reduced by 0.02 mm. The adapted dimensions of the tools are summarized in Figure 4.6. The equivalence between half cup and reduced model is also verified in Figure 4.5(b) and the same conclusions as for the initial case can be made. The comparison between initial and modified punch-force displacement curves is analyzed in the following results section.

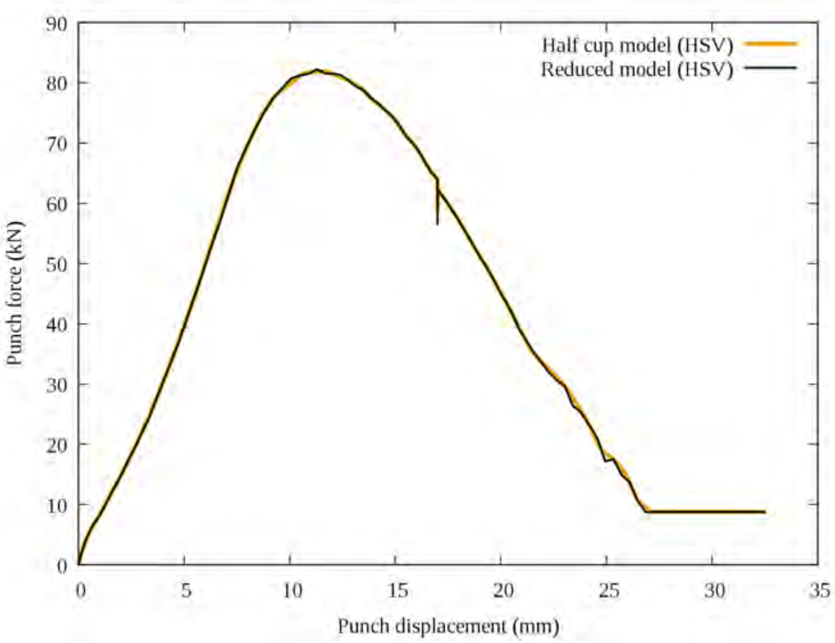

(a) RC1

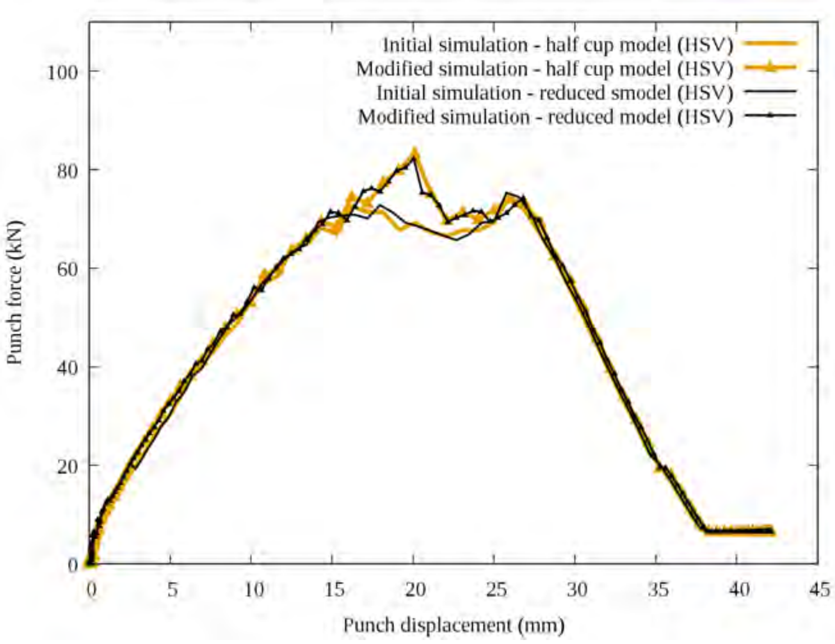

(b) RC2

Figure 4.5 – Comparison of the numerical punch force-displacement curves of RC1 and RC2 for half cup and reduced model

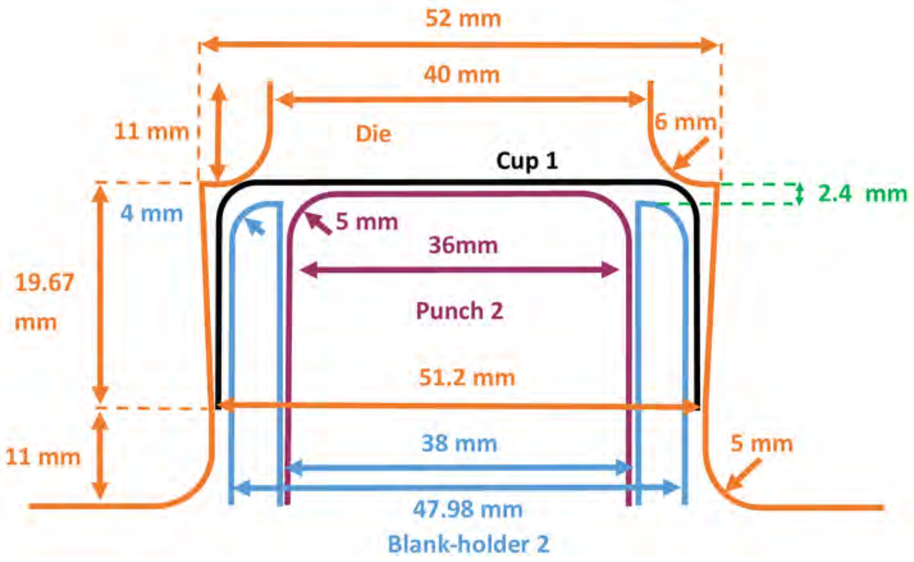

Figure 4.6 – Modification of the dimensions of RC2 to simulate this stage with e-HAH model

4.2.3 Springback simulations

To simulate the final springback of the cups, Abaqus Implicit is preferred to Abaqus Explicit as mentioned previously. The springback is simulated at the end of each entire process, i.e. C1, RC2 and RC1 when it is considered as a separate process, to extract the strain and stress fields to compare with the measurements. The final state of each forming simulation is used as an initial one for the springback simulation. Furthermore, e-HAH model with a fully implicit algorithm is not available and the springback simulation is in that case performed only with an elastic constitutive law. In order to validate this simplification, in the case of forming simulations with the isotropic hardening law, elasto-plastic and elastic simulations of springback are compared. The major and minor strains and the residual stresses of both springback cases are compared in Figures 4.7 and 4.8 for the redrawing process, RC1 and RC2, but they are analyzed in details in the following result section. For major and minor strains, the curves are similar, thus the use of only an elastic law to simulate springback has no influence on the strain evolutions. For residual stresses, the curves are exactly the same for RC1 whereas for RC2, some differences are observed between coordinates of 15 mm and 25 mm for both σ_{11} and σ_{22}. Considering these small differences, and in comparison with the influence of the modified simulation, it is assumed that the elastic law is sufficient to simulate springback and can be used with confidence for the forming simulations performed with both versions of the HAH model.

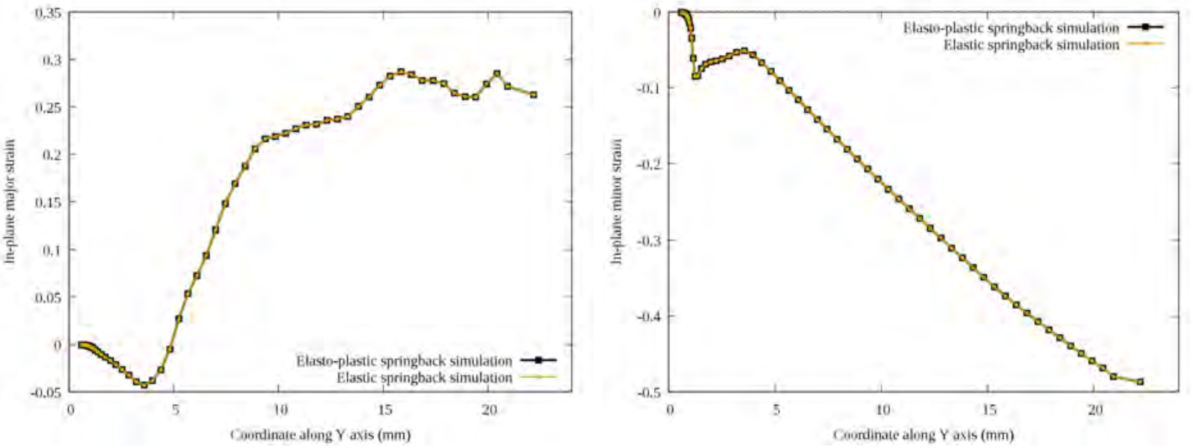

(a) RC1 - Major strain (b) RC1 - Minor strain

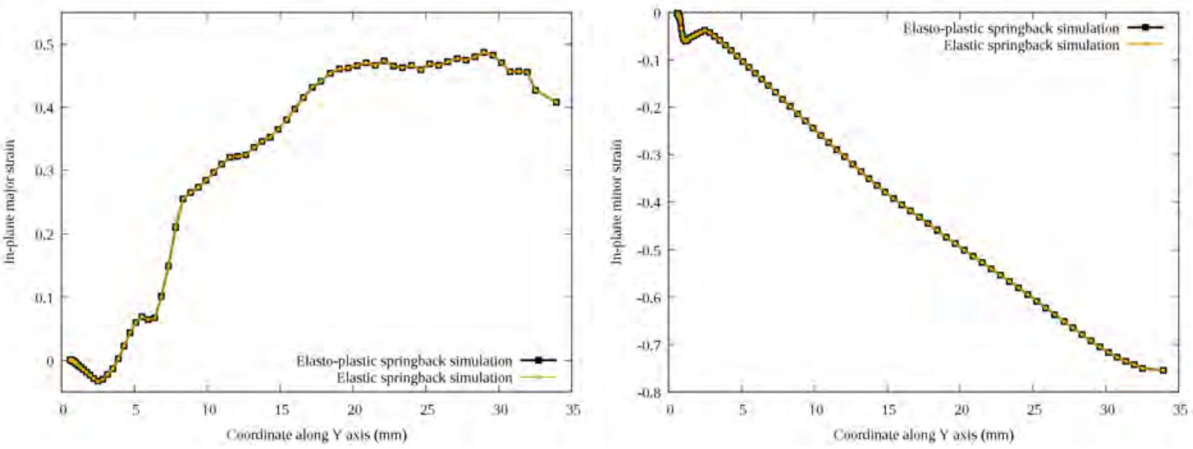

(c) RC2 - Major strain (d) RC2 - Minor strain

Figure 4.7 – Comparison of the numerical strain evolutions along the rolling direction obtained with elasto-plastic and elastic springback simulations for RC1 and RC2

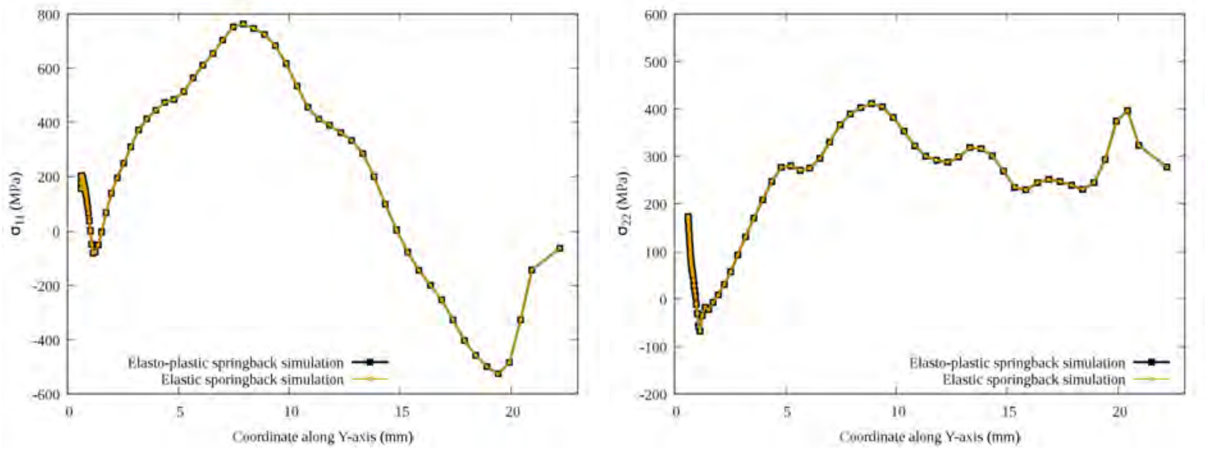

(a) RC1 - Major strain (b) RC1 - Minor strain

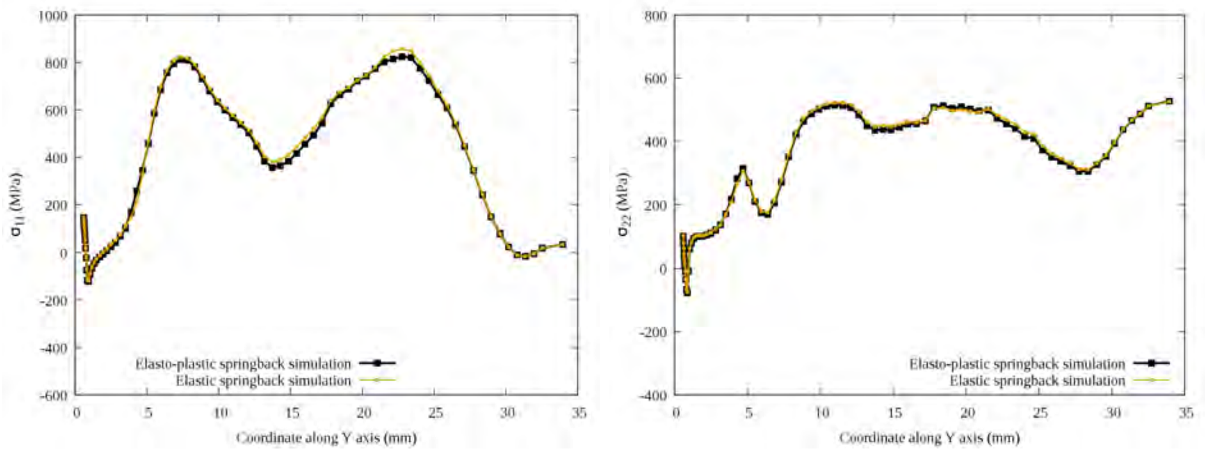

(c) RC2 - Major strain (d) RC2 - Minor strain

Figure 4.8 – Comparison of the numerical residual stress evolutions along the rolling direction obtained with elasto-plastic and elastic springback simulations for RC1 and RC2

4.3 Results

4.3.1 Punch force-displacement curves

The punch force-displacement curves are used numerically to calibrate the friction coefficients used to model the contact between the blank and the tools. The friction coefficient is adjusted to fit the levels of the maximum force and of the plateau at the end of the curve corresponding to the friction between the die and the cup to eject it from the tools. The friction coefficient value is calibrated with the curve obtained with the isotropic hardening law only and then, it is compared with the predictions of the two versions of HAH model. In the literature, the friction coefficient used to simulate the deep drawing of cylindrical cup in one or two stages are between 0.05 and 0.15 for lubricated conditions [65], [88], [111], [116], [121], [122] and can reach 0.22 in dry conditions [88]. These values vary as a function of the considered material. For example, in the case of Numisheet'99 benchmark about the reverse deep drawing process, different friction values are used for dual phase steel and mild steel [115] whereas the lubrication conditions are the same. In this study, most of the tests are performed with DIC measurement and thus painting is applied on the surface in contact with the punch. Only the surface in contact with the die is lubricated and these particular conditions can explain higher friction values than the literature ones.

Firstly, the punch force-displacement curve of C1 is calibrated, a friction coefficient equal to 0.15 is used for all the contacts between the tools and the blank. Only one value of the friction coefficient because the punch force level is mainly influenced by the friction between the die and the blank. A good description of the maximum force level and the end plateau level is observed with this value according to Figure 4.9. The numerical punch force increases until slightly over 60 kN at approximately 12 mm of punch displacement in the same way as the experimental curve. Then, a deviation appears between the predictions and the experiment for a punch displacement of approximately 16 mm corresponding to the loss of contact between the blank and the blank-holder. Finally, a change of slope in the decrease is observed numerically at a punch displacement of 22 mm. The three models give similar results with almost the same maximum force level, only the e-HAH model predict a force slightly lower than the two other models, but the deviation at the end of the curve is common to all the models. Indeed, the contact with the blank-holder is not removed the same way during the experiments and appears at a punch displacement value of 18 mm but it is not possible to keep contact between the blank and the blank holder until this value numerically. Moreover, a slight influence of the hardening models during one stage or first stage of deep-drawing of cylindrical cups is consistent with the literature [65], [117].

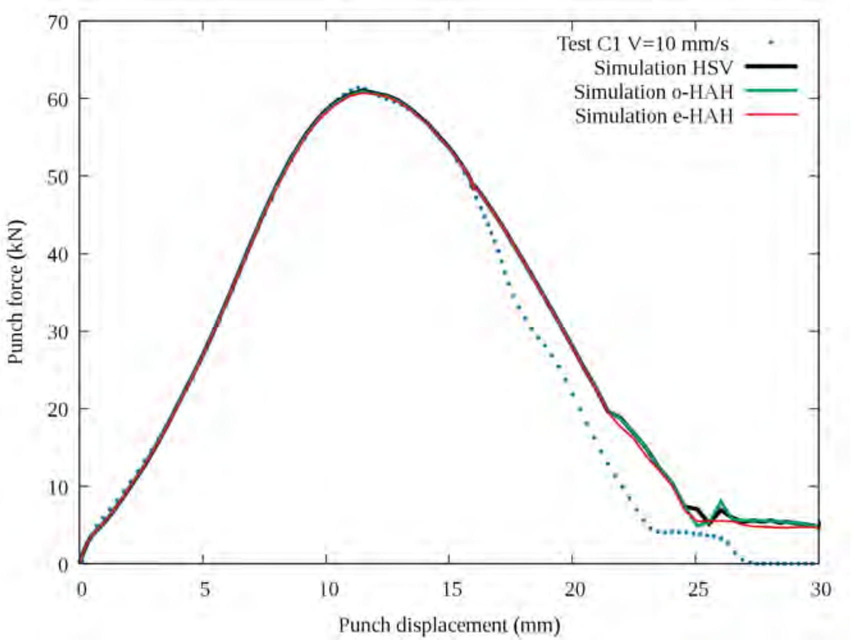

Figure 4.9 – Comparison of the experimental and the numerical punch force-displacement curves for the one-stage process

The isovalues of the equivalent plastic strain $\bar{\varepsilon}_p$ at the three characteristic values of punch displacement mentioned previously and at the end of the process are represented in Figure 4.10 for the inner surface of the cup. The amount of equivalent plastic strain increases progressively with the punch displacement value. For a punch displacement of 12 mm, the cup is half drawn and the most deformed part is the one in contact with the die radius with a maximum of $\bar{\varepsilon}_p$ equal to 0.35. Then, the cup is almost drawn for a punch displacement of 17 mm, only the edge remains to go through the die radius where the maximum of $\bar{\varepsilon}_p$ is still located and equal to 0.46. For a punch displacement of 22 mm, the cup is completely drawn but still needs to be ejected from the tools and the cup edge is the most deformed part of the cup at this point with a value of $\bar{\varepsilon}_p$ equal to 0.55. Finally, at the end of C1 simulation, $\bar{\varepsilon}_p$ is increased by friction compared to the punch displacement value of 22 mm and the maximum value of 0.65 is not located at the cup edge but a bit lower. Depending on the surface side (inner/outer), the maximum value of the equivalent plastic strain is between 0.5 and 0.65 and these values are consistent with the values obtained in the literature for similar processes [65], [102], [111], [117].

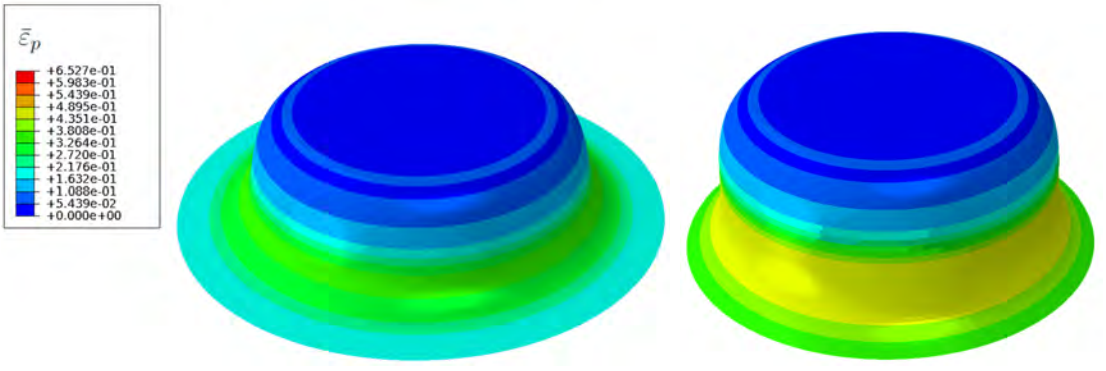

(a) Punch displacement = 12 mm (b) Punch displacement = 17 mm

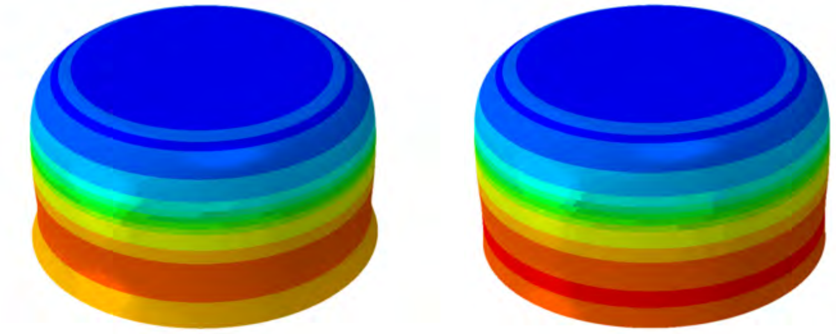

(c) Punch displacement = 22 mm (d) End of C1 simulation

Figure 4.10 – Evolution of the equivalent plastic strain for the HSV simulation of C1 test on the inner surface

The evolution of the strain path change indicator $\cos\chi$ is then followed. Firstly, strain path changes occur at the beginning of the process between 2 mm and 5 mm of punch displacement, as shown for the outer surface of the cup in Figure 4.11. The isovalues of $\cos\chi$ for a punch displacement of 4 mm in Figure 4.11 show that the strain path changes occur at the level of the punch and die radius. Once the cup radius is formed, there is no more strain path changes on this surface, only two lines of $\cos\chi = -1$ are noticed in Figure 4.11 for a punch displacement value of 12 mm because if the indicator has encountered a negative value, it converges then to the value -1, cf Figure 4.12. The definition of $\cos\chi = H\ \hat{\mathbf{h}} : \hat{\mathbf{s}}$ based on the comparison of the microstructure and stress deviator caused this phenomenon because when a strain path change occurs, the microstructure deviator rotates to find again a linearity with the stress deviator without considering if the direction is the same or the opposite one [10], [11]. The evolution of $\cos\chi$ and the equivalent stress of e-HAH model for four elements exhibiting strain path changes at a punch displacement value of 4 mm are represented in Figure 4.12 and their locations on the cup are shown in Figure 4.11(a). The evolution of $\cos\chi$ appears after a plateau of the equivalent stress observed between 2 and 4 mm of punch displacement at a value of approximately 400 MPa corresponding to the yield stress. These evolutions of $\cos\chi$ are very localized and may depend on numerical aspects as the mesh size. These first strain path changes can explain the slightly lower level of maximum punch force obtained for e-HAH model but they have overall no influence.

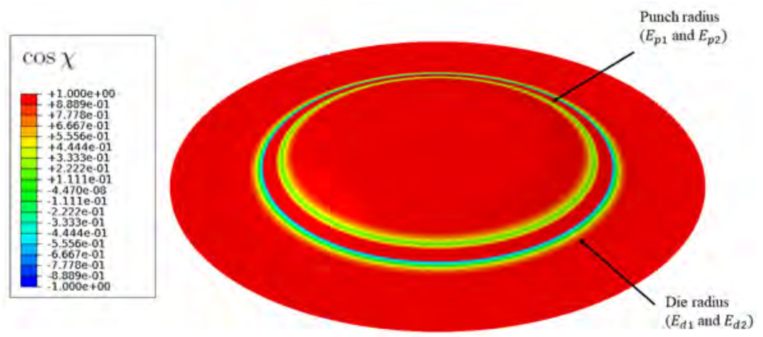

(a) Punch displacement = 4 mm

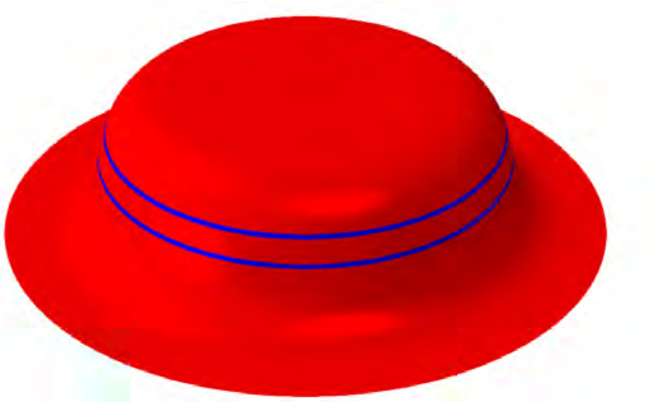

(b) Punch displacement = 12 mm

Figure 4.11 – Evolution of $\cos\chi$ for the e-HAH simulation of C1 test on the outer surface

Then, strain path changes are also observed at the end of the simulation between 22 mm of punch displacement and the end for the middle surface. The isovalues for the middle surface and a punch displacement of 22 mm in Figure 4.13 show that $\cos\chi$ is almost equal to 1 everywhere. And then, at the end of the simulation also represented in Figure 4.13 an evolution of $\cos\chi$ between 1 and 0.5 is observed mainly in the cup wall. These quasi-orthogonal strain path changes can explain the difference between the punch force displacement curves predicted by e-HAH model and the other models from the punch displacement of 22 mm.

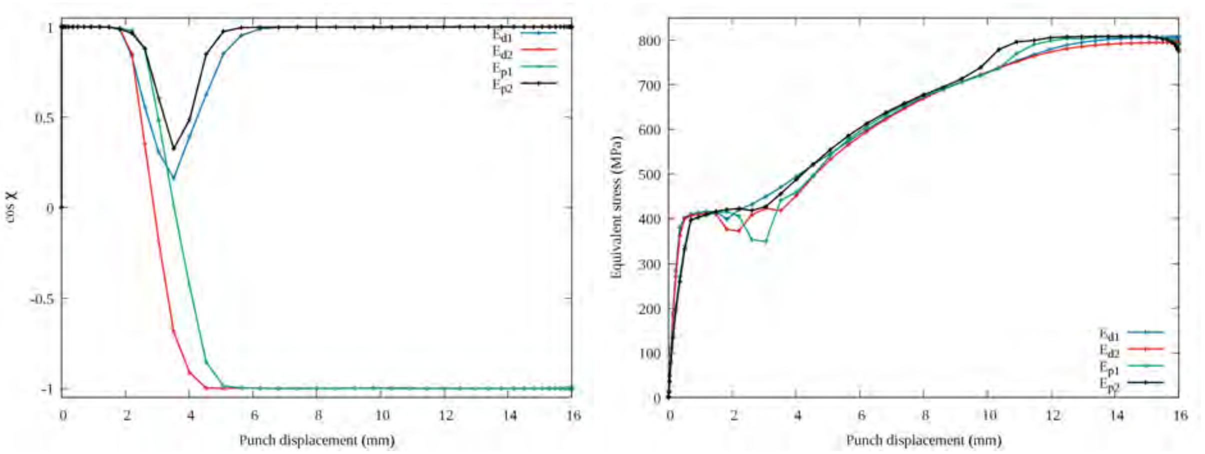

(a) $\cos\chi$ (b) Equivalent stress

Figure 4.12 – Evolutions of $\cos\chi$ and the equivalent stress of e-HAH model for the section points of the outer surface for the four elements E_{d1}, E_{d2},E_{p1} and E_{p2} during the forming step of C1 process

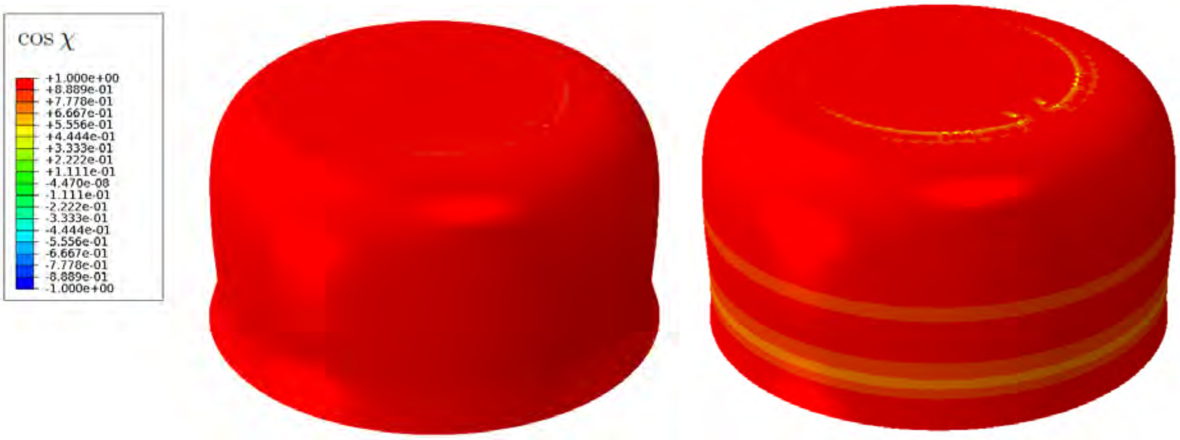

(a) Punch displacement = 22 mm (b) End of C1 simulation

Figure 4.13 – Evolution of $\cos\chi$ for the e-HAH simulation of C1 test on the middle surface

Then, for RC1, the friction coefficient of the redrawing simulation is calibrated with the punch force-displacement curve of the first stage similarly as C1, represented in Figure 4.14. A value of 0.18 is chosen and is appropriate to describe the maximum force level and the end plateau level. Similarly to C1, the numerical punch force increases until slightly over 80 kN at approximately 11 mm of punch displacement in the same way as the experimental curve. Then, a difference on the decrease slope is observed between the numerical curves and the experimental one. In that case, the difference between the curves starts before the blank-holder removal which corresponds to the variation of punch force at a displacement value of 17 mm. Even if there is a difference of slope at the end of stage 1, the numerical curves are closer to the experimental one than for C1. The three numerical curves are similar, the e-HAH one slightly lower, until a punch displacement value of 22 mm and then, the difference between e-HAH one and the two other models is larger.

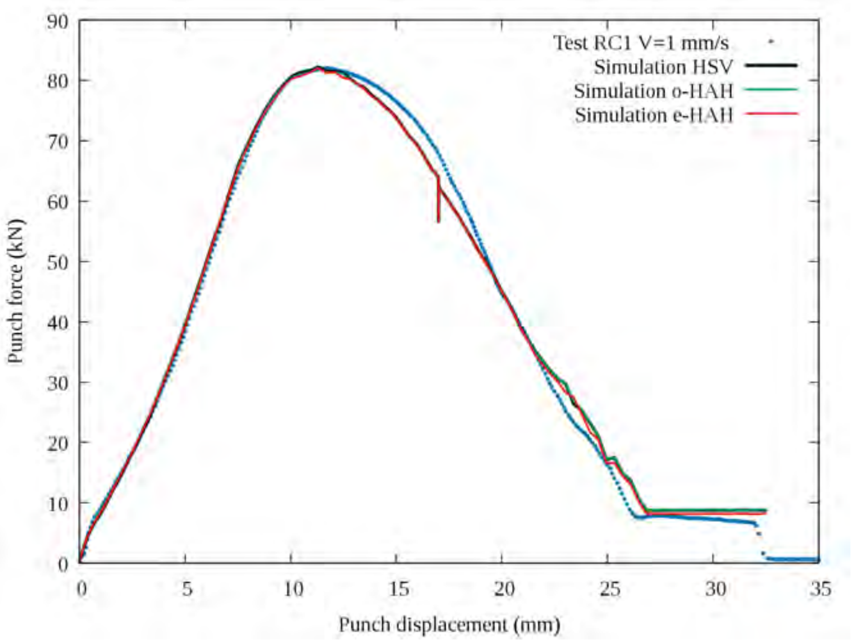

Figure 4.14 – Comparison of the experimental and the numerical punch force-displacement curves for the first stage of the redrawing process

As for C1, the evolution of the isovalues of the equivalent plastic strain is represented in Figure 4.15 for the inner surface of the cup. An evolution similar to C1 is observed but the values of $\bar{\varepsilon}_p$ are slightly lower for RC1. Indeed, the maximum value of $\bar{\varepsilon}_p$ located in the die radius is equal to 0.29 for a punch displacement of 11 mm corresponding to the maximum force. Then, the maximum value of $\bar{\varepsilon}_p$ increases until 0.38 at the time of contact loss with the blank-holder for a punch displacement of 17 mm. Finally, the maximum value of $\bar{\varepsilon}_p$ reaches 0.48 and 0.57 for a punch displacement of 22 mm and at the end of the simulation respectively. In a similar way as C1, the most deformed part at the end is located just below the edge.

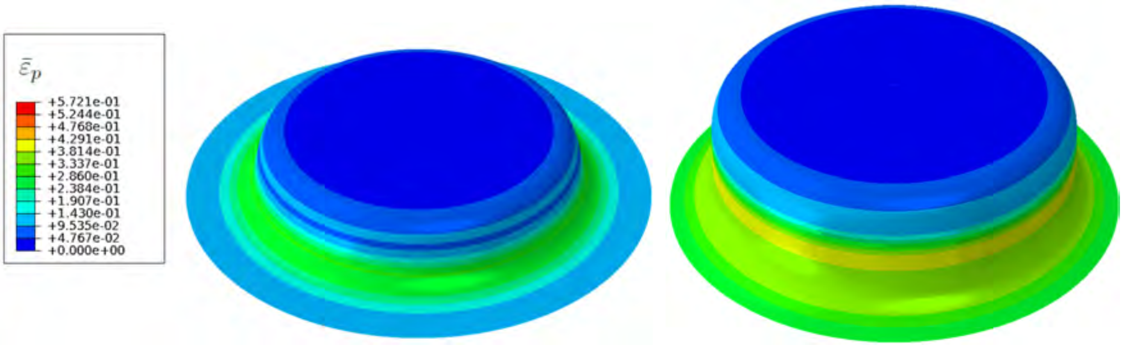

(a) Punch displacement = 11 mm

(b) Punch displacement = 17 mm

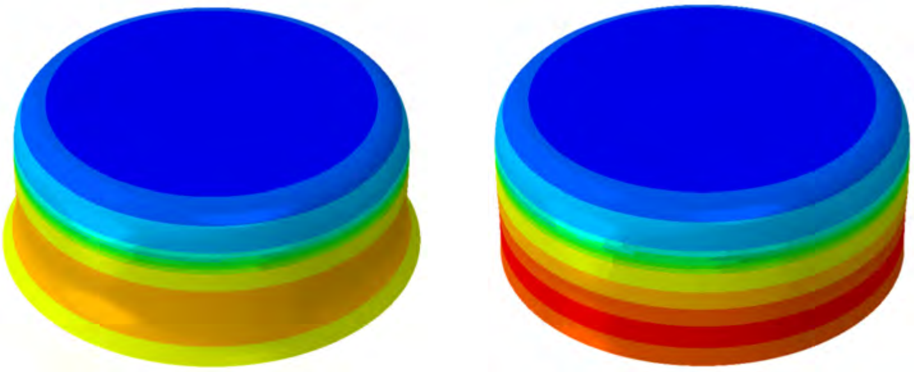

(c) Punch displacement = 22 mm

(d) End of RC1 simulation

Figure 4.15 – Evolution of the equivalent plastic strain for HSV simulation of RC1 test on the inner surface

Likewise, the strain path changes detected by $\cos\chi$ indicator are similar but less pronounced than for C1. There are strain path changes at the beginning of the simulation at the level of the punch radius for the outer surface and at the end of the simulation in the cup wall for the middle surface, cf. Figure 4.16.

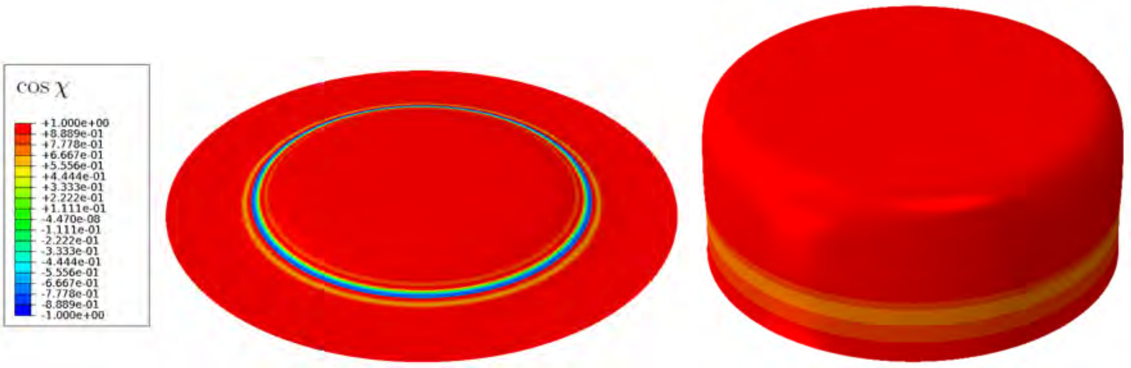

(a) Punch displacement = 3.5 mm - External surface

(b) End of RC1 simulation - Middle surface

Figure 4.16 – Evolution of $\cos\chi$ during e-HAH simulation of RC1 test

Finally, for the second stage of the redrawing process, the same friction coefficient value, equal to 0.18, is used because the plateau at the end of the punch force-displacement curves, represented in Figure 4.17, is well described with this value. Firstly, the process is simulated with the isotropic hardening law and without the modifications of the tools geometry. The experimental curve is well described up to a punch displacement value of 10 mm, but then the numerical punch force becomes higher than the experimental one. The evolution has a similar shape than the experimental curve with a first peak for a punch displacement of 15 mm then a decrease until a punch displacement of 23 mm and a second peak for a punch displacement of 26 mm but an upward offset of 8 kN is observed. Finally, during the force decrease, the numerical curve resumes progressively the experimental one. In comparison, the modification of the tools geometry leads to a difference on the first peak which is obtained for a punch displacement value of 20 mm and with a 10 kN higher force. This large first peak is similar to the one observed in Figure 3.5(b) for the experimental punch force-displacement curve in the case without spacers. Indeed, the contact kept at beginning of RC2 between the modified die and the cup flange can create a stretching of the blank similar to the one created when the blank is pinched between the die and the blank holder. After that, the two numerical curves obtained with the isotropic hardening law are at the same level for the second peak obtained in both case for a punch displacement of 26 mm. Comparing the three models in the case of the modified simulation, the curve predicted by e-HAH is slightly lower than the two others in particular between 10 mm and 20 mm. Even if the modeling of the transient behavior induced by strain path changes is taken into account with e-HAH model, the punch force is still overestimated and thus less influence of the material model is observed than in the case of the reverse process simulations for a mild steel [65]. Another study about the reverse process has shown that the contact modeling has a large influence on the punch force-displacement curves [117], thus a variation of the friction coefficient used for the contact between the die and the blank is tried. The friction coefficient is decreased from 0.18 to 0.1 for the link created between the two dies in the modified simulations and for the die radius of the second stage. A decrease of the force level is then observed on the punch force-displacement curves obtained with both HSV and e-HAH model in Figure 4.18. However, this modification of the friction coefficient is leading to an increase of the residual stresses along in both HSV and e-HAH cases. As this modification deviates from the measured stress distribution, the constant friction coefficient equal to 0.18 is finally kept. As suggested from other studies of the literature [13], [72], [119], [120], the degradation of the Young's modulus with plastic strain may also influence the results when non-linear strain path changes occur and could be a lead to improves the punch force-displacement curve of RC2.

The evolution of the equivalent plastic strain is represented for the initial simulation for punch displacement values of 10 mm, 15 mm, 20 mm, 23 mm, 26 mm and at the end for the inner surface in Figure 4.19. The isovalues for a punch displacement of 10 mm present the same maximal value equal to 0.57 as for the end of RC1 simulation but an evolution of the values of $\bar{\varepsilon}_p$ is visible in the cup radius which was almost not plastically deformed in the first drawing stage. The deviation, between the experimental punch force-displacement curves and the numerical ones, starts approximately for this punch displacement value corresponding to the beginning of the plastic deformation of RC2 cup. This observation suggests that the yield stress is overestimated and that the addition of the Young's modulus degradation may improves the predictions.

Once the radius of RC2 cup is formed, for a punch displacement of 15 mm, an increase of the maximum value of $\bar{\varepsilon}_p$ until 0.65 is observed. For the subsequent punch displacement of 20 mm, 23 mm and 26 mm, a localization of the plastic strain in the die radius is visible with an important increase of the maximum value which is respectively equal to 0.91, 0.97 and 0.98. Finally, at the end of the RC2 simulation, the most deformed part of the cup is the upper part of the wall with a maximum value of $\bar{\varepsilon}_p$ equal to 1.1. For the different surfaces, values of the equivalent plastic strain greater than 1 are observed at the end of the second stage as expected from the literature [65], [117]. In addition, during the modified simulation, the evolution of the equivalent plastic strain is similar with only minor variations of the equivalent plastic strain values. Indeed, the maximum values of $\bar{\varepsilon}_p$ are slightly lower during the simulations and somewhat higher at the end but the values do not vary by more than 0.1.

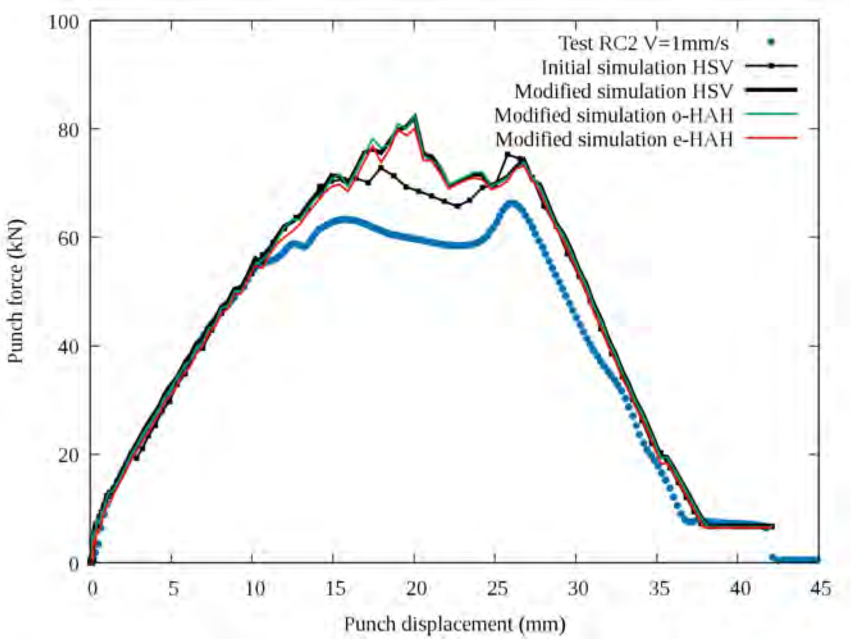

Figure 4.17 – Comparison of the experimental and the numerical punch force-displacement curves for the second stage of the redrawing process

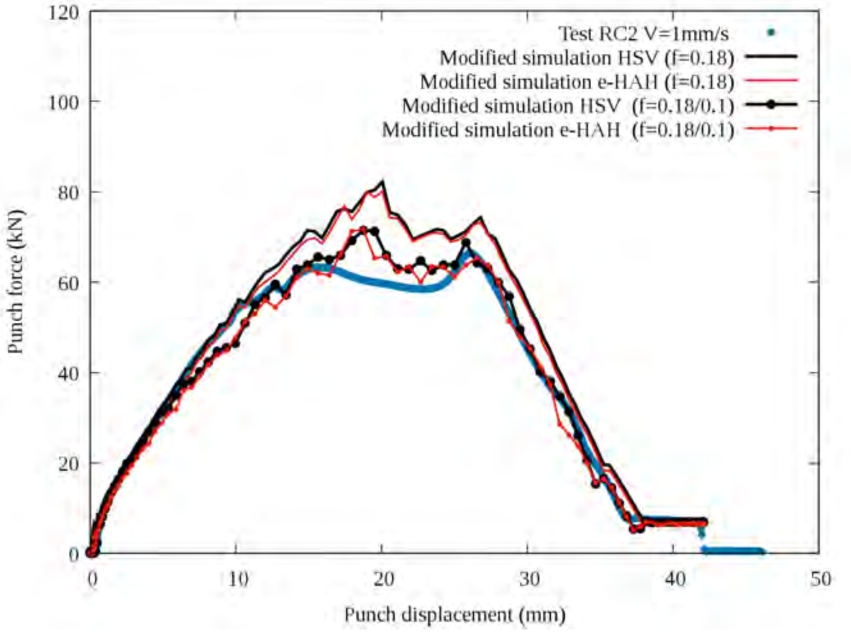

Figure 4.18 – Comparison of the experimental and the numerical punch force-displacement curves for the second stage of the redrawing process for a constant friction coefficient (f=0.18) and for a decrease of the friction coefficient at some locations of the die (f=0.18/0.1)

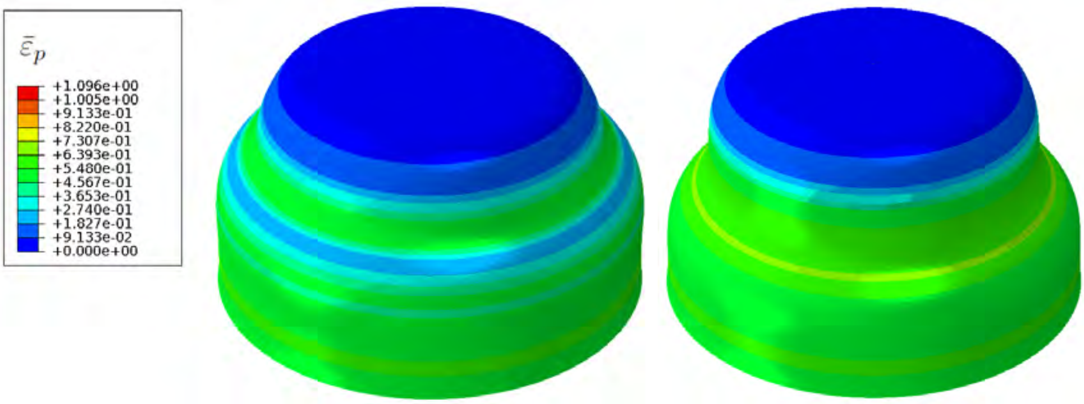

(a) Punch displacement = 10 mm (b) Punch displacement = 15 mm

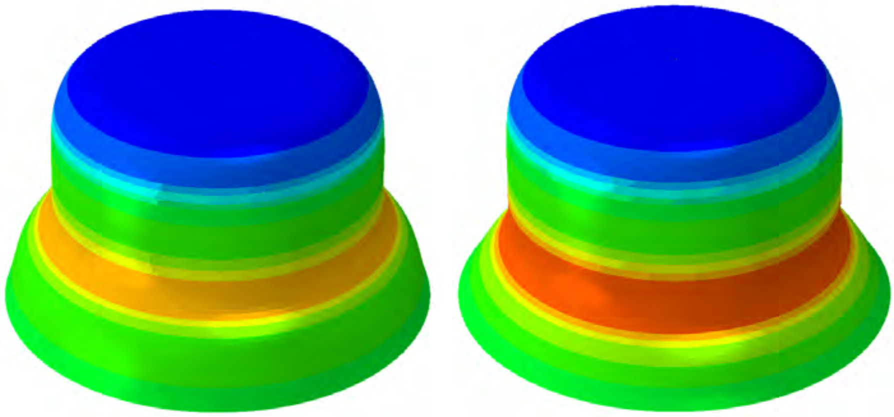

(c) Punch displacement = 20 mm (d) Punch displacement = 23 mm

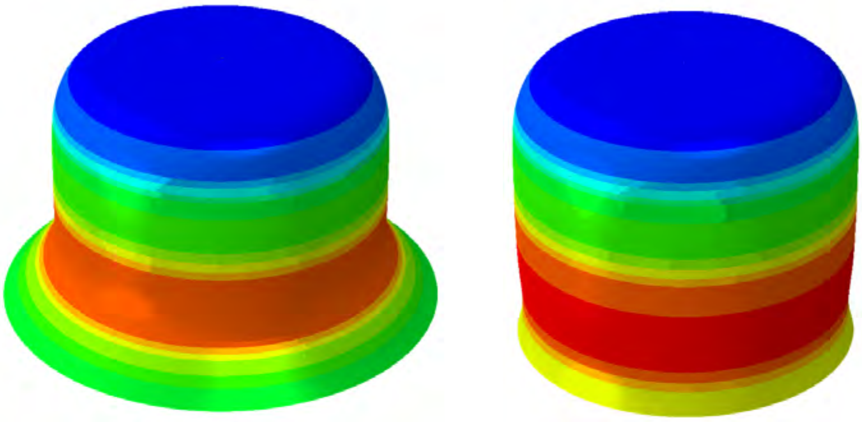

(e) Punch displacement = 26 mm (f) End of RC2 simulation

Figure 4.19 – Evolution of the equivalent plastic strain for the initial HSV simulation of RC2 test on the inner surface

The evolution of the strain path change indicator during the RC2 simulation performed with e-HAH model is then observed for the external, the middle and the inner surfaces respectively in Figures 4.20, 4.21 and 4.22. The isovalues of $\cos \chi$ are represented for three different punch displacements for each surface, one at the very beginning for a punch displacement of 2 mm, one intermediate value 10 mm or 15 mm depending on the surface and at the end of the simulation. Firstly, for a punch displacement of 2 mm, a variation of the indicator between 0 and -1 corresponding to orthogonal and reverse strain path changes is observed in the cup radius for the inner and outer surfaces. The strain path changes observed for the middle surface are more moderate with $\cos \chi$ values between 1 and 0.5 in the cup radius but also in the wall contrary to the other surfaces. The occurrence of these strain path changes at the very beginning of the RC2 simulation can explain that the punch force predicted by the e-HAH model is slightly lower than the other predictions during the whole simulation. Then, the isovalues presented for an intermediate punch values of 15 mm for the inner and outer surfaces show that the $\cos \chi$ indicator evolves only in the cup edge once the RC2 cup radius is formed. A wide blue band is also visible at the level of the RC1 cup radius due to the $\cos \chi$ evolution which remains negative when a strain path change occurred between 0 and -1. In the middle surface, a moderate evolution of the indicator is observed in the cup wall with values of $\cos \chi$ between 0.3 and 1 for a punch displacement of 10 mm. Finally, at the end of the simulation, an evolution of the indicator is again observed in the part of the cup corresponding to the former RC1 radius for the inner and outer surfaces and in the middle surface, an evolution of the indicator between 0.7 and 1 is observed in the cup wall.

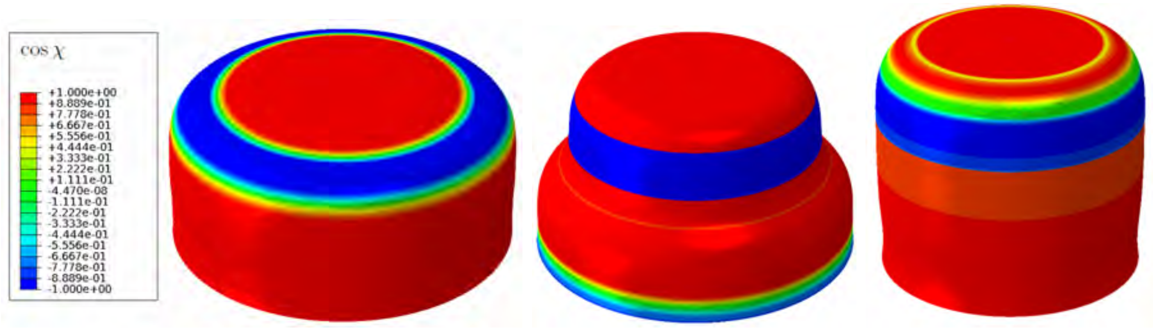

(a) Punch displacement = 2 mm

(b) Punch displacement = 15 mm

(c) End of RC2 simulation

Figure 4.20 – Evolution of $\cos \chi$ during the modified e-HAH simulation of RC2 test for the outer surface

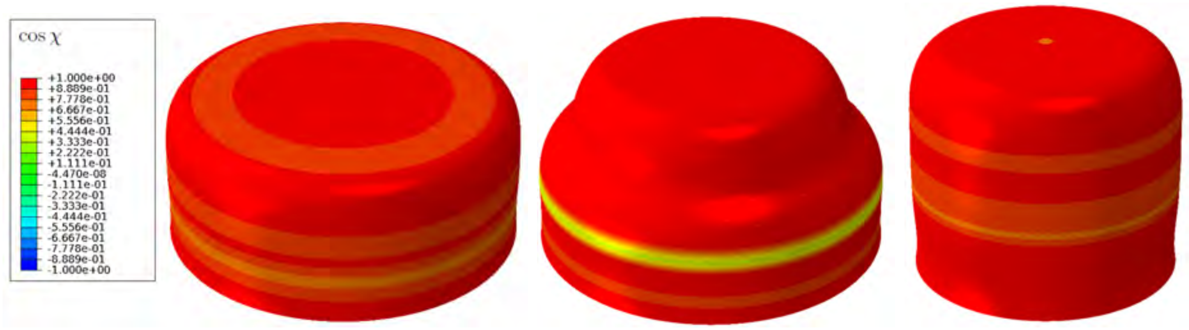

(a) Punch displacement = 2 mm (b) Punch displacement = 10 mm (c) End of RC2 simulation

Figure 4.21 – Evolution of $\cos \chi$ during the modified e-HAH simulation of RC2 test for the middle surface

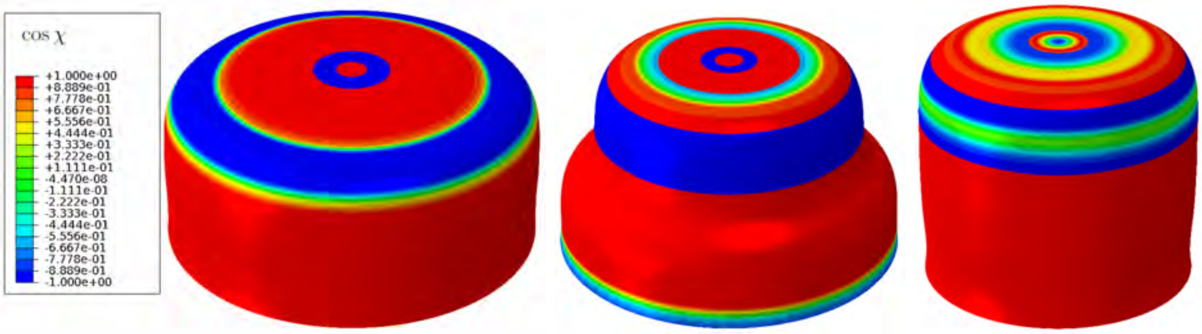

(a) Punch displacement = 2 mm (b) Punch displacement = 15 mm (c) End of RC2 simulation

Figure 4.22 – Evolution of $\cos \chi$ during the modified e-HAH simulation of RC2 test for the inner surface

Considering these evolutions of the punch force-displacement curves, the equivalent plastic strain and the strain path change indicator, the local evolutions of the major and minor strains and of the residual stresses along the rolling direction are then analyzed.

4.3.2 Major and minor strain fields

The evolution of the major and minor strains predicted by the finite element analysis are represented as a function of the coordinate along Y-axis defined as in the previous chapter, cf. Figure 3.6. The comparison is made along the rolling direction where the major and minor strains are extracted from a path of nodes, after the springback simulations performed at the end of C1, RC1 and RC2.

For C1, the evolutions of the numerical major and minor strains are compared in Figure 4.23 with one of the experimental measurement chosen as a reference. Between 0 and 10 mm along Y-axis, the major strain predictions are close to the experiment and then, a deviation is observed between the prediction and the experimental curve which is slightly higher. This difference can be explained by the decreased accuracy of the measurement due to the lower quality of the speckle pattern in the highest part of the cup. Moreover, the difference in the number of measuring points, which is half the size for the experiment, can also emphasize this difference because the subset size used in Aramis is equal to 0.8 mm whereas the mesh size in this part of the cup is equal to 0.4 mm. Even if there is some difference, the trend is similar and the three models show similar predictions with a slightly more moderate evolution for e-HAH model than for the two others. For the minor strain, the numerical predictions are consistent with the experimental curve. Some differences are observed for coordinates higher than 15 mm for the same reason as the major strain. For coordinates lower than 5 mm, the same evolution is observed for the predictions and the experiment but on different coordinate ranges which suggests a difference in the estimation of the coordinate along Y-axis between the DIC analysis and the finite element analysis.

The major and minor strains are also represented for RC1 in Figure 4.24, and compared with one experimental curve chosen as reference. Considering the die geometry of the first stage is not modified by the combination of the two dies to simulate the process with e-HAH model, thus initial and modified HSV simulations of the redrawing process gives the same results. Thereafter, there are no distinctions made between initial and modified simulations for RC1. The remarks made previously for C1 are also valid for RC1 because the strains evolutions are really similar and the same differences are observed between the experimental curve and the predictions. Apart from the cup height which seems lower for the strain measurements but it is actually not the case, cf. Table 3.1.2. Indeed, the measured height is equal to 22 mm similarly to the numerical cup but the difference of height observed on the curves is coming from an incomplete measurement of the cup due to poor quality of the speckle pattern in the highest part.

For RC2 simulations, the major and minor strain evolutions at a punch displacement equal to 15 mm are firstly analyzed. The predictions obtained with the initial and the modified HSV simulations are compared in Figure 4.25 to the smoothest curve of the three experiments performed for this case. For both cases, a plateau is observed for the major strain at a coordinate of 6 mm leading to numerical strains lower than the experimental ones until a coordinate of 15 mm. Above this value, the major strain is decreasing to return at the strain level of RC1 and the experimental and numerical evolutions are thus closer except at the end where the measured strain is higher. For minor strain, the evolution is smooth and similar for both simulations. Both predictions are in good agreement with the measurements with a slight gap observed when

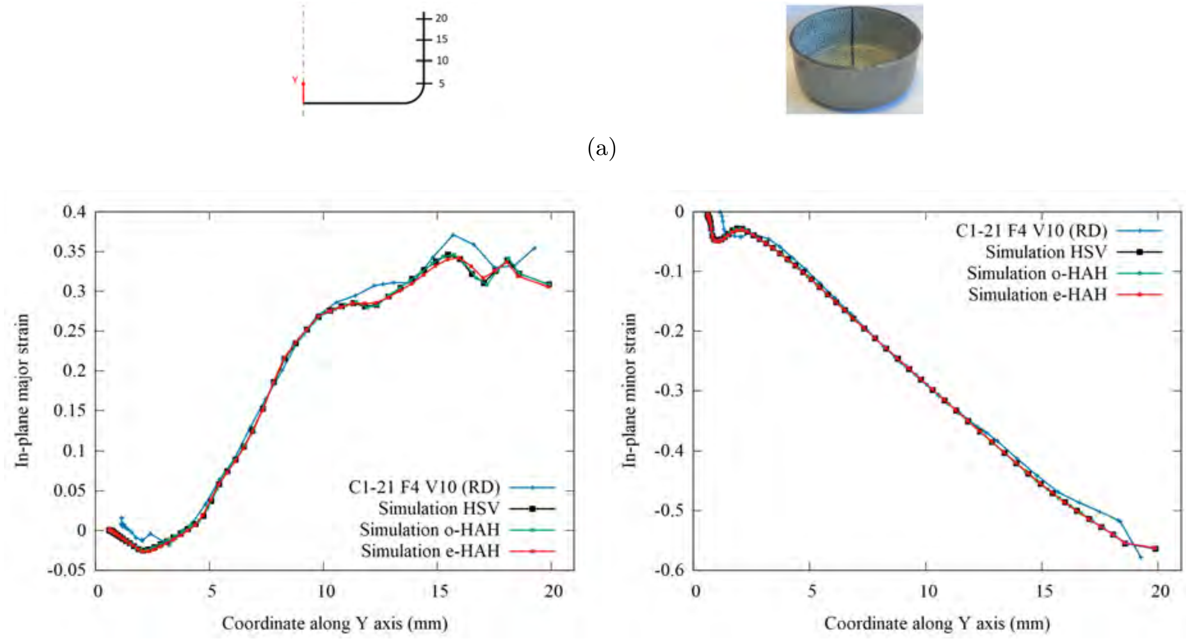

(a)

(b) Major strain

(c) Minor strain

Figure 4.23 – Comparison of the experimental and numerical strain evolutions along the rolling direction for the full C1 test

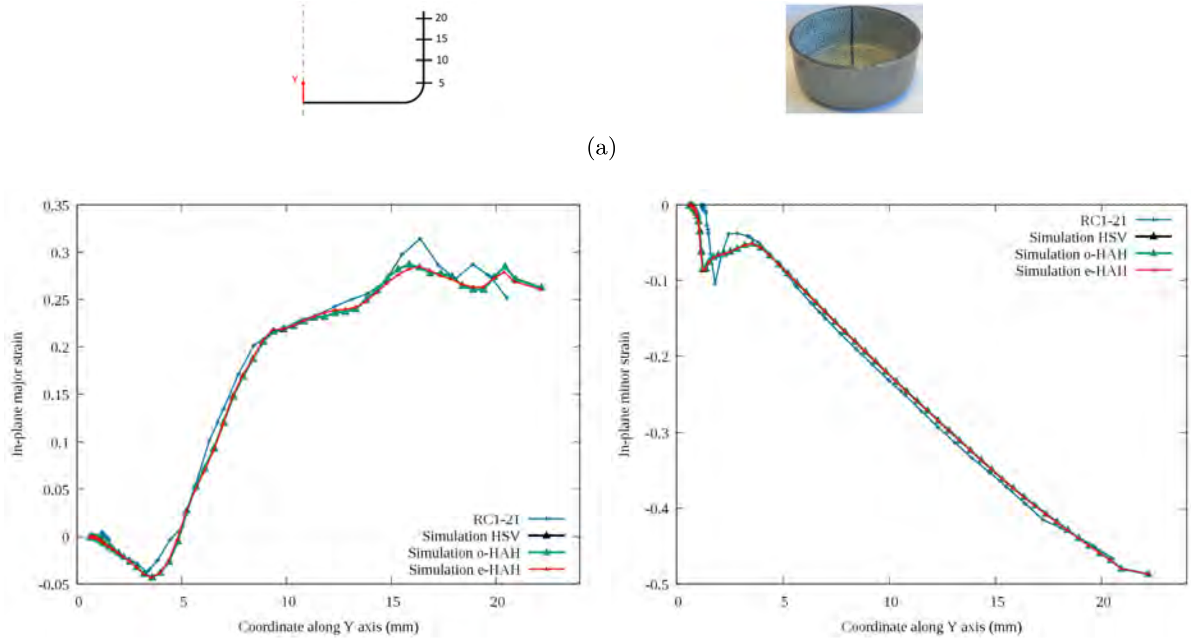

(a)

(b) Major strain

(c) Minor strain

Figure 4.24 – Comparison of the experimental and numerical strain evolutions along the rolling direction for RC1

the slope of the curve changed. Then, the comparison of the three models are presented for the modified simulations in Figure 4.26 and similar evolutions of the major and minor strains are obtained for all the models with only an influence of the model on the plateau value for the major strain which is lower with e-HAH model.

The major and minor strains evolutions obtained at the end of RC2 are also presented, firstly for the initial and the modified HSV simulations in Figure 4.27 with also an experimental curve chosen as reference. For the major strain, the predictions of the two simulations are consistent with the experimental values with the exception of particular locations where the experimental measurement is inaccurate such as between 5 mm and 8 mm, with again a plateau for major strains, and above 25 mm. The only noticeable difference between the two simulations is located between 17 mm and 30 mm along Y-axis where the strain predicted for the modified simulation is slightly higher than the one predicted by the initial simulation. For the minor strain, there is no difference between the two simulations and the predictions are similar to the experimental curve with a strain level somewhat higher from a coordinate of 12 mm. The predictions of the major and minor strains obtained with the modified simulation are then represented for the three models in Figure 4.28. For the major strain evolutions, o-HAH and e-HAH models predicts strains slightly lower than HSV hardening law whereas for the minor strain evolutions the predictions of the three models are similar.

Overall the cases, a good description of the major and minor strain evolution is obtained regardless of the model, or the simulation in RC2 case. Indeed, the strains are imposed by the tools geometries, explaining the low sensitivity to the constitutive law. Considering the good description of strains, the processes are correctly simulated and then, the strain path change influences can be analyzed with the comparison of the residual stresses predictions obtained with the three different models.

4.3.3 Residual stresses

One of the most important asset of the virtual forming regarding residual stresses is that the evolution in the whole cup is easily available in particular through thickness whereas it is a long and costly process experimentally. In fact, to measure the residual stress through thickness experimentally, it is necessary to electropolish the surface and perform for each thickness value the X-ray measurements which are time consuming. In the literature, the experimental study of the residual stresses through thickness for cylindical cups has already been performed notably for mild steel [113], stainless steel [123] and aluminium alloys [124] and some studies has also investigated the evolution along the wall for aluminum and stainless steel [123], [125]. The numerical evolutions of the residual stresses of cylindrical cups have been studied in much more examples [113], [115], [123], [126]–[128]. An example of the residual stress evolutions for a point at a middle height of a mild steel cup is presented in Figure 4.29 and synthesizes the results that

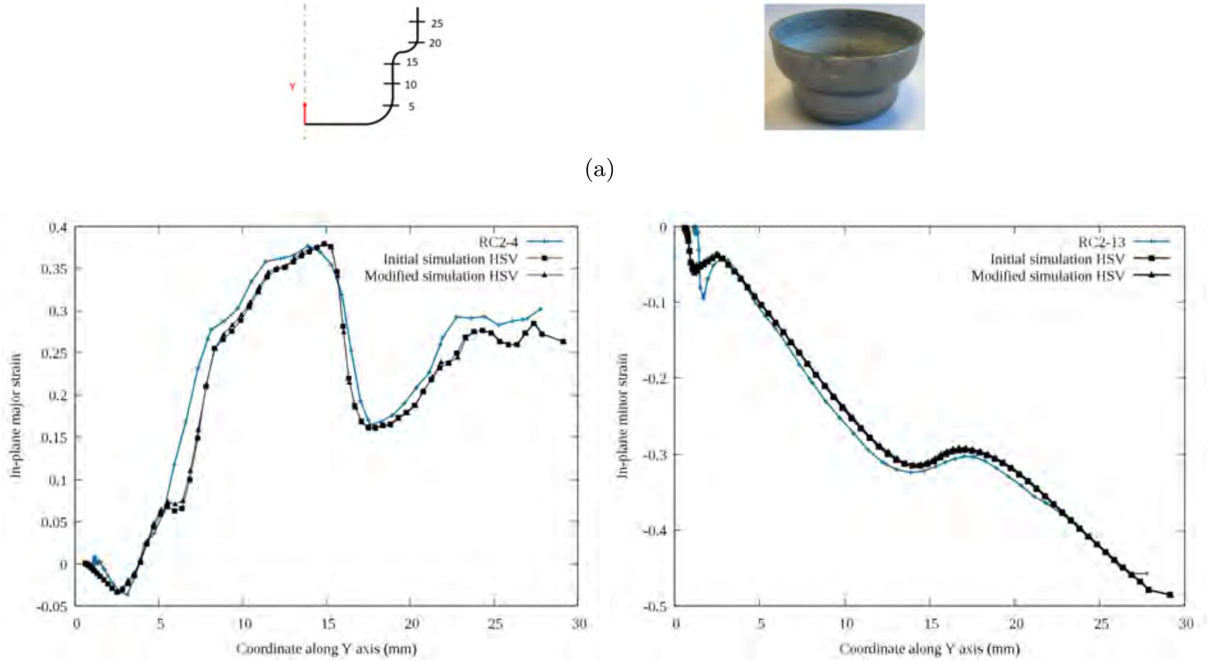

(a)

(b) Major strain

(c) Minor strain

Figure 4.25 – Comparison of the experimental and numerical strain evolutions along the rolling direction obtained with the initial and the modified RC2 simulations for the isotropic hardening at a punch displacement value equal to 15 mm

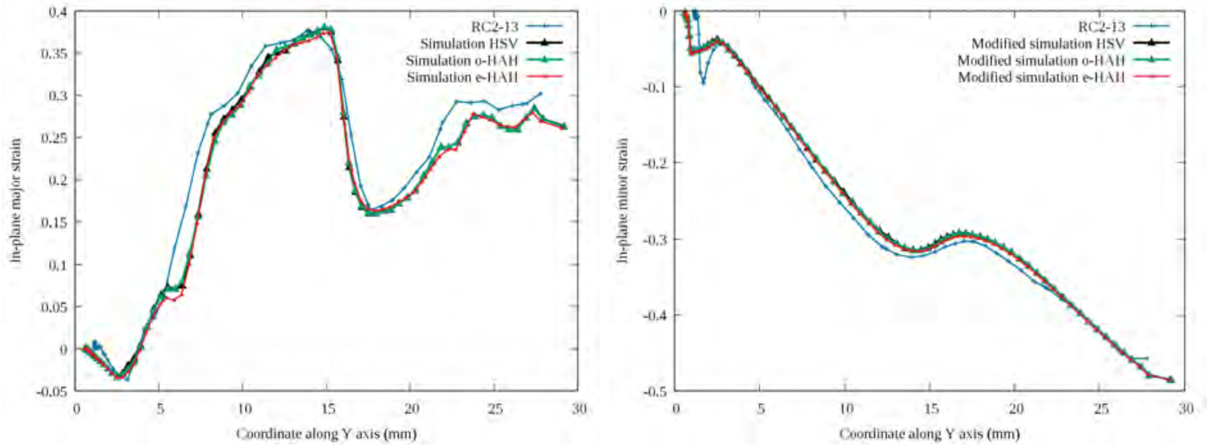

(a) Major strain

(b) Minor strain

Figure 4.26 – Comparison of the experimental and numerical strain evolutions along the rolling direction obtained with the modified RC2 simulations for the three models at a punch displacement value equal to 15 mm

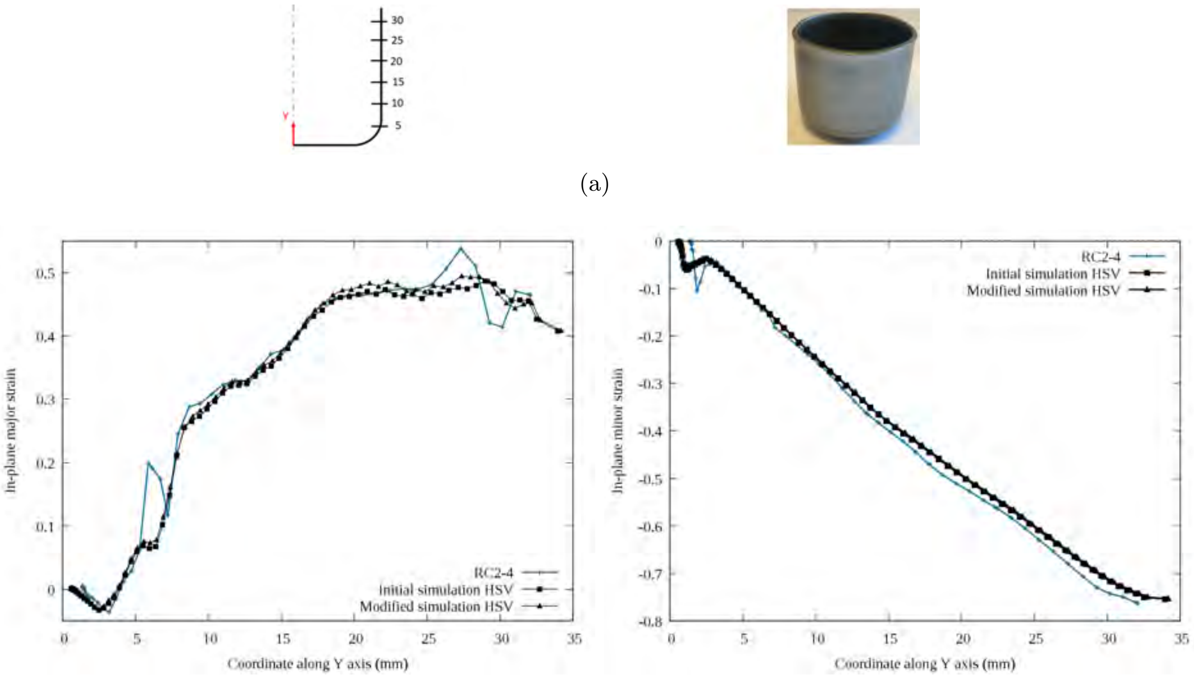

(a)

(b) Major strain

(c) Minor strain

Figure 4.27 – Comparison of the experimental and numerical strain evolutions along the rolling direction obtained with the initial and the modified RC2 simulations for the isotropic hardening

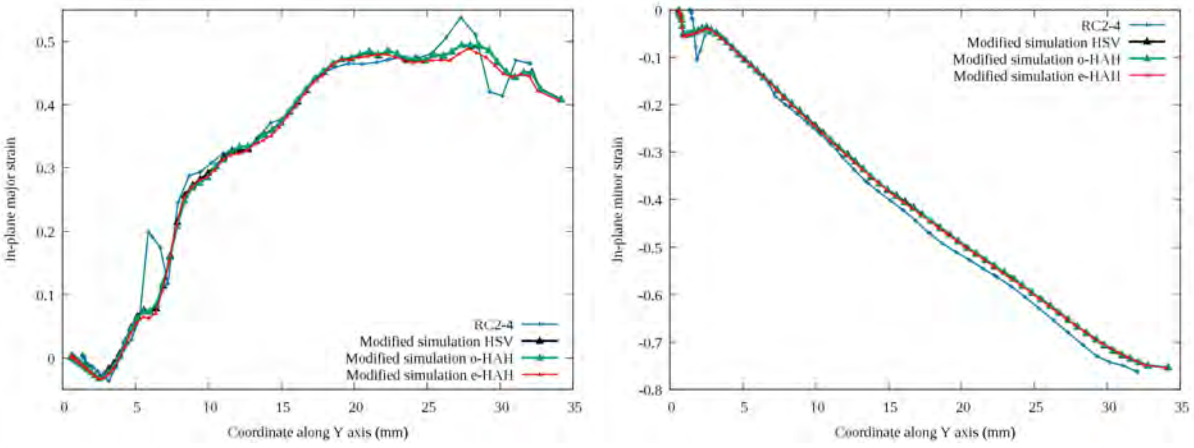

(a) Major strain

(b) Minor strain

Figure 4.28 – Comparison of the experimental and numerical strain evolutions along the rolling direction obtained with the modified RC2 simulations for the three models

are expected for C1, RC1 and RC2 cups. The longitudinal σ_l and circumferential σ_t stresses are corresponding to σ_{11} and σ_{22} respectively and 0% and 100% of the thickness are the inner and outer surfaces respectively. Both σ_l and σ_t show large compressive values, lower than −500 MPa on the inner surface and moderate tensile values between 0 MPa and 500 MPa on the outer surface. Strong evolutions are observed from negative to positive values between the inner and the middle surface whereas almost constant evolutions are observed between the middle surface and the outer surface. The evolutions of σ_{11} and σ_{22} presented as function of thickness in a similar way are shown in Figure 4.30 for elements at middle height of C1 and RC2 (9.7 mm and 16.7 mm respectively) and obtained with both HSV and e-HAH models. The evolutions obtained numerically with both models are very similar to the example. Between the inner and the middle surfaces, the evolution of both σ_{11} and σ_{22} are similar for both process with larger compressive values in RC2 case. While between the middle and the outer surfaces, the values of σ_{11} are greater than σ_{22} ones of about 200 MPa for RC1 whereas their values are approximately equals around 400 MPa for RC2. The hardening model has a small influence on the residual stress in comparison with their values but more influence is observed for RC2 than for C1 due to the strain path changes. Theses evolutions are in agreement with the literature but measurements through thickness are not available in this study to compare. Only comparison of the numerical and experimental evolutions along the cup wall on the outer surfaces are presented thereafter.

In order to compare the numerical residual stresses with the XRD measurement, it is necessary to change the coordinate system in which the stresses are expressed numerically to use the same as the measurements. The predictions of σ_{11} and σ_{22} are compared to one measurement for C1 in Figure 4.31. For σ_{11}, all the predictions have the same trend which is similar to the experimental one but the predicted stresses are much higher than the measured ones. The evolution of σ_{11} predicted by HSV and o-HAH models are close to each other whereas the one predicted by e-HAH model is lower in particular for the two extreme values obtained for coordinates similar to the measurement. Indeed, the maximum value of σ_{11} is predicted for a coordinate of 8 mm and is equal to approximately 850 MPa for HSV and o-HAH models whereas it is equal to 800 MPa for e-HAH model and to 400 MPa for the measurement. Likewise, the minimum value is predicted for a coordinate of 17 mm and is equal to approximately −450 MPa for the HSV and o-HAH models whereas it is equal to −400 MPa for the e-HAH model and to −200 MPa for the measurement. For σ_{22}, the predicted values are overall closer to the measurement than for σ_{11} and the predictions of the e-HAH model stands out from the two other models from a coordinate along Y-axis of 5 mm. A first peak is observed for a coordinate equal to approximately 8 mm, and in that case e-HAH model predicts a value of 510 MPa higher than the two other models which predict a value of 480 MPa whereas the measured value is equal to 400 MPa. A second peak is observed for a coordinate equal to approximately 18 mm, and in that case t e-HAH model predicts a value of 410 MPa lower than the two other models which predict

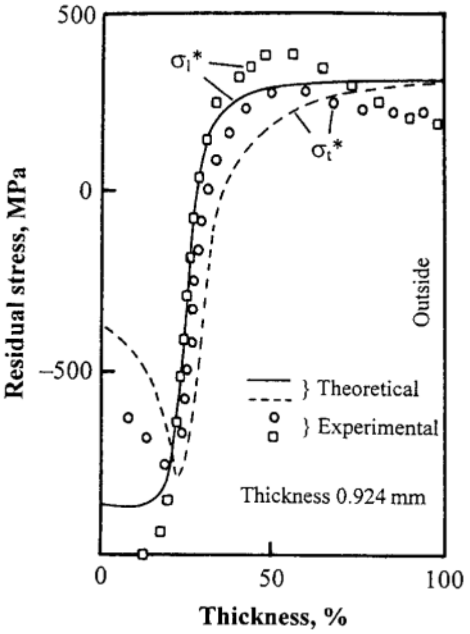

Figure 4.29 – Example of residual stress evolutions as a function of thickness for a point at a middle height for a mild steel cup [113] ($\sigma_l = \sigma_{11}$ and $\sigma_t = \sigma_{22}$)

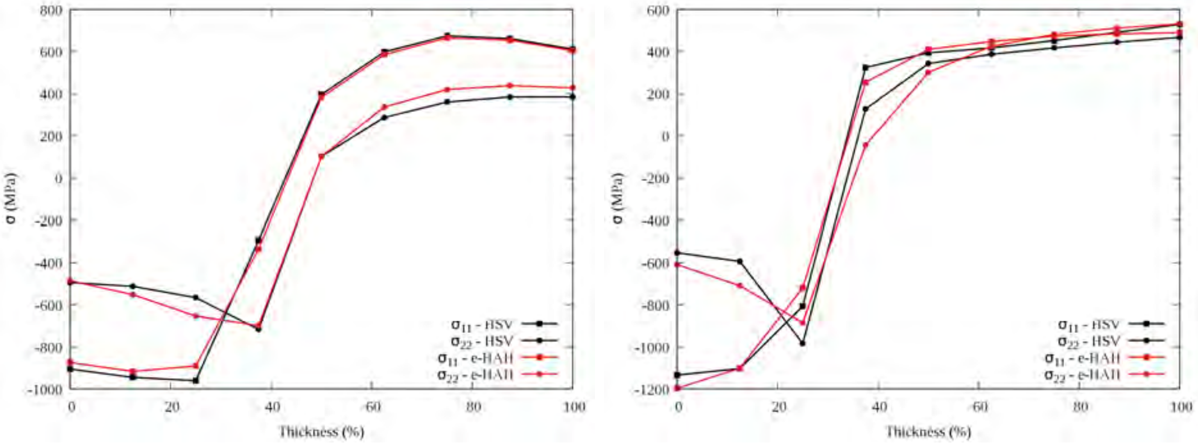

(a) C1

(b) RC2

Figure 4.30 – Residual stress evolutions as a function of thickness for a point at a middle height for C1 and RC2 with the HSV and e-HAH models

a value of 470 MPa whereas the measured value is equal to 350 MPa. Moreover, the numerical evolution of σ_{22} between 12 mm and 15 mm is different from the measured one. The differences between e-HAH model residual stresses and the predictions of the two other models may come from the quasi-ortogonal strain path changes observed in the cup wall.

Then, the predictions of σ_{11} and σ_{22} are compared to one measurement for RC1 in Figure 4.32. Similarly as C1, the predictions of HSV and o-HAH models are similar and different from those predicted by e-HAH model. For σ_{11}, the maximum value obtained for a coordinate equal to 8 mm is equal to approximately 780 MPa for the three models whereas the measured value is equal to 550 MPa. A difference is observed on the prediction of the minimum value which is equal to -550 MPa with HSV and o-HAH models, -500 MPa with e-HAH model and -350 MPa experimentally. For σ_{22}, the predictions of the three models are close to each other except between the coordinates of 4 mm and 14 mm where the predicted values by e-HAH model are higher than the ones predicted by HSV and o-HAH model. Indeed, a first peak is observed for a coordinate equal to 9 mm with a value predicted bye-HAH model equal to 460 MPa, whereas the one predicted by HSV and o-HAH model is closer to 400 MPa and the experimental one to 350 MPa. A second peak is observed for a coordinate equal to 19 mm but in that case the value predicted by the three models is approximately equal to 400 MPa and higher than the measured value of 300 MPa. The numerical evolutions have the same trend as C1 but the difference between e-HAH residual stress predictions and the two other model predictions are less pronounced for σ_{11} but more pronounced for σ_{22} than for C1 whereas fewer strain path changes are detected by the indicator $\cos\chi$.

For RC2, the residual stresses obtained after the initial and modified simulations with HSV are first compared in Figure 4.33. The stress predictions obtained after both simulations are similar except from two areas, one for each component, where the stress values coming from the modified simulations are lower than the initial ones. For σ_{11}, this area is located between the coordinates 2 mm and 8 mm and it includes the first stress peak observed where the initial simulation predict a value of 800 MPa and the modified one a value of 750 MPa whereas the measured value is equal to 550 MPa. In that case, the modification predicts stress values closer to the experimental ones but for σ_{22}, the opposite phenomenon occurs. Indeed, the area where the modified simulation predicts lower value than the initial one is located between 5 mm and 12 mm and the stress values predicted after the initial simulation are close to the measured values and thus the stress predicted by the modified simulation are lower than the experiments. Despite these differences, the predictions are overall close to each other and it seems reasonable to consider the modified simulation to be able to compare the three model predictions.

The residual stresses obtained after the modified simulations with the three models are compared to one measurement in Figure 4.34. Contrary to RC1, differences between the predictions of the three models are observed for σ_{11} in particular for the first peak at a coordinate equal

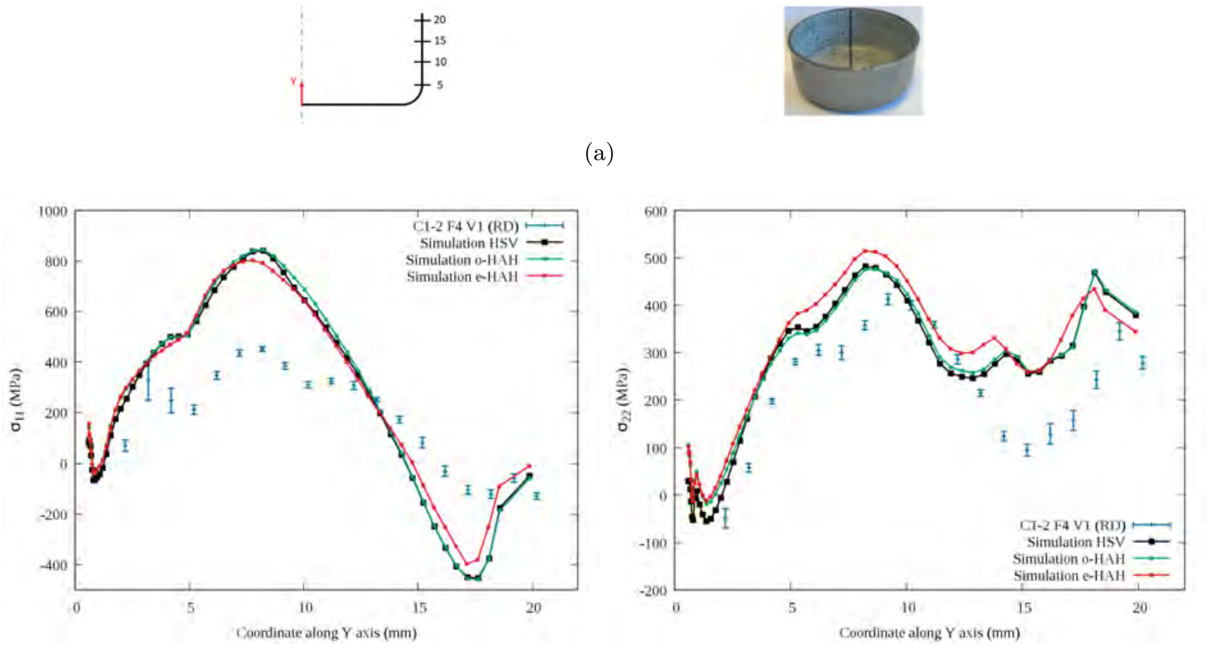

(a)

(b) σ_{11}

(c) σ_{22}

Figure 4.31 – Comparison of the experimental and numerical residual stresses for the cup 1

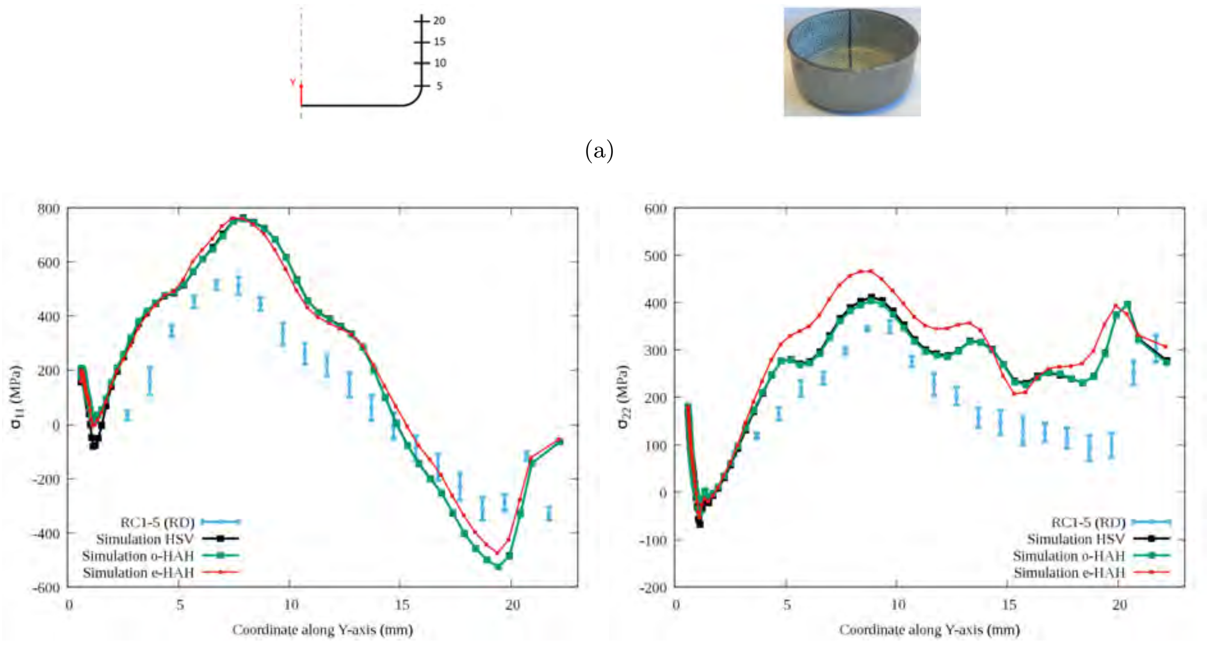

(a)

(b) σ_{11}

(c) σ_{22}

Figure 4.32 – Comparison of the experimental and numerical residual stresses for RC1

to 8 mm where a progressive decrease of the residual stresses from HSV with approximately 780 MPa to 650 MPa for o-HAH and then to 550 MPa e-HAH model which is similar to the measured value. For the second peak of σ_{11} evolution at a coordinate of 24 mm, both HSV and o-HAH gives similar values equal to approximately 800 MPa and e-HAH model predicts a slightly lower value close to 750 MPa but for all models the predict stresses are overestimated in this part of the cup considering the maximum measured value of the second peak is equal to approximately 350 MPa. The progressive stress evolutions for the first peak of σ_{11} is consistent with the evolution of the strain path change indicator $\cos\chi$ in this part of the cup corresponding to the cup radius of RC1. However, few strain path changes occur in the wall and thus the material model has few influences in the highest part of the cup. The strain path changes may have been limited by the modifications of the process and by neglecting the springback between the two stages. For σ_{22}, the predictions of HSV and o-HAH models are close to each other and difference with e-HAH models when the stress decrease at a coordinate of approximately 6 mm and between the coordinates of 15 mm and 25 mm where the predicted values by e-HAH model are higher than the ones predicted by HSV and o-HAH models. For the first area of difference, at a coordinate equal to 6 mm, the value predicted by e-HAH model is almost equal to 0 MPa, whereas the one predicted by HSV and o-HAH is closer to 100 MPa and the experimental one to 150 MPa. These difference is observed at the same coordinate than the plateau of the major strain evolution suggesting and the two deviations from the measurements may be linked. Overall, σ_{22} seems less sensitive to strain path changes than σ_{11} with distributions more linked with the evolution of the strain path change indicator.

Finally, after all forming stages, the numerical prediction of the residual stresses are larger than the measured ones. Two leads have been identified to explain this difference apart from the hardening model. The first one is the fact that residual stresses may be underestimated considering they have been measured only in the ferritic phase of the material. Moreover, the difference in the number of measuring points may also cause a difference because the stresses are measured only every 1 mm while numerically there is a point every 0.4 mm. Overall, σ_{22} seems less sensitive to strain path changes than σ_{11} with distributions more linked with the evolutions of the strain path change indicator. Thus for σ_{11}, modeling the strain path change behaviors improves significantly the final stress distribution of RC2 cup. A comparison of the strain path change occurence with the industrial finite element analysis of the redrawing process performed with PAM-STAMP is then presented.

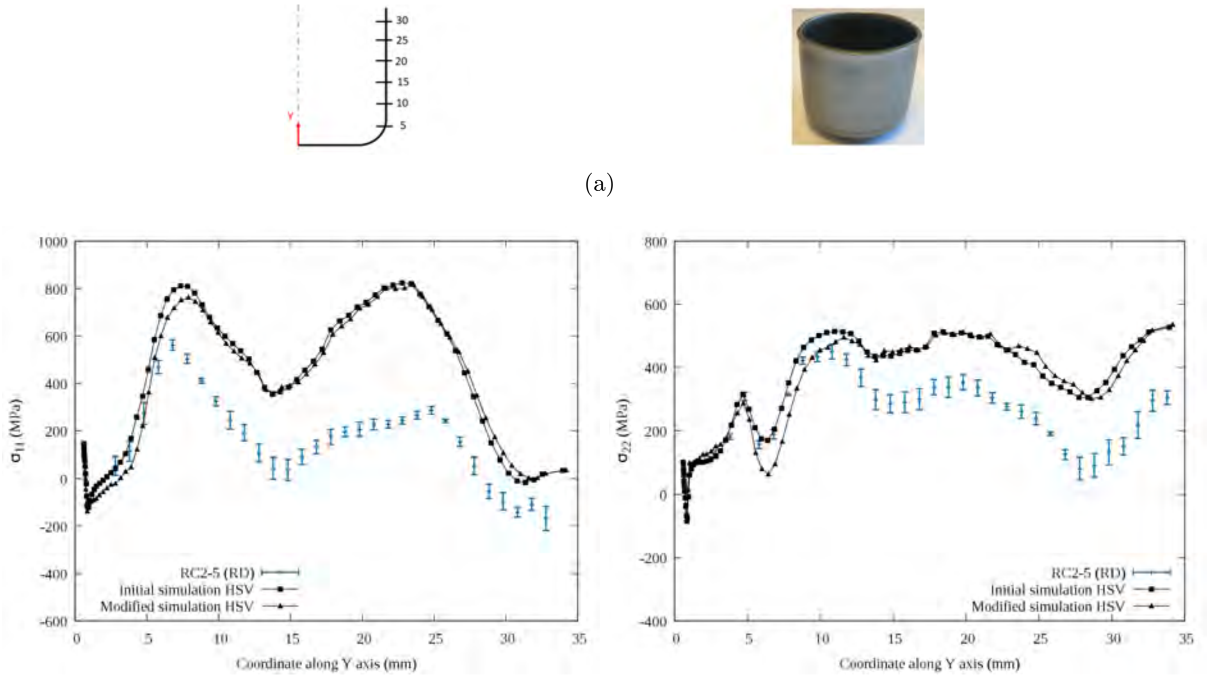

(a)

(b) σ_{11}

(c) σ_{22}

Figure 4.33 – Comparison of the experimental and numerical stresses evolutions along the rolling direction obtained with the initial and the modified RC2 simulations for the isotropic hardening

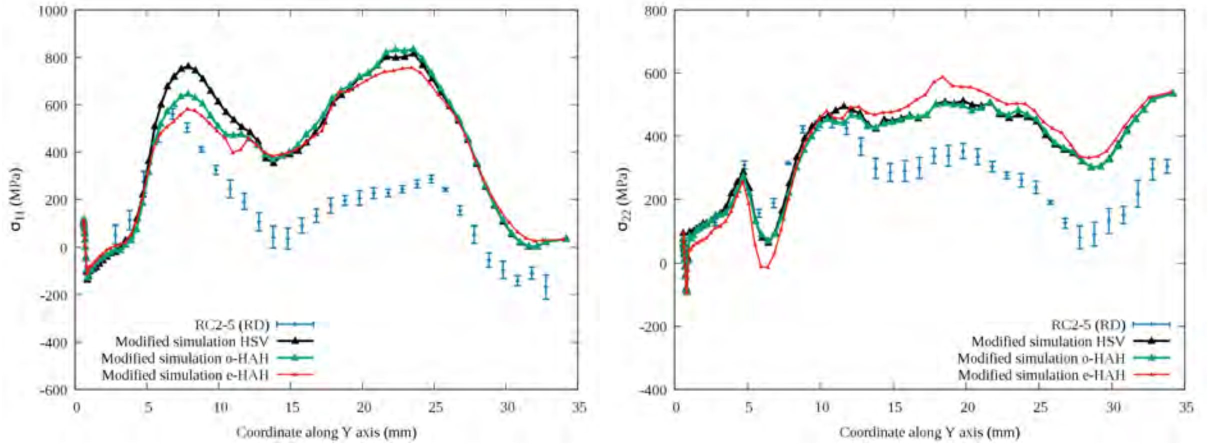

(a) σ_{11}

(b) σ_{22}

Figure 4.34 – Comparison of the experimental and numerical stresses evolutions along the rolling direction obtained with the the modified RC2 simulations for the three models

4.4 Comparison with finite element analysis performed with PAM-STAMP

4.4.1 Procedure

The finite element analysis is also performed with the code of ESI Group, PAM-STAMP, for both processes. The software Visual Body Stamping is used to create the computation file following the Validation template. The isotropic hardening law is available in standard and a subroutine developed especially for this project, by H. Choi and M.G. Lee in Seoul National University with the help of M. Ziane from ESI Group, is used for e-HAH model. In order to validate the implementation of e-HAH model, simulations of the characterization test used to calibrate the model are performed with one element. The results are compared with the experiments and the predictions obtained with Abaqus in Appendix D. Similar results are obtained for both finite element codes which validate the implementation of the e-HAH model in PAM-STAMP even if the cutting plane algorithm used in PAM-STAMP is weak contrary to Abaqus where it is strong, i.e. the hardening state variables are included in the plasticity calculation loop. The subroutine of e-HAH model is thus used for the simulation of the redrawing process. The results are compared with o-HAH model, obtained by setting the parameters S and k_S to defaults values 0.0 and 1.0 respectively, like in Abaqus. Both versions of HAH model are also compared to HSV isotropic hardening law which is available in standard in PAM-STAMP (via the material 117). The three hardening models considered are all coupled to von Mises criterion.

The whole blank is simulated and different mesh configurations are investigated. In fact, adaptive mesh used by default in PAM-STAMP is compared with two constant mesh size of 1 mm and 0.5 mm to check the mesh sensitivity. Without adaptative mesh, the blank is meshed homogeneously without partition of the geometry, the case of a mesh size of 1 mm is presented in Figure 4.35(a). With adaptative mesh, the initial mesh represented in Figure 4.35(b) is composed of large elements in the blank center and the mesh size progressively decrease until 1 mm for the blank edge. Then, during the simulation the mesh size is decreased in the blank regions that are deformed, i.e. the wall and the radius, until a mesh size value of 1 mm is reached, cf. Figure 4.35(c). In practice, the mesh evolution is mostly observed during the first stage of the process. For all mesh configurations, Belytschko – Tsay shell elements are used with uniform reduced integration and 5 integration points through thickness. The tools are also meshed with a refinement at the radius level for all the tools represented on one sectional view of the tools for the second stage in Figure 4.36.

Contrary to Abaqus, both forming stage are simulated in one step and a calculation step is performed before each stage for closing. The punch stroke is similar to those applied in Abaqus, 33 mm for RC1 and 42 mm for RC2, and it is the same for the other fixed boundary conditions

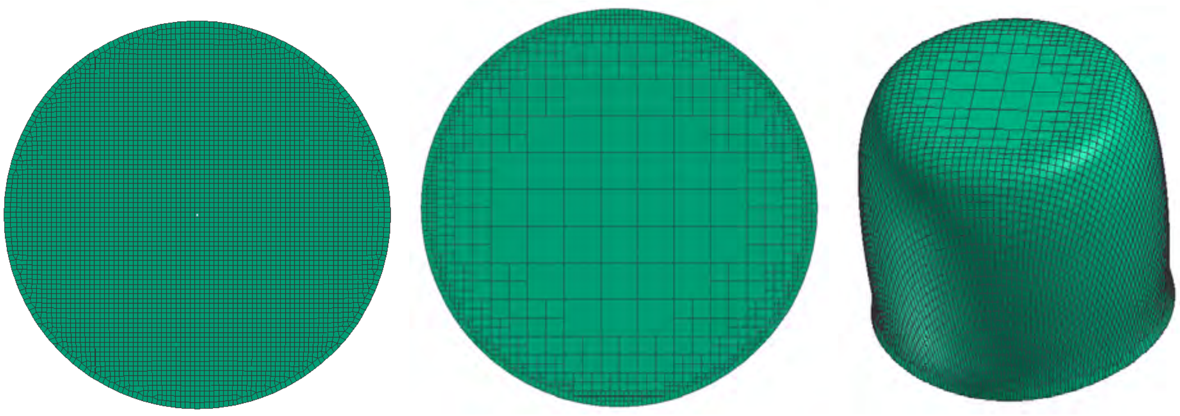

(a) Without adaptative mesh (b) Initial mesh with the adaptative one (c) Final mesh with the adaptative one

Figure 4.35 – Representation of the different blank mesh used for the redrawing simulations in PAM-STAMP

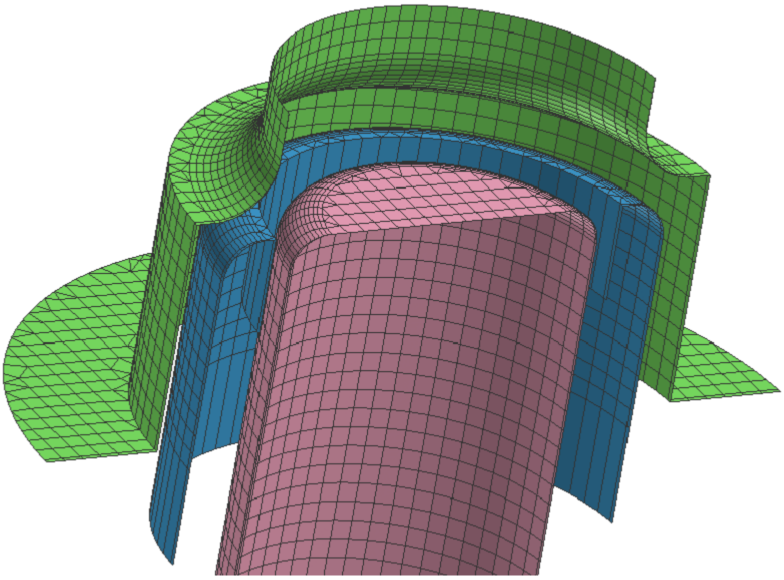

Figure 4.36 – Sectional view of the mesh of the tools for the second stage

with exception of the symmetries which are not used in PAM-STAMP. The computing station is a Windows PC with 12 cores, Intel(R) Core (TM) Gold i7-9850H CPU 2.60 GHz, and 32GB RAM. The simulations are run with double precision and with 8 cores in parallel leading to a CPU time of few hours even if the symmetries are not considered. Moreover, modification of the dies is not necessary to simulate the second stage with e-HAH and o-HAH models with PAM-STAMP. Only the modification of the blank-holder of the second stage is kept with the external diameter reduced of 0.02 mm because the springback between the two stages is neglected. The contact between the tools and the blank is defined with a node-segment model and the Coulomb law is used for friction. The friction is calibrated with the punch force-displacement curve of RC1 and a value of 0.22 is obtained, the value is higher than the Abaqus one and it can be explained by the use of different contact models.

4.4.2 Results

Only punch force-displacement curves are available in PAM-STAMP to compare with the experimental results and the predictions of Abaqus. The strain and stress profiles are thus not considered but the isovalues of the equivalent plastic strain and of the strain path change indicator are used to analyze the results. Firstly, the comparison of the experimental punch force-displacement curves of RC1 with both Abaqus and PAM-STAMP predictions obtained with HSV, is presented in Figure 4.37. For RC1, both finite element codes predict well the increase of punch forces but a deviation of PAM-STAMP prediction is starting from a punch displacement of 5 mm which leads to a maximum value of punch force a bit lower for PAMSTAMP than in experimental and Abaqus cases. Moreover, the punch displacement corresponding to the maximum value of force is higher in PAM-STAMP case and even if the highest part of the curve is not well described, the force decrease is better for PAM-STAMP than for Abaqus. The differences between the finite element codes for RC1 may come from the different contact model particularly between the blank and the blank-holder considering the model formulation but also the fact that the blank holder removal is dealt automatically by PAM-STAMP contrary to Abaqus. For RC2, the results from both finite element codes are closer than for RC1, a good prediction of the force increase is obtained until 10 mm of punch displacement and then both predictions are higher than the experimental curve. The shape of the predicted curves are in accordance with the experimental one but both codes predict the two force peaks observed experimentally for punch displacement values of 15 mm and 26 mm, approximately for 1 additional mm of punch displacement. Independently of the finite element code, the punch force is overestimated during the second stage and may be improved by adding the Young's modulus degradation in the material model as already suggested, but also by using a more accurate friction model. It could be interesting to use a model, available in PAM-STAMP, with a friction coefficient that can depend on the contact pressure andor the sliding speed between the blank and the tools.

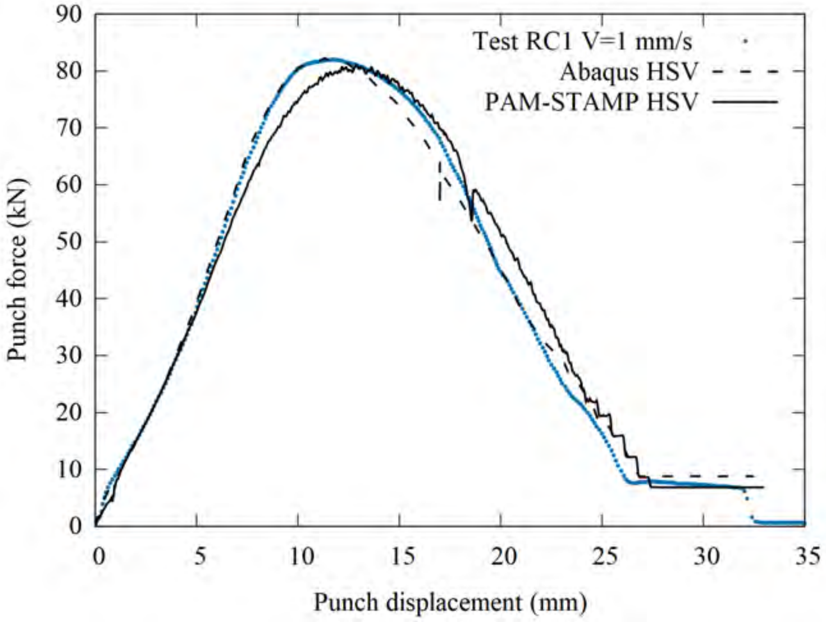

(a) RC1

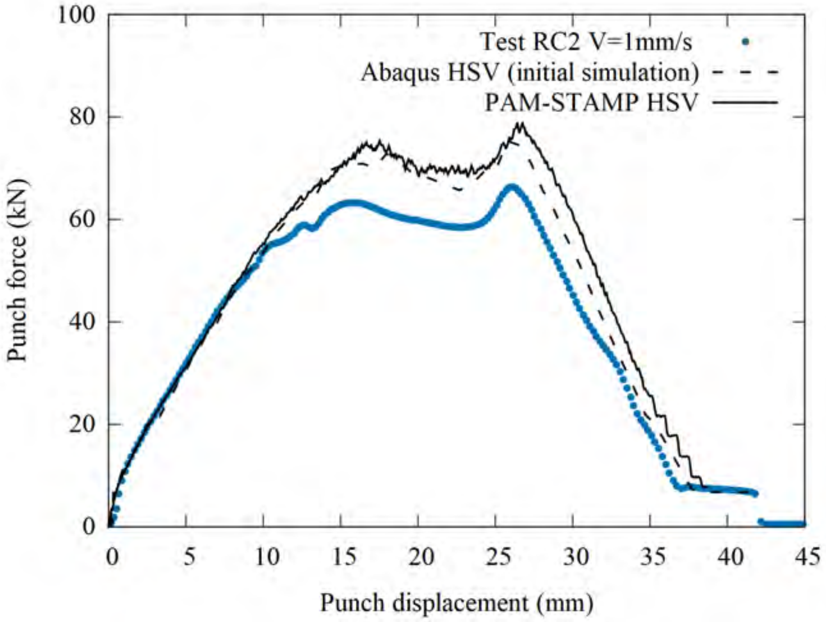

(b) RC2

Figure 4.37 – Comparison of the punch force-displacement curves obtained with PAM-STAMP and Abaqus at each stage for the istropic hardening law

Then, the mesh sensitivity is investigated by comparison of the punch force-displacement curves obtained for the three mesh configurations and each stage with the isotropic hardening law, represented in Figure 4.38. The simulation with adaptative mesh and the simulation of mesh size 1 mm without it give really similar results which are just a bit noisy whereas the simulation with a mesh size of 0.5 mm is much noisier for RC1 and less noisy for RC2. The use of a large mesh size seems adapted for RC1 and a refinement is more suited for RC2. The adaptative mesh is then used to compare the different models because it leads to the faster CPU time which is approximately 30 min for HSV and 2h30 for both HAH models.

Thus, the punch force-displacement curves obtained with the three considered models, HSV, o-HAH and e-HAH are presented in Figure 4.39. For RC1, the three models predicts similar curves as expected from Abaqus predictions. For RC2, the three models predict punch forces higher than the experimental one but a lower punch level is observed for o-HAH in comparison to HSV and for e-HAH in comparison to o-HAH starting at the very beginning of RC2 until the second peak of force. The difference between model predictions is the most pronounced for the first peak of force and is also more pronounced than in Abaqus because the modifications made in order to simulate the process with both HAH models may impact the results.

The isovalues of the equivalent plastic strain are then presented in Figures 4.40 and 4.40 for different punch displacement values during RC1 and RC2 respectively. The isovalues are really similar to Abaqus ones with maximum values at the end of each stage equal to 0.53 and 1.08 for RC1 and RC2 respectively. They are a bit lower than Abaqus ones but their locations on the cup are the same just between the flange and the wall. These slight differences certainly come from the mesh which is refined in Abaqus compared to PAM-STAMP and thus favors the strain and stress concentrations.

Finally, the isovalues of the strain path change indicator $\cos\chi$ are also presented in Figure 4.42. Only isovalues on the outer surface are presented for RC1 because few strain path changes occurs on the other surfaces. Due to the adaptative mesh, a non-circular evolution of the indicator is observed even if the considered model is isotropic. In fact, strain path changes are detected at the very beginning of the forming stage in the punch radius location and the mesh is not refined in this location yet. Thus, a particular repartition of $\cos\chi = -1$ is observed at the end of RC1 and is then kept until the end of the process.

Indeed, it is found again for the evolution of $\cos\chi$ on the outer surface represented for RC2 in Figure 4.43. This evolution of $\cos\chi$ depends significantly of the considered mesh and is almost not present with a constant mesh size, suggesting that these strain path changes are mainly introduced by numerical aspects and should perhaps not be considered as such. These variations of $\cos\chi$ have a very small influence on the results and it is more important to focus on the evolution observed in the second stage. For a punch displacement equal to 1 mm, an evolution of the indicator from 1 to -1 is observed in the punch radius location as expected from

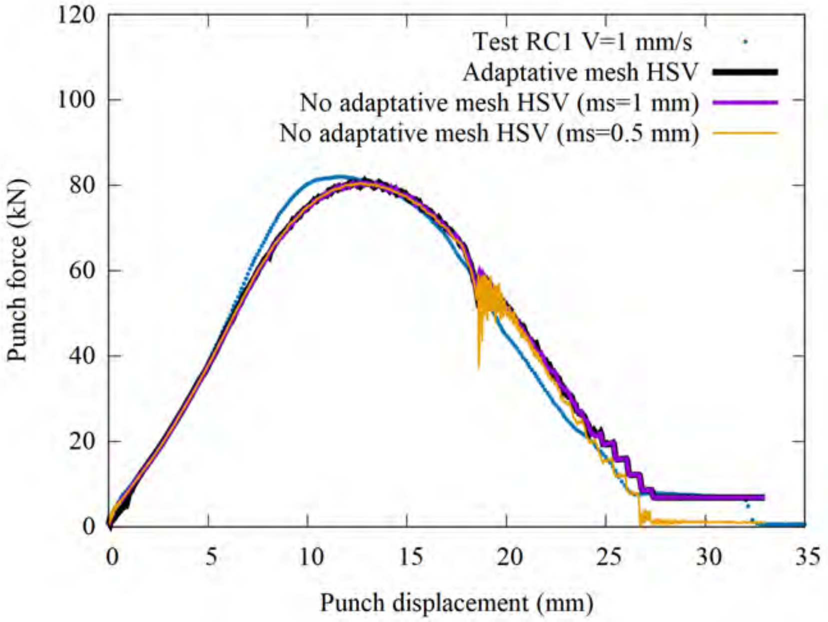

(a) RC1

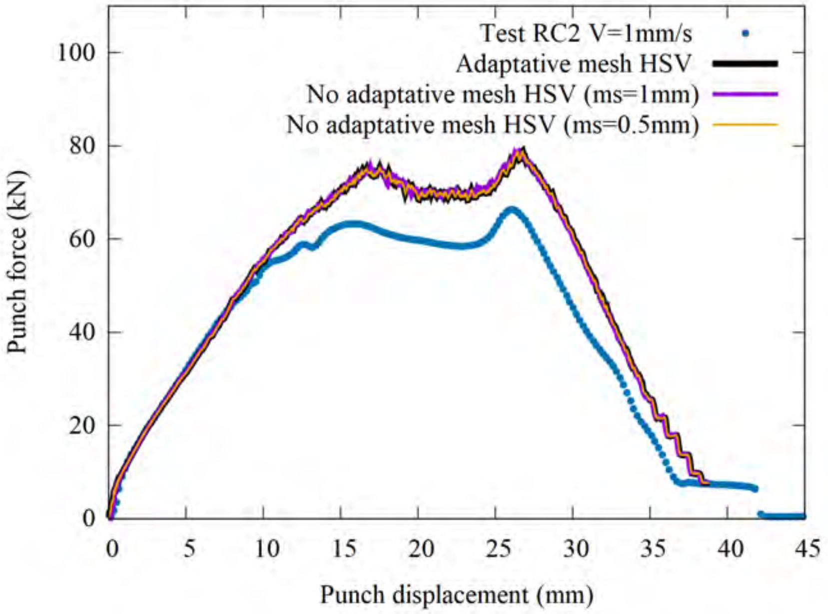

(b) RC2

Figure 4.38 – Comparison of the punch force-displacement curves obtained for the three mesh configurations at each stage with the isotropic hardening law (ms=mesh size)

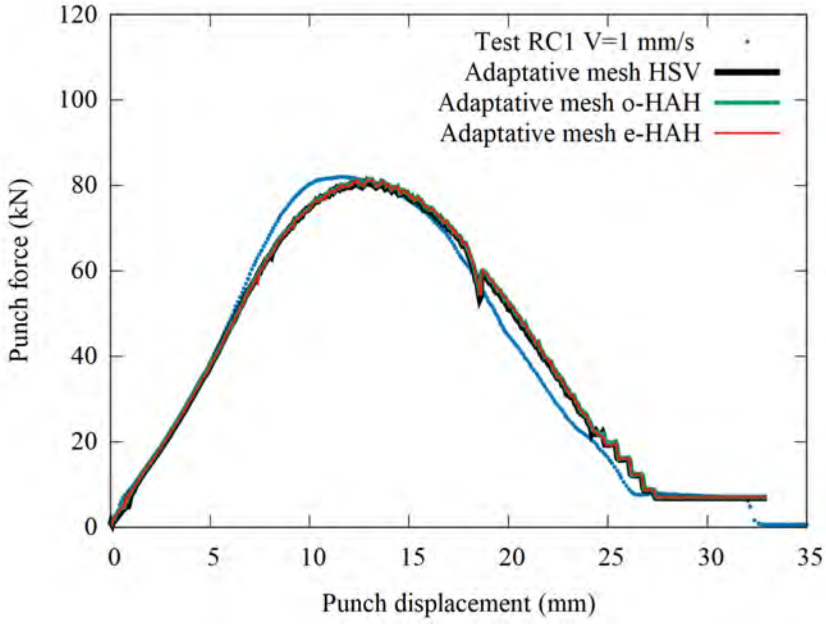

(a) RC1

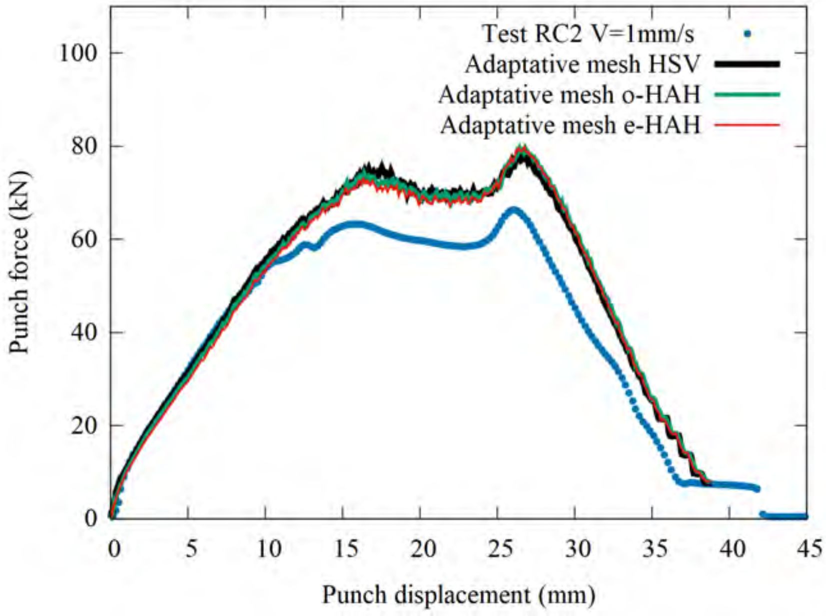

(b) RC2

Figure 4.39 – Comparison of the punch force-displacement curves obtained for the three models at each stage with PAM-STAMP

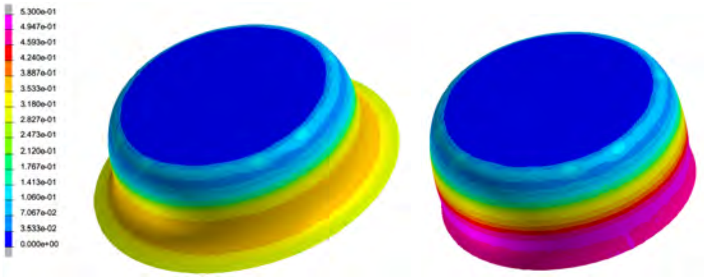

(a) Punch displacement = 18 mm (b) End of RC1 simulation

Figure 4.40 – Evolution of the equivalent plastic strain during the HSV simulation of RC1 test for the inner surface with adaptative mesh in PAM-STAMP

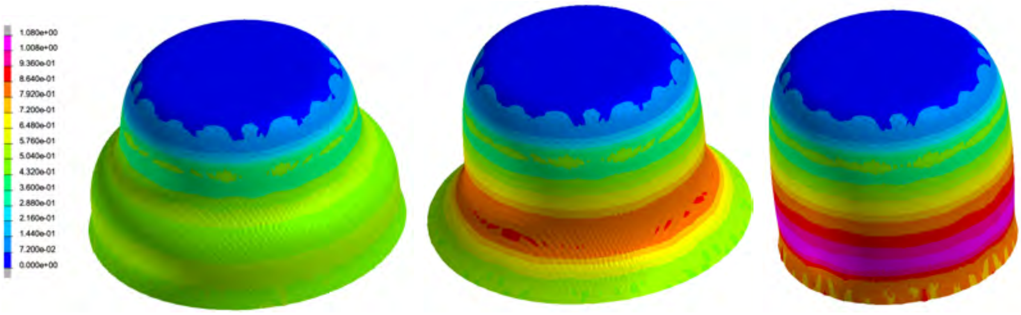

(a) Punch displacement = 15 mm (b) Punch displacement = 25 mm (c) End of RC2 simulation

Figure 4.41 – Evolution of the equivalent plastic strain during the HSV simulation of RC2 test for the inner surface with adaptative mesh in PAM-STAMP

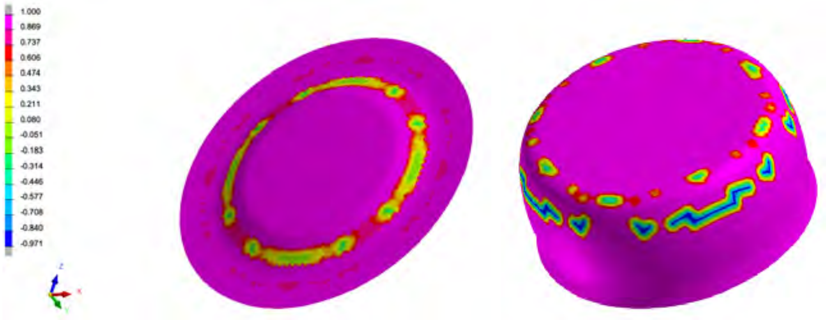

(a) Punch displacement = 4 mm (b) End of RC1 simulation

Figure 4.42 – Evolution of $\cos\chi$ during the e-HAH simulation of RC1 test for the outer surface with adaptative mesh in PAM-STAMP

Abaqus isovalues but a strong evolution of the indicator is observed in the wall and the flange corresponding to orthogonal and reverse strain path changes. The springback induced by the change of tools is not avoided in PAM-STAMP and is responsible for these strain path changes. An evolution similar to the Abaqus one is then observed with a progressive returns to $\cos\chi = 1$ in the cup wall and flange. A similar evolution is observed for the isovalues on the inner surface represented in Figure 4.44 which are also in agreement with Abaqus. In conclusion, the strong evolution of $\cos\chi$ at the beginning of the tests with both orthogonal and reverse strain path changes explain the difference observed on the punch force-displacement curves and explain also why less differences are observed in Abaqus.

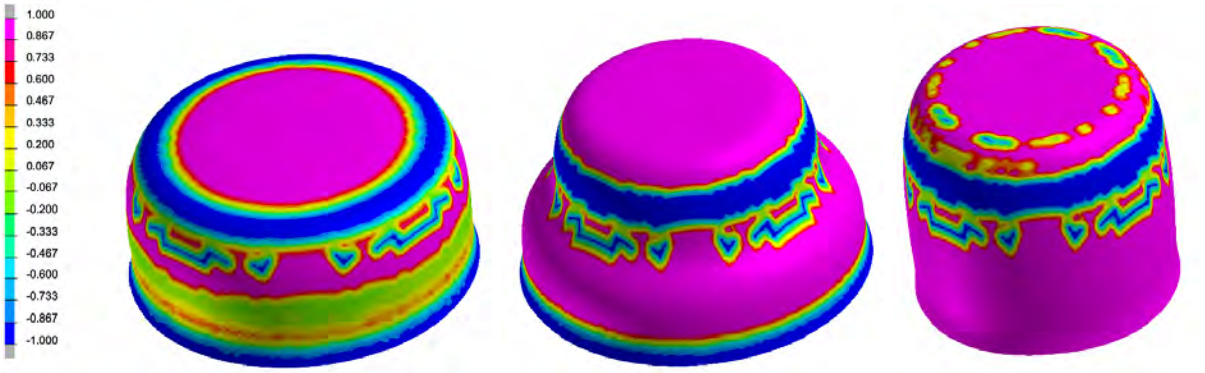

(a) Punch displacement = 1 mm (b) Punch displacement = 15 mm (c) End of RC2 simulation

Figure 4.43 – Evolution of $\cos\chi$ during the e-HAH simulation of RC2 test for the outer surface with adaptative mesh in PAM-STAMP

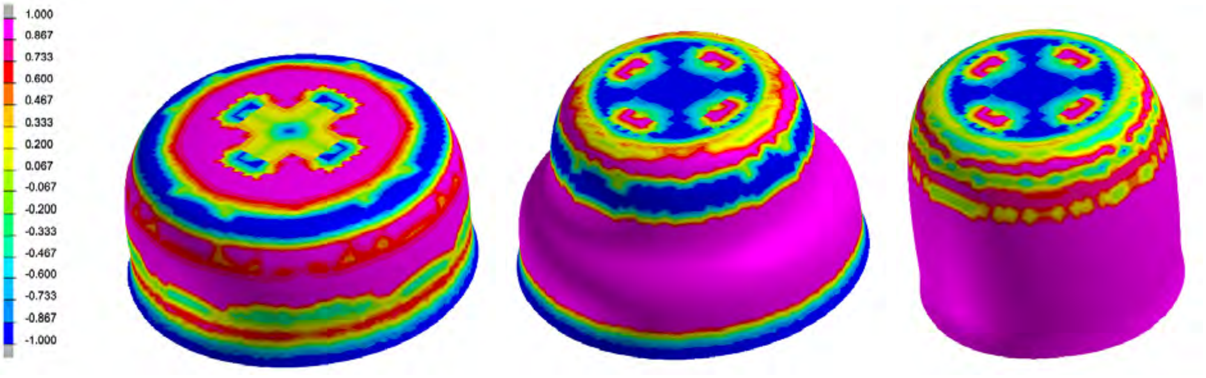

(a) Punch displacement = 1 mm (b) Punch displacement = 15 mm (c) End of RC2 simulation

Figure 4.44 – Evolution of $\cos\chi$ during the e-HAH simulation of RC2 test for the inner surface with adaptative mesh in PAM-STAMP

4.5 Conclusion

In conclusion, the virtual forming of cylindrical cups in one or two stages is presented in this chapter. First, some virtual forming cases already simulated with strain path changes models are presented. Then, the numerical procedure using Abaqus is detailed for the model dedicated to the subsequent fatigue analysis and the reduced one. Modifications necessary to simulate the second stage of the redrawing process and the necessity to use an elastic law for springback simulations are also presented. Then, the results obtained for the simulations of each process are presented beginning with the punch force-displacement curves used to calibrate the simulations. Such an evolution is analyzed by means of isovalues of the equivalent plastic strain and the strain path change indicator $\cos \chi$. It is observed that strain path changes are present for the three process C1, RC1, and RC2. In quantity, the one where there is the most is RC2 an the less is RC1. Finally, the local predictions along the rolling direction of major and minor strains and the residual stresses are compared to the experimental values. Major and minor strain evolutions are close to the test whatever the considered model and allow to validate the simulations whereas the influence of the model and thus of strain path changes is linked to the stress distributions. Strain path changes has a significant influence mostly in RC2 case for σ_{11} whereas σ_{22} seems less sensitive to strain path changes. Finally, the redrawing simulation is also performed with the industrial code PAM-STAMP which shows more strain path changes during RC2 because it is possible to simulate this forming stage without modifications and lead to more influence of the hardening model at least on the punch force-displacement curve. However, with both finite element codes, even if e-HAH model improves at some points the results, it is globally not enough to predict correctly the residual stresses and some aspects neglected in this study as the anisotropy or the Young modulus degradation may have an influence and could be tried to improve the results in the future. It is nevertheless possible to analyze the impact of the different residual stress fields on the service life. Indeed, the stress and strain fields obtained by e-HAH and HSV models with Abaqus are then used as inputs in a simulation of the fatigue loading in order to investigate the influence of strain path changes on the service life prediction.

Chapter 5

FATIGUE LIFE PREDICTION OF DEEP-DRAWN CUPS

Fatigue design of structural automotive components is usually performed without taking into account the forming effects such as the thickness reduction and the residual stresses and strain distribution due to the use of different finite element codes dedicated for only one of the two design phases [5]. Indeed, explicit finite element codes dedicated to non-linear analysis such as PAM-STAMP are used for forming simulations with adaptative mesh and thus large mesh refinement in certain areas which is not suited for fatigue analysis. To integrate forming effects in fatigue analysis, it is necessary to use mapping algorithms to project stress, strain and thickness fields from the final forming mesh to the fatigue one [4]. Different possibilities are available in the literature [4], [5], [7], [129] but a loss of information is often encountered with these algorithms. Nevertheless, using mapping, the influence of the thinning, the plastic strain and the residual stresses can be considered in the fatigue analysis separately or all at once. These three phenomena are mainly influencing the fatigue analysis but not all in the same way [7]. A beneficial effect of plastic strain is often observed [4], [5] whereas thinning and residual stresses can have a detrimental effect [6], [7]. It is thus better to take into account as much as possible the whole modifications of the material behavior due to the forming process during the fatigue analysis .

The aim of this study is to investigate the influence of the forming process on the fatigue life for the cylindrical cups that are representative of deep-drawn automotive parts. In this study, final strain, stress and thickness fields after springback simulation are used as an input of the fatigue one because the same finite element code is used to simulate the whole sequence of simulation (forming, springback and fatigue loading). The number of cycles until crack initiation and its location is predicted using an extension of the fatigue criterion previously calibrated to multi-axial loads. The resolution of the fatigue criterion is performed via a post-processing script which does not require a mesh change.

In this chapter, fatigue analysis of formed parts already studied in the literature are firstly presented. Then, the fatigue loading considered for this study is presented as well as different trials performed beforehand. The numerical procedure is also presented with the adaptation of the fatigue criterion to multi-axial loads and the fatigue loading simulation. Finally, results of the fatigue analysis are presented in two cases, the fully drawn C1 and RC2 cups.

5.1 Fatigue analysis considering forming effects

As mentioned in the introduction, three linked phenomena occur during the forming process that are known to influence the fatigue behavior of structural parts [7]:

- the increase of yield stress with plastic strain
- a non-homogeneous thinning
- a residual stress distribution

Firstly, the influence of plastic strain coming from forming is the most studied effect because it is possible to perform uniaxial fatigue tests with pre-strained specimens. Several studies related to the pre-straining effect on the uniaxial fatigue behavior of steel sheet have been carried out for pre-strain in uniaxial tension [28], [44], [130]–[133]. However, the strain range in uniaxial tension is limited by necking, most of the studies are performed with pre-strain values between 5 and 25 % and for certain material 30 % is reached. Some studies proposed alternative pre-strain paths such as equibiaxial tension [131], [132], simple shear [133] or plane strain tension, already mentioned in section 2.1.3. However, plastic strain levels higher than 30% have not been investigated yet.

Different pre-straining effects are observed as function of the amount of pre-strain and of the pre-strain path. Indeed, for low pre-strain values, between 2 and 5 % of plastic strain, an increase of fatigue strength is observed due to hardening for uniaxial fatigue tests performed with a load ratio equal to 0 [44] whereas less influence of the pre-strain is observed when the ratio is equal to -1 [131]. With uniaxial tensile pre-strain, the positive effect of hardening on fatigue strength is observed in high cycle fatigue for dual phase steels but in low cycle fatigue, cyclic softening occurs and compensates the hardening induced by the pre-strain [28], [44], [132]. With a strain ratio equal to -1, comparison between pre-strained and as received specimens for low cycle fatigue tests has shown that the dislocation structures are less stable for pre-strained materials and thus cyclic softening is more important than in the as-received case [28], [131]. This phenomenon has been observed for values of pre-strain in uniaxial tension under 15% but above this value, studies have shown an improvement of the fatigue strength that may be caused by more stable dislocation structures [132], [134]. With these large pre-strain values, an induced non-zero mean stress is also observed and its relaxation is dependent of the fatigue life range [132]. Indeed, around 10^4 cycles, the mean stress is progressively relaxed during the fatigue test, whereas closer to the endurance limit, around 10^6 cycles, the mean stress is kept until crack initiation [132].

The influence of pre-straining on the fatigue behavior appears to be directly linked to the microstructure evolution. Indeed, it has been observed that the ferritic phase is more affected by pre-straining than the martensitic one [130]. Comparison between two different microstructures obtained with different heat treatments performed on the same dual phase steel, with a martensite volume fraction around $35 - 36\%$, has shown that martensite can stop the propagation of micro-cracks appearing in ferrite. The first microstructure is composed of isolated martensite grains dispersed in ferrite and the second one of martensite continuously surrounding ferrite grains and thus in the second case, an improvement of the fatigue life is observed [45]. Considering pre-strain of these two microstructures, micro-crack initiation is limited by pre-straining of the ferritic phase because the cracks are concentrated in the created deformation band. However, the propagation rate of micro-cracks appears to be accelerated by pre-straining. These two observations may explain why an enhancement of the fatigue life with pre-straining is observed in the high cycle range whereas it is not the case in the low cycle fatigue range, where more micro-cracks are observed. As for the as-received material, the comparison of the two microstructures in the pre-strained case shows that the martensite surrounding the ferrite improved fatigue properties for both high and low cycle range [45]. The microstructure of the dual phase steel considered in this study, cf. Figure 1.10, has a martensite distribution which is situated between the two cases presented in the litterature [45], but with a lower volume fraction of martensite ($14\% \pm 4\%$).

The influence of plastic strain is linked to the two other phenomena, less studied because they are more difficult to reproduce in the uniaxial case. Some studies have delt with the influence of the non-homogeneous thinning and the residual stress distribution as well by considering formed parts. Few examples of studies on demonstrators like the cylindrical cup are available [132], [135] but there are more examples of industrial parts like wheels [136]–[138], steering kuckles [4], bellows [5], suspension arms [6], [129], valves [139], or engine brackets [7]. Some of theses studies using mapping algorithms have thus investigated thinning, plastic strain and residual stress effects separately and provide a better understanding of the influence of the three main phenomena [4]–[7]. Mainly high cycle fatigue is considered and thus a beneficial effect of plastic strain is observed as for uniaxial tests [6]. A detrimental effect of thinning is observed but it is less important than the positive effect of plastic strain [6] and thus, if both thinning and plastic strain are considered an improvement of fatigue life is still observed [4], [5]. However, the detrimental effect of tensile residual stresses is reported to be more important than the thinning one and thus a decrease of the fatigue life is observed when the three phenomena are considered simultaneously [6], [129]. It is the behavior usually observed in the literature but the balance between the three phenomena is dependent of a lot of parameters including the material itself and the part geometry. In particular, an excessive thinning can be the most detrimental effect in some case [7]. As a consequence of these three linked phenomena, the location of the critical fatigue area of the part can depend on the residual stress distributions [6], [129] and on the variation of thickness [7]. Most of these studies are predicting fatigue life with a local extrapolation of S-N curve as a function of the effective plastic strain [4], [5], [7]. However, a more recent study shown that the use of E-N curve, as in the MCB and modified Morrow criterion, extrapolated with pre-strain effect gives a good prediction of lifespan in both high and low cycle range contrary to S-N curve extrapolation which is rather suitable for high cycle range only [137]. In this study, the E-N curve is used and modified to take into account the forming effects by the addition of the mean stress influence, linked to the plastic strain influence, in MCB criterion with the modified Morrow criterion, cf. section 2.1.3. Before the presentation of the fatigue life prediction method using this criterion, the research of a fatigue loading adapted for cylindrical cups is presented.

5.2 Fatigue loading

Considering a demonstrator raises a difficulty to define a fatigue loading due to the absence of an industrial problematic. Though, a review of fatigue tests performed on formed parts or demonstrators with similar geometries is performed. The circular geometry of the cup may be adapted to the Brazilian tensile strength test used to characterize concrete behavior [140]. This test consists in applying a cyclic compression on a concrete disc placed between two platens or curved jaws, as represented in Figure 5.1. It should be emphasized that such a test requires to cut the cup and kept only the wall. Indeed, considering only the wall, it is possible to perform a ring compression test [141] similar to the brazilian test but for a hollow specimen.

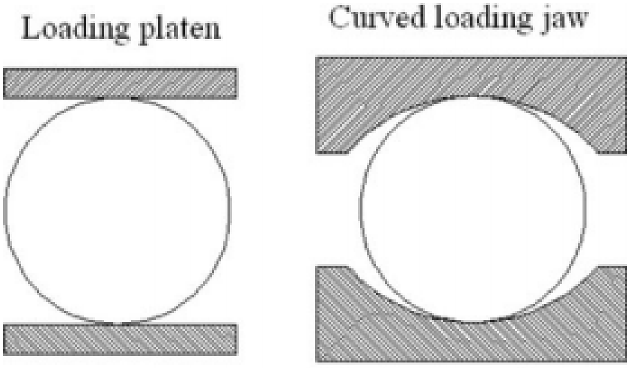

Figure 5.1 – Illustration of the Brazilian test on a disc with compressive platens or curved jaws [142]

However, the cutting of the cup, leading to the addition of another step in the numerical chain of simulations, is not considered in this study. Thus, different loadings adapted from a previous study about fatigue of cylindrical cups [135] are investigated on a completely drawn cup. An attachment is modeled at the cup floor and the displacement is applied on two areas of the cup wall facing each other but not on the entire circular edge, cf. Figure 5.2(a). In that case, the crack initiation is always predicted just next to the boundary conditions. The same loading is also tried on a partially drawn cup, cf. Figure 5.2(b) and gives crack initiation far from the boundary conditions but this approach is discarded as it cannot be applied to RC2 cups. Then, an opposite strategy is investigated consisting to fix the cup flange and to apply an alternated displacement on the cup floor. The load is first applied in the center of the cup, cf. Figure 5.2(c) but this configuration does not create significant strain amplitude in the wall where an influence of the strain path changes is observed for RC2. Thus, it is tried to apply the displacement on a circle in the cup floor close to the radius, cf. Figure 5.2(d) but similarly to the precedent case, it is not enough to create significant strain amplitude in the wall. Finally, an horizontal displacement is applied on the cup floor center, cf. Figure 5.2(e) and not a vertical one like the precedent cases and the fixation of the cup flange is conserved. This loading is inspired from fatigue tests performed on a wheel in the literature [137] and illustrated in Figure 5.3(a).

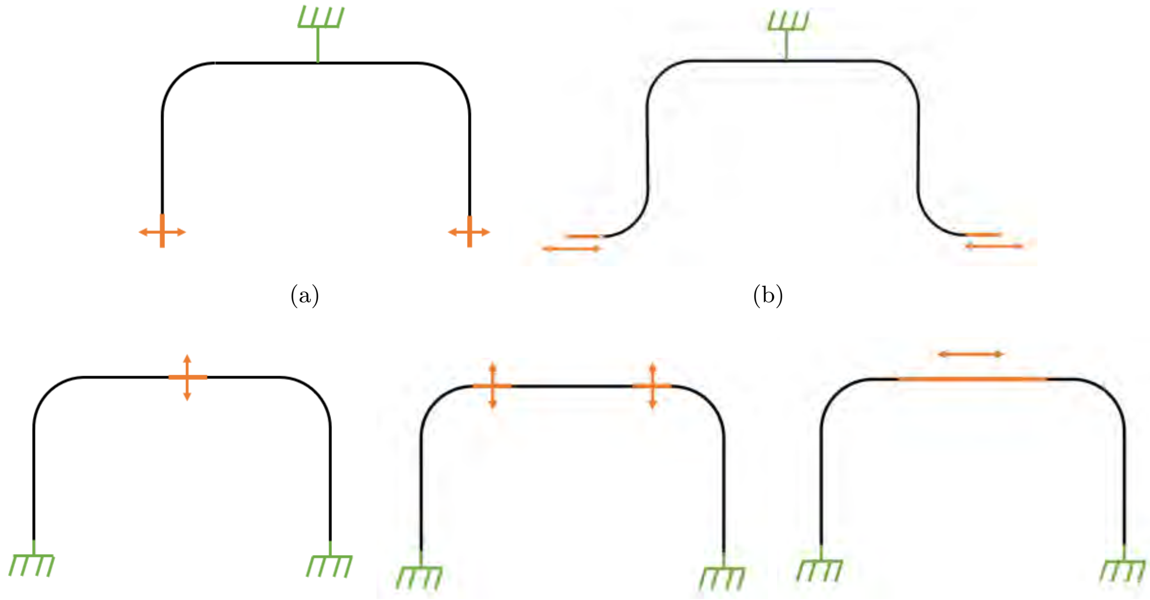

(a) (b)

(c) (d) (e)

Figure 5.2 – Representation of the different fatigue loadings investigated

The mechanical design of an experimental device has been performed in order to apply this fatigue loading on cylindrical cups detailed in Figure 5.3(b). To ensure a fatigue loading of the cup wall, counter-forms including the cup radius are used to apply the alternated displacement. To fix the cup on the side of the flange, a base with the same diameter than the cup and a height of 5 mm is used. In addition a compressive force is applied on the cup to maintain the contact of the cup flange with the base during the fatigue loading. Details about the design of the experimental device are given in Appendix E. However, due to difficulties with the application of the compressive force, the tests could not be carried out during the time allocated for this study. Thus, only numerical analysis of this fatigue loading are presented thereafter. The method used to predict the service life of the cup under this fatigue loading is then presented.

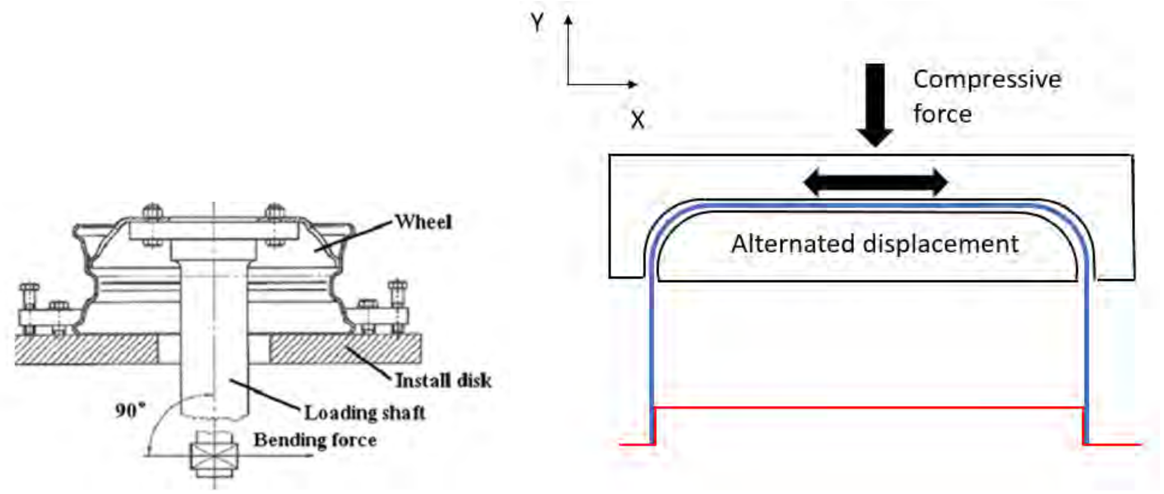

(a) Illustration of the fatigue loading applied on a wheel [137]

(b) Adaptation of this fatigue loading to the cup

Figure 5.3 – Representation of the considered fatigue loading on one cup compared to the literature example [137]

5.3 Fatigue life prediction method

5.3.1 Extension of the uniaxial criteria to multiaxial loads

The modified Morrow criterion previously defined and calibrated, cf. sections 2.1.3 and 2.2.5 respectively, is used to predict the fatigue life of cylindrical cups. In order to use this uniaxial criteria to predict the fatigue life of a part under multi-axial loads, one of the possibility is to define an equivalent strain amplitude $\frac{\Delta\varepsilon_{eq}}{2}$ and an equivalent mean stress σ_m^{eq} and use them directly in the uniaxial criterion [87]. It is possible to rewrite the criterion as follows :

$$\frac{\Delta\varepsilon_{eq}}{2} = \frac{\sigma_f^{'} - < \sigma_m^{eq} >}{E}(2N_f)^b + \varepsilon_f^{'}(2N_f)^c \tag{5.1}$$

A von Mises formulation is used to define the equivalent strain amplitude [143],

$$\Delta\varepsilon_{eq} = \Delta\varepsilon^{e}_{eq} + \Delta\varepsilon^{p}_{eq} = \sqrt{\frac{\boldsymbol{\Delta\varepsilon^{e}} : \boldsymbol{\Delta\varepsilon^{e}}}{1+2\nu^{2}}} + \sqrt{\frac{2}{3}\boldsymbol{\Delta\varepsilon^{p}} : \boldsymbol{\Delta\varepsilon^{p}}} \tag{5.2}$$

which takes into account all the components of the strain tensor via the amplitudes of the plastic and elastic strain tensors, respectively $\boldsymbol{\Delta\varepsilon^{p}}$ and $\boldsymbol{\Delta\varepsilon^{e}}$. For the equivalent mean stress, it is also possible to consider von Mises definition [143]. However, an asymmetric effect of the mean stress is observed in the literature and the use of the first invariant is proposed instead [87] :

$$\sigma_{m}^{eq1} = \mathrm{tr}(\boldsymbol{\sigma_{m}}) \tag{5.3}$$

The Macaulay brackets <> in Eq. 5.1 indicates that the equivalent mean stress σ_{m}^{eq} is considered only if it is positive. Out of comparison's sake, a second definition of the equivalent mean stress is proposed in this study which is a combination of both first and second invariants to take into account the sign of the mean stress and also the shear components of the stress tensor:

$$\sigma_{m}^{eq2} = \mathrm{sign}(\mathrm{tr}(\boldsymbol{\sigma_{m}}))\sqrt{\frac{3}{2}\boldsymbol{s_{m}} : \boldsymbol{s_{m}}} \text{ with } \boldsymbol{s_{m}} = \boldsymbol{\sigma_{m}} - \frac{1}{3}\mathrm{tr}(\boldsymbol{\sigma_{m}})\boldsymbol{I_{3}} \tag{5.4}$$

To calculate these equivalents and thus determine the lifespan of a part, it is necessary to simulate at least one cycle of the fatigue loading. The constitutive models used in this study to simulate the forming processes are not taking into account the cyclic behavior of the material. Indeed, the alternated tension-compression tests performed to calibrate the fatigue criterion show a cyclic softening of the material. However, with both isotropic hardening and HAH model, the simulation of several cycles would lead to a cyclic hardening of the material. Moreover, in the case of HAH model, the springback simulation have to be simulated with an elastic law, cf. section 4.2.3, and it is not then possible to use again the e-HAH model. Subsequently to the forming simulations performed with HSV or e-HAH, the springback and fatigue loading simulations are thus performed with an elastic law for both models to compare fatigue predictions obtained in the same conditions. In order to minimize the impact of this limitation, the values of the alternated displacement are adapted to obtain equivalent strain amplitudes close to 0.002, which corresponds to the lowest value tested during uniaxial experiments. Comparisons between elastic and elasto-plastic simulations of the fatigue loading with HSV are performed and presented thereafter with the results of each cup.

5.3.2 Numerical procedure

The simulation of the fatigue loading is performed with Abaqus Implicit using the springback final state as an input. The fatigue loading consists in an alternated displacement applied along X axis which is the axis of symmetry of the half cup model. The displacement is applied via a master node tie to a set of nodes corresponding to the floor and the radius of the cup, cf. Figure 5.4(a). The contact of the cup with the base is modeled with a fixation of all the degree of freedom of the flange nodes and some of the wall over a height of 5 mm corresponding to the one of the base, cf. Figure 5.4(b). Different displacement values are applied as a function of the considered cup in order to obtain equivalent strain amplitudes of the same order, i.e. ±0.02 mm and ±0.06 mm are used in C1 and RC2 simulations respectively. The simulation is composed of four steps with a duration of 1 s:

1) Application of the compressive force
2) Displacement of 0.02 mm or 0.06 mm applied along X axis for C1 and RC2 respectively
3) Displacement of -0.04 mm or -0.12 mm applied along X axis for C1 and RC2 respectively
4) Displacement of 0.04 mm or 0.12 mm applied along X axis for C1 and RC2 respectively

The displacements applied and the reaction forces obtained at the nodes where the displacements are applied in both C1 and RC2 cases are represented in function of the time in Figure 5.5 for the steps 2, 3 and 4. A larger displacement value is applied for RC2 but it leads to a lower reaction force which is equal to ±17 kN whereas ±16.5 kN is obtained for C1, certainly because it is more compact and thus more rigid than RC2.

The fatigue simulations are performed subsequently to HSV and e-HAH forming and springback simulations in C1 case. However, due to convergence issues for the half cup simulation with e-HAH model in RC2 case, only the cases of HSV and o-HAH are compared. After the simulation of one cycle of the fatigue loading, the logarithmic strain and stress components are extracted at each integration point at the end of the steps 3 and 4, to calculate the equivalent strain amplitude and the equivalent mean stresses. Considering the equivalent values, three different criteria are solved using a Newton-Raphson algorithm to obtain the number of cycles until crack initiation N_f. The first one,equivalent to MCB, is not taking into account the mean stress and the two others corresponds to the modified Morrow criterion with consideration of σ_m^{eq1} or σ_m^{eq2} (called thereafter MM1 and MM2). In all cases, the negative values of the means stress are not considered and, in that case, the modified Morrow criterion reduces to MCB criterion. A python script is used in post-processing to calculate the different equivalents and the numbers of cycle until crack initiation N_f of the three criteria for each integration point and then plot isovalues of these different quantities.

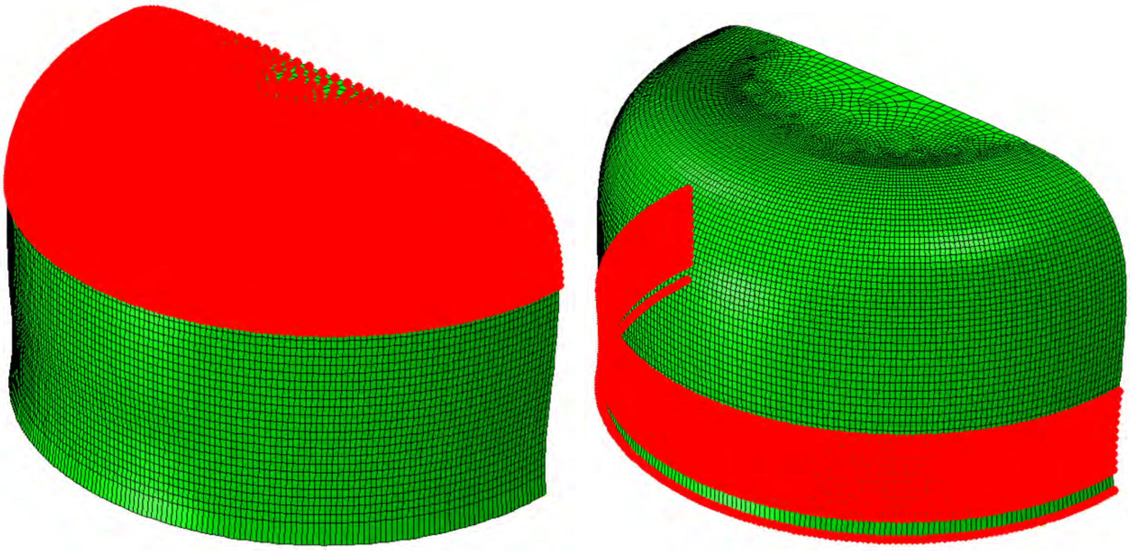

(a) Full C1 - Floor + Radius (b) Full C1 - Flange + Wall

Figure 5.4 – Illustration of the node sets used in the fatigue simulation

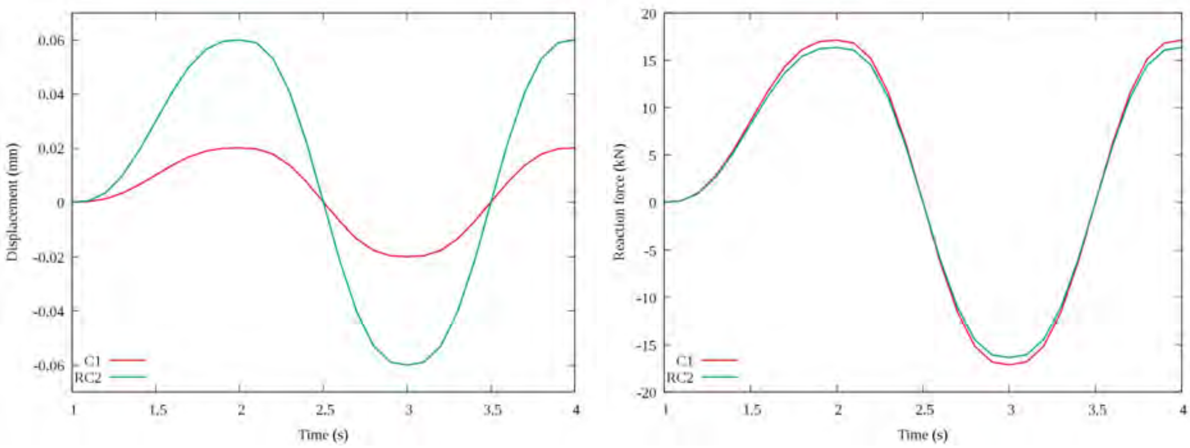

(a) Displacement (b) Reaction force

Figure 5.5 – Representation of the alternated displacement and the reaction forces, obtained at the nodes where the displacement is applied, as a function of time during the steps 2, 3, and 4 of C1 and RC2 fatigue loading simulations

5.4 Results

The equivalent strain amplitudes, both equivalent mean stresses, and the number of cycles until crack initiation are discussed for both C1 and RC2 case in the following section.

5.4.1 C1 cup

For fully drawn C1 cups, the application of an alternated displacement of ± 0.02 mm on the cup floor and radius combined with a compressive force of 2 kN leads to the isovalues of equivalent strain amplitude presented in Figure 5.6. Only the inner and outer surfaces are presented because they are the most relevant of the nine sections points considered through thickness for this cup. The same results with minor variations are obtained when the fatigue loading simulation is performed subsequently to e-HAH forming simulation. The maximum values of equivalent strain amplitude are equal to 0.22 and 0.214 for the inner and outer surfaces respectively but they are not located in the same place of the cup. Indeed, the maximum value of the equivalent strain amplitude is obtained in the center of the cup wall for the element E1 on the inner surface whereas it is closer of the cup radius on the outer surface and is obtained for E2 or E3, which are side by side, depending on the model, HSV or e-HAH respectively, used for the previous forming simulation.

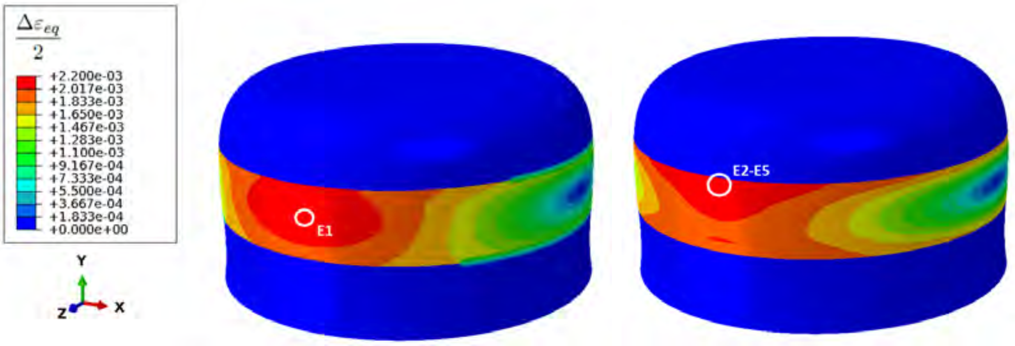

(a) Inner surface (b) Outer surface

Figure 5.6 – Isovalues of the equivalent strain amplitude for the inner and outer surfaces of C1 cup

The maximum value of the equivalent strain amplitude for the whole cup indicates the location of crack initiation in the case of MCB criterion, i.e. when the residual stresses are not considered via the equivalent mean stress in the fatigue criterion. In that case, the location of crack initiation is obtained for the element E1 on the inner surface with a number of cycles until crack initiation equal to 36200. The isovalues of the number of cycles until crack initiation N_f are represented in Figure 5.7 on the inner and outer surfaces for MCB criterion and for both versions of the modified Morrow criterion on the outer surface. The N_f isovalues of both modified Morrow criteria are not presented on the inner surface because the equivalent mean stresses do not influence the number of cycles until crack initiation on this surface. As for the equivalent strain amplitude, the use of HSV or e-HAH model for the forming simulation slightly influence the distribution of N_f, thus only the isovalues obtained after HSV forming simulation are presented in Figure 5.7.

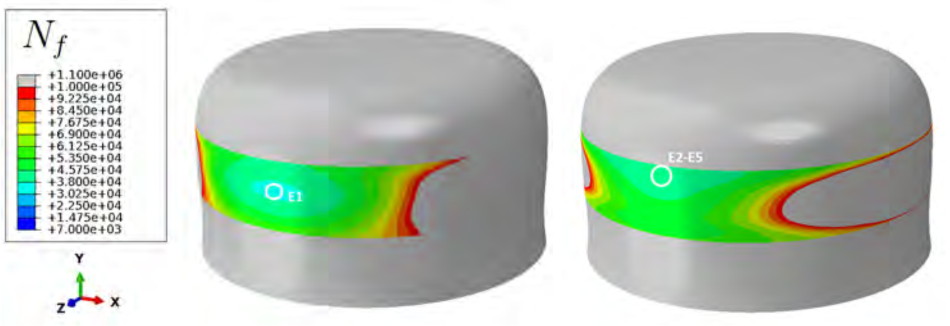

(a) MCB - Inner surface (b) MCB - Outer surface

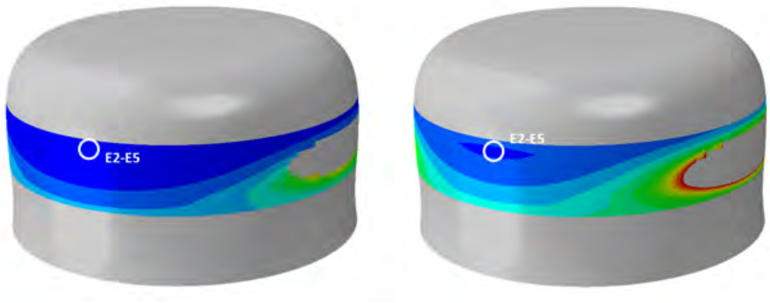

(c) MM1 - Outer surface (d) MM2 - Outer surface

Figure 5.7 – Isovalues of the number of cycles until failure N_f on the inner and outer surfaces of C1 cup for the three criteria

In the case of MCB criterion, N_f values close to the minimum one, obtained on the inner surface, are observed on the outer surface near the cup radius for several elements including E2 and E3 with 38900 and 40200 cycles until the crack initiation respectively. The group of elements, E2-E5 surrounded in Figure 5.7, including E2 and E3 but also E4 and E5 mentioned thereafter, is interesting because an influence of the equivalent mean stress is observed at this location. Indeed, considering MM1 or MM2 criteria, the location of crack initiation is changed by taking into account the mean stress and is obtained for elements in this area, not E2 and E3 but close elements, E4 and E5, depending on the model considered for the previous forming simulation. In the case of MM1 criterion, the number of cycles until crack initiation is reduced to 7500 and 7400 for E4 and E5 respectively, whereas a smaller decrease in lifespan is observed in MM2 case with 14300 for both E4 and E3. The MM1 and MM2 criteria are represented in comparison with MCB for E2 and E4 in HSV case and for E3 and E5 in e-HAH one in Figures 5.8(a) and 5.8(b).

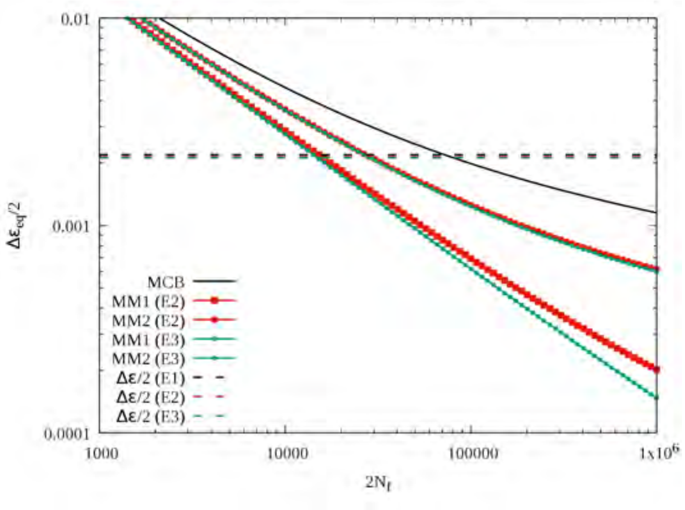

(a) HSV

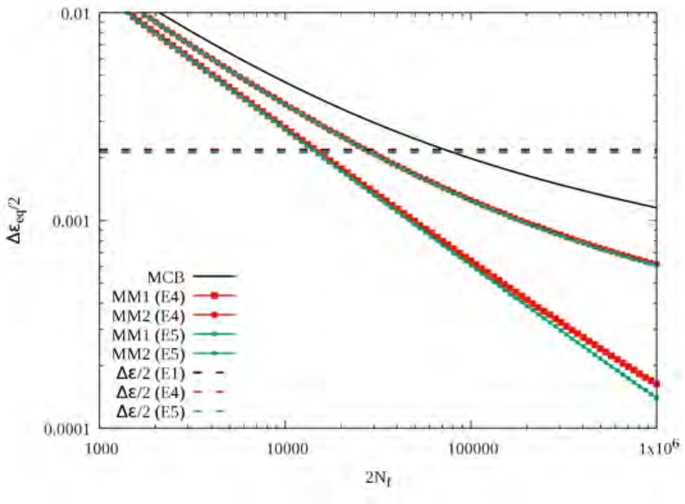

(b) e-HAH

Figure 5.8 – Comparison of the criteria for the different elements of C1 cup and both HSV and e-HAH models

The details of the equivalent strain amplitudes, the equivalent mean stresses and the numbers of cycles until crack initiation obtained for the five elements E1 to E5 are also summarized in Tables 5.1 and 5.2. Results obtained with both elastic and elasto-plastic simulations of the fatigue loading in HSV case are also presented in the table, some variations of hundreds of cycles are observed for MM1 and MM2 criteria but overall the fatigue behavior is similar.

Table 5.1 – Comparison of the service life obtained on the inner surface with the different criteria and both HSV and e-HAH models for the element E1 located on C1 cup in Figure 5.7 (* Negative mean stresses are fixed equal to 0, E-P and E are corresponding to elasto-plastic or elastic simulations of the fatigue loading)

Element	1		
Model	HSV		e-HAH
	E-P	E	E
$\frac{\Delta\varepsilon_{eq}}{2}$	2.19 10^{-3}	2.19 10^{-3}	2.19 10^{-3}
σ_m^{eq1} (MPa)	0*	0*	0*
σ_m^{eq2} (MPa)	0*	0*	0*
N_f (MCB)	36200	36200	36200
N_f (MM1)	36200	36200	36200
N_f (MM2)	36200	36200	36200

Table 5.2 – Comparison of the service life obtained on the outer surface with the different criteria and both HSV and e-HAH models for the elements E2, E3, E4 and E5 located on C1 cup in Figure 5.7 (E-P and E are corresponding to elasto-plastic or elastic simulations of the fatigue loading)

Element	2		3	4		5
Model	HSV		e-HAH	HSV		e-HAH
	E-P	E	E	E-P	E	E
$\frac{\Delta\varepsilon_{eq}}{2}$	2.14 10^{-3}	2.14 10^{-3}	2.14 10^{-3}	2.12 10^{-3}	2.12 10^{-3}	2.12 10^{-3}
σ_m^{eq1} (MPa)	1150	1230	1270	1240	1290	1300
σ_m^{eq2} (MPa)	630	690	690	680	710	700
N_f (MCB)	38900	38900	38900	40200	40200	40200
N_f (MM1)	8500	7800	7500	7900	7500	7400
N_f (MM2)	15500	14300	14300	14800	14300	14400

It can also be noticed that the crack initiation location is obtained for different elements depending on the equivalent mean stress definition in the case of e-HAH forming simulation but not for HSV. However, the different elements involved for both MM1 and MM2 criterion are all in the same area of the outer surface. With the same definition of the equivalent mean stress, the variations between HSV and e-HAH are about hundred cycles and are minor compared to the variations between MM1 and MM2 with double number of cycles in MM2 case. These differences come directly from the equivalent mean stress values which are presented on the inner and outer surfaces of the cup in Figures 5.9 and 5.10 for σ_m^{eq1} and σ_m^{eq2} respectively. This difference of mean stress sign, between the inner and outer surfaces, leads to a change of crack initiation location from the inner to the outer surface when the influence of the mean stress is taken into account in the criterion. Then, for MM1 and MM2, the crack initiation is located at the place where the equivalent mean stress is maximum for both definitions and both models. However, maximum values are considerably different depending on the definition, σ_m^{eq1} reaches 1300 MPa for both HSV and e-HAH models whereas σ_m^{eq2} is equal at the most to 770 MPa and 700 MPa for HSV and e-HAH models respectively.

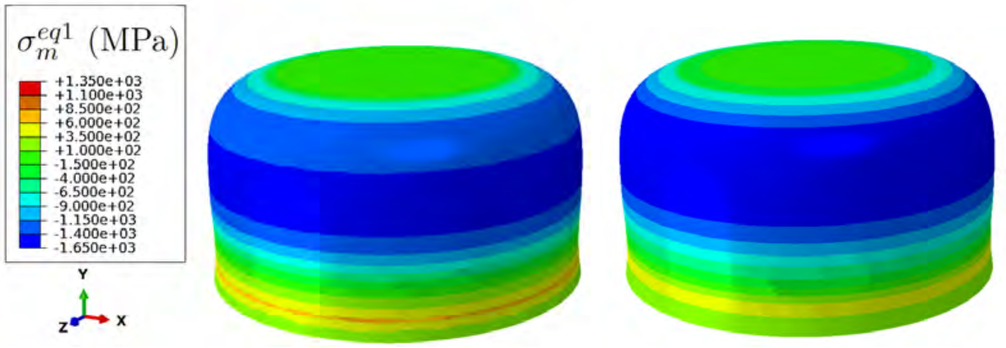

(a) HSV - Inner surface (b) e-HAH - Inner surface

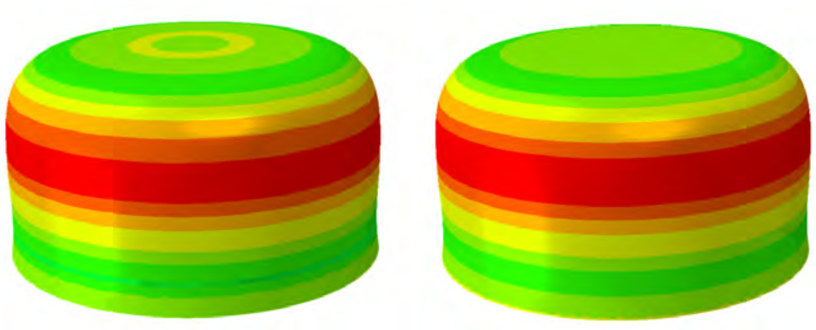

(c) HSV - Outer surface (d) e-HAH - Outer surface

Figure 5.9 – Isovalues of the first equivalent mean stress $\sigma_m^{eq1} = \mathrm{tr}(\boldsymbol{\sigma_m})$ for the inner and outer surfaces and both HSV and e-HAH models

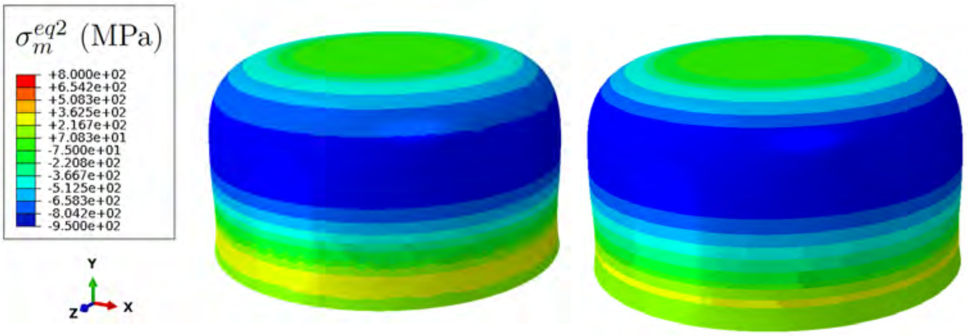

(a) HSV - Inner surface (b) e-HAH - Inner surface

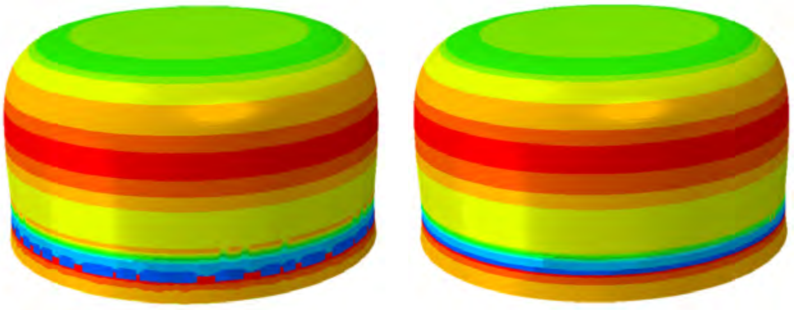

(c) HSV - Outer surface (d) e-HAH - Outer surface

Figure 5.10 – Isovalues of the second equivalent mean stress $\sigma_m^{eq2} = \mathrm{sign}(\mathrm{tr}(\boldsymbol{\sigma_m}))\sqrt{\frac{3}{2}\boldsymbol{s_m} : \boldsymbol{s_m}}$ for the inner and outer surfaces and both HSV and e-HAH models

In fact, the simplified method used in this study tends to overestimate the residual stresses because the relaxation of the mean stress observed in some cases after few loading cycles and the cyclic softening of the material are not modeled. Indeed, some studies about fatigue simulation of formed proposed to arbitrarily divide by two the mean stress in order to model the relaxation [5], [129]. Moreover, the modified Morrow criterion is validated for mean stress values equal to no more than half the yield stress [87], corresponding to 200 MPa approximately for the considered DP600. Thus, the use of σ_m^{eq2} is more suitable than σ_m^{eq1} and only the second definition of the equivalent mean stress is used for RC2 case. However, some improvements on the equivalent mean stress definition may be performed in the future with the help of experimental fatigue tests.

5.4.2 RC2 cup

The fatigue loading applied on RC2 cup leads to similar values of the equivalent strain amplitude as C1 cup according to Figure 5.11. The maximum values are obtained on the inner surface of the cup and are equal to 0.219% for elements E1 and E2 in the center of the cup wall depending on HSV or o-HAH model considered for the forming simulation respectively. The isovalues are similar for both models and thus only those obtained with HSV are presented. Considering the outer surface, for both HSV and o-HAH models, the maximum values are obtained for the element E2 and are equal to 0.215% and 0.217% respectively. Two other elements E3 and E4 are considered because they became the location of crack initiation when the equivalent mean stress is considered via MM2 criterion.

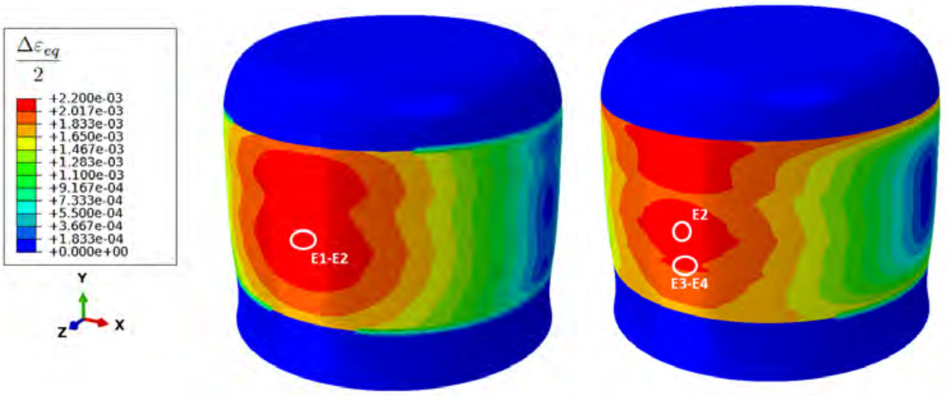

(a) Inner surface (b) Outer surface

Figure 5.11 – Isovalues of the equivalent strain amplitude on the inner and outer surfaces of RC2 cup for HSV model

As for C1 cup, the crack initiation is initially located on the inner surface with MCB criterion and taking into account the equivalent mean stress changes its location to the outer surface. Indeed, the isovalues of the number of cycles until crack initiation are represented for both MCB and MM2 criteria in Figure 5.12. The isovalues obtained with MCB criterion considering HSV forming simulation are firstly presented for the inner and outer surfaces with minimum values obtained for E1 and E2, which are equal to 36300 and 38500 respectively. The isovalues obtained after o-HAH forming simulation are not presented for this criterion because they are similar to those obtained with HSV. Differences appear between the model predictions when the equivalent mean stress is taken into account (MM2). Indeed, for HSV, two areas with minimum values of N_f are observed, the same as MCB criterion and another one, close to the cup radius, where the element E5 is surrounded. Contrary to HSV, the isovalues obtained with o-HAH shows only one area with minimum values of N_f which is the same as MCB criterion. However, for both models the crack initiation is located in the same place for elements E3 and E4 with numbers of cycles equal to 14400 and 14500 respectively.

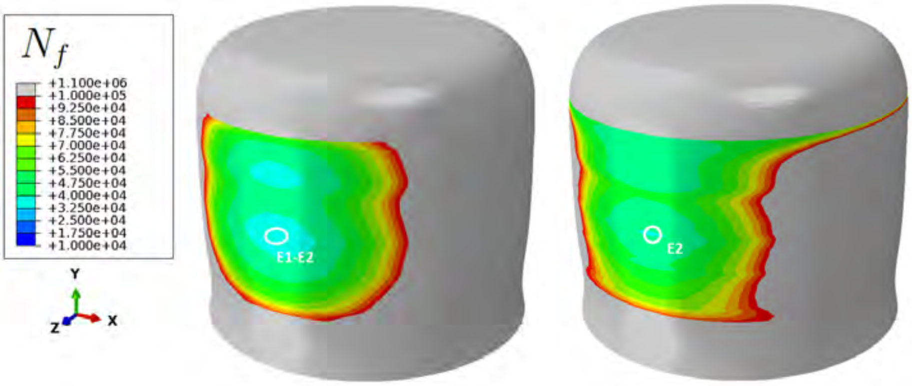

(a) MCB - Inner surface - HSV (b) MCB - Outer surface - HSV

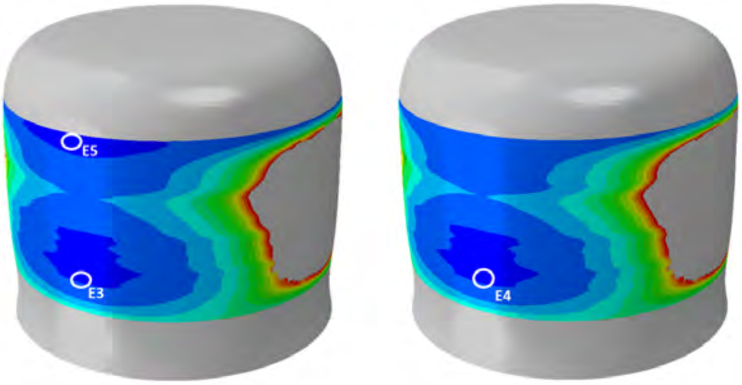

(c) MM2 - Outer surface - HSV (d) MM2 - Outer surface - o-HAH

Figure 5.12 – Isovalues of the number of cycles until failure N_f obtained with MCB and MM2 criteria on the inner and outer surfaces of RC2 cup and both HSV and o-HAH models

The MCB and MM2 criteria are represented for the elements corresponding to each initial state in Figure 5.13. For the elements leading to the crack initiation, the two models predict similar results but there are still differences in other locations. The details of the equivalent strain amplitudes, the equivalent mean stresses and the numbers of cycles until crack initiation obtained for the four elements E1 to E4 are also summarized in Tables 5.3 and 5.4. Results obtained with both elastic and elasto-plastic simulations in HSV case are also presented, some variations of hundreds of cycles are observed for MCB and MM2 criterion but overall the fatigue behavior is similar.

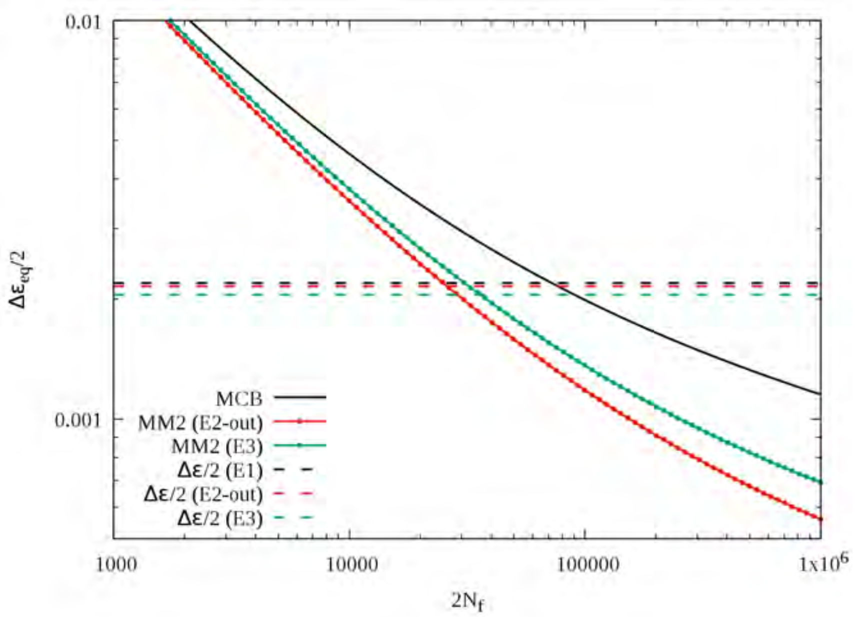

(a) HSV

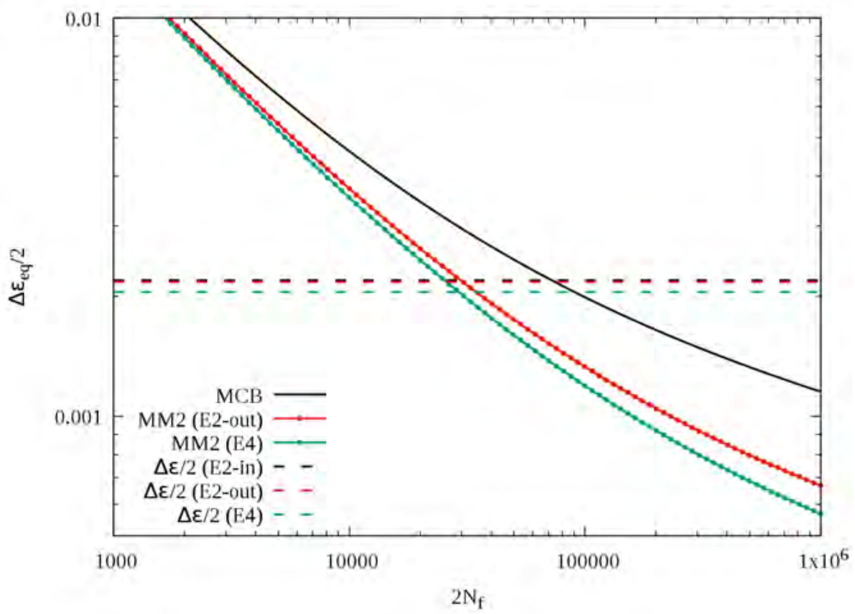

(b) e-HAH

Figure 5.13 – Comparison of the criteria for the different elements of RC2 cup and both HSV and e-HAH models

Table 5.3 – Comparison of the service life obtained on the inner surface with the different criteria and both HSV and o-HAH models for the elements E1 and E2 located on RC2 cup in Figure 5.12 (* Negative values are fixed equal to 0, E-P and E are corresponding to elasto-plastic or elastic simulations of the fatigue loading)

Element	1		2
Model	HSV		o-HAH
	E-P	E	E
$\frac{\Delta\varepsilon_{eq}}{2}$	$2.19\ 10^{-3}$	$2.19\ 10^{-3}$	$2.19\ 10^{-3}$
σ_m^{eq2} (MPa)	0*	0*	0*
N_f (MCB)	36300	36300	36300
N_f (MM2)	36300	36300	36300

Table 5.4 – Comparison of the service life obtained on the outer surface with the different criteria and both HSV and o-HAH models for the elements E2, E3 and E4 located on RC2 cup in Figure 5.12 (E-P and E are corresponding to elasto-plastic or elastic simulations of the fatigue loading)

Element	2			3		4
Model	HSV		o-HAH	HSV		o-HAH
	E-P	E	E	E-P	E	E
$\frac{\Delta\varepsilon_{eq}}{2}$	$2.15\ 10^{-3}$	$2.15\ 10^{-3}$	$2.17\ 10^{-3}$	$2.06\ 10^{-3}$	$2.05\ 10^{-3}$	$2.05\ 10^{-3}$
σ_m^{eq2} (MPa)	560	590	620	720	760	750
N_f (MCB)	38500	38500	37400	44300	45000	45100
N_f (MM2)	16800	16100	15200	15000	14400	14500

The different values obtained for the element E5 are also presented in the Table 5.5 because a difference is observed between the two models for this element and those nearby. Indeed, a reduction of the equivalent mean stress about 100 MPa is observed between the one predicted considering HSV forming simulation equal to 650 MPa and and the one predicted considering o-HAH. This area of the cup, corresponding to a coordinate along Y axis equal to 7 mm, exhibits strain path changes including reverse ones, cf. Figures 4.20. A reduction of the residual stress component σ_{11} is observed in Figure 4.34 for this coordinate along Y axis by considering strain path change effect whereas few influence of the material model is observed for the coordinates corresponding to the other elements, 17 mm for E1 and E2 and 21 mm for E3 and E4. The evolution of the strain path change indicator $\cos\chi$ and the respective evolutions of the von Mises equivalent stress are compared during RC2 simulation for the elements E5 and E4 in Figure 5.14. A reverse strain path change is detected by the indicator for the elements E5 at the beginning of the forming stage with the evolution from 1 to -1 whereas only a quasi-ortohogonal strain path change is observed for the element E4 with a minimum value of the indicator equal to 0.5. However, only reverse strain path changes are modeled with o-HAH and thus the von Mises equivalent stress is the same considering HSV or o-HAH for the element E4 whereas a large difference is observed between HSV and o-HAH simulations for the element E5. At the end of RC2 simulation, the gap, between von Mises equivalent stress predicted by both models, is approximately equal to 100 MPa and it is kept during the fatigue loading simulation.

Table 5.5 – Comparison of the service life obtained on the outer surface with the different criteria and both HSV and o-HAH models for the element E5

Element	5	
Model	HSV	o-HAH
$\frac{\Delta\varepsilon_{eq}}{2}$	$2.12\ 10^{-3}$	$2.12\ 10^{-3}$
σ_m^{eq2} (MPa)	650	550
N_f (MCB)	40300	40300
N_f (MM2)	15400	17600

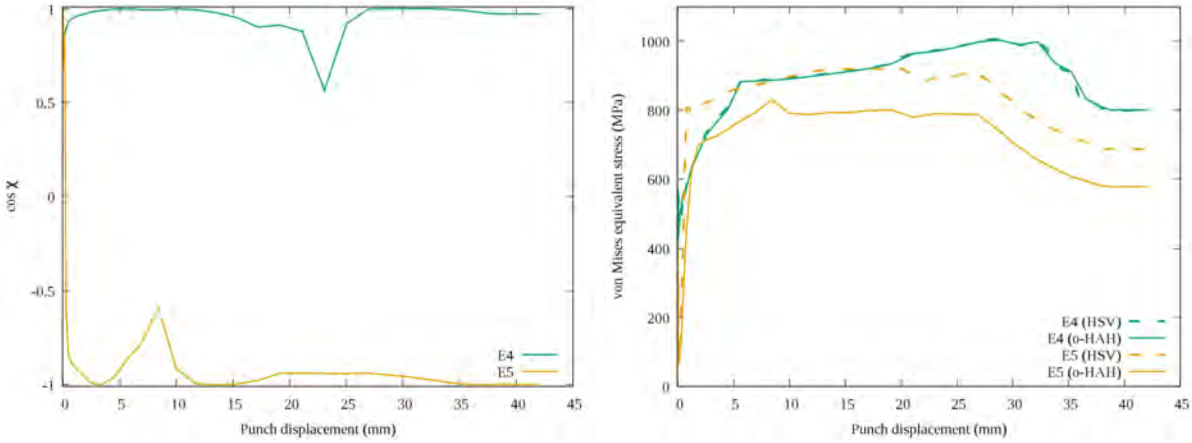

(a) $\cos\chi$

(b) von Mises equivalent stress

Figure 5.14 – Evolutions of the strain path change indicator $\cos\chi$ and the von Mises equivalent stress during RC2 simulation as function of the punch displacement for the elements E4 and E5

This difference is also illustrated on the isovalues of the equivalent mean stress represented for both HSV and o-HAH model on the inner and outer surfaces in Figure 5.15. Thus, considering o-HAH model in the area around E5 reduces the residual stresses and thus increases the number of cycles until crack initiation of approximately 2000 cycles. For the remaining cup wall of the outer surface, the equivalent mean stresses are approximately the same for both models as for the inner surface because reverse strain path changes are not detected in this part of the cup.

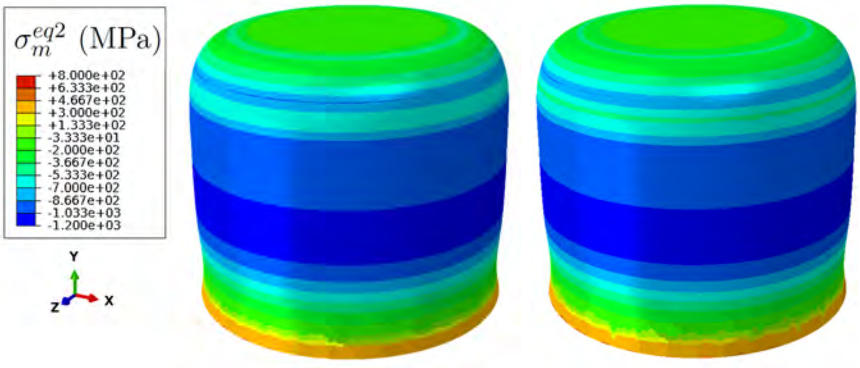

(a) Inner surface - HSV (b) Inner surface - o-HAH

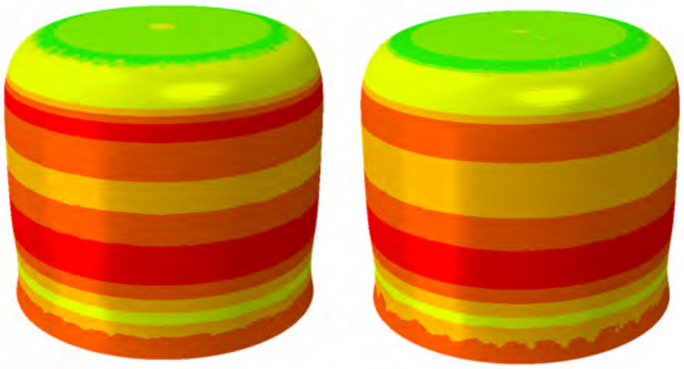

(c) Outer surface - HSV (d) Outer surface - o-HAH

Figure 5.15 – Isovalues of the second equivalent mean stress $\sigma_m^{eq2} = \mathrm{sign}(\mathrm{tr}(\boldsymbol{\sigma_m}))\sqrt{\frac{3}{2}\boldsymbol{s_m} : \boldsymbol{s_m}}$ on the inner and outer surfaces of RC2 cup for both HSV and o-HAH models

To conclude, a better prediction of the residual stress distribution, obtained when the strain path changes are considered in the material constitutive law, is improving the service life prediction. However, the lifespan predicted for RC2 in this study is the same considering HSV or o-HAH previous forming simulations due to an overestimation of the residual stress distribution in the cup wall common to all the material model considered in this study.

5.5 Conclusion

In this chapter, fatigue analysis considering forming effects from the literature are firstly presented and a fatigue loading dedicated to cylindrical cups is then selected. The numerical procedure used to predict the service life of the cups is detailed including the use of equivalents to adapt the modified Morrow criterion to multiaxial loads and the simulation of one cycle of the fatigue loading. Both fully drawn C1 and RC2 cups are considered for the fatigue analysis with respective loadings that lead to similar lifespan range. During C1 analysis, two definitions of the equivalent mean stress are considered but due to the overestimating trend of the method used in this study, the second definition $\sigma_m^{eq2} = \mathrm{sign}(tr(\boldsymbol{\sigma_m}))\sqrt{\frac{3}{2}\boldsymbol{s_m} : \boldsymbol{s_m}}$ is preferred because it leads the lowest mean stress values. However, this definition may be improved with experimental results in the future because it appears to influence a lot the results, which makes it difficult to analyze the influence of the constitutive law. With this second definition, the same behavior is obtained for both C1 and RC2 cups which consists in a change of the location of crack initiation when the equivalent mean stress is considered and a reduction of about half the lifespan. The same results are obtained with HSV and e-HAH or o-HAH depending on the cups in the critical area but in RC2 case, the modeling of the strain path change behavior leads to an improvement of the lifespan in the area close to the cup radius.

CONCLUSIONS AND PERSPECTIVES

The study presented in this manuscript deals with the influence of strain path changes, occurring during sheet metal forming process of sheet metals on the service life prediction. The considered material is a dual phase steel DP600 of thickness 1.2 mm. For the forming process, deep drawing of cylindrical cups is used as a demonstrator, able to reproduce complex phenomena that occurs during the forming process of industrial parts, including large strains and strain path changes. For the service life prediction, due to the absence of an industrial application, a specific fatigue loading is proposed for the cylindrical cups.

Conclusions

In the first chapter, the behaviors exhibited by metallic materials and in particular dual phase steels regarding strain path changes and cyclic strain paths are presented though a bibliographic review. The DP600 behavior is then characterized for different linear, non-linear and cyclic strain paths. Firstly, a wide range of linear strain path experiments are performed with uniaxial tensile tests for different orientations between the rolling and the transverse direction, simple shear tests along the rolling direction, bulge tests and in-plane biaxial tests. A consistent behavior of the material is observed for the different strain paths with a small anisotropy regarding stress levels but slightly more pronounced regarding strains. Non-linear strain paths are also considered to characterize the material behavior under reverse and orthogonal strain path change with respectively forward-reverse shear tests and simple shear tests after a pre-strain in tension performed along the rolling direction. After reverse strain path changes, the material exhibits the Bauschinger effect with a rounded yield point and a work-hardening stagnation, increasing progressively with the amount of forward strain, followed by a resumption of the work-hardening with permanent softening whereas cross-contraction is observed after orthogonal strain path changes with a transient behavior followed by a hardening resumption of the monotonic level. Finally, alternated tension-compression tests are also performed to characterize the low cycle fatigue behavior of the material. Cyclic softening is observed for the first hundred of cycles and then a stabilized behavior is reached and kept until crack initiation. The E-N curve representing the total strain amplitude as a function of the number of reversals until crack initiation, is obtained and is in good agreement with previous other dual phase steels from the literature.

In the second chapter, the characterization tests, presented in the first one, are used to calibrate the hardening and fatigue models. A distortional hardening is considered with e-HAH model coupled to an isotropic hardening law and the anisotropic yield criterion Yld2000-2d. A decrease of the Yld2000-2d criterion exponent, from 6 recommended for bcc materials to 3.6, is used to model accurately the different linear strain path and particularly simple shear which is used to characterize also strain path change. This value gives a consistent prediction of the wide range of strain paths and is used for the calibration of e-HAH model performed in two cases, with and without considering one tension-compression test from fatigue characterization tests. Orthogonal and reverse parameters of e-HAH model are identified separately beginning with the orthogonal ones not influenced by the addition of tension-compression. Difficulties are encountered to identify the parameter k that controls the microstructure deviator evolution due to an hardening stagnation predicted by the model but not observed experimentally. A good description of the orthogonal tests is finally obtained by using a high value of k to suppress the hardening stagnation.

For reverse parameters, the addition of the tension-compression test in the database influences significantly the identified values identified because the strain level before reversal is largely lower than the one of the forward-reverse shear tests. The model gives a good prediction of both reverse tests when the tension-compression test is considered and this identification is then used for the forming simulations. Different fatigue criteria are also presented and the modified Morrow criterion is selected for this study as it takes into account the mean stress effect, which can be related to the residual stresses from the forming process. The calibration of this criterion, possible with only the alternated tests, is performed and a good prediction of the different low cycle fatigue tests is obtained and also a good agreement with the literature.

In the third chapter, the deep-drawing processes of cylindrical cups in one and two stages are presented with a specific device design for this study in the last case. The in-plane major and minor strain fields and the residual stress fields are measured by DIC and X-ray diffraction respectively. Local evolution of the strains and stresses along the rolling and transverse directions is compared for the different cups. A good repeatability of these measurements, as well as a rather isotropic behavior. Overall, the one-stage process, C1, and the first stage of the redrawing process, RC1 exhibit similar results, the strain values are just slightly lower for RC1 whereas the residual stresses are larger but the distributions are the same. The cups obtained in one stage, C1, and two stages, RC2, have similar geometries except from the height which is larger after two deep drawing stages, but different strains and stresses states are reached. For the redrawing process in two stages, RC2 cup exhibits larger strains than C1 but the residual stresses values are of the same magnitude. However, the distribution of residual stresses are significantly different. The occurrence of strain path changes during the second stage of the forming process is expected from the literature and the finite element simulations and may explain these different residual stress distributions.

In the fourth chapter, e-HAH model and a standard isotropic hardening model are used, coupled to the von Mises criterion considering the small anisotropy, to simulate both forming processes in order to quantify the strain path changes and evaluate their influence. The numerical procedure to perform finite element simulations in Abaqus is firstly presented. Difficulties are encountered to simulate the redrawing process with the user subroutine used for e-HAH model due to the springback of the cup between the two drawing stages and thus some dimensions of the tools are adapted. Due to this difficulty, the final springback of the cup is simulated with an elastic law, which gives the same results than the elasto-plastic law considering the standard model. Firstly, punch force-displacement are used to calibrate simulations to compare the overall influence of the material model. Only a small influence of the material model is observed for both C1 and RC1 and all the models predicts correctly the punch force-displacement curves except for the contact removal with the blank holder. For RC2, slightly more differences between models are observed. The punch force-displacement evolutions are well predicted by all models but the punch force level is always over-estimated. The evolution of the equivalent plastic strain and of the major and minor strains along the rolling direction is in good agreement with the experiments for all models, even in the case of the modified redrawing simulation, which validates the simulations.

The evolution of the strain path change indicator $\cos\chi$ of e-HAH model is also presented to evaluate the occurrence of strain path changes during both processes. Some strain path changes are observed for both C1 and RC1 leading to small differences between numerical predictions of the residual stresses whereas more strain path changes are observed during the second stage of the redrawing process, located in particularly in the cup wall close to the radius corresponding to the previous RC1 cup radius. An influence of the model is then observed for this location on the residual stress distribution along the rolling direction. One of the residual stress component is particularly decreased when the strain path changes are taken into account and is then in good agreement with the measurement. However, residual stresses are overestimated for all models in the other locations of the cup.

Finally, the implementation of e-HAH model in the industrial finite element code, PAM-STAMP developed by ESI Group is validated and the results of the redrawing simulations are compared with the experiments and Abaqus simulations. For the first stage, differences are observed between the two finite element codes due to the blank-holder modeling. Similarly to Abaqus simulations, minor strain path changes are observed with the evolution of $\cos\chi$ leading to the same results regardless of the material model. During the second stage of the redrawing process which is not modified in PAM-STAMP, a stronger evolution of the strain path indicator is observed due to the springback present between the two stages and thus slightly more difference between the models are observed on the predicted punch force-displacements. However, with both finite element codes, the punch force level is overestimated for RC2 suggesting that the numerical model could be further improved.

In the last chapter, fatigue analysis considering forming effects from the literature are presented and numerical difficulties to chain the simulations are highlighted. A simplified methodology is considered to predict the fatigue life of the cups in this study with the adaptation of the modified Morrow criterion to multiaxial load via the definition of equivalent quantities. This method is able to predict the lifespan of the cups after the simulation of only one cycle of the fatigue loading. After different trials, one fatigue loading adapted from the literature is selected for the cup and an experimental device is designed to perform the fatigue tests. However, it was not possible to carry out tests in the time dedicated to this study and thus only a numerical fatigue analysis is presented. The fatigue analysis is performed for C1 and RC2 cups, the fatigue loading simulation is performed with an elastic law due to the difficulties encountered with the user subroutine in Abaqus, previously mentioned, considering either isotropic hardening or HAH model to simulate the previous forming.

After the fatigue loading simulations, the number of cycles predicted by MCB and modified Morrow criteria are compared. For both cups, the addition of the residual stress influence via the equivalent mean stress in modified Morrow criterion leads to a decrease of the lifespan and a location change of the crack initiation from the inner surface to the outer surface of the cups. However, as the equivalent mean stress definition is influencing significantly the predictions, two definitions are compared but both of them leads to high values of the mean stress due to the overestimation of residual stresses after forming and also because the mean stress relaxation is not taken into account. The definition of the equivalent mean stress leading to the lowest values of mean stress is thus preferred but this definition may be improved in the future. Considering this definition in the modified Morrow criterion, the predicted lifespan of the cups is really similar whether isotropic hardening or HAH model is considered for the previous forming simulations. In particular for RC2, the location of crack initiation is in the area of the cup wall with few strain path changes whereas an increase of the number of cycles until crack initiation is observed by considering HAH model in the area subjected to strain path changes.

Perspectives

A first step towards a coupling of forming and fatigue analysis is performed in this study and brings out many perspectives.

Firstly, one of the main barriers to this coupling is the difference in numerical techniques used to simulate the forming and fatigue analysis. The objective is to switch from explicit to implicit without difficulties to keep the same material model during the whole chain of simulation. It would be particularly interesting in the case of HAH model that takes into account the loading history but the model formulations used actually in user subroutine need to be improved. Cutting plane algorithms are used usually in explicit and gives good results for forming but they are not stable enough to simulate springback and it will be interesting to use instead a fully implicit algorithm.

Considering the forming analysis separately, it would be interesting to perform a parametric study in order to estimate the influence of parameters from the finite element simulation and from the material model on the overestimated residual stress distribution. The hardening model could be improved to better predict the residual stress distributions in particular for the second stage of the redrawing process with also an overestimation of the punch force-displacement curve. As suggested from the literature [13], [119], [120], the degradation of the Young modulus is influencing the springback and thus the residual stress distributions in particular for multi-stage processes. It would be interesting to consider this aspect of the material behavior in addition of the e-HAH model. The anisotropy, neglected in this study, could also be considered in the material model with Yld2000-2d, to quantify its influence on the results. Independently of the material model, other possibilities could be investigated for the friction model as it influences significantly the prediction of the punch force-displacement curve. Models are available in PAM-STAMP with a dependence of the friction coefficient on the contact pressure and/or the sliding speed between the blank and the tools. These models could be compared with the use of a constant coefficient as in this study, in order to evaluate the friction influence on the residual stress distribution.

Considering the fatigue analysis, the e-HAH model predicts a cyclic hardening without stabilization of the material behavior contrary to the behavior observed for the dual phase steel of this study. The integration of cyclic softening in the model could lead to an improvement of the fatigue life predictions. In the same way, the consideration of the mean stress relaxation should improve the results. Thus, the definition of the equivalent mean stress may be improved with the results of fatigue tests on the cup and validated on pre-strained uniaxial fatigue tests.

Finally, the performance of fatigue tests on the cups is difficult to execute without cutting the cups. Other fatigue loadings could be envisaged with cutting and may be easier to carry out as the Brazilian test.

BIBLIOGRAPHY

[1] Lotus-Engineering, « An assesment of mass reduction opportunities for 2017-2020 model year vehicle programs », 2010, p. 308.

[2] Audi, *Audi Q2*, 2016. [Online]. Available: `https://www.audi-mediacenter.com/en/audi-q2-5574`.

[3] M. Tisza and I. Czinege, « Comparative study of the application of steels and aluminium in lightweight production of automotive parts », *International Journal of Lightweight Materials and Manufacture*, vol. 1, pp. 229–238, 2018.

[4] D. K. Kose and D. B. Rietman, « Plasticity effects in subsequent simulations of sar structures », *in VII International Conference on Computational Plasticity*, Barcelona: E. Oñate and D. R. J. Owen (Eds), 2003, p. 7.

[5] C. Gaier, K. Kose, H. Hebisch, and G. Pramhas, « Coupling forming simulation and fatigue life prediction of vehicle components », *in NAFEMS Word Congress 17th–20th May*, 2005.

[6] M. L. Facchinetti, B. Weber, C. Doudard, and S. Calloch, « Taking into account the forming process in fatigue design computations », *Fatigue Design, November*, pp. 21–22, 2007.

[7] W.-R. Wang, G. Chen, and Z.-Q. Lin, « The study on the fatigue FEM analysis considering the effect of stamping », *Materials & Design*, vol. 30, pp. 1588–1594, 2009.

[8] K. B. Slima, L. Penazzi, C. Mabru, and F. Ronde-Oustau, « Fatigue analysis-based numerical design of stamping tools made of cast iron », *The International Journal of Advanced Manufacturing Technology*, vol. 67, *5-8*, pp. 1643–1650, 2013.

[9] Z. Yue, « Ductile damage prediction in sheet metal forming processes », Ph.D. dissertation, Université de Technologie de Troyes and Technische Universität Dortmund, 2014.

[10] F. Barlat, J. J. Gracio, M.-G. Lee, E. F. Rauch, and G. Vincze, « An alternative to kinematic hardening in classical plasticity », *International Journal of Plasticity*, vol. 27, *9*, pp. 1309–1327, 2011.

[11] F. Barlat, G. Vincze, J. J. Grácio, M.-G. Lee, E. F. Rauch, and C. N. Tomé, « Enhancements of homogenous anisotropic hardening model and application to mild and dual-phase steels », *International Journal of Plasticity*, vol. 58, pp. 201–218, 2014.

[12] ArcelorMittal, *Dual phase steels*, 2021. [Online]. Available: `https://automotive.arcelormittal.com/product_sheet`.

[13] J. Liao, X. Xue, M.-G. Lee, F. Barlat, G. Vincze, and A. B. Pereira, « Constitutive modeling for path-dependent behavior and its influence on twist springback », *International Journal of Plasticity*, vol. 93, pp. 64–88, 2017.

[14] J. H. Schmitt, E. Aernoudt, and B. Baudelet, « Yield loci for polycrystalline metals without texture », *Materials Science and Engineering*, vol. 75, pp. 13–20, 1985.

[15] S. Bouvier, B. Gardey, H. Haddadi, and C. Teodosiu, « Characterization of the strain-induced plastic anisotropy of rolled sheets by using sequences of simple shear and uniaxial tensile tests », *Journal of Materials Processing Technology*, vol. 174, pp. 115–126, 2006.

[16] M. v. Riel, « Strain path dependency in sheet metal Experiments and models », Ph.D. dissertation, Universiteit Twente, 2009.

[17] T. Carvalho-Resende, T. Balan, S. Bouvier, F. Abed-Meraim, and S.-S. Sablin, « Numerical investigation and experimental validation of a plasticity model for sheet steel forming », *Modelling and Simulation in Materials Science and Engineering*, vol. 21, p. 015 008, 2013.

[18] D. Herault, S. Thuillier, P.-Y. Manach, and J.-L. Duval, « Strain path changes in Reverse Redrawing of DP Steels », *in IOP Conference Series: Materials Science and Engineering*, vol. 418, IOP Publishing, 2018, p. 012 042.

[19] B. Gardey, S. Bouvier, V. Richard, and B. Bacroix, « Texture and dislocation structures observation in a dual-phase steel under strain-path changes at large deformation », *Materials Science and Engineering: A*, vol. 400-401, pp. 136–141, 2005.

[20] J.-W. Lee, M.-G. Lee, and F. Barlat, « Finite element modeling using homogeneous anisotropic hardening and application to spring-back prediction », *International Journal of Plasticity*, vol. 29, pp. 13–41, 2012.

[21] L. Sun and R. H. Wagoner, « Proportional and non-proportional hardening behavior of dual-phase steels », *International Journal of Plasticity*, vol. 45, pp. 174–187, 2013.

[22] M. Zecevic, Y. P. Korkolis, T. Kuwabara, and M. Knezevic, « Dual-phase steel sheets under cyclic tension–compression to large strains: Experiments and crystal plasticity modeling », *Journal of the Mechanics and Physics of Solids*, vol. 96, pp. 65–87, 2016.

[23] H Haddadi, S Bouvier, M Banu, C Maier, and C Teodosiu, « Towards an accurate description of the anisotropic behaviour of sheet metals under large plastic deformations: Modelling, numerical analysis and identification », *International Journal of Plasticity*, vol. 22, pp. 2226–2271, 2006.

[24] V. Tarigopula, O. S. Hopperstad, M. Langseth, and A. H. Clausen, « An evaluation of a combined isotropic-kinematic hardening model for representation of complex strain-path changes in dual-phase steel », *European Journal of Mechanics - A/Solids*, vol. 28, pp. 792–805, 2009.

[25] A. Galtier, R. Munier, A. Philippot, and B. Weber, « Essais de fatigue - Domaine des grands nombres de cycles », *Techniques de l'ingénieur. Matériaux métalliques*, p. 30, 2019.

[26] F. Ellyin, *Fatigue damage, crack growth and life prediction*, Springer Science & Buisness Media. Springer Science & Buisness Media, 1997.

[27] P. Rabbe, H.-P. Lieurade, and A. Galtier, « Essais de fatigue. partie ii », *Techniques de l'ingénieur. Matériaux métalliques, M4171*, pp. M4171–1, 2000.

[28] Q Le, H Kang, G Kridli, A Khosrovaneh, and B Yan, « Effect of prestrain paths on mechanical behavior of dual phase sheet steel », *International Journal of Fatigue*, vol. 31, pp. 607–615, 2009.

[29] Z. G. Hu, P. Zhu, and J. Meng, « Fatigue properties of transformation-induced plasticity and dual-phase steels for auto-body lightweight: Experiment, modeling and application », *Materials & Design*, vol. 31, pp. 2884–2890, 2010.

[30] S. K. Paul, N. Stanford, A. Taylor, and T. Hilditch, « The effect of low cycle fatigue, ratcheting and mean stress relaxation on stress–strain response and microstructural development in a dual phase steel », *International Journal of Fatigue*, vol. 80, pp. 341–348, 2015.

[31] B. Das, A. Singh, and S. Kumar Paul, « Low cycle fatigue performance of DP600 steel under various pre-straining paths », *International Journal of Fatigue*, vol. 132, p. 105 331, 2020.

[32] R. K. Boger, R. H. Wagoner, F. Barlat, M. G. Lee, and K. Chung, « Continuous, large strain, tension/compression testing of sheet material », *International Journal of Plasticity*, vol. 21, pp. 2319–2343, 2005.

[33] G. Joo, H. Huh, and M. K. Choi, « Tension/compression hardening behaviors of auto-body steel sheets at intermediate strain rates », *International Journal of Mechanical Sciences*, vol. 108-109, pp. 174–187, 2016.

[34] A. L. Ly, « The effects of pre-straining conditions on fatigue behavior of multiphase TRIP steels », Ph.D. dissertation, Colorado School of Mines. Arthur Lakes Library, 2015.

[35] S. J. Marcadet and D. Mohr, « Effect of compression–tension loading reversal on the strain to fracture of dual phase steel sheets », *International Journal of Plasticity*, vol. 72, pp. 21–43, 2015.

[36] J. Dallmeier, O. Huber, H. Saage, and K. Eigenfeld, « Uniaxial cyclic deformation and fatigue behavior of AM50 magnesium alloy sheet metals under symmetric and asymmetric loadings », *Materials & Design*, vol. 70, pp. 10–30, 2015.

[37] F. Yoshida, T. Uemori, and K. Fujiwara, « Elastic–plastic behavior of steel sheets under in-plane cyclic tension–compression at large strain », *International Journal of Plasticity*, vol. 18, pp. 633–659, 2002.

[38] S. Zhang, S. Mao, D. Arola, and D. Zhang, « Characterization of the strain-life fatigue properties of thin sheet metal using an optical extensometer », *Optics and Lasers in Engineering*, vol. 60, pp. 44–48, 2014.

[39] Q. Li, M. Jin, Z. Zou, S. Zhao, Q. Zhang, and P. Li, « Experiment Research on Tensile and Compression Cyclic Loading of Sheet Metal », *Procedia Engineering*, vol. 207, pp. 1916–1921, 2017.

[40] J. Cao, W. Lee, H. S. Cheng, M. Seniw, H.-P. Wang, and K. Chung, « Experimental and numerical investigation of combined isotropic-kinematic hardening behavior of sheet metals », *International Journal of Plasticity*, vol. 25, pp. 942–972, 2009.

[41] C. S. Aitchison and L. B. Tuckerman, « The" pack" method for compressive tests of thin specimens of materials used in thin-wall structures », 1939.

[42] C. C. Tasan, M. Diehl, D. Yan, *et al.*, « An overview of dual-phase steels: advances in microstructure-oriented processing and micromechanically guided design », *Annual Review of Materials Research*, vol. 45, pp. 391–431, 2015.

[43] A. Kalhor, « A review of recent progress in mechanical and corrosion properties of dual phase steels », *Archives of Civil and Mechanical Engineering*, p. 14, 2020.

[44] J Sperle, « Fatigue strength of high strength dual-phase steel sheet », *International Journal of Fatigue*, vol. 7, pp. 79–86, 1985.

[45] K. Nakajima, T. Urabe, Y. Hosoya, S. Kamiishi, T. Miyata, and N. Takeda, « Influence of Microstructural Morphology and Prestraining on Short Fatigue Crack Propagation in Dual-phase Steels », *ISIJ International*, vol. 41, pp. 298–305, 2001.

[46] F. S. M. Mballa, « Modélisation du comportement magnéto-mécanique d'un acier Dual Phase à partir de sa description microstructurale », Ph.D. dissertation, ENS Cachan, 2013.

[47] M. Delincé, Y. Bréchet, J. D. Embury, M. G. D. Geers, P. J. Jacques, and T. Pardoen, « Structure–property optimization of ultrafine-grained dual-phase steels using a microstructure-based strain hardening model », *Acta Materialia*, vol. 55, *7*, pp. 2337–2350, 2007.

[48] G. Avramovic-Cingara, Y. Ososkov, M. K. Jain, and D. S. Wilkinson, « Effect of martensite distribution on damage behaviour in DP600 dual phase steels », *Materials Science and Engineering: A*, vol. 516, pp. 7–16, 2009.

[49] R. Padmanabhan, A. J. Baptista, M. C. Oliveira, and L. F. Menezes, « Effect of anisotropy on the deep-drawing of mild steel and dual-phase steel tailor-welded blanks », *Journal of Materials Processing Technology*, vol. 184, pp. 288–293, 2007.

[50] H. Livatyali, M. Firat, B. Gurler, and M. Ozsoy, « An experimental analysis of drawing characteristics of a dual-phase steel through a round drawbead », *Materials & Design*, vol. 31, pp. 1639–1643, 2010.

[51] M. Firat, « A finite element modeling and prediction of stamping formability of a dual-phase steel in cup drawing », *Materials & Design*, vol. 34, pp. 32–39, 2012.

[52] F. Ozturk, S. Toros, and S. Kilic, « Effects of Anisotropic Yield Functions on Prediction of Forming Limit Diagrams of DP600 Advanced High Strength Steel », *Procedia Engineering*, vol. 81, pp. 760–765, 2014.

[53] C. C. Roth and D. Mohr, « Effect of strain rate on ductile fracture initiation in advanced high strength steel sheets: Experiments and modeling », *International Journal of Plasticity*, vol. 56, pp. 19–44, 2014.

[54] K. Bandyopadhyay, S. K. Panda, P. Saha, and G. Padmanabham, « Limiting drawing ratio and deep drawing behavior of dual phase steel tailor welded blanks: FE simulation and experimental validation », *Journal of Materials Processing Technology*, vol. 217, pp. 48–64, 2015.

[55] S. L. Zang, S. Thuillier, A. Le Port, and P.-Y. Manach, « Prediction of anisotropy and hardening for metallic sheets in tension, simple shear and biaxial tension », *International Journal of Mechanical Sciences*, vol. 53, pp. 338–347, 2011.

[56] M. S. Wi, S. Y. Lee, J. H. Kim, J. M. Kim, and F. Barlat, « Experimental and theoretical plasticity analyses of steel materials deformed under a nonlinear strain path », *International Journal of Mechanical Sciences*, vol. 182, p. 105 770, 2020.

[57] Y. Hanabusa, H. Takizawa, and T. Kuwabara, « Numerical verification of a biaxial tensile test method using a cruciform specimen », *Journal of Materials Processing Technology*, vol. 213, pp. 961–970, 2013.

[58] S. VDEh, *STAHL-EISEN-Prüfblätter (SEP 1240)Testing and Documentation Guideline for the Experimental Determination of Mechanical Properties of Steel Sheets for CAE-Calculations*, 2006.

[59] *ISO 12106 - Metallic materials — Fatigue testing — Axial-strain-controlled method*, 2017.

[60] D. Hérault, S. Thuillier, S.-Y. Lee, P.-Y. Manach, and F. Barlat, « Calibration of a strain path change model for a dual phase steel », *International Journal of Mechanical Sciences*, vol. 194, p. 106 217, 2021.

[61] J. Lemaitre and J. L. Chaboche, « Mechanics of solid mechanics », *Cambridge University, Cambridge, United Kingdom*, pp. 161–241, 1990.

[62] C. Teodosiu and Z. Hu, « Evolution of the intragranular microstructure at moderate and large strains: modelling and computational significance », *Simulation of materials processing: theory, methods and applications*, pp. 173–182, 1995.

[63] B. Haddag, T. Balan, and F. Abed-Meraim, « Investigation of advanced strain-path dependent material models for sheet metal forming simulations », *International Journal of Plasticity*, vol. 23, pp. 951–979, 2007.

[64] M Oliveira, J Alves, B Chaparro, and L Menezes, « Study on the influence of work-hardening modeling in springback prediction », *International Journal of Plasticity*, vol. 23, pp. 516–543, 2007.

[65] S. Thuillier, P.-Y. Manach, and L. F. Menezes, « Occurence of strain path changes in a two-stage deep drawing process », *Journal of Materials Processing Technology*, vol. 210, *2*, pp. 226–232, 2010, ISSN: 09240136. DOI: `10.1016/j.jmatprotec.2009.09.004`.

[66] T. Mánik, B. Holmedal, and O. S. Hopperstad, « Strain-path change induced transients in flow stress, work hardening and r-values in aluminum », *International Journal of Plasticity*, vol. 69, pp. 1–20, 2015.

[67] W. J. He, S. H. Zhang, and H. W. Song, « An extended homogenous yield function based anisotropic hardening model for description of anisotropic hardening behavior of materials », *International Journal of Mechanical Sciences*, vol. 77, pp. 343–355, 2013.

[68] J. Qin, B. Holmedal, and O. S. Hopperstad, « A combined isotropic, kinematic and distortional hardening model for aluminum and steels under complex strain-path changes », *International Journal of Plasticity*, vol. 101, pp. 156–169, 2018.

[69] T. Clausmeyer, A. Güner, A. E. Tekkaya, V. Levkovitch, and B. Svendsen, « Modeling and finite element simulation of loading-path-dependent hardening in sheet metals during forming », *International Journal of Plasticity*, vol. 63, pp. 64–93, 2014.

[70] F. Barlat, J. Ha, J. J. Grácio, M.-G. Lee, E. F. Rauch, and G. Vincze, « Extension of homogeneous anisotropic hardening model to cross-loading with latent effects », *International Journal of Plasticity*, vol. 46, pp. 130–142, 2013.

[71] J. S. Choi, J. W. Lee, J.-H. Kim, F. Barlat, M. G. Lee, and D. Kim, « Measurement and modeling of simple shear deformation under load reversal: Application to advanced high strength steels », *International Journal of Mechanical Sciences*, vol. 98, pp. 144–156, 2015.

[72] X. Xue, J. Liao, G. Vincze, A. B. Pereira, and F. Barlat, « Experimental assessment of nonlinear elastic behaviour of dual-phase steels and application to springback prediction », *International Journal of Mechanical Sciences*, vol. 117, pp. 1–15, 2016.

[73] S.-Y. Lee, J.-M. Kim, J.-H. Kim, and F. Barlat, « Validation of homogeneous anisotropic hardening model using non-linear strain path experiments », *International Journal of Mechanical Sciences*, vol. 183, p. 105 769, 2020.

[74] J. Lee, M.-G. Lee, F. Barlat, and J. H. Kim, « Stress integration schemes for novel homogeneous anisotropic hardening model », *Computer Methods in Applied Mechanics and Engineering*, vol. 247-248, pp. 73–92, 2012.

[75] J.-Y. Lee, J.-W. Lee, M.-G. Lee, and F. Barlat, « An application of homogeneous anisotropic hardening to springback prediction in pre-strained U-draw/bending », *International Journal of Solids and Structures*, vol. 49, pp. 3562–3572, 2012.

[76] Y. Li, J. He, B. Gu, and S. Li, « Identification of advanced constitutive model parameters through global optimization approach for DP780 steel sheet », *Procedia Engineering*, vol. 207, pp. 125–130, 2017.

[77] J. Ha, M.-G. Lee, and F. Barlat, « Strain hardening response and modeling of EDDQ and DP780 steel sheet under non-linear strain path », *Mechanics of Materials*, vol. 64, pp. 11–26, 2013.

[78] G. Vincze, F. Barlat, E. F. Rauch, C. N. Tomé, M. C. Butuc, and J. J. Grácio, « Experiments and modeling of low carbon steel sheet subjected to double strain path changes », *Metallurgical and Materials Transactions A*, vol. 44, pp. 4475–4479, 2013.

[79] S. B. Zaman, F. Barlat, and J.-H. Kim, « Deformation-induced anisotropy of uniaxially prestrained steel sheets », *International Journal of Solids and Structures*, vol. 134, pp. 20–29, 2018.

[80] F. Dallinger, « Adaptive process control strategy based on accurate modeling of a two-step micro bending process », Ph.D. dissertation, ETH Zurich, 2016.

[81] F. Barlat, J. C. Brem, J. W. Yoon, *et al.*, « Plane stress yield function for aluminum alloy sheets—part 1: theory », *International Journal of Plasticity*, vol. 19, pp. 1297–1319, 2003.

[82] S. Manson, « Fatigue: a complex subject—some simple approximations », *Experimental mechanics*, vol. 5, pp. 193–226, 1965.

[83] L. F. Coffin Jr, « A study of the effects of cyclic thermal stresses on a ductile metal », *Transactions of the American Society of Mechanical Engineers, New York*, vol. 76, pp. 931–950, 1954.

[84] J. Morrow, « Low cycle fatigue behavior of quenched and tempered SAE 1045 steel », 1965.

[85] S. S. Manson and G. R. Halford, « Correction: Practical implementation of the double linear damage rule and damage curve approach for treating cumulative fatigue damage », *International Journal of Fracture*, vol. 17, R35–R42, 1981.

[86] Q. Le, H. Kang, G. Kridli, A. Khosrovaneh, and B. Yan, « Modified strain-life equation to consider the effect of different prestrain paths for dual phase sheet steel », *Journal of Materials Processing Technology*, vol. 209, pp. 3525–3531, 2009.

[87] B. Levieil, C. Doudard, D. Thevenet, F. Bridier, A. Ezanno, and S. Calloch, « An original simplified method based on the use of an adjustable localization operator for low-cycle fatigue life predictions in the case of confined plasticity », *Theoretical and Applied Fracture Mechanics*, vol. 104, p. 102 383, 2019.

[88] N. Souto, A. Andrade-Campos, and S. Thuillier, « Material parameter identification within an integrated methodology considering anisotropy, hardening and rupture », *Journal of Materials Processing Technology*, vol. 220, pp. 157–172, 2015.

[89] A Pradeau, S Thuillier, and J. W. Yoon, « Prediction of failure in bending of an aluminium sheet alloy », *International Journal of Mechanical Sciences*, vol. 119, pp. 23–35, 2016.

[90] J. Lee, D. Kim, Y.-S. Lee, H. J. Bong, F. Barlat, and M.-G. Lee, « Stress update algorithm for enhanced homogeneous anisotropic hardening model », *Computer Methods in Applied Mechanics and Engineering*, vol. 286, pp. 63–86, 2015.

[91] G. Cailletaud and P. Pilvin, « Identification and inverse problems: a modular approach », *ASME Applied Mechanics Division-Publications-AMD*, vol. 168, pp. 33–33, 1993.

[92] J. Liao, J. A. Sousa, A. B. Lopes, X. Xue, F. Barlat, and A. B. Pereira, « Mechanical, microstructural behaviour and modelling of dual phase steels under complex deformation paths », *International Journal of Plasticity*, vol. 93, pp. 269–290, 2017.

[93] K. Levenberg, « A method for the solution of certain non-linear problems in least squares », *Quarterly of Applied Mathematics*, vol. 2, pp. 164–168, 1944.

[94] D. W. Marquardt, « An algorithm for least-squares estimation of nonlinear parameters », *Journal of the Society for Industrial and Applied Mathematics*, vol. 11, pp. 431–441, 1963. DOI: `10.1137/0111030`.

[95] J. Choi, J. Lee, H. J. Bong, M.-G. Lee, and F. Barlat, « Advanced constitutive modeling of advanced high strength steel sheets for springback prediction after double stage U-draw bending », *International Journal of Solids and Structures*, vol. 151, pp. 152–164, 2018, ISSN: 00207683. DOI: `10.1016/j.ijsolstr.2017.09.030`.

[96] M. G. Lee, J. W. Lee, J. J. Gracio, G. Vincze, E. F. Rauch, and F. Barlat, « A dislocation-based hardening model incorporated into an anisotropic hardening approach », *Computational Materials Science*, vol. 79, pp. 570–583, 2013.

[97] X. Feaugas, « On the origin of the tensile flow stress in the stainless steel AISI 316L at 300 K: back stress and effective stress », *Acta Materialia*, vol. 47, pp. 3617–3632, 1999.

[98] J. Qin, B. Holmedal, K. Zhang, and O. S. Hopperstad, « Modeling strain-path changes in aluminum and steel », *International Journal of Solids and Structures*, vol. 117, pp. 123–136, 2017.

[99] F. Barlat, S.-Y. Yoon, S.-Y. Lee, M.-S. Wi, and J.-H. Kim, « Distortional plasticity framework with application to advanced high strength steel », *International Journal of Solids and Structures*, vol. 202, pp. 947–962, 2020.

[100] A. D. Santos and P. Teixeira, « A study on experimental benchmarks and simulation results in sheet metal forming », *Journal of Materials Processing Technology*, vol. 199, pp. 327–336, 2008.

[101] L. Marretta, G. Ingarao, and R. Di Lorenzo, « Design of sheet stamping operations to control springback and thinning: A multi-objective stochastic optimization approach », *International Journal of Mechanical Sciences*, vol. 52, pp. 914–927, 2010.

[102] M. Schwarze, I. N. Vladimirov, and S. Reese, « Sheet metal forming and springback simulation by means of a new reduced integration solid-shell finite element technology », *Computer Methods in Applied Mechanics and Engineering*, vol. 200, pp. 454–476, 2011.

[103] M. Jain, J. Allin, and M. J. Bull, « Deep drawing characteristics of automotive aluminum alloys », *Materials Science and Engineering: A*, vol. 256, pp. 69–82, 1998.

[104] D. Banabic, D. S. Comsa, M. Sester, *et al.*, « Influence of constitutive equations on the accuracy of prediction in sheet metal forming simulation », *in Numisheet*, 2008, pp. 37–42.

[105] E. H. Ouakdi, « Evaluation of springback under the effect of holding force and die radius in a stretch bending test », *Materials and Design*, p. 7, 2012.

[106] Z. Marciniak, J. L. Duncan, and S. J. Hu, *Mechanics of sheet metal forming*, 2. ed. Oxford: Butterworth-Heinemann, 2002, OCLC: 248369976, ISBN: 978-0-7506-5300-8.

[107] A. Barata da Rocha and J. Ferreira Duarte, *Technologia da Embutidura*, APTCP - Associação Portuguesa das technologias de Conformação Plàstica. Porto, 1992.

[108] R. Pearce, *Sheet metal forming.* Springer Science & Business Media, 1991.

[109] R. K. Verma and S. Chandra, « An improved model for predicting limiting drawing ratio », *Journal of Materials Processing Technology*, vol. 172, pp. 218–224, 2006.

[110] D.-K. Leu, « The limiting drawing ratio for plastic instability of the cup-drawing process », *Journal of Materials Processing Technology*, vol. 86, *1-3*, pp. 168–176, 1999.

[111] J. Coër, H. Laurent, M. C. Oliveira, P.-Y. Manach, and L. F. Menezes, « Detailed experimental and numerical analysis of a cylindrical cup deep drawing: Pros and cons of using solid-shell elements », *International Journal of Material Forming*, vol. 11, pp. 357–373, 2018.

[112] E. M. Jones, M. A. Iadicola, *et al.*, « A good practices guide for digital image correlation », *International Digital Image Correlation Society*, vol. 10, 2018.

[113] Z. Wang and B. Gong, « Residual Stress in the Forming of Materials », *in Handbook of Residual Stress and Deformation*, G. Totten, M. Howes, T. Inoue, ASM International, 2002, pp. 141–149.

[114] M. François, « Unified description for the geometry of X-ray stress analysis: proposal for a consistent approach », *Journal of Applied Crystallography*, vol. 41, pp. 44–55, 2008.

[115] « NUMISHEET'99 benchmarks », *in Proceedings of the 4th International Conference and Workshop on Numerical Simulation of 3D Sheet Forming processes*, Besançon, France: J. C. Gelin, P. Picart, 1999.

[116] J.-W. Yoon, F. Barlat, R. E. Dick, K. Chung, and T. J. Kang, « Plane stress yield function for aluminum alloy sheets—part II: FE formulation and its implementation », *International Journal of Plasticity*, vol. 20, pp. 495–522, 2004.

[117] D. Neto, M. Oliveira, J. Alves, and L. Menezes, « Influence of the plastic anisotropy modelling in the reverse deep drawing process simulation », *Materials & Design*, vol. 60, pp. 368–379, 2014.

[118] A. Col, « Emboutissage des tôles: importance des modes de déformation », *Techniques de l'ingénieur. Génie mécanique*, *BM7510*, BM7510–1, 2011.

[119] J. Liao, S. Chen, X. Xue, and H. Xiang, « On twist springback of a curved channel with pre-strain effect », *International Journal of Lightweight Materials and Manufacture*, vol. 3, pp. 108–112, 2020. (visited on 04/13/2021).

[120] S. Chen, J. Liao, H. Xiang, X. Xue, and A. B. Pereira, « Pre-strain effect on twist springback of a 3d p-channel in deep drawing », *Journal of Materials Processing Technology*, vol. 287, p. 116 224, 2021.

[121] S. H. Kim, S. H. Kim, and H. Huh, « Finite element inverse analysis for the design of intermediate dies in multi-stage deep-drawing processes with large aspect ratio », *Journal of Materials Processing Technology*, vol. 113, pp. 779–785, 2001.

[122] M. Nick, R. Mannens, D. Trauth, and T. Bergs, « Load path modelling in single-step deep drawing of rotationally symmetric cups », *Procedia Manufacturing*, vol. 29, pp. 520–527, 2019.

[123] J. Danckert, « The Residual Stress Distribution in the Wall of a Deep-Drawn and Ironed Cup Determined Experimentally and by FEM », *CIRP Annals*, vol. 43, pp. 249–252, 1994.

[124] T. Gnaeupel-Herold, H. J. Prask, R. J. Fields, T. J. Foecke, Z. Xia, and U. Lienert, « A synchrotron study of residual stresses in a Al6022 deep drawn cup », *Materials Science and Engineering: A*, vol. 366, pp. 104–113, 2004.

[125] M. Ragab and H. Orban, « Effect of ironing on the residual stresses in deep drawn cups », *Journal of Materials Processing Technology*, vol. 99, pp. 54–61, 2000.

[126] H. Laurent, R. Grèze, P.-Y. Manach, and S. Thuillier, « Influence of constitutive model in springback prediction using the split-ring test », *International Journal of Mechanical Sciences*, vol. 51, pp. 233–245, 2009.

[127] H. Laurent, R. Grèze, M. C. Oliveira, L. F. Menezes, P.-Y. Manach, and J. L. Alves, « Numerical study of springback using the split-ring test for an AA5754 aluminum alloy », *Finite Elements in Analysis and Design*, vol. 46, pp. 751–759, 2010.

[128] R. Grèze, P.-Y. Manach, H. Laurent, S. Thuillier, and L. F. Menezes, « Influence of the temperature on residual stresses and springback effect in an aluminium alloy », *International Journal of Mechanical Sciences*, vol. 52, pp. 1094–1100, 2010.

[129] W. J. Kang and G. H. Kim, « Analysis of manufacturing effects on fatigue failure of an automotive component using finite element methods », *Fatigue & Fracture of Engineering Materials & Structures*, vol. 32, pp. 619–630, 2009.

[130] J. Wasén, K. Hamberg, and B. Karlsson, « The influence of prestrain and ageing on fatigue crack growth in a dual-phase steel », *Scripta Metallurgica*, vol. 18, pp. 621–624, 1984.

[131] K Fredriksson, A Melander, and M Hedman, « Influence of prestraining and ageing on fatigue properties of high-strength sheet steels », *International Journal of Fatigue*, vol. 10, *3*, pp. 139–151, 1988.

[132] A. Gustavsson and A. Melander, « Fatigue of a highly prestrained dual-phase sheet steel », *Fatigue & Fracture of Engineering Materials and Structures*, vol. 18, pp. 201–210, 1995.

[133] R. Munier, C. Doudard, S. Calloch, and B. Weber, « Towards a faster determination of high cycle fatigue properties taking into account the influence of a plastic pre-strain from self heating measurements », *Procedia Engineering*, vol. 2, pp. 1741–1750, 2010.

[134] A Gustavsson, M Larsson, and A Melander, « Fatigue life of pressed steel sheet components », *International Journal of Fatigue*, vol. 19, pp. 613–619, 1997.

[135] O. Aytekin, « Numerical and experimental investigation of fatigue life in deep drawn parts », Ph.D. dissertation, Middle East Technical University, 2005.

[136] P. McGrath, D. Hattingh, M. James, and A Els-Botes, « Effects of forming process on fatigue performance of wheel centre discs », *ECF13, San Sebastian*, vol. 2013, 2000.

[137] J Meng, P Zhu, Z Liu, and Q Ji, « Integration of multi-step stamping effects in the bending fatigue analysis of a steel wheel », *Fatigue & Fracture of Engineering Materials & Structures*, vol. 36, *8*, pp. 795–808, 2013.

[138] D. Shang, X. Liu, Y. Shan, and E. Jiang, « Research on the stamping residual stress of steel wheel disc and its effect on the fatigue life of wheel », *International Journal of Fatigue*, vol. 93, pp. 173–183, 2016.

[139] J. A. Martins, L. P. Cardoso, J. A. Fraymann, and S. T. Button, « Analyses of residual stresses on stamped valves by X-ray diffraction and finite elements method », *Journal of Materials Processing Technology*, vol. 179, pp. 30–35, 2006.

[140] ASTM, « C 496m-04 », *Standard test method for splitting tensile strength of cylindrical concrete specimens*, vol. 4, p. 5, 2004.

[141] L. Bizet, L. Charleux, P. Balland, and L. Tabourot, « Influence of heterogeneities introduced into the modelling of a ring compression test », *Archives of Civil and Mechanical Engineering*, vol. 17, pp. 365–374, 2017.

[142] D. Li and L. N. Y. Wong, « The brazilian disc test for rock mechanics applications: review and new insights », *Rock mechanics and rock engineering*, vol. 46, pp. 269–287, 2013.

[143] X Chen, J Song, and K Kim, « Low cycle fatigue life prediction of 63Sn–37Pb solder under proportional and non-proportional loading », *International Journal of Fatigue*, vol. 28, pp. 757–766, 2006.

APPENDIX A

REPEATABILITY OF THE MECHANICAL TESTS

The repeatability of all the mechanical tests performed for the characterization of the DP600 are presented in this Appendix. In general, 2 to 3 tests are performed for each condition. Firstly, the Cauchy stress evolution as function of the logarithmic strain is presented for all the orientations of the uniaxial tensile tests in Figures A.1 and A.2. The bulge stress-strain curves, cf. Figure A.3, the shear stress-strain curves, cf. Figure A.4, and the biaxial Cauchy stress components as function of the equivalent plastic strain, cf. Figure A.5, are also presented for monotonic tests. Then, the shear stress-strain curves of the sequential tests are presented in Figure A.6, for the forward-reverse shear tests and the simple shear tests performed after pre-strain in tension respectively. Finally, the repeatability of the fatigue tests performed along RD is shown with the stabilized cycle of each total strain amplitude in Figures A.7 and A.8. Overall, a good repeatability is observed for all the mechanical tests.

A.1 Monotonic tests

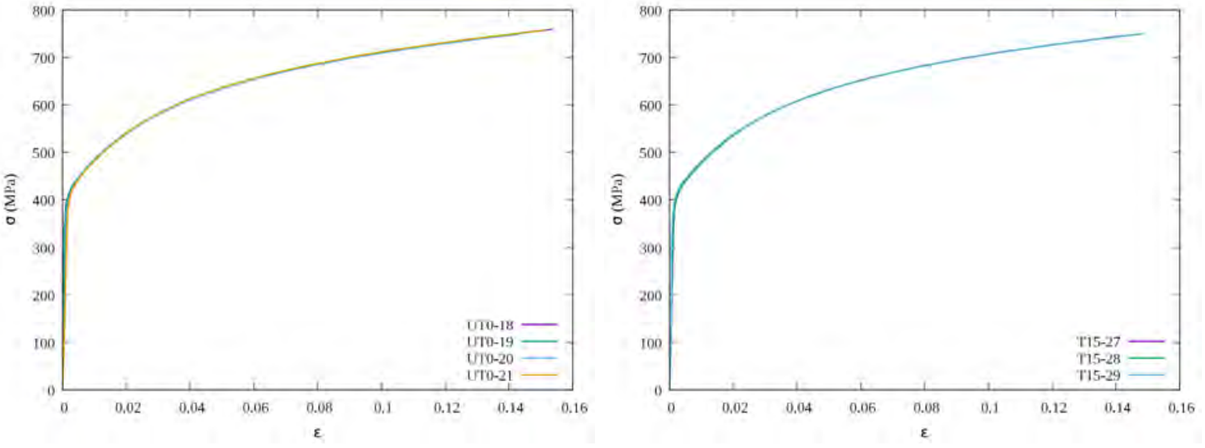

(a) 0°

(b) 15°

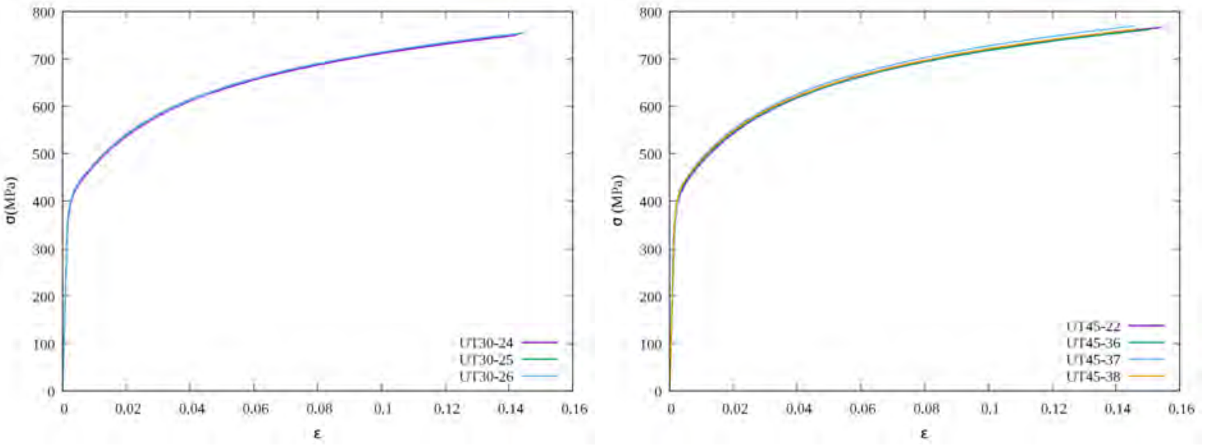

(c) 30°

(d) 45°

Figure A.1 – Cauchy stress as a function of the logarithmic strain for uniaxial tensile tests with orientations of 0°, 15°, 30°, and 45° from RD

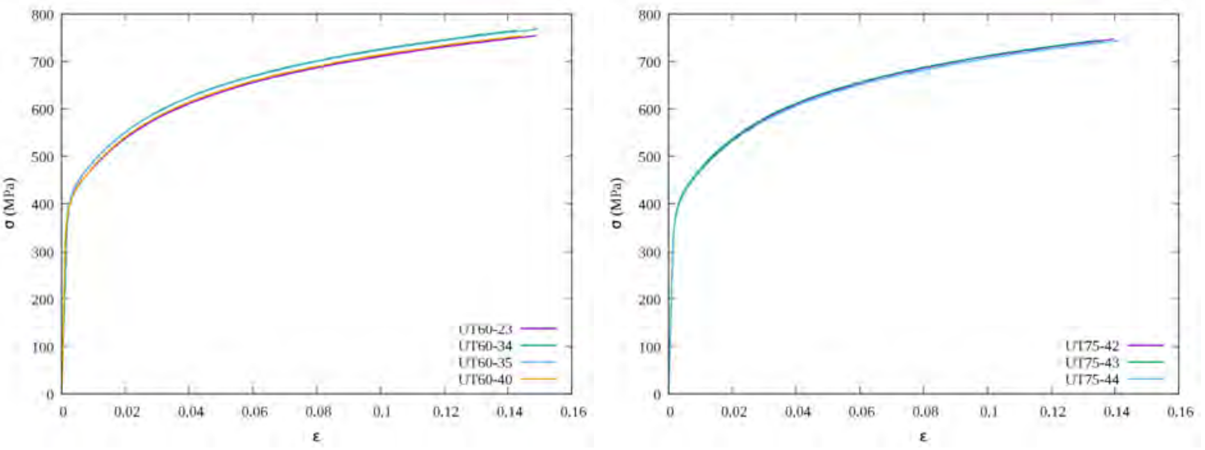

(a) 60°

(b) 75°

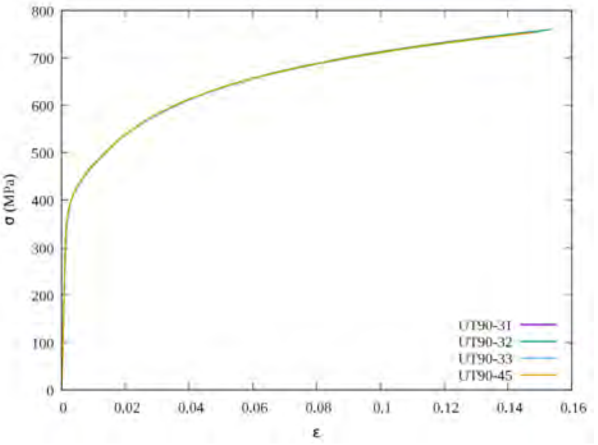

(c) 90°

Figure A.2 – Cauchy stress as a function of the logarithmic strain for uniaxial tensile tests with orientations of 60°, 75° and 90° from RD

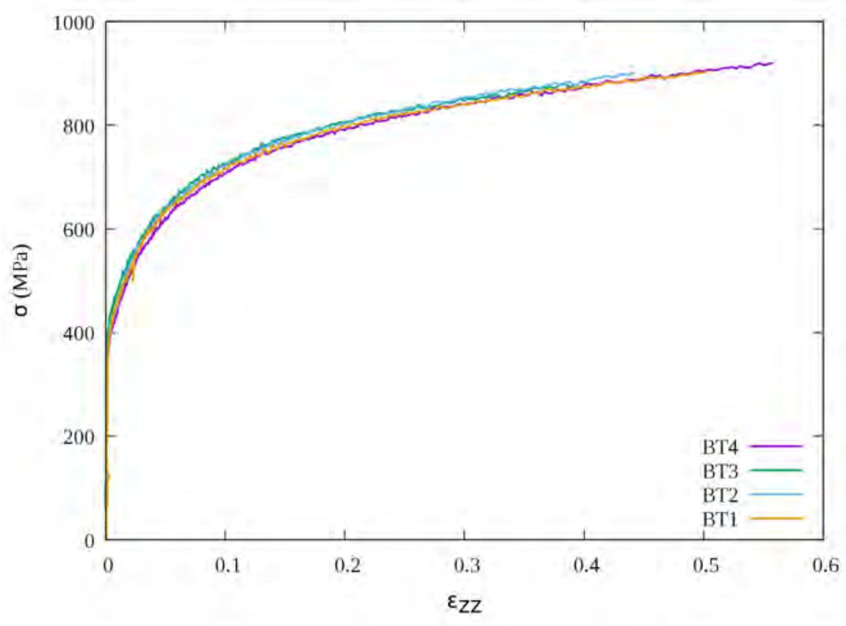

Figure A.3 – Stress-strain curves of the bulge tests

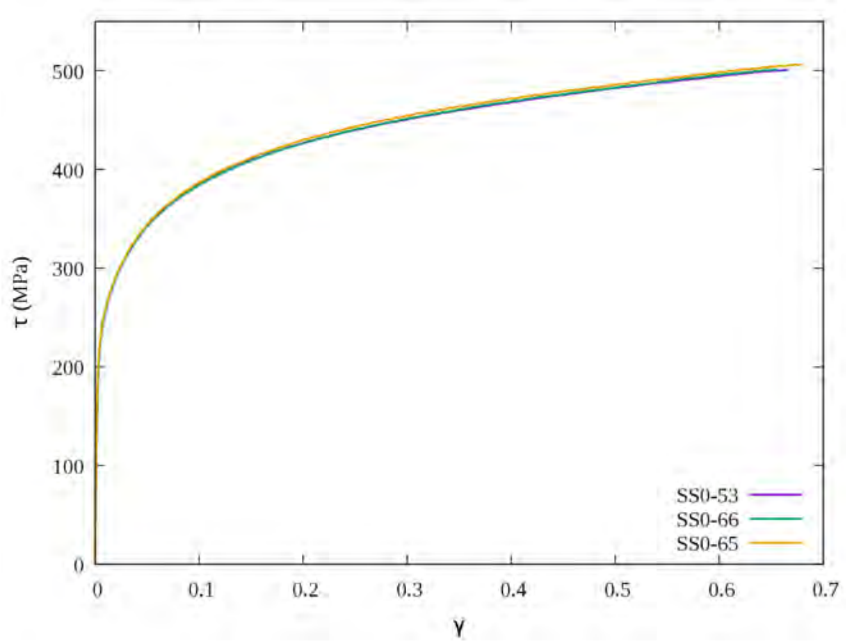

Figure A.4 – Shear stress-strain curves of the monotonic tests

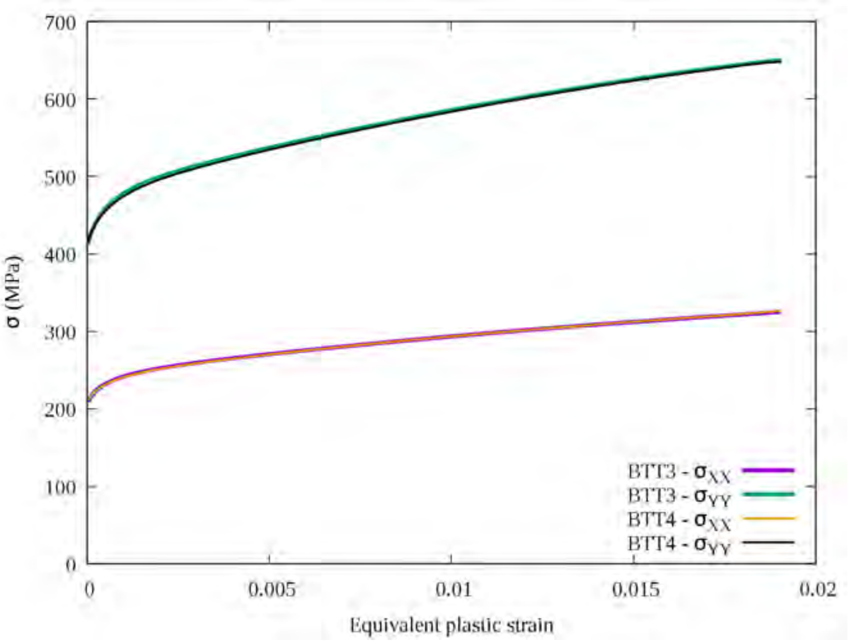

(a) $F_X = \frac{1}{2}F_Y$

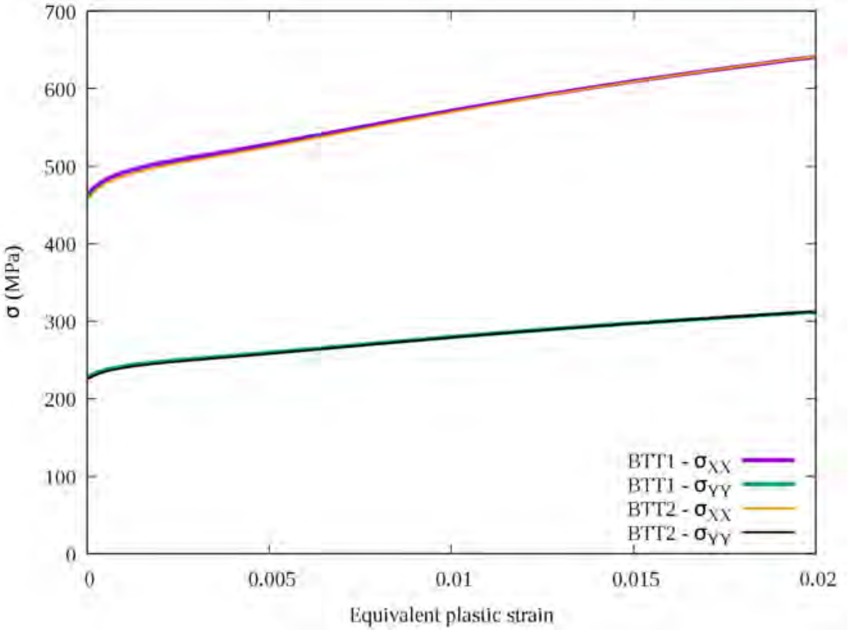

(b) $F_X = 2F_Y$

Figure A.5 – Cauchy stress in function of the equivalent plastic strain of the in-plane biaxial tensile tests

A.2 Sequential tests

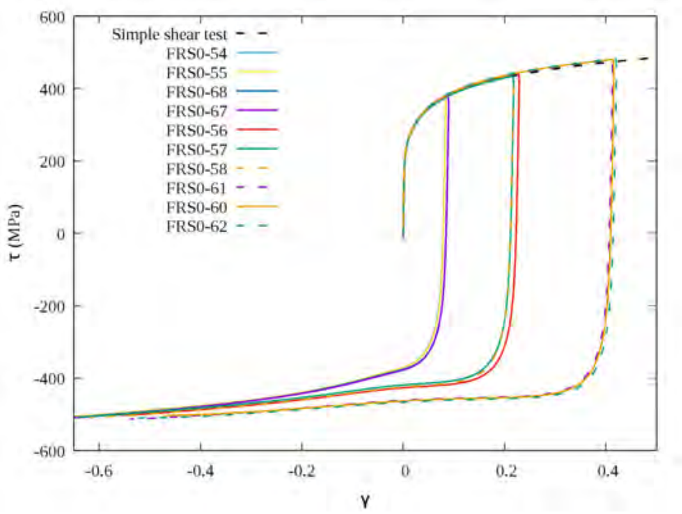

(a) Forward-reverse shear tests performed along RD

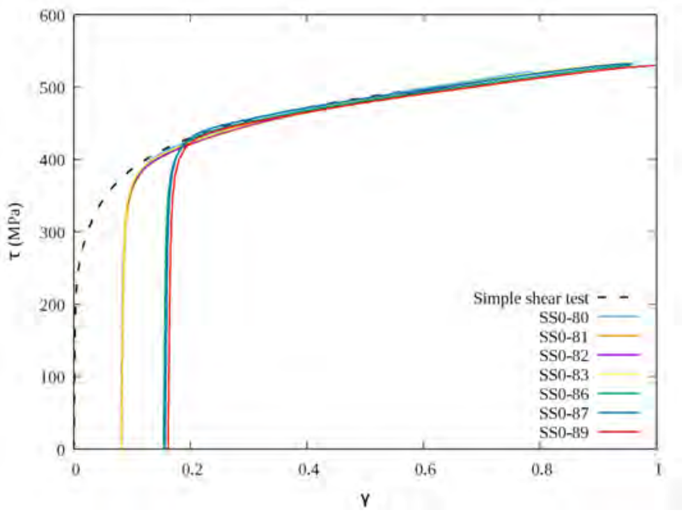

(b) Simple shear tests performed along RD after pre-strains along RD

Figure A.6 – Shear stress-strain curves of the sequential tests

A.3 Fatigue tests

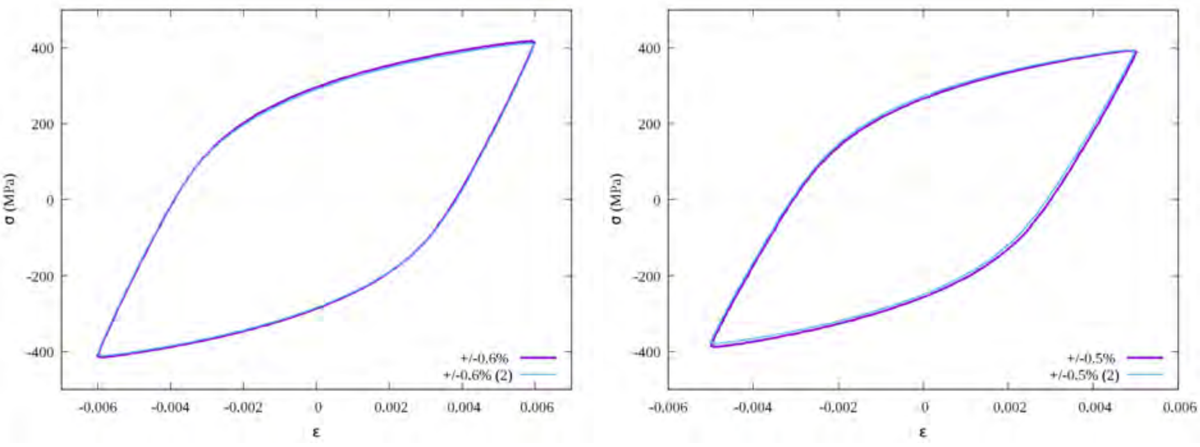

(a) 0.6 %

(b) 0.5 %

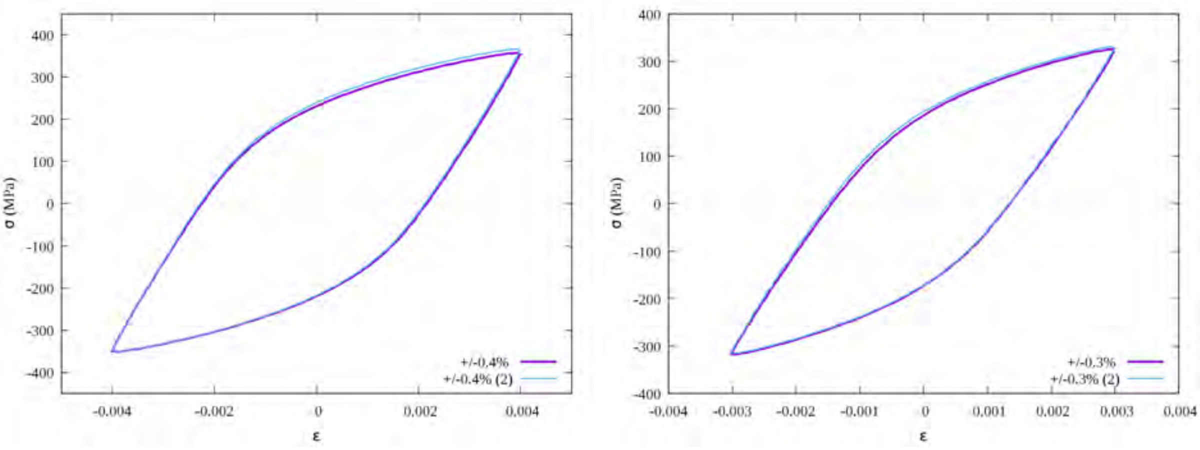

(c) 0.4 %

(d) 0.3 %

Figure A.7 – Superposition of the stabilized cycles $\frac{N_f}{2}$ for the strain levels 0.6 %, 0.5 %, 0.4 % and 0.3 % along the rolling direction

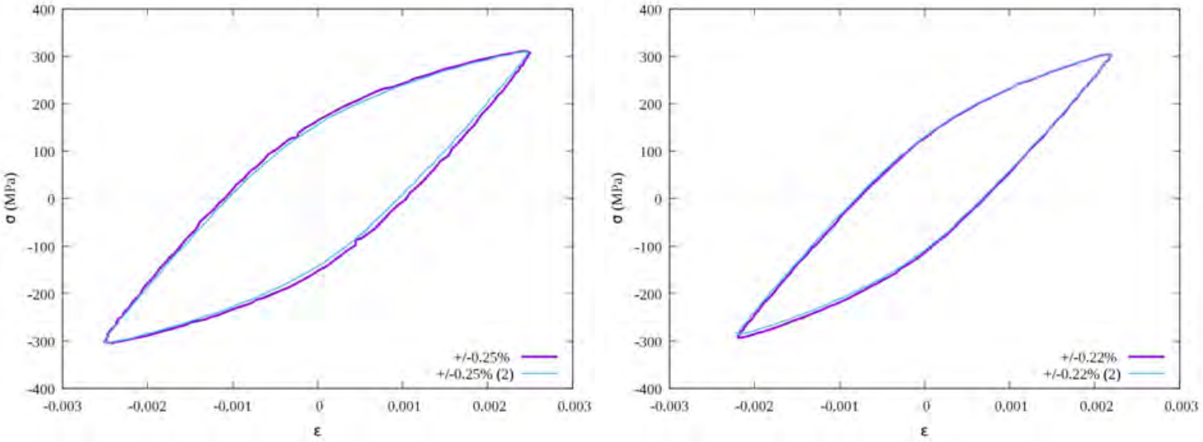

(a) 0.25 %

(b) 0.22 %

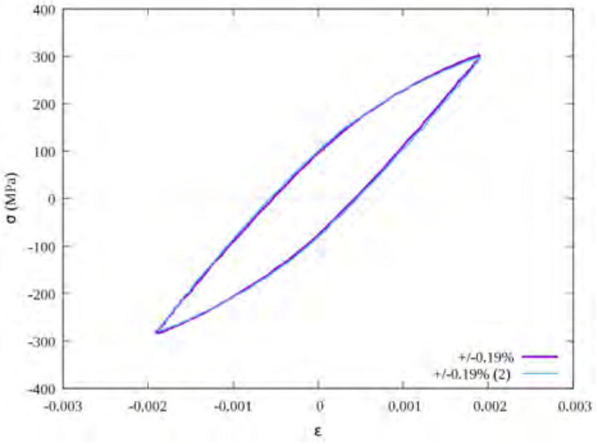

(c) 0.19 %

Figure A.8 – Superposition of the stabilized cycles $\frac{N_f}{2}$ for the strain levels 0.25 %, 0.22 % and 0.19 % along the rolling direction

Appendix B

MECHANICAL DESIGN OF THE REDRAWING PROCESS

The direct redrawing of cylindrical process is designed especially for this study from the Numisheet'99 benchmark for reverse deep-drawing. The aim is to minimize the dimensions of the benchmark to be able to perform experiments on the BUP200 machine. Moreover, the direct redrawing is chosen instead of the reverse deep-drawing to facilitate testing on this machine. The tools dimensions chosen according to specifications from the literature [107] for the redrawing process are presented in Figures B.1 and B.2 respectively for the first and second stages. The different radius are not mentioned on the drawings but they are summarized in Table B.

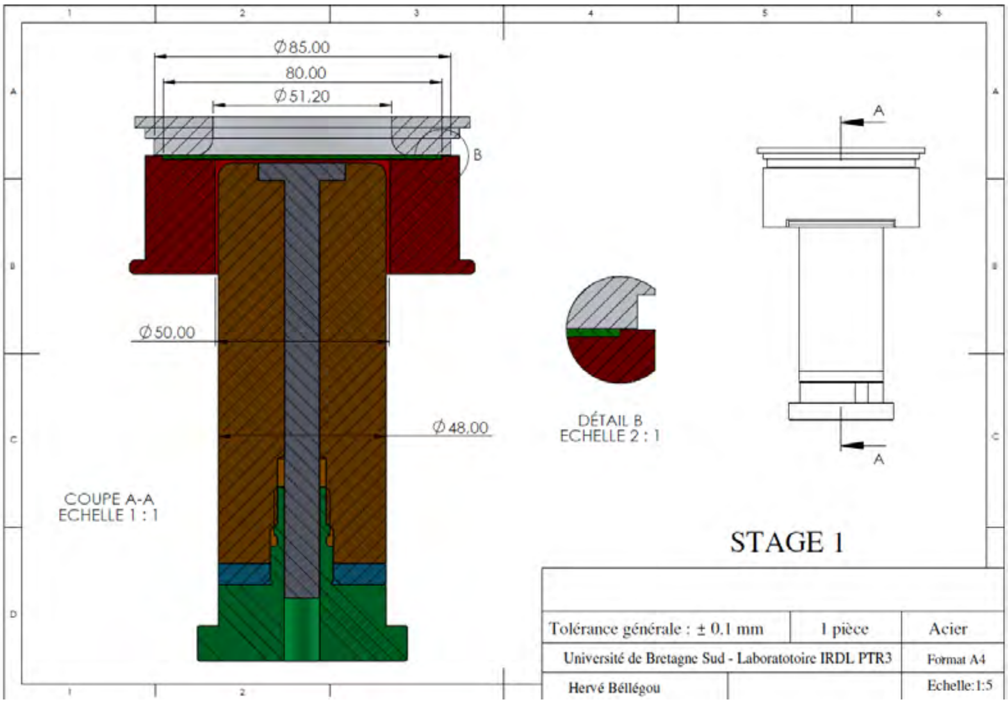

Figure B.1 – Assembly of the first stage of the redrawing process (RC1)

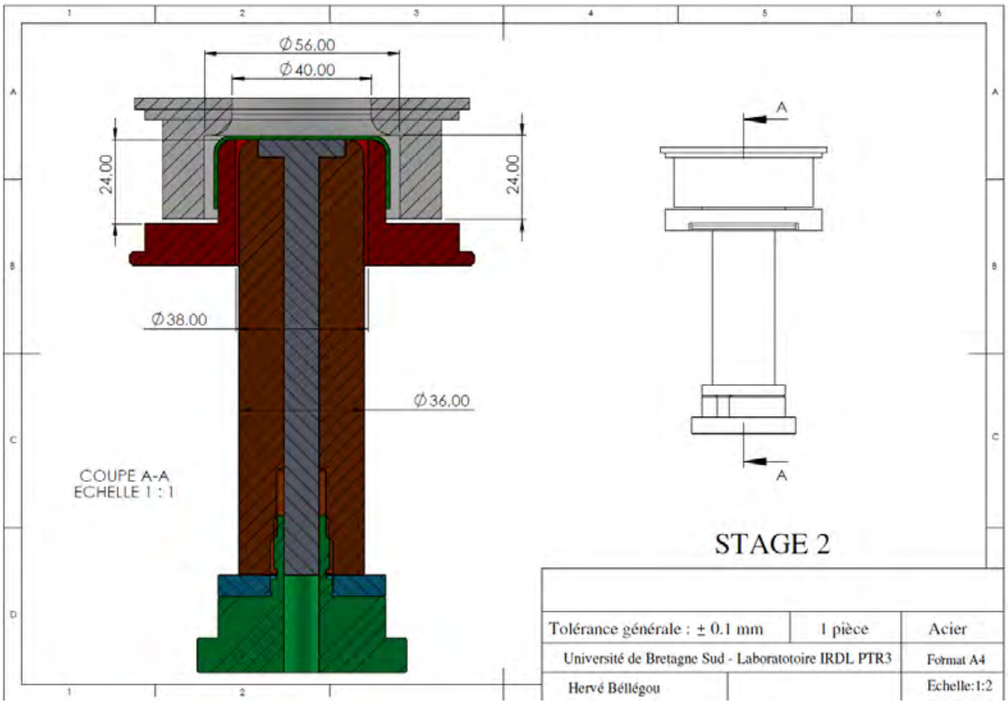

Figure B.2 – Assembly of the second stage of the redrawing process (RC2)

Table B.1 – Synthesis of the tools radius

Stage	Punch radius (mm)	Die radius (mm)
1	4	5
2	5	6

In order to validate the dimensions selected for the process, a preliminary finite element analysis is performed with the code PAM-STAMP. The material behavior is modeled with the hybrid Swift and Voce hardening law presented in Eq. 2.9 and the parameters of Table 2.4 and von Mises yield criterion. In addition, a forming limit diagram already registered for DP600 steel in PAM-STAMP is adapted for the thickness of the studied material, 1.2 mm, with the Keeler method which consists in translating the curve along the ordinate axis in function of the thickness. The forming limit curves is compared with the strain state of the cup elements at the end of each stage in Fig. B.3. The strain state of the different elements being lower than the forming limit curves for both stage, the design of the redrawing process is validated.

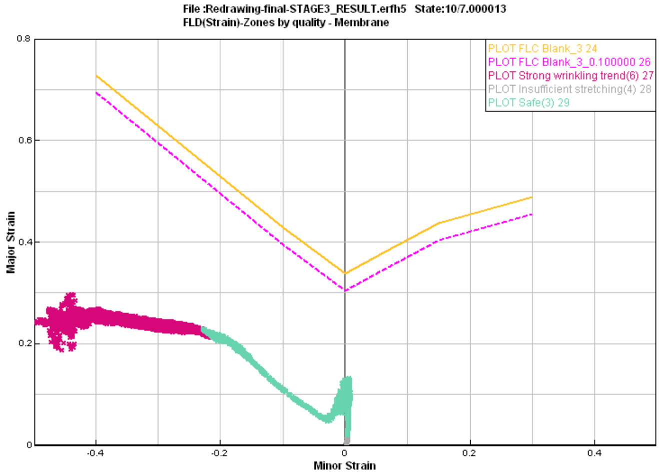

(a) RC1

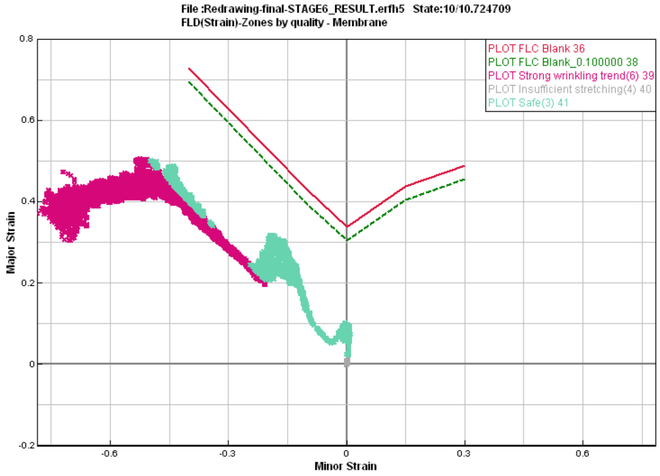

(b) RC2

Figure B.3 – Forming limit curves used for the numerical validation of the redrawing process with PAM-STAMP compared with the strain state distribution at the end of each stage

Appendix C

CORRECTIONS OF THE PUNCH-FORCE DISPLACEMENT CURVES

A difference is observed during the redrawing test between the force displayed directly on the machine and the force written in the result file. Thus, the maximal value of the force have been compared for different configurations of the redrawing test in order to investigate a large range of forces. A linear evolution of the difference is observed as a function of the average force displayed in the results files, cf. Fig. C.1(a). The equation of the linear regression is used to correct each punch force value written in the results files with the value coming from the machine, assumed to be the exact value. Likewise, this observation was not made during the tests in one stage and thus it is not possible to be sure that the correction is necessary in that case. Considering the small influence of the correction on the punch force-displacement curves of one redrawing test represented in Fig. C.1(b), the correction is neglected in the case of cups 1.

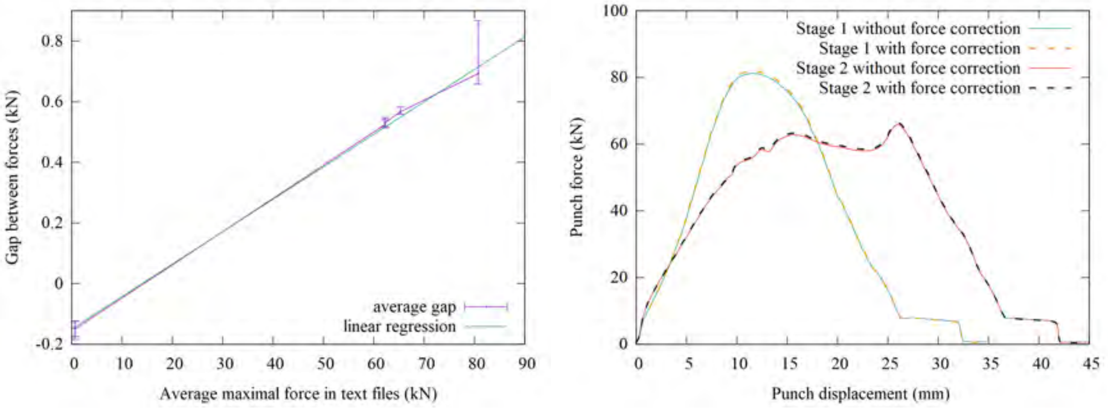

(a) Force gap

(b) Force correction

Figure C.1 – Estimation of the gap between forces and influence of the force correction on the punch force-displacement curve of one redrawing test

Furthermore, offsets are visible on the punch force-displacement curves presented above for both processes at the beginning and at the end of the test. This offset seems to increase with the punch speed, thus no-load tests are performed at different punch speeds to investigate the influence on the force value. It is observed that the no-load force increases with the punch speed value and that explains the increase of the offset value. Thus, no-load tests have been performed before each test of the redrawing process performed for strain measurement presented thereafter. These tests show that a force is present even if no load is applied. The value of the offset is also present at the end of each curve where a second plateau is visible. In order to compare the experimental results with the model prediction, the offset value present during the no-load test is deduced on the force value of the subsequent test. The offset correction applied on the punch force-displacement curve is represented for the same example than the force correction in Fig. C.2(a). This correction has a small influence on the punch force-displacement curves of the redrawing tests because the offset value is quite low with a punch speed of $1\,\mathrm{mm\,s^{-1}}$. However, the offset is important with high value of punch speed used for the forming of cups 1 but the no-load tests were not carried out in that case. The offset values obtained during the no-load tests performed before redrawing tests are very close to the values of the second plateau obtained at the end of the punch force-displacement curves. Thus, when the no-load tests are not available, the value of the force at the end of the test is deduced from the total force. Once this correction is made for C1 test, it is visible in Fig. C.2(b) that the punch speed does not have that much influence on the force level.

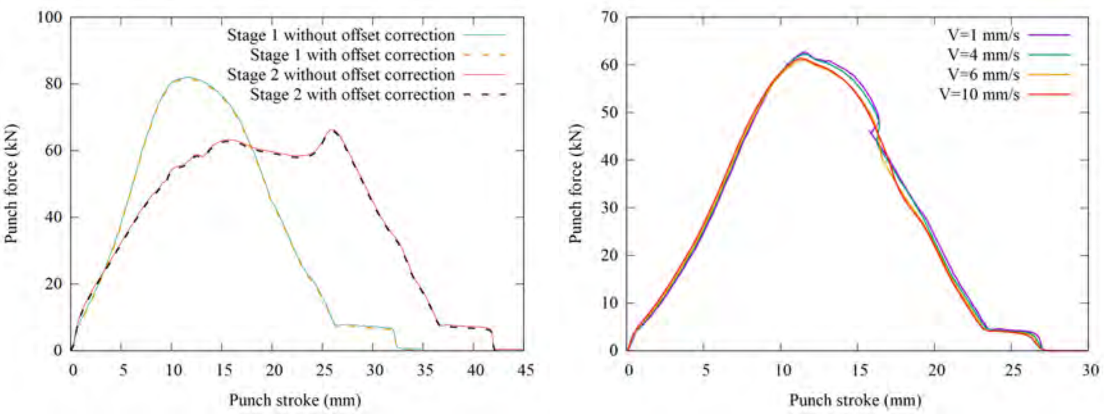

(a) RC1 and RC2 tests

(b) C1 test

Figure C.2 – Influence of the offset correction on the punch force-displacement curves

APPENDIX D

VALIDATION OF THE IMPLEMENTATION OF THE e-HAH MODEL IN PAM-STAMP

In order to validate the implementation of the e-HAH model in PAM-STAMP, the different characterization tests performed for the calibration of the model presented in the first chapter are simulated with one element. The e-HAH model is coupled to the hybrid Swift and Voce (HSV) law and von Mises yield criterion. The parameters of the identification 2 presented in Table 2.6 are used for the e-HAH model with the parameters of the isotropic hardening law presented in Table 2.4. Firstly, monotonic strain paths are simulated with a unixial tensile test and a simple shear test both along the rolling direction. The stress-strain curves presented in Figure D.1 shows an agreement between Abaqus and PAM-STAMP which validate the implementation of the isotropic hardening law in the subroutine. Then, reverse strain path changes are considered with one forward-reverse shear test and one tension-compression test, both along the rolling direction. The stress-strain curves predicted by PAM-STAMP represented in Figure D.2 are in accordance with the results expected from the Abaqus simulations. Finally, one sequential test composed of a pre-strain in tension followed by a simple shear test is simulated in PAM-STAMP to represent orthogonal strain path changes. Only the shear stress-strain curves are compared in Figure **??** and similar results are obtained for both Abaqus and PAM-STAMP simulations. Both modelings of the reverse and orthogonal strain path change behaviors are thus correctly implemented in the subroutine.

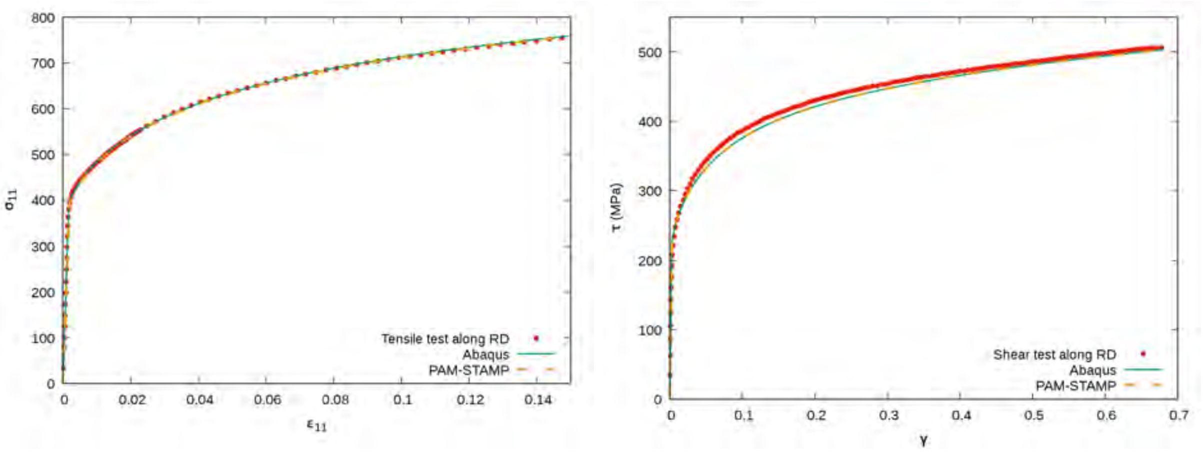

(a) Uniaxial tensile test (RD)

(b) Simple shear test (RD)

Figure D.1 – Comparison of the stress-strain curves obtained with Abaqus and PAM-STAMP for two monotonic tests

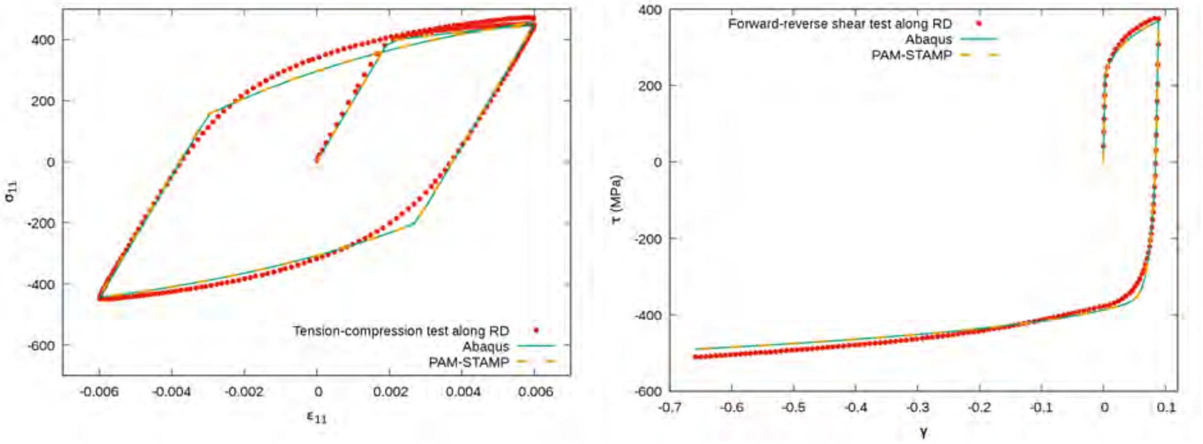

(a) Tension-compression test (RD)

(b) Forward-reverse shear test (RD)

Figure D.2 – Comparison of the stress-strain curves obtained with Abaqus and PAM-STAMP for two tests representative of reverse strain path changes

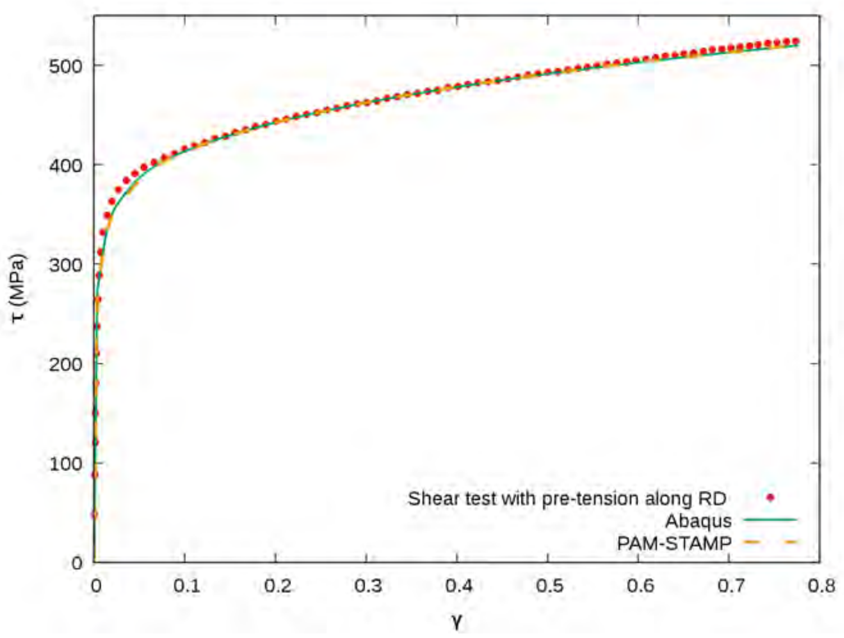

Figure D.3 – Comparison of the shear stress-strain curves obtained with Abaqus and PAM-STAMP for a simple shear test performed after a pre-strain in tension and representative of orthogonal strain path change

Appendix E

DESIGN OF THE EXPERIMENTAL FATIGUE DEVICE

The aim of this device is to apply small displacements on a cylindrical cups clamped along the top edge and subject to a slight compression. Firstly, the different parts of the fatigue device are presented in Figure E.1. The device is composed of three plates, the cup is positioned on the first one (H+U) and the two others (F+G) are connected to the hydraulic actuator (T) and the force sensor (S) that are respectively applying and measuring the compressive force on the cup. The alternated displacement is measured by a Linear Variable Differential Transformer (LVDT) represented in cyan, which controls the machine displacement. The fatigue device is designed to be installed on an hydraulic testing machine via the two purple parts (A+B). A plan with some dimensions is also available in Figure E.2.

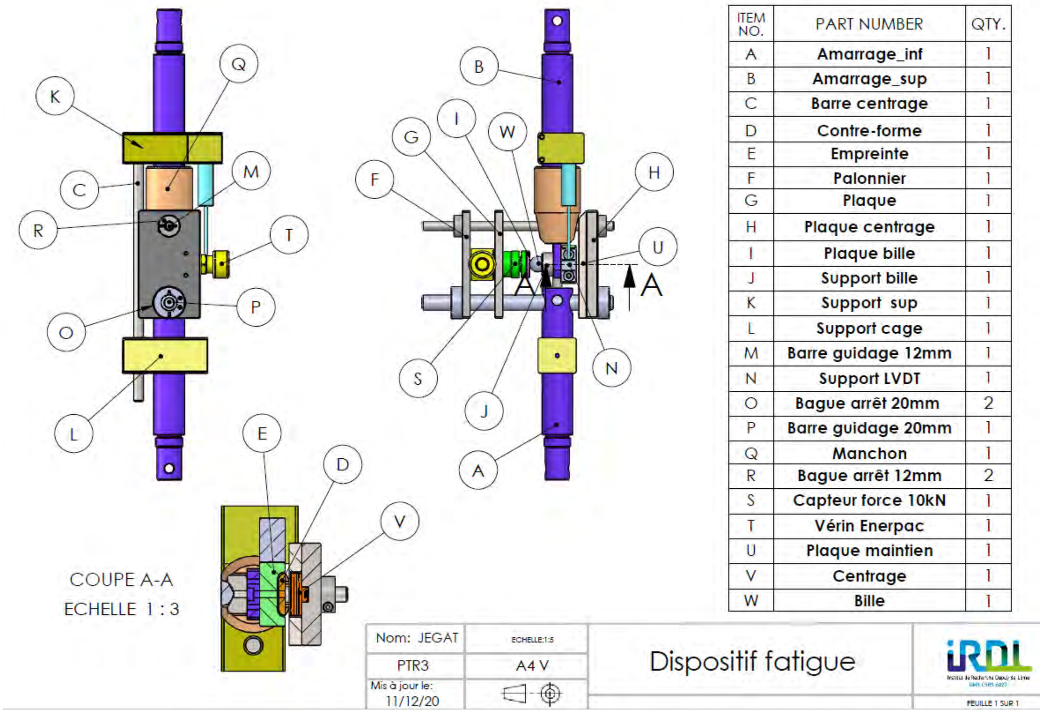

ITEM NO.	PART NUMBER	QTY.
A	**Amarrage_inf**	1
B	**Amarrage_sup**	1
C	**Barre centrage**	1
D	**Contre-forme**	1
E	**Empreinte**	1
F	**Palonnier**	1
G	**Plaque**	1
H	**Plaque centrage**	1
I	**Plaque bille**	1
J	**Support bille**	1
K	**Support sup**	1
L	**Support cage**	1
M	**Barre guidage 12mm**	1
N	**Support LVDT**	1
O	**Bague arrêt 20mm**	2
P	**Barre guidage 20mm**	1
Q	**Manchon**	1
R	**Bague arrêt 12mm**	2
S	**Capteur force 10kN**	1
T	**Vérin Enerpac**	1
U	**Plaque maintien**	1
V	**Centrage**	1
W	**Bille**	1

Nom: JEGAT
ECHELLE:1:5
PTR3
A4 V
Mis à jour le: 11/12/20
Dispositif fatigue
FEUILLE 1 SUR 1

Figure E.1 – Representation of the different parts of the fatigue device

A finite element analysis with Solidworks has been performed in order to validate the design within the elastic domain to verify that only the cup will be deformed during the test. The distribution of von Mises equivalent stress and strain obtained with these simulations is represented in Figure E.3. A weakness on the fixation due to the compressive force is found and is surrounded in red and thus the part Q is added to strengthen the original part.

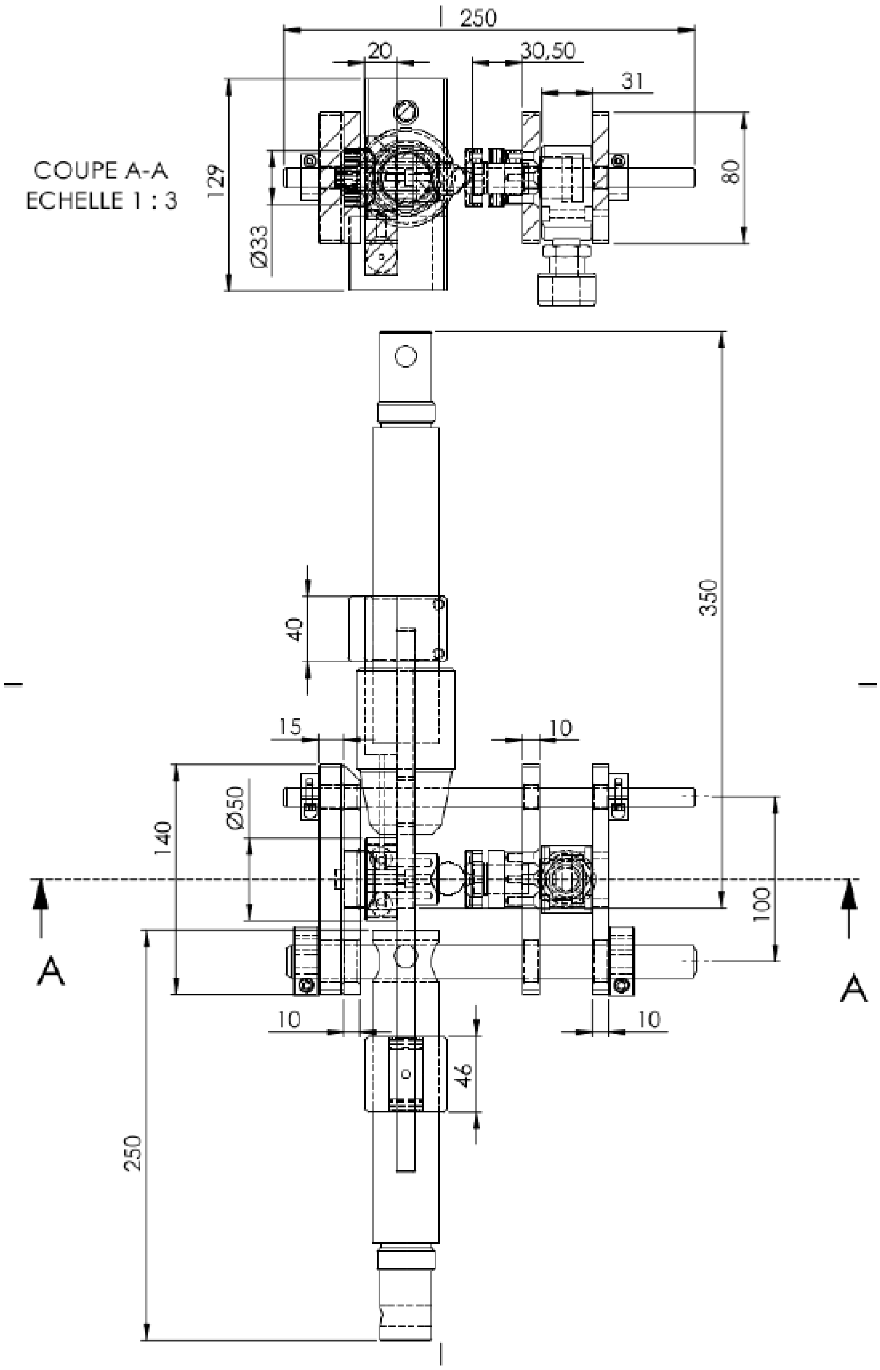

Figure E.2 – Some dimensions (in mm) of the fatigue device

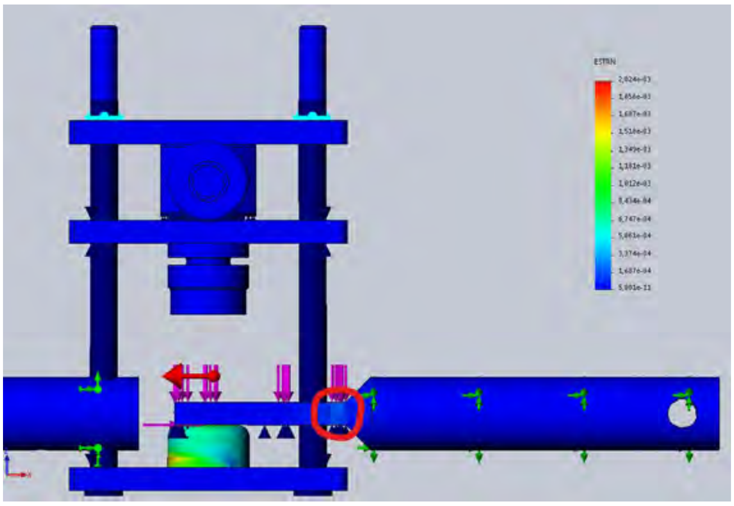

(a) Engineering strain

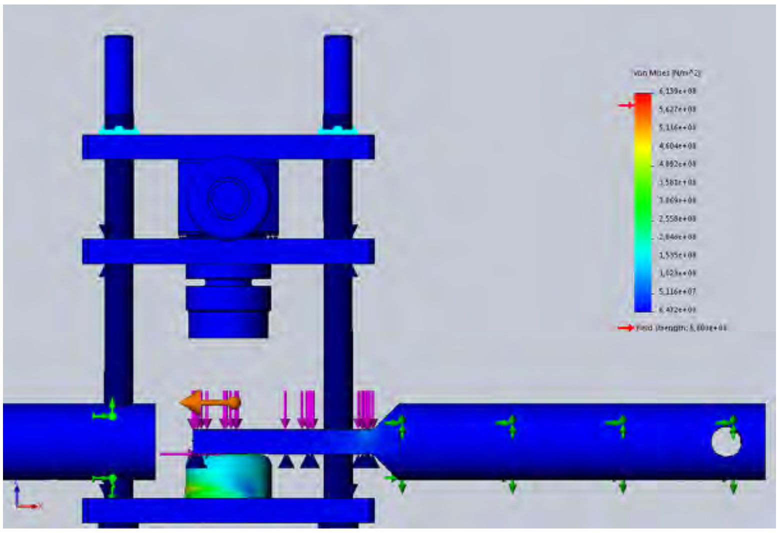

(b) von Mises equivalent stress

Figure E.3 – Strain and stress distribution the elastic simulation with Solidworks

DOCTORAT
BRETAGNE SCIENCES
LOIRE POUR L'INGENIEUR

Université
Bretagne Sud

Titre : Du formage virtuel à la tenue en service de pièces métalliques : influence des trajets complexes de déformations

Mot clés : Conception intégrée, Emboutissage, Acier biphasé, Changements de trajets de déformation, Fatigue oligocyclique

Résumé : Dans le but d'atteindre une conception intégrée des pièces de structure automobile, une première étape du chaînage numérique est mise en place dans ces travaux de thèse commençant par la mise en forme du matériau et jusqu'à la prédiction de la durée de vie de la pièce formée. L'emboutissage de godet cylindrique est considéré comme une référence capable de retranscrire les trajets complexes de déformation intervenant lors de la fabrication de pièces industrielles. Le matériau sélectionné est un acier biphasé DP600 à haute résistance couramment utilisé pour ce type d'application dans l'industrie automobile. Le comportement de ce matériau est tout d'abord caractérisé pour des trajets de déformation linéaires, non-linéaires et cycliques afin de calibrer une loi de comportement avancée, dédiée à l'emboutissage, et un critère de fatigue. L'emboutissage en une et deux étapes de godets cylindriques est réalisé expérimentalement et analysé en détails grâce aux mesures du champ de déformation et des contraintes résiduelles. Une comparaison de ces différents éléments avec les prédictions numériques permet de mettre en évidence les différents trajets de déformations intervenant lors des deux procédés et d'analyser leur influence. Numériquement, l'état final et particulièrement les champs de contraintes et de déformations obtenus après emboutissage et retour élastique sont utilisés en entrée de la simulation du chargement en fatigue. Une méthode simplifiée, basée sur l'adaptation de critères uniaxiaux pour des chargements multiaxiaux, est ensuite utilisée pour estimer la durée de vie des godets.

Title: Virtual forming of metallic sheet materials: influence of complex strain paths on service life prediction

Keywords: Integrated design, Deep drawing, Dual phase steel, Strain path change, Low cycle fatigue

Abstract: In order to reach an integrated design of car body components, a first step towards an end-to-end chain of simulations is established in this thesis beginning with the sheet metal forming process until the service life prediction of the formed part. The deep drawing of cylindrical cup in one or two stages is considered as a reference able to reproduce complex strain paths occurring during the manufacturing of industrial parts. The selected material is a DP600 dual phase steel with high strength and commonly used for this kind of application in the automotive field. The material behavior is firstly characterized for linear, non-linear and cyclic strain paths in order to calibrate an advanced constitutive law dedicated to sheet metal forming and a fatigue criterion. The deep drawing in one and two stages is experimentally performed and analyzed with measures of the strain field and the residual stresses. A comparison of these different elements with numerical predictions is carried out to highlight the occurrence of strain path changes and their influence. Numerically, the final state and particularly the strain and stress fields obtained after deep-drawing and springback are used as inputs in the fatigue loading simulation. A simplified method, based on the adaptation of uniaxial criteria to multiaxial loads, is then used to estimate the service life of cylindrical cups.